

Forschungsberichte aus dem
wbk Institut für Produktionstechnik
Karlsruher Institut für Technologie (KIT)

Nikolas Sven Matkovic

**Additive Individualization of
Continuous-Discontinuous Reinforced
Thermoplastics**

Band 287



Research report from
wbk Institute of Production Science
Karlsruhe Institute of Technology (KIT)

Editor: Prof. Dr.-Ing. Jürgen Fleischer
Prof. Dr.-Ing. Gisela Lanza
Prof. Dr.-Ing. habil. Volker Schulze
Prof. Dr.-Ing. Frederik Zanger

Nikolas Sven Matkovic

Additive Individualization of Continuous- Discontinuous Reinforced Thermoplastics

Volume 287

Additive Individualization of Continuous-Discontinuous Reinforced Thermoplastics

Zur Erlangung des akademischen Grades eines
Doktors der Ingenieurwissenschaften (Dr.-Ing.)

von der KIT-Fakultät für Maschinenbau des
Karlsruher Instituts für Technologie (KIT)

angenommene

Dissertation

von

Nikolas Sven Matkovic, M.Sc.

Tag der mündlichen Prüfung: 06.09.2024
Hauptreferent: Prof. Dr.-Ing. Jürgen Fleischer
Korreferentin: Prof. Dr. Jill Urbanic

Bibliographic information published by the Deutsche Nationalbibliothek

The Deutsche Nationalbibliothek lists this publication in the Deutsche Nationalbibliografie; detailed bibliographic data are available in the internet at <http://dnb.d-nb.de>.

Zugl.: Karlsruhe, Karlsruher Institut für Technologie, Diss., 2024

Copyright Shaker Verlag 2024

All rights reserved. No part of this publication may be reproduced, stored in a retrieval system, or transmitted, in any form or by any means, electronic, mechanical, photocopying, recording or otherwise, without the prior permission of the publishers.

Printed in Germany.

ISBN 978-3-8440-9689-7
ISSN 0724-4967

Shaker Verlag GmbH • Am Langen Graben 15a • 52353 Düren
Phone: 0049/2421/99011-0 • Telefax: 0049/2421/99011-9
Internet: www.shaker.de • e-mail: info@shaker.de

Editor's Preface

The fast and efficient implementation of innovative, sustainable and economical technologies is the decisive economic factor for manufacturing companies. Universities can add a significant contribution to the competitiveness of industry as “value-adding partners” by developing scientific fundamentals, methods and technologies as well as actively supporting the transfer process into practical application.

Within this context, this series of publications reports on the latest research results from the Institute of Production Science (wbk) at the Karlsruhe Institute of Technology (KIT). Our research work is aimed at both performance enhancement of additive and subtractive manufacturing processes, production facilities and process automation, as well as at the holistic consideration and optimization of production systems and networks. In all cases, technological as well as organizational aspects are considered.

Prof. Dr.-Ing. Jürgen Fleischer

Prof. Dr.-Ing. Gisela Lanza

Prof. Dr.-Ing. habil. Volker Schulze

Prof. Dr.-Ing. Frederik Zanger

Author's Preface

The work for this thesis was carried out as part of the DFG Research Training Group GRK2078, Integrated Engineering of Continuous-Discontinuous Long Fiber Reinforced Polymer Structures (CoDiCoFRP). This thesis was created and written during my work as a research associate at the wbk Institute of Production Science.

I would like to thank Prof. Dr.-Ing. Jürgen Fleischer for supervising my work at the wbk and for his scientific support. I would also like to thank Prof. Dr. Jill Urbanic for co-supervising this work and especially for her hospitality during my visit to the University of Windsor in Canada. Furthermore, I would like to thank Prof. Dr.-Ing. habil. Thomas Böhlke, who, as speaker of the GRK2078, ensured a successful international research exchange.

I would also like to thank all my colleagues at the wbk, especially those in the MAP research department and the service centers. My special thanks go to the colleagues who supported me during the writing of my thesis.

Special thanks go to my mother, Andjelina Matković, who has always supported me during my studies and the doctoral dissertation. Thanks also go to my siblings, Kristina and Stefan.

I would like to dedicate this work to my grandfather, Pavle Kerčević, who always inspired and supported me in my practical and technical education during my youth.

Shanghai, October 2024

Nikolas Sven Matkovic

Abstract

Components made from thermoplastic fiber-reinforced polymers (FRP), which consist of discontinuous (DiCo) and continuous (Co) fibers, offer a great opportunity to reduce weight while saving material costs compared to pure Co-reinforced components. The excellent formability of DiCoFRP is used to produce complex shapes such as ribs, while CoFRP is used to selectively improve mechanical properties. Various approaches based on conventional thermoplastic manufacturing processes, such as compression molding, can be used to produce CoDiCoFRP in larger quantities. Due to the required complexity of the tools and molds, such processes are only economical for medium to large quantities. The increasing demand for individualization cannot be met with such conventional processes. Tool-free additive manufacturing processes such as layer-by-layer material extrusion are suitable for the economical production of individual thermoplastic components in small quantities. Overall, the additive approaches from the state of the art for the production of CoDiCoFRP are still immature and are not suitable for the efficient production of large-volume components and large quantities.

The objective of this thesis is therefore to enable the individual production and subsequent individualization of CoDiCoFRP by combining conventional processes and the approach of additive manufacturing. In order to achieve this objective, a suitable process and corresponding experimental setup is developed. In the experimental setup, robotic direct extrusion is employed for processing the DiCo component, while approaches from robotic automated tape laying are adapted, combined, and further optimized for processing the Co component. With additional experimental investigations, thermal simulations, and kinematic analysis, a suitable hybridization process consisting of individually combinable process steps is developed. As the most relevant process step consolidation is identified, which increases the bonding between the Co and DiCo components during the hybridization process. Consolidation and further relevant process steps are experimentally optimized to increase the bonding for a selected material system by using the experimental setup. As input material for the DiCo component carbon short fiber reinforced granulate and for the Co component unidirectional tapes are used. The matrix material for both is polyamide 6.

For the validation of the individual production of CoDiCoFRP tensile specimens are produced. Based on tensile test according to DIN EN ISO 527-4, a high degree of fulfillment of 67 % is achieved. This value indicates that the CoDiCo composite has reached 67 % of its theoretically calculated strength, which indicates an effective hybridization and bonding process. For the process of subsequent individualization of conventionally manufactured components, a demonstrator component is produced and interface bonding tests based on ASTM D5868-01 are carried out. Long fiber thermoplastic direct molding was used as the conventional reference manufacturing process. The subsequent individualization process is developed in such a way that it can also be applied to other conventional production processes.

Kurzfassung

Bauteile aus thermoplastischen faserverstärkten Kunststoffen (FVK), die aus diskontinuierlichen (DiCo) und kontinuierlichen (Co) Fasern bestehen, besitzen ein großes Potential zur Gewichtsreduzierung bei gleichzeitiger Einsparung von Materialkosten im Vergleich zu rein Co-verstärkten Bauteilen. Die hervorragende Formbarkeit von DiCoFVK wird zur Herstellung komplexer Formen wie Rippen genutzt, während CoFVK zur gezielten Verbesserung der mechanischen Eigenschaften eingesetzt wird. Für die Herstellung von CoDiCoFVK in größeren Stückzahlen stehen verschiedene Verfahren zur Verfügung, die auf traditionellen thermoplastischen Fertigungsprozessen basieren, z. B. das Formpressen. Aufgrund der erforderlichen Komplexität der Presswerkzeuge sind solche Verfahren jedoch nur für mittlere bis große Stückzahlen wirtschaftlich. Die zunehmende Nachfrage nach Individualisierung kann mit solchen traditionellen Verfahren nicht erfüllt werden. Werkzeuglose additive Fertigungsverfahren wie die Materialextrusion im Schmelzschichtverfahren eignen sich für die wirtschaftliche Herstellung individueller thermoplastischer Bauteile in kleinen Stückzahlen. Insgesamt sind die additiven Ansätze aus dem Stand der Technik für die Herstellung von CoDiCoFVK noch unreif und eignen sich nicht für die effiziente Fertigung großvolumiger Bauteile und großer Stückzahlen.

Ziel dieser Arbeit ist es daher, durch die Kombination von traditionellen Verfahren und dem Ansatz der additiven Fertigung die individuelle Herstellung und nachträgliche Individualisierung von CoDiCoFVK zu ermöglichen. Um dieses Ziel zu erreichen, werden ein geeignetes Verfahren und ein entsprechender Versuchsaufbau entwickelt. Für die Verarbeitung der DiCo-Komponente werden robotergestützte Direktextrusion und für die Verarbeitung der Co-Komponente Verfahren des robotergestützten Tapelegen adaptiert, kombiniert und mit dem Versuchsaufbau weiter optimiert. Mit zusätzlichen experimentellen Untersuchungen, thermischen Simulationen und kinematischen Analysen wird ein geeigneter Hybridisierungsprozess aus individuell kombinierbaren Prozessschritten entwickelt. Als relevantester Prozessschritt wird die Konsolidierung identifiziert, die die Bindung zwischen den Co- und DiCo-Komponenten während des Hybridisierungsprozesses erhöht. Die Konsolidierung und weitere relevante Prozessschritte werden für ein ausgewähltes Materialsystem mit Hilfe des Versuchsaufbaus experimentell für die Erhöhung der Bindung der Komponenten optimiert. Als Ausgangsmaterial werden für die DiCo-Komponente kohlenstoffkurzfaserverstärktes Granulat und für die Co-Komponente unidirektionale Tapes verwendet. Das Matrixmaterial für beide ist Polyamid 6.

Zur Validierung der individuellen Herstellung von CoDiCoFRP werden Zugproben hergestellt. Basierend auf Zugversuchen nach DIN EN ISO 527-4 wird ein hoher Erfüllungsgrad von 67 % erreicht. Dieser Wert gibt an, dass der CoDiCo-Verbund 67 % seiner theoretisch berechneten Festigkeit erreicht hat, was auf einen effektiven Hybridisierungs- und Bindungsprozess hindeutet. Für den Prozess der nachträglichen Individualisierung von traditionell hergestellten Bauteilen werden ein Demonstratorbauteil hergestellt und Untersuchungen zu Anhaftung nach ASTM D5868-01 durchgeführt. Als traditionelles Referenz-Verfahren wurde das Langfaser-Thermoplast-Direktformpressen verwendet. Der nachträgliche Individualisierungsprozess wurde so entwickelt, dass dieser auch auf andere traditionelle Fertigungsverfahren angewendet werden kann.

Table of Contents

Table of Contents	I
Abbreviations	IV
Terms	VI
1 Introduction	1
1.1 Motivation	1
1.2 Structure of the Thesis	3
2 Background and State of the Art	5
2.1 Characteristics and Processing of FRP	5
2.1.1 Characteristics of Co, DiCo and CoDiCoFRP	6
2.1.2 Main Process Steps for FRP Processing	8
2.1.3 Conventional Processing of Co, DiCo and CoDiCoFRP	13
2.1.4 Evaluation of CoDiCoFRP and Conventional Processing	20
2.2 Additive Manufacturing of Co, DiCo and CoDiCoFRP	20
2.2.1 Classification of Fiber Reinforcement in MEX	21
2.2.2 Defects and Drawbacks of Fiber Reinforcement in MEX	24
2.2.3 Consolidation Approaches in MEX	26
2.2.4 Evaluation of the Consolidation Approaches in MEX	29
2.3 Robotic Multi-Axis MEX with Direct Extrusion	30
2.3.1 General Setup of MEX Direct Extrusion Systems	31
2.3.2 Six-Axis Industrial Robots	31
2.3.3 Multi-Axis Non-Planar AM	35
2.3.4 Fiber Reinforcement with Multi-Axis MEX	36
2.3.5 Evaluation of Robotic Multi-Axis MEX	37
2.4 Conclusion from the State of the Art	37
3 Objective and Approach	40
3.1 Objective	40
3.2 Approach	40

4	Requirements Analysis and Process Development	43
4.1	Identification of Functions and Subsystems	43
4.2	Identification of Process Parameters and Requirements	45
4.2.1	Material Selection	46
4.2.2	Process Requirements	47
4.3	Process Development and Analysis	48
4.3.1	Experimental Investigation of Hybridization Strategies	49
4.3.2	Thermal Simulations and Analysis of Consolidation I and II	63
4.4	Conclusion and Definition of the Target System	80
5	Experimental Setup Development	83
5.1	Kinematic Analysis	83
5.1.1	Kinematic Analysis of the Consolidation Unit	84
5.1.2	Kinematic Analysis of the Assembly Table	86
5.1.3	Kinematic Analysis of the Entire System	88
5.2	System Overview, Development and Functionality	90
5.2.1	Development and Testing of the Consolidation Unit	91
5.2.2	Development and Testing of the Assembly Table	102
5.2.3	Development of the Control Architecture	106
5.2.4	Development of the Digital Process Chain	107
5.3	Conclusion	118
6	Experimental Optimization of the Hybridization Steps	120
6.1	Optimization of Consolidation I	121
6.1.1	Process Window Identification and Damage Modeling	124
6.1.2	Analysis of Global Variance	127
6.1.3	Consolidation I Modeling	134
6.1.4	Experimental Optimization of Consolidation I	135
6.2	Optimization of Consolidation II	138
6.2.1	Process Window Identification and Damage Modeling	140
6.2.2	Analysis of Variance	143

6.3	Optimization of Overprinting	146
6.3.1	Pressure Build-Up During Over-Extrusion	146
6.3.2	Effect Analysis of Over-Extrusion	148
6.4	Conclusion of the Experimental Optimizations	149
7	Validation and Evaluation	150
7.1	Validation of the Optimized Process Parameters	150
7.2	Validation of Subsequent Individualization	155
7.2.1	Application of Consolidation I for Subsequent Individualization	156
7.2.2	Additive Subsequent Individualization	159
7.3	Conclusion of the Validation and Evaluation	161
8	Summary and Outlook	162
8.1	Summary	162
8.2	Outlook	165
	List of Own Publications	168
	References	170
	List of Figures	I
	List of Tables	IX
	Appendix	XII

Abbreviations

Abbreviation	Description	Unit
3D	Three dimensions	
AM	Additive manufacturing	
ANOVA	Analysis of variance	
APF	ARBURG Plastic Freeforming	
ASTM	American Society for Testing and Materials	
ATL	Automated tape laying	
CAD	Computer-aided design	
CAM	Computer-aided manufacturing	
CF	Carbon fiber	
Co	Continuous	
CoDiCo	Continuous-discontinuous	
CT	Computed tomography	
CTE	Coefficient of thermal expansion	[1/K]
DES	Direct extrusion system	
DiCo	Discontinuous	
DIN	Deutsches Institut für Normung	
DoE	Design of experiments	
DOF	Degree of freedom	
DD	Damage degree of the consolidation process	
FAST	Function Analysis System Technique	
FDM	Fused deposition modeling	
FEM	Finite element method	
FR4	Flame retardant grade 4, glass-reinforced epoxy laminate material	
FRP	Fiber-reinforced polymers	
GF	Glass fiber	
GUI	Graphical user interfaces	

I/O	Input/Output communication	
IR	Infrared	
KRL	KUKA robot language	
LFT	Long fiber thermoplastics	
LFT-D	Long fiber thermoplastics direct process	
LSAM	Large Scale Additive Manufacturing	
MEX	Material extrusion	
NC	Numeric control	
No.	Number	
PA6	Polyamide 6	
PCC	Pearson correlation coefficient	
PGE	Product generation engineering	
PLC	Programmable logic controller	
ROI	Region of interest	
RPM	Revolutions per minute	[1/min]
SPALTEN	Universal problem-solving methodology	
STL	Standard triangle language	
S1 - S5	Hybridization strategies 1 to 5	
TCP	Tool-center-point	
UD	Unidirectional fiber orientation	
w.t.	Samples without tapes	

Terms

Term	Description	Unit
A_C	Consolidated area	[mm ²]
A_{FRP}	Cross-sectional area of an FRP	[mm ²]
A_f	Cross-sectional area of fibers	[mm ²]
b	Width of rectangular element	[mm]
b_0	Initial width of rectangular element	[mm]
C_L	Lower chamber conversion factor from pressure to force, effective piston surface area	[N/bar]
C_U	Upper chamber conversion factor from pressure to force, effective piston surface area	[N/bar]
d	Half the contact length of a roller resulting from the Hertzian contact model	[mm]
d_E	Nozzle diameter of the used single screw extruder	[mm]
D_{au}	Degree of autohesion	[%]
D_b	Degree of bonding	[%]
D_f	Degree of fulfillment of the theoretical tensile strength	[%]
D_{ic}	Degree of intimate contact	[%]
E^*	Replacement E-module for contact pairing of materials 1 and 2	[GPa]
E_1	E-Modulus of material 1 for the Hertzian contact model	[GPa]
E_2	E-Modulus of material 2 for the Hertzian contact model	[GPa]
E_F	E-Modulus of a fiber	[GPa]
$E_{FRP, ,th}$	Theoretical E-Modulus of a CoFRP parallel to the fiber direction	[GPa]
E_M	E-Modulus of a matrix material	[GPa]
$F_{C,i}$	Specific value for contact force roller perpendicular to the surface, numbered with the index i	[N]
F_C	Contact force roller perpendicular to the surface	[N]
$F_W(\alpha)$	Weight force of the roller and the other moving parts depending on the orientation	[N]
$F_{max,C1}$	Maximum achievable force in the interface area for Consolidation I	[N]
g	Gravitational acceleration	[N/Kg]

H_A	Height above the UD-tape of a component	[mm]
H_S	Height of the support structure of a component	[mm]
H_T	Hight of UD-tapes in a component, quantified using number of tapes	
H_U	Height directly under the UD-tape of a component	[mm]
ID	Infill density of the support structure of a component	[%]
l_{eff}	Effective width of a roller for the Hertzian contact model	[mm]
L_H	Layer height during material direct extrusion	[mm]
m	General mass of an object	[Kg]
m_{FRP}	Total mass of an FRP composite from the individual masses of the components	[Kg]
m_i	Mass of a component i in a composite	[Kg]
n_{C1}	Number of samples per factor level combination for Consolidation I of PA6 CoDiCo CF	
n_f	Number of factor level combinations	
n_i	Number of samples for hybridization strategy i	
N_{C1}	Total number of samples for the statistical evaluation of Consolidation I PA6 CoDiCO CF	
N_i	The total number of samples required to compare two hybridization strategies	
p	Pressure during consolidation and solidification	[MPa]
$p(x)$	Pressure distribution in a contact area in x-direction	[MPa]
$p^*_{max,CR}$	Equivalent stress in the contact area of the consolidation roller	[MPa]
$p^*_{max,SR}$	Equivalent stress in the contact area of the solidification roller	[MPa]
p^*_{max}	Equivalent stress in contact area according to Hertzian contact theory	[MPa]
p_L	Lower chamber pressure in double-acting pneumatic cylinder	[bar]
p_U	Upper chamber pressure in double-acting pneumatic cylinder	[bar]
\dot{Q}_A	Summarized heat flows between CoDiCoFRP component and surroundings (Ambient)	[W]
\dot{Q}_{HP}	Summarized heat flows between CoDiCoFRP component and heated print bed	[W]
r	Radius of a compaction roller	[mm]

R_F	Tensile strength fiber	[MPa]
$R_{FRP, ,re}$	Actual achieved tensile strength of a CoFRP parallel to the fiber direction	[MPa]
$R_{FRP, ,th}$	Theoretically achievable tensile strength of a CoFRP parallel to the fiber direction	[MPa]
$S_{D,C1}(T_{CR}, F_C, v)$	Regression model for determining the damage during Consolidation I for PA6 CoDiCo CF	
$S_{D,C2}(T_{CR}, F_C, v)$	Regression model for determining the damage during Consolidation II for PA6 CoDiCo CF	
t	General variable for time duration	[s]
T	General temperature	[°C]
T_A	Ambient temperature	[°C]
$T_{CR,i}$	Specific value for temperature of consolidation roller, numbered with the index i	[°C]
T_{CR}	Temperature of compactions or consolidation roller	[°C]
T_E	Extrusion temperature for single screw extruder	[°C]
T_G	Glass transition temperature	[°C]
T_{HP}	Temperature of heated print bed	[°C]
T_M	Melting temperature	[°C]
T_{PH}	Surface preheating temperature	[°C]
U_E	Single screw extruder rotational speed in revolutions per minute	[RPM]
v	Velocity of consolidation and solidification roller	[mm/s]
v_E	Velocity of the extruder during material direct extrusion	[mm/s]
w	Width of a component	[mm]
w_0	Distance between two elements	[mm]
W	Width of a component	[mm]
x_B, y_B, z_B	Base coordinate system	
x_T, y_T, z_T	Tool coordinate system	
x_U, y_U, z_U	User coordinate system	
x_W, y_W, z_W	World coordinate system	
α	Angle between surface normal and direction of gravitation	[°]

γ	General thermal property of an FRP composite resulting from several components	
γ_i	Thermal property of the component i of an FRP composite	
μ_1	Poisson's ratio of material 1 for the Hertzian contact model	
μ_2	Poisson's ratio of material 2 for the Hertzian contact model	
$\Delta\mu_{C1}$	The effect to be identified in the statistical evaluation of Consolidation I PA6 CoDiCo CF	[MPa]
$\Delta\mu_{i,j}$	The effect to be identified between the hybridization strategy i and j	[MPa]
σ_{C1}	Estimated standard deviation for Consolidation I of PA6 CoDiCo CF	[MPa]
σ_i	Estimated standard deviation for hybridization strategy i	[MPa]
$\tau^{*max,C1,i}$	Specific value for the maximum achievable shear stresses according to the Consolidation I PA6 CoDiCo CF model, numbered with the index i	[MPa]
$\tau^{*max,C1}$	Maximum achievable shear stresses according to the Consolidation I PA6 CoDiCo CF model	[MPa]
τ_{fI}	Maximum transferable shear stress of the fiber-matrix interface before debonding	[MPa]
$\tau_{max,C1}$	Maximum achievable shear stresses in the interface area for Consolidation I	[MPa]
$\bar{\tau}_{max,OP}$	Mean maximum shear stress of test specimens from Overprinting PA6 Co with PA6 DiCo CF	[MPa]
$\bar{\tau}_{max,C1}$	Mean maximum shear stress of test specimens from Consolidation I PA6 CoDiCo CF	[MPa]
$\bar{\tau}_{max,C1S}$	Mean maximum shear stress from subsequent individualization with Consolidation I	[MPa]
$\bar{\tau}_{max,C2}$	Mean maximum shear stress of test specimens from Consolidation II PA6 CoDiCo CF	[MPa]
φ_F	Fiber volume fraction in an FRP	[%]

1 Introduction

1.1 Motivation

The use of fiber-reinforced polymers (FRP) has many advantages and is therefore widely used for industrial applications. From 2023 to 2030, the global market for composites is expected to grow at an annual rate of 7.2% (Grand View Research 2023). Due to their high specific strength and stiffness, FRPs are often used as lightweight materials to reduce CO₂ emissions in mobility applications. Their adjustable thermomechanical and chemical properties also make FRPs very suitable as construction materials for applications beyond lightweight construction. Examples include hydrogen tanks and battery housings for electromobility, numerous applications in aviation and aerospace as well as orthoses and prostheses in the field of healthcare technology. (Böhlke & Henning et al. 2020; Henning & Moeller 2020)

FRPs are material systems in which reinforcement fibers are surrounded by a polymer matrix and the two components perform different tasks. The matrix embeds the fibers, protects them from environmental influences and conducts and distributes the forces into and between the fibers. As part of a composite, fibers increase the thermomechanical properties such as stiffness and strength (Chawla 2019). In order to achieve specific mechanical properties, the type of fiber and matrix material must be matched to each other. One class of matrix materials is thermoplastics, which are easy to handle in production due to their meltability. Fibers can be distinguished not only by material but also by length. A superordinate classification distinguishes between continuous (Co) and discontinuous (DiCo) fibers. With Co-fibers, FRP can generally achieve higher mechanical properties, whereas DiCoFRP is more cost-effective and easier to process and form. By combining the two, continuous-discontinuous (CoDiCo) FRP can be produced with the advantages of both material systems, leading to an optimized overall structure according to the principle of multi-material design. (Böhlke & Henning et al. 2020; Fleischer 2021)

Manufacturing and design processes for advanced CoDiCoFRP are still immature and cannot economically utilize the advantages of combining the material systems. Current research therefore focuses on different aspects of CoDiCoFRP, such as characterization, simulation, design and new production technologies (Böhlke & Henning et al. 2020). For this reason, the investigation of new manufacturing processes with this material system is one of the subjects of this thesis.

A variety of conventional manufacturing processes exist for thermoplastic DiCoFRP, such as injection and compression molding, which allow the economical production of components in large quantities. Various state-of-the-art approaches extend these manufacturing processes for the production of CoDiCoFRP (Neitzel & Mitschang et al. 2014). The production of individual, custom-made products is not economical due to high tooling costs with conventional manufacturing processes. Tool-free additive manufacturing (AM) processes such as layer-by-layer material extrusion are suitable for the economical production of individual thermoplastic components (Leichtbau BW GmbH 2015). With suitable materials and technical equipment, Co, DiCo, or even CoDiCoFRP can be produced using material extrusion-based processes (Baumann 2020; Pandelidi & Bateman et al. 2021). The first systems for the laser sintering process now also allow the planar integration of Co-fibers and thus the production of CoFRP (Baranowski & Scholz et al. 2024). The disadvantages of most additive approaches are the long production times and only small component dimensions, which can generally be summarized in a low output rate, and various defects such as high void content in the produced composite. (Pandelidi & Bateman et al. 2021; Wickramasinghe & Do et al. 2020)

Therefore, there is currently no suitable process and production technology for the economical production of individual CoDiCoFRP with high output rates. **The objective of this thesis is therefore to enable the individual production and individualization of CoDiCoFRP through the combination of conventional processes and the approach of additive manufacturing.** Individual production means the production of FRP components from scratch with as few tools as possible. Individualization refers to the subsequent customization of FRP components manufactured using conventional processes. For example, individual components manufactured using compression molding can subsequently be individually reinforced with Co, DiCo, or CoDiCo areas.

In order to achieve the objective, the fundamental idea of additive manufacturing, i.e. the layer-by-layer and largely tool-free production of components from scratch in combination with the flexibility of industrial robots, is being used. A suitable process and an associated experimental setup are being developed in interaction with each other. The experimental production setup is used to carry out experimental optimizations for the newly developed process in order to improve the understanding of the process, among other things.

1.2 Structure of the Thesis

The objectives identified in Chapters 2 & 3 and the resulting subtasks which are processed in Chapters 4 - 7 of the thesis are shown in Figure 1-1.

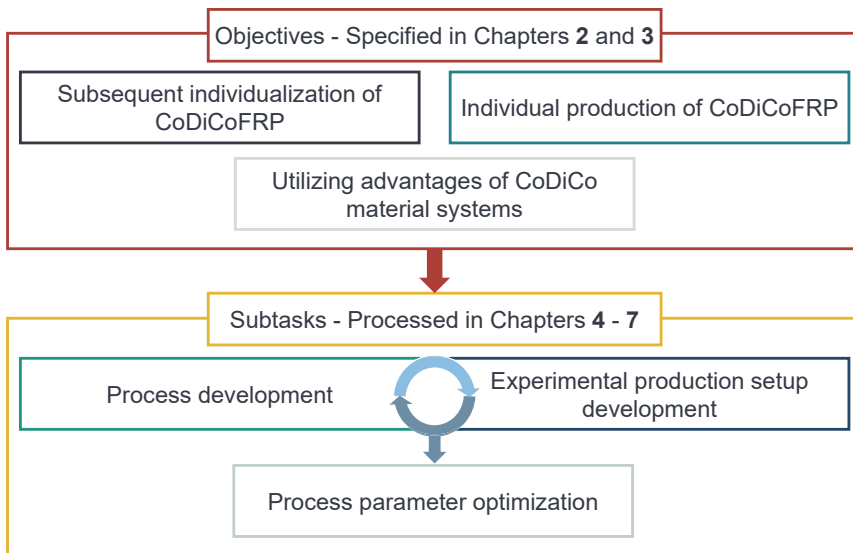


Figure 1-1: Overview of the objectives and derived subtasks of the thesis

In order to gain a better understanding of thermoplastic CoDiCoFRP and its production technology, a literature review is carried out at the beginning of Chapter 2. Conventional processes and their potential for subsequent individualization are examined. The same is done for additive processes with regard to individual production. Due to their relevance for this thesis, robotic additive processes are examined separately. In addition to creating a general understanding of materials and processes for CoDiCoFRP, research gaps, questions and potentials are identified, which are used to further define the objective. In addition, reference systems are identified that are used for the system and process development in Chapters 4 and 5.

Based on the research gaps and research questions identified in Chapter 2, precise objectives are defined in Chapter 3. The methodological approaches are derived for the following Chapters. In Chapter 4, a suitable process and its process steps for the objectives are identified with the help of a requirements analysis, experimental preliminary

investigations and thermal simulations. Based on the findings in Chapter 4, the development of a suitable prototypical experimental setup for the identified process is carried out and presented in Chapter 5. The experimental setup is further investigated and optimized with the help of individual experiments.

Relevant process steps and their process parameters identified in Chapter 4, using the experimental setup developed in Chapter 5, are experimentally optimized in Chapter 6. The optimization takes place for a selected material system. In addition to the development of an experimental procedure for identifying suitable process parameters, the process understanding is also increased. A multi-stage validation is carried out in Chapter 7. In addition to the validation of the optimized process parameters, it is generally validated whether the developed process is suitable for the subsequent individualization and individual production of CoDiCoFRP. Chapter 7 concludes by summarizing the development of the novel process and the experimental setup and provides an outlook on further processing.

2 Background and State of the Art

The aim of this chapter is to analyze relevant manufacturing processes for the production of CoDiCoFRP and to identify research gaps. First, the mechanical characteristics of CoDiCoFRP as well as basic manufacturing steps and their influence on the mechanical characteristics are briefly described. This is followed by an analysis of the state of the art of conventional manufacturing processes for thermoplastic FRP. Additionally, relevant additive manufacturing processes and robotic approaches for the individual production of CoDiCoFRP are analyzed in separate sections due to their relevance to this thesis. The findings of the analysis and literature review, including identified production systems, are used as reference systems in the later Chapters 4 - 6.

2.1 Characteristics and Processing of FRP

FRP is a composite material consisting of a polymer matrix with embedded fibers. The main function of the matrix is to hold the fibers in position and support them, to protect them from environmental influences, and to transfer and distribute stresses into and between the fibers. Based on the matrix material used, FRP can be classified as fiber-reinforced thermoplastics, thermosets, or elastomers (Thomas & Kuruvilla et al. 2013, p. 7; Schürmann 2007, p. 108). The various matrix materials can be combined with different fiber materials to create specific mechanical characteristics. The most common fiber materials are carbon, glass and aramid fibers, although natural fibers are also being used more and more frequently (Prashanth & Subbaya et al. 2017). This thesis focuses explicitly on thermoplastic FRP with carbon and glass fibers, as these are the most common fibers for technical applications.

A further subdivision and classification of FRP can be made based on the length of the fibers. Fiber lengths in the range of 0.1 - 1 mm are usually referred to as discontinuous short fibers, 1 - 50 mm as discontinuous long fibers, and lengths greater than 50 mm as continuous fibers (Schürmann 2007, p. 138). In this thesis, no further distinction is made between short and long fibers and the term DiCo-fibers is used to refer to both. The combination of Co and DiCo-fibers as well as a matrix results in CoDiCoFRP composites with hybrid properties (Böhlke & Henning et al. 2020). In the following subsections, the qualitative characteristics of thermoplastic Co, DiCo and CoDiCoFRP are described and the processing methods relevant to the thesis are presented.

2.1.1 Characteristics of Co, DiCo and CoDiCoFRP

The following section explains the influence of Co, DiCo and CoDiCo-fibers on the mechanical properties and failure behavior of FRP.

2.1.1.1 Mechanical Characteristics

Due to their high specific strengths and stiffnesses, FRPs have a very high lightweight construction potential. In addition, they have a high energy absorption capacity and can be used for impact elements. Co and DiCoFRP possess distinct characteristics as can be seen in the generalized and normalized Figure 2-1.

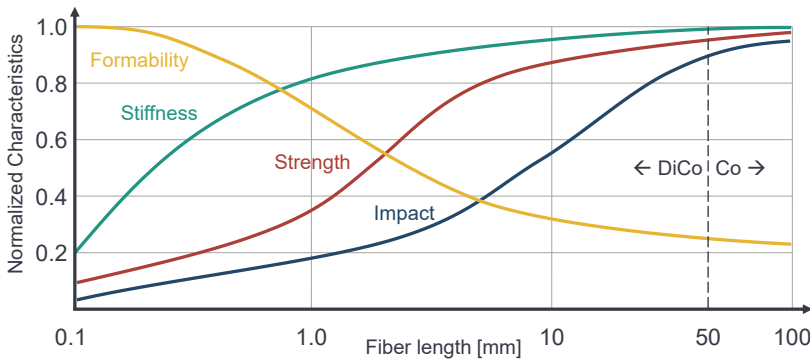


Figure 2-1: Qualitative illustration of normalized characteristics of composites for increasing fiber lengths with constant fiber content (based on (Chawla 2019, p. 155))

Assuming a constant fiber volume fraction φ_F in a composite and standard ambient temperature of approx. 20 °C, the increase of the characteristics is correlated to the fiber length. The strength and impact absorption only improve significantly with increasing fiber length, whereas the stiffness already improves with short DiCo-fibers (Chawla 2019, p. 154). In general, the formability of DiCoFRP is considerably better than that of CoFRP. In general, reinforcement with fibers leads to an improvement in thermomechanical properties, i.e. stiffness and strength remain relatively high at increasing temperatures compared to non-reinforced thermoplastics (Schürmann 2007, p. 247–253).

Overall, Co and DiCoFRP have varying advantages and disadvantages. When combined to form a CoDiCoFRP, the disadvantages of the individual components can be eliminated for the most part, and their advantages utilized. The formability of DiCoFRP yields a higher degree of design freedom, allowing the economic production of complex

geometries which can be reinforced with Co-fibers (Böhlke & Henning et al. 2020, p. 1–2). An example of a CoDiCoFRP application is shown in Figure 2-2, where the floor for a lightweight vehicle is largely made of CoFRP due to the high requirements for stiffness, strength and impact resistance.

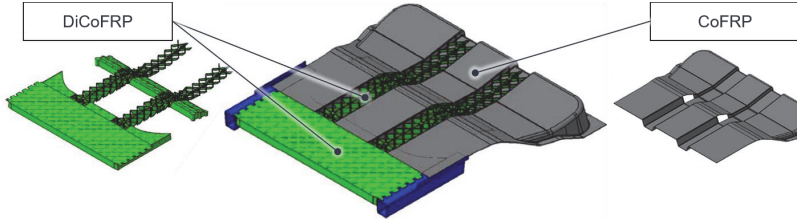


Figure 2-2: Flor structure of a vehicle made of continuous and discontinuous reinforced polyamide 6¹

Areas with complex shapes such as ribs or areas for inserts are made from DiCoFRP, as these cannot be formed from CoFRP. Hybridization can lead to an optimal overall structure that utilizes the positive properties of the individual material systems (Fleischer 2021; Böhlke & Henning et al. 2020).

Various approaches can be used to estimate the mechanical properties of FRP. According to Voigt (1889), the theoretical modulus of elasticity $E_{FRP,||,th}$ of CoFRP parallel to the fiber direction can be estimated based on a simple ratio rule as shown in Equation 2-1. The resulting E-modulus depends on the fiber volume fraction φ_F and the E-modulus of the fiber E_F and the matrix E_M .

$$E_{FRP,||,th} = \varphi_F \cdot E_F + (1 - \varphi_F) \cdot E_M \quad 2-1$$

Assuming that the E-modulus of the fiber is several times higher than that of the matrix and that failure only occurs under tension, Equation 2-2 (Schürmann 2007, p. 348) can be used to estimate the theoretical tensile strength $R_{FRP,||,th}$ of CoFRP under ideal conditions.

$$R_{FRP,||,th} = R_F \cdot \frac{E_F \cdot \varphi_F + E_M \cdot (1 - \varphi_F)}{E_F} \quad 2-2$$

¹ Continuous tapes, D-LFT meet up in new compression molding process, <https://www.compositesworld.com/articles/continuous-tapes-d-lft-meet-up-in-new-compression-molding-process> [Accessed: 07.03.2024]

2.1.1.2 Failure Behavior

Common failure mechanisms for an FRP are matrix cracking, fiber break, fiber pull-out and debonding (Chawla 2019, p. 431; Ehrenstein 2006, p. 135). Although these types of failures can occur for Co, Dico and CoDiCoFRP there are differences in the exact causes, which are discussed below.

If the main failure mode of a composite is fiber breakage, the reinforcement effect of the fiber has been fully utilized leading to a brittle material behavior. To achieve this, certain conditions must be met such as sufficient fiber-matrix bonding and fiber length (Chawla 2019, p. 431). In the case of a DiCoFRP with particularly short fibers, this can only be achieved if the interface quality and thus the bonding between fiber and matrix is especially high. For CoFRP, this condition is achieved more easily due to the significantly greater length of fibers. However, in the case of defects such as voids in the interface, fiber pull-out can occur despite theoretical fulfillment of the conditions.

The bond between the matrix-fiber interface, which can be characterized by the maximum transferable shear stress τ_{fI} before debonding, has a major influence on the utilization of the fibers as described above. Processing, especially the process steps impregnation, consolidation and solidification, have a significant impact on τ_{fI} and are discussed in more detail in the following section.

2.1.2 Main Process Steps for FRP Processing

Regardless of whether it is for a Co or DiCoFRP or a combination of both, processing follows a very similar sequence. As can be seen in Figure 2-3, the processing generally consists of impregnation, consolidation and solidification.

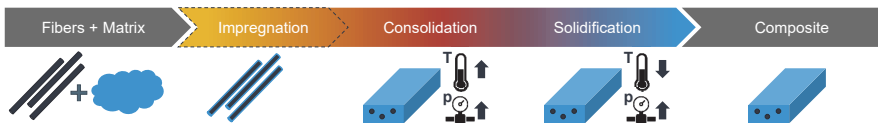


Figure 2-3: Basic principle and sequence of FRP processing (based on (Neitzel & Mitschang et al. 2014, p. 207))

As shown in the figure, the transition between the individual process steps is often not clearly separated or even occurs simultaneously. Depending on the context, the three process steps are often grouped and referred to solely as consolidation. When the individual steps are considered separately, as shown here, consolidation is seen as the

step to reduce the void content in the composite. During solidification, the thermoplastic component in the composite solidifies again. (Neitzel & Mitschang et al. 2014, p. 207–208)

The crucial process parameters for all three process steps are temperature, pressure and time. The pressure is kept high in all three steps, while the temperature is lowered during solidification. A more detailed explanation of the micro- and macroscopic processes involved in impregnation, consolidation and solidification is given in the following subsections.

2.1.2.1 Impregnation

Impregnation is the wetting of the individual fibers with the matrix material and the filling of cavities between the fibers. A major influencing factor in the processing of FRP is whether the fibers are already pre-impregnated or dry. Dry fibers must be impregnated before or during processing, whereas pre-impregnated fibers – so-called prepregs – are already impregnated with the matrix and can be processed directly, and can therefore lower manufacturing costs under certain conditions (Henning & Moeller 2020, p. 359). The quality and degree of impregnation – which increases with surface coverage of the fibers and low void content – has a significant influence on the bonding between fibers and matrix and can therefore affect the mechanical properties of manufactured composites (Vedernikov & Minchenkov et al. 2022, p. 12). Due to the high viscosities compared to thermoset matrix materials, impregnation with thermoplastics is usually performed in a specialized impregnation unit (Henning & Moeller 2020, p. 366; Hopmann & Wilms et al. 2021, p. 1300). As seen in Figure 2-4 it is more difficult with a matrix material with higher viscosity to completely impregnate a fiber roving.

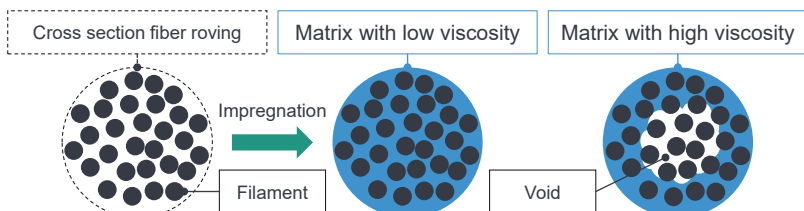


Figure 2-4: Cross section of fiber rovings and influence of matrix viscosity on the degree of impregnation (based on (Shi & Mizuno et al. 2022, p. 6))

Individual fiber filaments, especially on the inside (cf. Figure 2-4 right), are often not fully impregnated and voids remain. Since the matrix material cannot transmit forces to

these non-impregnated fibers, they contribute only to a limited extent to the reinforcement effect. (Shi & Mizuno et al. 2022)

A widely used example of pre-impregnated Co-fiber semi-finished products is unidirectional(UD)-tape. As shown in Figure 2-5, these consist of Co-fibers surrounded by a thermoplastic matrix. UD-tapes are designed for automated processes with little waste and offer many customization options (Hopmann & Wilms et al. 2021, p. 1300).

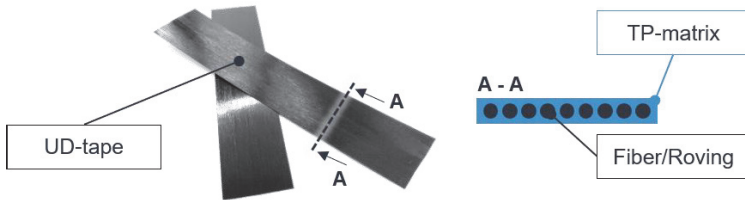


Figure 2-5: Simplified representation of the cross-section of an UD-tape consisting of Co carbon fibers and thermoplastic matrix

A main advantage of UD-tapes is the high impregnation quality, which can be traced back to the good surface accessibility due to the flat shape and UD orientation of the fiber and advanced impregnation processes (Henning & Moeller 2020, p. 366–369; Link 2022, p. 5–9). Due to the mentioned advantages of UD-tapes, this thesis uses UD-tapes to produce the Co component of CoDiCoFRP.

2.1.2.2 Consolidation and Solidification

To quantitatively describe the consolidation and solidification process, the degree of bonding D_b , also frequently referred to as the degree of consolidation, of a thermoplastic interface can be used. D_b represents the achieved percentage of the theoretical maximum bond strength of an interface. Where $D_b = D_{ic} \cdot D_{au}$ results from the multiplication of the degree of intimate contact D_{ic} and the degree of autohesion D_{au} (Bourban & Bernet et al. 2001, p. 1053). The intimate contact describes in practical terms what percentage of an interface between two objects is in physical contact (Stokes-Griffin & Matuszyk et al. 2012, p. 64). Figure 2-6 and Equation 2-3 describe a simple model for D_{ic} (Lee & Springer 1987, p. 1031).

$$D_{ic} = \frac{b}{b_0 + w_0}, \quad D_{ic} \in [0 \% ; 100 \%] \quad 2-3$$

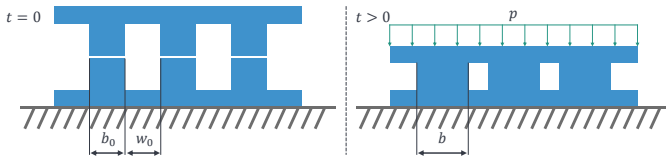


Figure 2-6: Illustration of an idealized rough interface at time $t = 0$ without any pressure and $t > 0$ with applied pressure (based on (Lee & Springer 1987, p. 1030))

Since no surface is perfectly smooth, the roughness at time $t = 0$ is idealized by a series of rectangular elements with the initial width b_0 and distance w_0 . After an applied pressure p at the time $t > 0$ the elements spread to the width b . Once there are no more voids in the interface, D_{ic} is 100% and a completely intimate contact is achieved. Assuming a thermoplastic material, D_{ic} is a function of temperature, pressure and time (Lee & Springer 1987, p. 1031). The time to achieve complete intimate contact decreases significantly with increasing temperature and pressure (Bourban & Bernet et al. 2001).

Once intimate contact is achieved and sufficient temperature and pressure are applied, bonding takes place, which can mainly be traced back to autohesion. As shown in Figure 2-7 b), diffusion of the polymer chains across the interface occurs, resulting in stronger bonding with increasing time. The degree of autohesion D_{au} describes the percentage achieved of the theoretical maximum bonding strength (Lee & Springer 1987, p. 1035–1037).

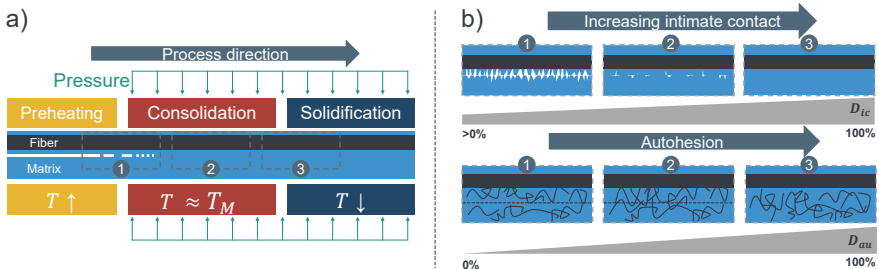


Figure 2-7: a) Process sequence from heating to consolidation to solidification; b) Development of intimate contact and autohesion in the interface area (based on (Narnhofer & Schledjewski et al. 2013, p. 707; Yang & Pitchumani 2002, p. 425))

Using UD-tapes as an example, Figure 2-7 a) shows the whole process sequences of the consolidation and solidification process. The UD-tape is brought together with the

thermoplastic matrix material and both are preheated. If the thermoplastic is amorphous, the processing temperature is above the glass transition temperature T_G , whereas for a semi-crystalline thermoplastic it has to be above the melting temperature T_M (Katayama 2013, p. 282–283). After preheating, additional pressure is applied, consolidation and the formation of intimate contact begins. The consolidation pressure is usually less than 1 MPa, but can be significantly higher in some manufacturing processes (Amirkhosravi & Pishvar et al. 2018, p. 1). As can be seen in Figure 2-7 b) the degree of intimate contact D_{ic} and autohesion D_{au} increases as the process and time progress. Corresponding to Figure 2-7, Figure 2-8 shows the qualitative ideal curves of the process parameters temperature and pressure.

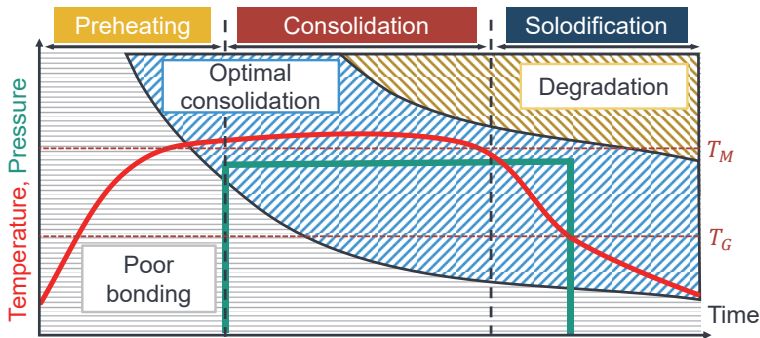


Figure 2-8: Optimal qualitative curves of process parameters during consolidation and solidification for a semi-crystalline thermoplastic as matrix material (based on (Bourban & Bernet et al. 2001, p. 1047–1051))

In order to achieve a high degree of bonding D_b , the parameters must be within a certain range depending on each other. Although high pressure and temperature generally lead to a higher value of D_b , they can also lead to degradation of the composite and/or deformation of the FRP. Transitioning from consolidation to solidification, the temperature decreases while the pressure remains high (Neitzel & Mitschang et al. 2014, p. 208). If the pressure is removed before the thermoplastic has cooled sufficiently and the thermoplastic is still above the glass transition temperature, voids can grow or form due to expanding air that may still be present in the composite (Colton & Muzzy et al. 1992; Elsner & Eyerer et al. 2012, as cited in Link 2022, p. 13). This negative effect can be intensified with hydrophilic matrix materials such as polyamide 6 (PA6), which is used in this thesis, due to evaporation of the moisture and the formation of vapor bubbles (Gröschel & Drummer 2014).

Consolidation and solidification with the right process parameters generally have a positive effect not only on the fiber-matrix interface in a composite, but on the composite as a whole. Overall, the void content in the composite can be reduced, thus increasing the strength of the component. This is due to the fact that voids in the material cause an increase in stress due to the notch effect, which quickly leads to failure (Schürmann 2007, p. 25; Mehdikhani & Gorbatikh et al. 2019). Finding suitable process parameters for consolidation and solidification that follow the principle of Figure 2-8 is part of this thesis and is carried out experimentally in Chapter 6. After the general discussion of relevant process steps in the manufacturing of FRP, the following section examines selected conventional manufacturing processes for FRP from the state of the art.

2.1.3 Conventional Processing of Co, DiCo and CoDiCoFRP

In the following section, conventional processes relevant to this thesis, for the production of thermoplastic Co, DiCo and CoDiCoFRP are presented and analyzed. Figure 2-9 shows an overview and tendential classification of the common manufacturing processes for thermoplastics that can be used to produce FRP.

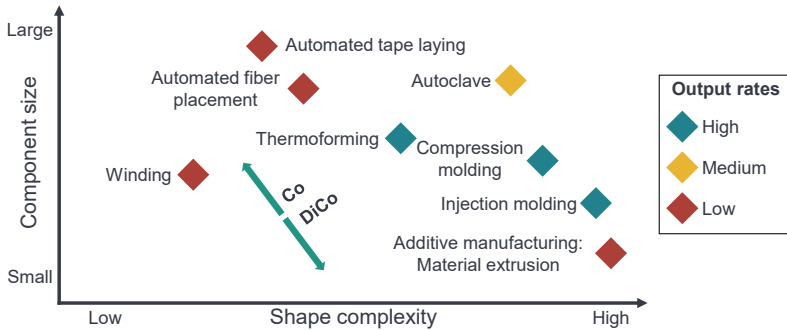


Figure 2-9: Tendencies of selected thermoplastic manufacturing processes in terms of component size, shape complexity and output rates (based on (Neitzel & Mitschang et al. 2014, p. 203))

The tendential classification in Figure 2-9 is not always valid due to many special variants of the manufacturing processes. However, there is a tendency for large and simply shaped CoFRP to be manufactured using variations of tape-laying processes. The output rate is low in terms of quantities. Compression and injection molding are suitable for large quantities and are often used for the production of small to medium-sized Di-

CoFRP with relatively complex shapes. In the following, automated tape laying, compression molding and thermoforming are briefly explained individually. It is then shown how these can be combined for the production of CoDiCoFRP. The potential with regard to individualization is evaluated. Since the production of CoDiCoFRP through AM material extrusion is the main focus of this thesis and is not considered a conventional process, the state-of-the-art is presented and evaluated in detail in Chapter 2.2. Robotic AM approaches for the production of large components are also analyzed separately in Chapter 2.3.

2.1.3.1 Processing of CoFRP

Many different manufacturing processes for the production of CoFRP exist. Since the focus of this work is on the use of UD-tapes, relevant manufacturing processes for these will be presented.

Thermoforming of CoFRP

The manufacturing processes for composites from UD-tapes can be divided into thermoforming or tape-laying processes (see Figure 2-10). Thermoforming refers to different processes that use heat and a tool to consolidate and shape the composite (Fleischer & Teti et al. 2018, p. 607; Neitzel & Mitschang et al. 2014, p. 393–402; Chawla 2019, p. 153). Processes that can be classified as thermoforming include a molding step as shown in Figure 2-10 a).

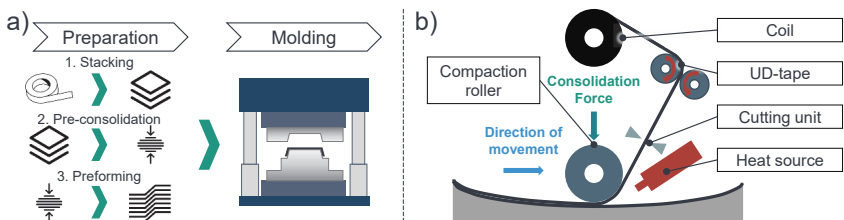


Figure 2-10: a) Thermoforming process chain for the production of components from UD-tapes with a press (based on (Link 2022, p. 9; Kupzik 2022, p. 9)); b) Basic principle of automated tape laying

In this example, the tapes are first cut to size, stacked on top of each other, pre-consolidated and, if necessary, preformed. Final forming and consolidation then take place in a press. (Henning & Moeller 2020, p. 623–624; Kropka & Muehlbacher et al. 2017, p. 97–99; Link 2022, p. 9)

Automated Tape Laying

Automated tape laying (ATL), or similar automated fiber placement processes, offer a flexible alternative to thermoforming processes. Since stacking and consolidation are performed in-situ, significantly less equipment is required (Yassin & Hojjati 2018, p. 1677). As shown in Figure 2-10 b), the end-effectors of ATL systems mainly consist of a feeding system for the UD-tapes and a compaction roller including a heat source for the consolidation and are often referred to as tape-laying-head in the literature. The end-effectors are mostly handled by robots or by multi-axis portal systems (Neitzel & Mitschang et al. 2014, p. 325). Sophisticated feeding systems enable special tape-laying-heads to process several types of tape in different widths at the same time, which increases flexibility but also complexity and the dimensions of the end-effector (Fleischer & Gebhardt 2013). Most commonly hot gas, laser, or infrared(IR)-heaters are used as the heating source (Yassin & Hojjati 2018, p. 1680). End-effectors with a single compaction roller design are the most common, even though they can have a high void content with a single pass, due to a low consolidation time. In general, a low void content – and therefore a high degree of intimate contact D_{ic} (cf. Chapter 2.1.2.2) – can be achieved, if the process parameters (consolidation pressure, time and temperature, cf. Chapter 2.1.2.2) are optimized. A higher energy input generally leads to a higher degree of bonding D_b , but can also lead to thermal instability and damage of the UD-tapes, if the individual process parameters are not properly adjusted to each other (Yassin & Hojjati 2018, p. 1684–1685; Khan & Mitschang et al. 2010, p. 110). These process-related correlations are used as reference knowledge in the experimental optimization in Chapter 6 of the consolidation process developed in this thesis.

In addition to the above-mentioned factors, the shape and, in particular, the stiffness of the compaction roller has a considerable influence on the in-situ consolidation process. Compaction rollers with a soft covering lead to a relatively homogeneous and large-area pressure distribution in the contact interface to the UD-tape, which increases the effective consolidation time and also reduces the risk of damage due to stress increases (Jiang & He et al. 2019, p. 868; He & Jiang et al. 2022; Bakhshi & Hojjati 2020, p. 20). The disadvantage is that the exact pressure distribution can only be predicted to a limited extent with very complex dynamic contact modeling (Cheng & Zhao et al. 2018, p. 1421). These conclusions are used in this thesis for the development of a specific consolidation unit in Chapter 5.2.1

Since the in-situ consolidation process in ATL does not take place in a closed environment with constant or controllable boundary conditions, like in thermoforming, the process is not yet fully mature despite decades of research. With the help of more advanced simulation models for the formation of the intimate contact, autohesion, heat transfer, void growth and migration, pressure distribution, etc., the behavior of in-situ consolidation can be predicted more precisely (Yassin & Hojjati 2018, p. 1685–1708). Nevertheless, the models are still not accurate enough on their own and have to be combined with experimental trial and error methods to determine optimal process parameters (Yassin & Hojjati 2018, p. 1708). The optimization goal is to maximize bonding and reduce void content without causing damage to the composite or thermal degradation. The same principle is applied to the optimization of the developed consolidation process in this thesis in Chapter 6.

In comparison to thermoforming processes, ATL is only suitable for small quantities, as the in-situ consolidation process is time-consuming. The advantages of ATL are their higher flexibility for simple shapes, as they are not bound to fixed mold tools, and their ability to produce very large composites with robot systems using additional linear axes (Yassin & Hojjati 2018, p. 1714).

2.1.3.2 Processing of DiCoFRP

Compared to CoFRP components, DiCoFRP are significantly less expensive, and due to their better formability, more complex component shapes can be produced in large quantities. Compression molding enables the production of large components with long DiCo-fibers with relatively low cycle times. As shown in Figure 2-11, the process consists of three main steps.

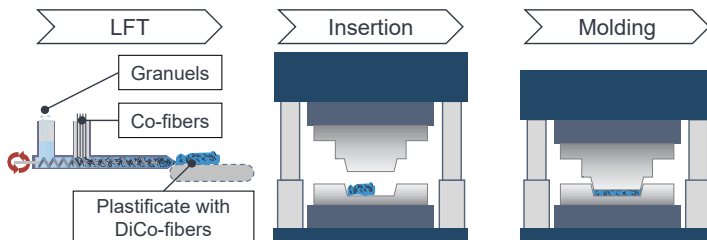


Figure 2-11: Direct compression molding of LFT (based on (Chawla 2019, p. 155; Kupzik 2022, p. 8))

In the first step, the long fiber thermoplastic (LFT) plastificate is prepared by using an extruder. One method is the LFT-(D)direct process, where the Co-fibers are shredded into DiCo-fibers and mixed with the thermoplastics directly in the extruder. An alternative method is to use LFT pallets. The advantage of LFT-D is that the fiber content and length as well as the desired material combination can be set directly on the plant (Neitzel & Mitschang et al. 2014, p. 384–391). After preparation, the still hot plastificate can be inserted into the heated press with the use of a robot. The mold is significantly cooler than the plastificate, which requires a quick closing and compression molding to enable consolidation before the plastificate cools down (Neitzel & Mitschang et al. 2014, p. 384; Davis & Gramann et al. 2003). The advantage of this approach is that the solidification takes place directly after the forming and consolidation in the mold under pressure, which suppresses the formation and enlargement of voids by the expansion of air pockets. The component is afterwards removed from the mold by a robot and can be further processed.

One objective of this thesis is the subsequent individualization of components produced using conventional manufacturing processes. To validate the results for this objective, compression molding of LFT is used as a reference. In Chapter 7.2, the corresponding tests are carried out with LFT components.

2.1.3.3 Processing of CoDiCoFRP

In the following two sections, two different combinations of the previously introduced processes for the production of CoDiCoFRP are presented as shown in Figure 2-12, which are discussed in more detail below.

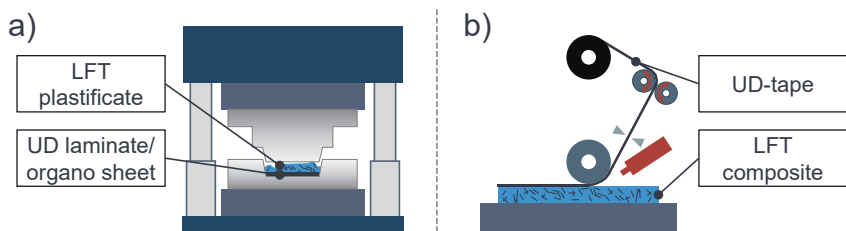


Figure 2-12: a) Hybridization combining thermoforming and compression molding; b) Hybridization combining compression molding and tape laying

Thermoforming and Compression Molding

Since thermoforming for CoFRP and compression molding for DiCoFRP use similar equipment technologies, they can be used for the production of hybrid CoDiCoFRP. As the preparation of the DiCo (plasticate) and the Co part (laminated UD-tapes) can be performed in parallel and the hybridization takes place simultaneously in one molding step (cf. Figure 2-12 a)), there is ideally no increase in the cycle time. This makes such hybridization approaches suitable for the economical production of high quantities of parts (Neitzel & Mitschang et al. 2014, p. 420–422). As the thermoforming of UD-tapes can generally lead to defects, which can be reduced by appropriate preforming, Kupzik (2022) developed the Robotic Swing Folding process for the flexible production of three-dimensional preforms from individually cut UD-tapes. With this approach, expensive preforming tools can be avoided, making the hybridization more economical and flexible. The experimental setup of the Robotic Swing Folding process, consisting of an industrial robot with a heated gripper and a feeding and cutting unit for the UD-tapes, is shown in Figure 2-13.

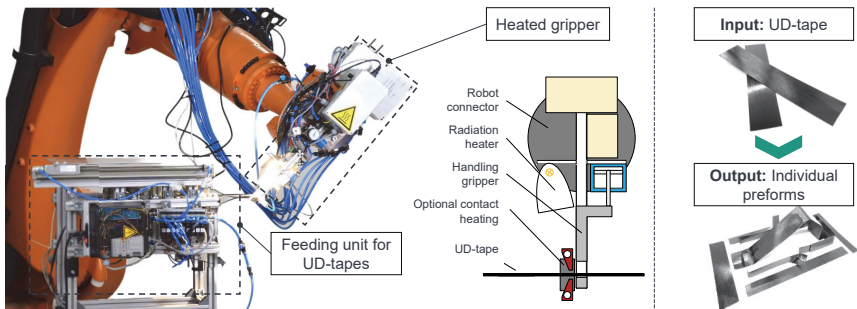


Figure 2-13: (Left) Experimental setup of the Robotic Swing Folding process; (Right) Production of individual preforms from UD-tapes (based on (Kupzik 2022))

The main process steps and influencing factors of the Robotic Swing Folding process are shown in Figure 2-14. In general, the UD-tape matrix is melted by the heated gripper and then brought into the desired shape by a controlled bending movement and subsequent cooling. This process can be performed iteratively to obtain three-dimensional preforms. After preforming, the feed unit cuts the UD-tape and the heated gripper can place the preform in a press, for example, where hybridization with LFT plasticate can take place.

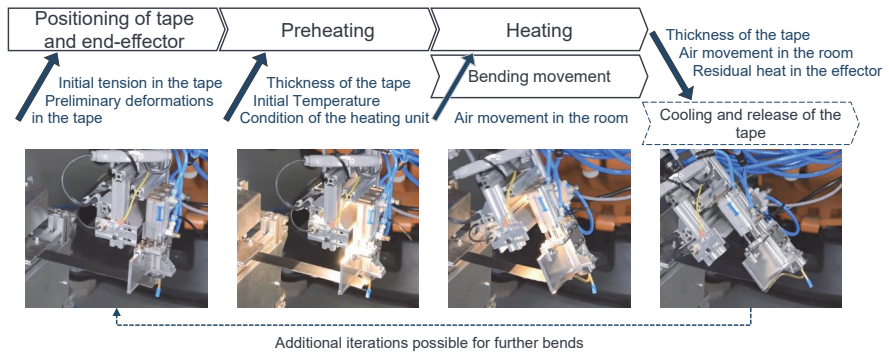


Figure 2-14: Process steps and main influencing factors of the Robotic Swing Folding (based on (Matkovic & Kupzik et al. 2022; Kupzik 2022))

Due to the high degree of flexibility and potential for individualization in the automated provision and handling of the UD-tapes, the Robotic Swing Folding is integrated as a subsystem of the experimental setup in Chapter 5.

Compression Molding and Tape Laying

Instead of producing entire composites with ATL, the in-situ consolidation process can also be used in a subsequent process step (cf. Figure 2-12 b)) to reinforce compression molded parts with tapes along the load path. As a result, the Co-fibers are used in a more focused manner, resulting in higher part strength and stiffness than with compression molding alone, without the long process times associated with a solely ATL process. In addition to faster cycle times, this hybridization also reduces material costs by reducing the amount of expensive UD-tape used (Neitzel & Mitschang et al. 2014, p. 422–423; Holschuh & Becker et al. 2012). Engelhardt & Ehard et al. (2019) investigated the shear strength between in-situ consolidated LFT components and UD-tapes and proved that this hybridization process is suitable to reduce the weight of components and thus to be used in the aerospace industry.

Subsequent in-situ consolidation for hybridization with ATL processes has some disadvantages. The Co-fibers can only be placed on simply shaped surfaces with low curvatures. As a result, the design freedom of the hybrid composites is very limited, and the Co-fibers cannot be placed inside the composite. This process is therefore only suitable to a very limited extent for subsequent individualization of CoDiCoFRP.

2.1.4 Evaluation of CoDiCoFRP and Conventional Processing

In the previous sections, the advantages of CoDiCoFRP were highlighted. Characteristics, mechanics, processes and relevant parameters for the production of Co, DiCo and CoDiCoFRP were discussed. The advantages of processing pre-impregnated UD-tapes, such as a high automation capability and higher reinforcement effects due to a higher degree of impregnation, were shown. The micro- and macroscopic mechanisms of consolidation and solidification were explained, and the goal of improving bonding in or between composites by reducing void content was explained in detail.

The review of the state of the art for manufacturing CoDiCoFRP using conventional manufacturing processes has shown that they are not suitable for lower quantities and individualized components. ATL systems have a certain potential for individualization due to their flexibility. However, since they are combined with very inflexible processes such as compression molding, their potential remains unused. The following Chapter therefore analyzes the state of the art in the field of flexible manufacturing processes such as AM material extrusion for the production of Co, DiCo and CoDiCoFRP.

2.2 Additive Manufacturing of Co, DiCo and CoDiCoFRP

Additive manufacturing, colloquially known as 3D printing, refers to various processes and technologies for the rapid production of parts directly from 3D models. The main approach of AM is to slice 3D models from computer-aided design (CAD) data into layers and derive machining paths for a layer-by-layer material buildup (Gibson & Rosen et al. 2015, p. 2). According to (DIN EN ISO/ASTM 52900) different classes of AM processes can handle a variety of different materials, with polymers being widely used because of their ease of processing. In order to produce highly durable lightweight components made of polymers, the processes are being further developed for the integration of Co and DiCo-fibers. Recent works have developed and investigated DiCo-fiber integration in stereolithography processes and Co-fiber integration in laser sintering processes (Schlotthauer & Nolan et al. 2021; Baranowski & Scholz et al. 2024). Systems based on material extrusion (MEX), in which the thermoplastic material is deposited via a nozzle, are among the most widely used due to their simple operation. Accordingly, there is a large number of works investigating and developing fiber integration for these systems. In the following sections, the different approaches for fiber integration in MEX-based systems are classified and the current state of the art is evaluated.

2.2.1 Classification of Fiber Reinforcement in MEX

The most common MEX process is fused deposition modeling (FDM). In FDM a continuous filament of thermoplastic is melted and deposited in most cases with a three-axis system on a heated bed (Gibson & Rosen et al. 2015, p. 147; Penumakala & Santo et al. 2020). Other MEX systems, such as ARBURG Plastic Freeforming (APF) or most robotic MEX systems use thermoplastic granulate as raw material, which has its own advantages and disadvantages compared to the processing of filaments (Mele & Pisaneschi et al. 2022; Matkovic & Götz et al. 2021). Robotic extrusion systems are addressed separately in Chapter 2.3 due to their relevance to this thesis.

In order to better understand the many different Co-fiber reinforcement approaches in MEX, Baumann & Scholz et al. (2017) proposed a simple classification consisting of the three types: Extrusion of a pre-impregnated Co-fiber filament, in-situ impregnation and dual-nozzle extrusion as shown in Figure 2-15 a) - c).

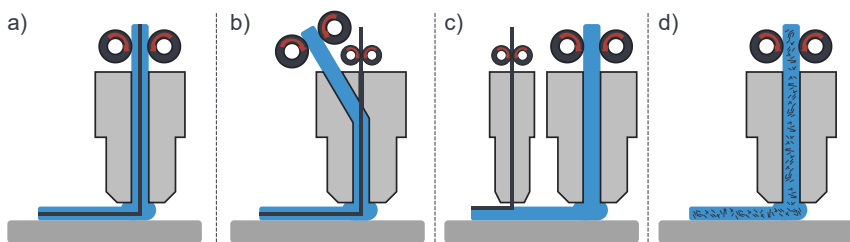


Figure 2-15: Four types of material extrusion of fiber reinforced composites: a) Extrusion of pre-impregnated Co-fiber filaments; b) Extrusion and in-situ impregnation; c) Dual-nozzle extrusion; d) Extrusion of pre-impregnated DiCo-fiber filament (based on (Baumann & Scholz et al. 2017, p. 324))

These three approaches usually use rovings or individual fibers. Adding DiCo-fiber reinforcement, this classification can be extended by the extrusion of pre-impregnated DiCo-fibers, as shown in Figure 2-15 d). These various approaches and relevant studies were analyzed in (A_Garcia-Vasquez 2023) and are discussed in the following sections.

2.2.1.1 Extrusion of Pre-Impregnated Co and DiCo-Fiber Filaments

As described in chapter 2.1.2.1, pre-impregnated fibers generally offer many advantages that also apply to MEX processes, especially eliminating a high void content and poor bonding between the fibers-matrix interface (Goh & Dikshit et al. 2018, p. 3). The need for such filaments is recognized, but only DiCo reinforced filaments are readily

available (Pandelidi & Bateman et al. 2021, p. 3058). The lack of supply of Co reinforced filaments can be attributed to several reasons such as high costs and the lack of flexibility in changing the fiber volume fraction (Goh & Dikshit et al. 2018, p. 3).

2.2.1.2 Extrusion and In-Situ Impregnation

Pandelidi & Bateman et al. (2021, p. 3063) identified in a review three methods for in-situ impregnation (cf. Figure 2-15 b)) of fibers during material extrusion. The first method uses a common entrance for the thermoplastic and for the fibers. As several studies have shown, this method is highly error-prone, since the feeding rates of the thermoplastic and the fibers cannot be adjusted to each other, which can lead to curling and damage of the fibers (Nakagawa & Mori et al. 2017; Akhoundi & Behravesh et al. 2020; Pandelidi & Bateman et al. 2021, p. 3062). In order to control the two feed rates and to obtain better control of the fiber tension and impregnation, different systems with separate entrances for the fibers and the thermoplastic have been developed and investigated. This second method of in-situ impregnation appears to be more promising than the common entrance method (Pandelidi & Bateman et al. 2021, p. 3064). Since the fibers and thermoplastic are brought together laterally in the first two methods, the position of the fibers is off-center. The third method, the central feeding of the fiber tow, offers a solution for aligning the fibers centrally in the thermoplastic. This method seems to be promising, however, it is technically very complex (Pandelidi & Bateman et al. 2021, p. 3066).

2.2.1.3 Dual-Nozzle Extrusion

The dual-nozzle extrusion technology as shown in Figure 2-15 c) was patented by Mark & Woodruff et al. (2017) and is commercially available by Markforged. As an industrial solution, this technology of Co-fiber reinforcement in material extrusion is currently the most mature approach (Pandelidi & Bateman et al. 2021, p. 3061). Similar approaches also exist for other MEX processes such as APF (Baumann 2020). In the literature, many studies show a significant increase in mechanical properties with good print quality, upon the addition of reinforcement (Dickson & Barry et al. 2017; Chacón & Caminero et al. 2019; Pandelidi & Bateman et al. 2021, p. 3061). Nevertheless, the process does have some issues. As with all the processes presented for Co-fiber integration in MEX, the dual extrusion process is also quasi-pressureless, which effectively means that no consolidation is performed. This results in high void contents and reduced mechanical properties (Dickson & Barry et al. 2017, p. 150; van de Werken & Hurley et al. 2019).

2.2.1.4 CoDiCo-Fiber MEX

Theoretically, all methods of Co-fiber extrusion can be combined with the DiCo-fiber extrusion shown in Figure 2-15 d). Since Markforged also offers DiCo-fiber filaments, it is possible to combine them with Co-fibers using dual-nozzle extrusion to improve the overall mechanical properties (Pandelidi & Bateman et al. 2021). Due to the complexity of adding Co-fibers alone, the combination with DiCo-fibers and thus CoDiCo-fiber extrusion as a whole is still relatively unexplored.

2.2.1.5 MEX Combined with ATL

Approaches for combining MEX and ATL are presented in the work of Hopmann & Ophüls et al. (2019) and Raspall & Velu et al. (2019), who subsequently print individual structures on ATL manufactured parts using the MEX process and thus creating individualized parts. The first promising successes in combining these two processes to produced reinforced 3D printed parts were achieved in the work of Hirsch & Scholz et al. (2024), demonstrating the potential. Polyamide 6 printed tensile specimens were reinforced with glass fiber UD-tapes with the help of ATL. This approach for fiber reinforcement in the MEX process is similar to the basic principle of dual-nozzle extrusion (see Figure 2-15 c)), as the material extrusion and Co-fiber reinforcement take place separately from each other. The mechanical properties could be increased by several times for certain samples. However, the conclusions of the work show that the process combination still needs to be significantly optimized. Optimum process parameters have to be identified in order to improve the void content and the bonding between the MEX layer and the UD-tape. To the author's knowledge, there are no systematic studies that investigate in depth the interactions and optimization of these hybridization approaches of MEX and ATL and their actual potential for the individual production and subsequent individualization of FRP.

Overall, the process of fiber reinforcement in MEX can be described as immature. As shown in the following section, the processes have considerable disadvantages and, in some cases, cause defects in the composites which, among other things, greatly reduce the theoretical reinforcement effect of the added fibers.

2.2.2 Defects and Drawbacks of Fiber Reinforcement in MEX

Typical composites such as carbon fiber reinforced PA6 processed with material extrusion, can have 30 - 40 % weaker stiffness and strength when compared with conventionally produced composites (Oztan & Karkkainen et al. 2019, p. 279). As described in Chapter 2.1.1.2 common failure mechanisms for FRP are matrix cracking, fiber breakage, fiber pull-out and debonding. Compared to conventional manufacturing processes, composites made with MEX processes are more prone to these failure mechanisms (Agarwal & Kuchipudi et al. 2018, p. 3174; Penumakala & Santo et al. 2020; Wickramasinghe & Do et al. 2020). As shown by Oztan & Karkkainen et al. (2019) the overall poorer mechanical properties can be traced back to poor fiber impregnation, high void content, and an overall weak fiber-matrix and interlayer bonding. The main causes are briefly explained in the following sections.

2.2.2.1 Insufficient Impregnation

As explained in Chapter 2.2.1, the fibers in MEX can be impregnated in-situ, or pre-impregnated fibers can be used. With an increasing degree of impregnation, the fiber matrix interface can improve and enhance the transfer of stresses, thus increasing the reinforcement effect of the fibers (Zhuang & Zou et al. 2023). Due to the limited supply of pre-impregnated continuous fibers for material extrusion, in-situ impregnation must often be used. The difficulties of in-situ impregnation and infiltration, especially with thick rovings, were described in Chapter 2.1.2.1. Insufficient impregnation can be overcome by implementing a consolidation process step.

2.2.2.2 High Void Content

Besides the insufficient impregnation explained in the previous section, void formation during material extrusion has two further main causes, which can be reduced to the condition of the matrix raw material, and the processing of the material. Input material in the form of filament or granulate may already contain voids, which can grow through gas expansion when the thermoplastic is melted, due to the lack of pressure (Willemstein 2021, p. 5). The second main cause can be traced back to a poorly controlled deposition process, such as an insufficient flow of the matrix material, unmatching layer heights and nozzle diameters, and poorly or not optimized tool paths (Mauricio Guajardo-Trevino & Ahuett-Garza et al. 2022; Wickramasinghe & Do et al. 2020). Several studies on unreinforced (Chacón & Caminero et al. 2019; Wu & Geng et al. 2015)

and Co-fiber reinforced thermoplastic composites (Caminero & Chacón et al. 2018; Ning & Cong et al. 2015; Tian & Liu et al. 2016) have concluded that the voids between layers can be reduced by adjusting process parameters, such as through the reduction of layer thicknesses. Some of the causes, especially those due to the condition of the material, cannot be controlled, so the formation of voids is inevitable, and with the addition of reinforcement fibers, this effect is exacerbated. In addition, all voids can grow further due to the nature of a quasi-pressureless process, this is referred to as deconsolidation (Willemstein 2021, p. 6).

It is widely accepted that the mechanical properties of Co-fiber reinforced thermoplastic composites produced by material extrusion are limited due to the formation of voids (Blok & Woods et al. 2017; Dickson & Barry et al. 2017; He & Wang et al. 2020; Matsuzaki & Ueda et al. 2016; van Der Klift & Koga et al. 2016). He & Wang et al. (2020) identified in their study, analyzing the effects of voids in Co carbon fiber reinforced PA6, a high concentration of voids near the crack initiation point of fracture. Blok & Woods et al. (2017) indicated that a void content of more than 10 % is common in material extruded Co-fiber thermoplastic composites.

2.2.2.3 Weak Fiber-Matrix and Interlayer Bonding

Poor bonding between fibers and the thermoplastic matrix is a common problem and not exclusive to the AM process of MEX. The formation of the interface includes in detail different mechanisms, such as physical attraction between electrically neutral bodies, molecular entanglement, electrostatic attraction, chemical bonding, reaction bonding, and mechanical bonding (Drzal & Rich et al. 1983, as cited in Huang & Fu et al. 2021, p. 1446). A detailed review of the mechanisms and challenges of fiber-matrix bonding is given in (Huang & Fu et al. 2021). Regardless of the exact mechanisms and causes, sufficient impregnation and consolidation can increase the fiber-matrix bonding.

Since MEX is a layer-by-layer process, the composite produced is basically a laminate. To avoid premature delamination under load, sufficient bonding between the individual layers must be ensured. As Caminero & Chacón et al. (2018) concluded, material extruded composites show weak interlaminar bonding strength due to high void content and insufficient autohesion between the layers, which can be attributed to a lack of consolidation.

A lot of research work in the field of MEX focuses on overcoming the mentioned issues, e.g. with an additional consolidation process that can be applied in-situ or in a post-

processing step (Andreu & Kim et al. 2022). Relevant scientific research regarding such consolidation processes is analyzed in more detail in the next section.

2.2.3 Consolidation Approaches in MEX

Adding an additional consolidation process can reduce the aforementioned drawbacks and defects. The following chapter therefore analyzes different approaches from the current state of the art for the consolidation of fiber reinforced MEX components to increase the degree of bonding D_b . As shown in Figure 2-16 the approaches can be classified into four categories.

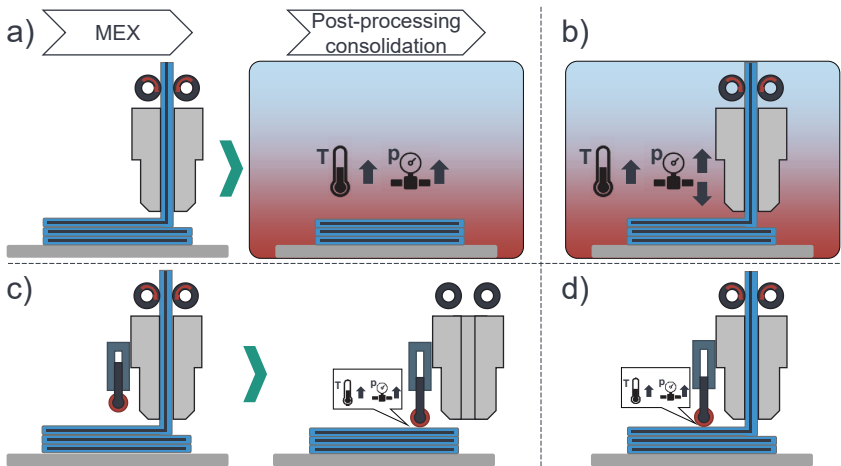


Figure 2-16: Consolidation approaches in MEX: a) Post-processing consolidation; b) In-situ consolidation with controlled ambient conditions; c) Semi-in-situ consolidation with compaction roller; d) In-situ consolidation using a compaction roller

In the following sections, selected studies for each category are reviewed. The focus is on Co-fiber reinforced MEX components, although the approaches are also used for DiCo reinforced and unreinforced MEX components.

2.2.3.1 Post-Processing Consolidation

There are two different approaches for consolidation in a post-processing step investigated in various studies. In these, consolidation takes place either under increased ambient pressure and temperature in an autoclave or in heated molds (cf. Figure 2-16 a)).

Ali & Yan et al. (2023) have carried out a study on carbon, glass and aramid fiber-reinforced PA6 composites printed by FDM using a dual extrusion system and post-processing in an autoclave. It was found that the autoclaved samples all showed improved fiber to matrix bonding. Another example comes from Mori & Maeno et al. (2014), who printed carbon fiber-reinforced Acrylnitril-Butadien-Styrol-Copolymer composites using FDM and thermally treated them in an oven. Unlike Ali & Yan et al. (2023), they did not apply elevated ambient pressure. Comparing the printed specimens with their post-treated counterparts, they found that the strength nearly increased by 100 %. Hetrick & Sanei et al. (2022) used a two-part mold into which they inserted FDM-printed glass fiber-reinforced PA6 and then consolidated the specimens in a heated press. Their results showed that the process was successful, reducing the void content by an average of 2 %.

2.2.3.2 In-Situ Consolidation with Controlled Ambient Conditions

As shown in Figure 2-16 b), in some approaches the 3D printers have been enclosed in order to influence the ambient conditions during printing. Shaik & Schuster et al. (2022) have investigated the influence of high ambient pressures and temperatures on FDM printed specimens. For this purpose, samples were produced with an FDM printer inside an autoclave at a temperature of 50 °C and up to 1 MPa above the normal ambient pressure. It was shown that the void content could be reduced, while increasing the flexural strength by almost 150 %. In a similar setup, O'Connor & Dowling (2019) investigated the effect of low ambient pressure on the mechanical properties of carbon, glass, and Kevlar Co-fiber reinforced PA6 composites. It was found that the void content of carbon, glass, and Kevlar printed composites could be reduced by 5.7 %, 1.0 %, and 1.7 %, respectively. This resulted in an increase in interlaminar shear strength of 33 %, 22 % and 12 % for the carbon, glass and Kevlar fiber-reinforced composites respectively.

2.2.3.3 Semi-In-Situ Consolidation with Compaction Roller

Semi-in-situ consolidation refers to processes in which consolidation does not take place immediately during or after extrusion, but usually after the completion of one, several, or all layers. Since the printing process has to be paused, this consolidation can only be considered a semi-in-situ consolidation. For this approach, compaction rollers are often used as shown in Figure 2-16 c). Andreu & Kim et al. (2022) modified an FDM printer with such a compaction roller to increase the interlaminar bonding, which

resulted in an increase of the tensile strength by 38 % of the specimens. However, this approach has not been researched thoroughly and thus there does not appear to be any relevant literature for reinforced components.

2.2.3.4 In-Situ Consolidation with Compaction Roller

In comparison to semi-in-situ consolidation, in this approach (cf. Figure 2-16 d)) consolidation takes place immediately after extrusion and does not have to be paused. The lack of a mold and the rapid solidification of the thermoplastics used in MEX makes it difficult to incorporate in-situ consolidation mechanisms into the process chain. Recently, attempts have been made to incorporate such a process with varying success.

Using a Markforged Mark-Two printer, Oberlercher & Laux et al. (2023) installed a thermomechanical compaction roller after the nozzle tip. No mechanical coupling was installed between the nozzle and the consolidation unit, so the fiber could only be deposited in the x-direction without the ability to print on curved paths. The microstructures of consolidated and unconsolidated samples were examined and compared. Individual layers with insufficient intimate contact could be clearly seen in the microstructural analysis, and horizontal cracks in the samples were indicative of delamination in the printed parts. The specimens printed with the in-situ consolidation unit attached showed hardly any micro and macro voids in their microstructures and an overall reduction in deconsolidation.

In further studies (Ueda & Kishimoto et al. 2020; Zhang & Zhou et al. 2020) similar setups with rotatable compaction rollers were analyzed, allowing a deposition in x- and y-direction and thus the printing of curves. Similar to Oberlercher & Laux et al. (2023), a reduction in the void content and an increase in the mechanical properties were observed. It should also be mentioned here that although the in-situ and semi-in-situ approaches are mostly carried out with compaction rollers, the literature contains isolated approaches that consider other geometries, e.g. flat ironing shapes (Willemstein 2021).

Another variant of MEX with in-situ consolidation is Large Scale Additive Manufacturing (LSAM) from Thermwood. As the name suggests, this is a process and system that focuses specifically on the production of large-volume components. Due to the dimensions of the components and the high material output, the cooling speeds are completely different to those of conventional FDM-based processes. As shown in (Wang & Ju et al. 2019), this has an influence on the surface temperature and thus the adhesion

between the layers. Due to the low cooling rates, an uncooled compaction roller can be used, which can significantly increase the adhesion between the layers.

2.2.4 Evaluation of the Consolidation Approaches in MEX

As described in Chapter 2.2.1, there are various approaches for the production of fiber-reinforced MEX components. Due to the lack of pre-impregnated Co-fiber filaments, in-situ approaches are increasingly being investigated. In general, fiber-reinforced components produced using the MEX process are characterized by poorer mechanical properties compared to conventional processes, which can be attributed to a high void content and an overall weak fiber-matrix and interlayer bonding (cf. Chapter 2.2.2). This is due to the lack of pressure, i.e. a lack of consolidation during processing, and in the case of in-situ impregnation, due to additional insufficient impregnation. To overcome this issue, different approaches for consolidation are being investigated as described in the previous Chapter 2.2.3. Figure 2-17 gives a quantitative evaluation of the different approaches.

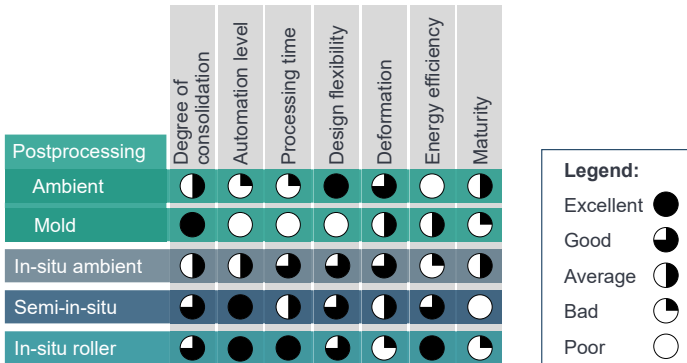


Figure 2-17: Qualitative evaluation of the four consolidation approaches based on Figure 2-16

Post-processing using additional molds provides the highest level of consolidation of all approaches, but the additional tools and process steps result in a poor level of automation, processing time and design flexibility, which completely cancels out the advantage of additive manufacturing. Post-processing in a controlled ambient environment (autoclave), offers significantly higher design flexibility of the components as no molds are required, but the achievable degree of consolidation is lower and still difficult to auto-

mate. In-situ consolidation with controlled ambient conditions has a better level of automation and lower processing times, as the printer is already in an autoclave or oven, and consolidation does not have to take place in post-processing. What all three mentioned approaches have in common, is their relatively poor energy efficiency, as either the entire surroundings (autoclave) or additional molds have to be heated.

The semi-in-situ approach and the in-situ approach with compaction roller both have the advantage that a high level of automation can be achieved, as the modification of existing 3D printers is sufficient, and no additional post-processing in an autoclave or additional molds are required. This means that the simplicity and accessibility of 3D printing using the MEX process are not lost. Looking at the degree of maturity of the individual approaches, none of them are ready for industrial use or commercialization.

In addition to the general immaturity of the individual consolidation approaches in MEX FDM, these have the following disadvantages compared to the conventional manufacturing processes for FRP:

- **Low output** in terms of achievable component sizes and production time
- **No true 3D fiber reinforcement** is possible, as fiber integration is only possible within the printed layers (planar 2D reinforcement)
- **Use of insufficiently impregnated fibers** due to lack of supply

Moving away from the widely used filament FDM systems, which generally only use three axes, the first two disadvantages can be overcome by using industrial robots and direct extrusion. The following section will therefore look at robot-based MEX systems with direct extrusion, which allow true 3D extrusion of thermoplastic granulate.

2.3 Robotic Multi-Axis MEX with Direct Extrusion

Most available 3D printers have been developed for personal use and not for industrial applications. High material output rates and reachable component sizes are not orientated toward the requirements of industrial applications. For this reason, there has been a trend towards robot-based MEX systems with direct extrusion for industrial applications. In the following sections, the general structure and functionality as well as the advantages and disadvantages are explained, followed by a review of the current state of research into fiber reinforcement using such systems.

2.3.1 General Setup of MEX Direct Extrusion Systems

In contrast to conventional FDM printers, MEX direct extrusion systems (DES) do not require pre-processed filaments. Instead, as the name suggests, they can process granulate directly. This is however not an officially standardized classification and manufacturers who offer such systems use their own terminology. As shown in Figure 2-18, in most cases MEX DES consists of a heated single screw extruder mounted on a six-axis industrial robot. The heated printing bed or surrounding area is heated differently depending on the material. Complete systems are offered, for example, by the manufacturer Hans Weber Maschinenfabrik GmbH. As companies often use existing robots to set up such a system, the extruders can also be purchased individually. One example of this is the supplier Massive Dimension.

MEX DES can achieve material output rates of over 30 kg/h, which is significantly higher than with conventional FDM printers. Using six axes the orientation of the extruder can be controlled in addition to the translational movement in the cartesian space. For AM systems with more than 3-axes, the term multi-axis or multi-degree of freedom (DOF) 3D printing is often used. Due to the relevance of six-axis industrial robots to this work, their basic functionality is described below and the most important terms are clarified.

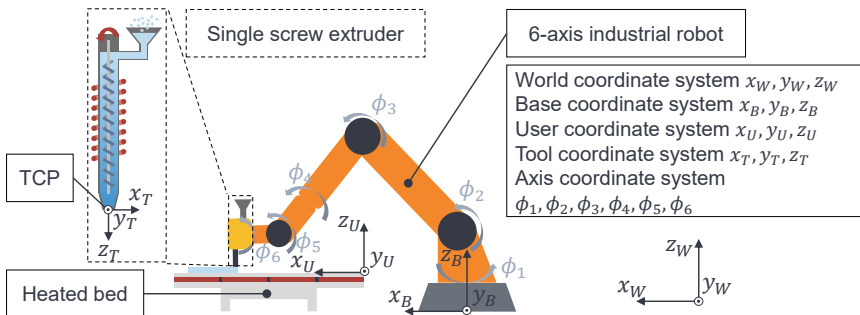


Figure 2-18: Setup of a multi-axis MEX DES with a six-axis industrial robot

2.3.2 Six-Axis Industrial Robots

Figure 2-18 shows a typical industrial robot consisting of six rotary axes and the most relevant coordinate systems. The world coordinate system is often located at the base of the robot. A fixed definition of the world coordinate system outside the base is useful if, for example, the industrial robot is repositioned within the production cell, or if several

robots are used within a cell and they all refer to the world coordinate system. (Frigeni 2023, p. 21–30)

The use of the user coordinate system is particularly helpful with MEX DES, which is used to describe the position and orientation of the heated bed. Paths created for MEX DES 3D printing therefore refer to the user coordinate system. If the heated bed needs to be moved slightly or generally remeasured to increase accuracy, the user coordinate system can be moved corresponding with the heated bed. For this frequently occurring case, existing 3D printing programs can be reused.

The same principle is also used for the tool coordinate system, which is defined relative to the robot flange. Setting the tool coordinate system also describes the position of the tool-center-point (TCP). In the case of MEX DES usually the nozzle tip is defined as the TCP. Created 3D printing programs describe the relative movement from the TCP to the user coordinate system. If the nozzle is replaced by a longer or shorter one, the TCP can simply be moved together with the tool coordinate system. Again as for the movement of the user coordinate system, robot programs that have already been created do not need to be newly generated. (Frigeni 2023, p. 21–30)

In addition to the cartesian coordinate systems described, typical industrial robots have six rotational axis coordinates within the respective joint. The relationship between axis coordinates and cartesian coordinates is described in the next section.

2.3.2.1 Kinematics

The industrial robot discussed in this chapter has serial kinematics. In serial kinematics, the movement takes place from link to link, with the links connected by joints. This structure forms an open chain in which the movement is continuous from one link to the next. The TCP position is calculated sequentially by the rotation of the joints. (Frigeni 2023, p. 2–6; Siciliano & Khatib 2016, p. 11–30)

Robot controllers allow direct control of the rotary axes (joints) and therefore control in the axis coordinate system. For easier use and path planning of serial industrial robots, programming in cartesian coordinates (e.g. in the tool coordinate system) is the default. This requires a transformation to and from the axis coordinate system. These are the forward and inverse transformations shown in Figure 2-19 in simplified form.

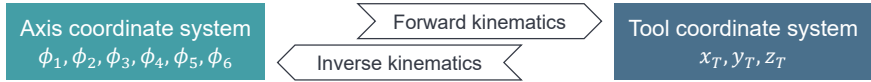


Figure 2-19: Coordinate transformation for robots using forward and inverse transformation based on (Gevatter & Grünhaupt 2006, p. 760)

Forward kinematics is the analytical process for solving kinematic problems in which the position and orientation of the end-effector (or TCP) are determined from the joint angles. The solution of inverse kinematics is not unique, as several joint angle configurations can lead to the same position and orientation of the TCP, which makes the calculation noticeably more complex than with forward kinematics. In addition, singularities can occur, i.e. configurations in which an infinite number of solutions for the joint angles exist. Solutions to the problem of inverse kinematics can basically be based on analytical and numerical methods. Analytical solutions are closed mathematical equations that enable the direct reversal of the forward kinematics, but which are only possible under specific conditions and simple robot geometries. Although they are noticeable faster in these cases, they often reach their limits in more complex systems. In contrast, numerical methods use iterative processes to approximate the solution. (Weber 2009, p. 58; Siciliano & Khatib 2016, p. 29–31; A_Larsch 2024)

Coordinate transformations using matrix multiplications are an essential method for describing the position and orientation of robot links in space. Common methods rely on the Denavit-Hartenberg notation, which is a standardized method to systematically describe the kinematic structure of robot systems. By introducing Denavit-Hartenberg conventions, the kinematic relationships between neighboring joints are described with only four parameters. These conventions offer a simplified yet precise way to characterize the position of the joint axes in relation to each other. (Denavit & Hartenberg 1955; A_Larsch 2024)

When programming the paths of typical industrial robots, the forward and inverse kinematics are usually calculated in the background by the controller and the user does not deal with them any further. However, it is important to be aware of the problem of inverse kinematics consisting of ambiguous solutions and singularities (Werner & Aburaia et al. 2021; Krčma & Paloušek 2022, p. 7119). The significance of path planning in the context of MEX DES is briefly explained in the next section.

2.3.2.2 Path Planning

Trajectories are used to determine the path of the TCP and are made up of simple curve types such as lines and parabolas or spline curves. The curves are calculated by defining a discrete number of interpolation points as a function of time and using a suitable interpolation method, to obtain a continuous curve (Gevatter & Grünhaupt 2006, p. 765). Typical types of movement in path planning and programming are point-to-point movements or linear movements. For MEX DES 3D printing, the paths are mainly made up of linear movements.

The paths can be programmed online or offline. With online programming, the paths are created directly using the industrial robot, which means that the paths can be tested on the spot. However, this method is very time-consuming and not suitable for 3D printing, where several thousand individual linear movements are often generated. For this reason, offline programming methods are more suitable, where the robot program is created and tested in a simulation and only then transferred to the robot controller. (Gevatter & Grünhaupt 2006, p. 766)

2.3.2.3 Layout Planning

The layout planning of a robot cell is a multidisciplinary problem that deals with the efficient arrangement of one or more robots. Robot cells often contain other automation equipment, such as conveyor belts, which must also be considered when optimizing the layout. Layout planning processes are usually concerned with maximizing throughput and not with expanding the usable workspace, which is relevant for MEX DES. (Zhang & Fang 2017)

To optimize the usable workspace, layout planning can be carried out based on reachability analysis, which checks if there is a solution for the inverse kinematics. Alongside the definition of the general workspace, the dexterous workspace is also used. The general workspace comprises the entirety of all reachable points in space that the TCP of a robot covers during all possible movements. This workspace is determined by the geometry of the robot and the limits of the joint movements. On the other hand, the dexterous workspace represents a subset of the general workspace. In the dexterous workspace, points can be reached while maintaining a defined TCP orientation. This definition is more specific and takes into account the possibility of positioning the TCP in different orientations. (Siciliano & Khatib 2016, p. 27; A_Larsch 2024)

Regardless of the considered workspace, reachability analyses can be performed based on analytical and numerical kinematic calculations (see previous section 2.3.2.1). A corresponding analysis is executed in Chapter 5.1.

2.3.3 Multi-Axis Non-Planar AM

Using of multi-axis robotic AM setup offers different advantages and difficulties. In general, conventional AM machines are limited to three axes of motion with a fixed orientation of the print head/extruder. With only three axes they are unable to optimally adapt the print head paths to the shape of the part which results in poor adhesion between layers, staircase effects, poor surface quality, support requirements, limited functionality and other disadvantages (Jiang & Newman et al. 2021, p. 195). Multi-axis 3D printing can eliminate or at least reduce these problems through optimized path planning and the ability to adjust the orientation of the print head to the part surface (Krčma & Paloušek 2022, p. 7109).

There are several categories of multi-axis 3D printing. The terms non-planar 3D printing and curved layer fused deposition modeling are often used in the literature (Krajangsawadi & Blok et al. 2021). However, this is not necessarily multi-axis 3D printing. The comparison of Figure 2-20 a) and b) shows that for three-axis non-planar 3D printing the individual layers can be variable in height to the heated bed, allowing the part contour to be followed compared to the traditional planar 3D printing

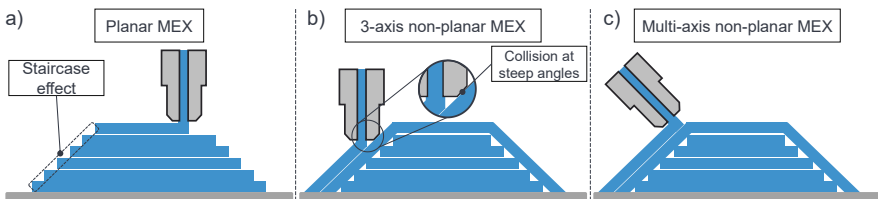


Figure 2-20: Difference in printing strategies illustrated by the example of MEX: a) Planar MEX; b) three-axis non-planar MEX; c) Multi-axis non-planar MEX

In this context, traditional planar 3D printing is often referred to as 2.5D printing due to the constant height between the individual layers and the heated bed. As Ahlers & Wasserfall et al. (2019) show in their study, the surface quality in FDM can be improved up to a certain angle of the surface contour. For steep angles of the outer contour, collisions between the nozzle and already printed areas occur (see Figure 2-20 b)). During extrusion, smearing can occur at certain angles, which can result in worse surface

roughness than with the staircase effect with planar MEX (cf. Figure 2-20a)). According to Elkaseer & Müller et al. (2020), the surface roughness of the three-axis non-planar MEX is only lower than that of the conventional planar MEX up to an inclination of 25 degrees for a specific nozzle shape. As shown in Figure 2-20 c) this limitation can be overcome with multi-axis non-planar 3D printing, by orientating the nozzle perpendicular to the printing direction.

If a six-axis industrial robot is combined with a single screw extruder for MEX DES as described in Chapter 2.3.1, there are further advantages in addition to the benefits of multi-axis non-planar 3D printing. The high material output quantities and the large build space of the industrial robots compared to their footprint enable the rapid production of large-volume thermoplastic components. In addition, the extreme anisotropy of planar MEX components, which is characterized by the reduced mechanical properties perpendicular to the layers, can be significantly reduced by using non-planar layers (Fang & Zhang et al. 2020). However, such systems also have considerable disadvantages compared to conventional FDM printers. Many problems can be traced back to the high-temperature differences that occur with large components and large-area heated beds. In addition to significant material distortion, this can cause the component to detach from the heated bed (Ali & Kurokawa et al. 2023).

2.3.4 Fiber Reinforcement with Multi-Axis MEX

Since MEX DES can process granulate directly and DiCo-fiber-reinforced granulates are available in a wide selection, DiCo-fiber reinforcement with such systems is very common. Co-fiber reinforcement with multi-axial MEX with and without DES is not yet industrially mature and has been little explored. As for conventional three-axis FDM 3D printers (cf. Chapter 2.2), the Co-fibers can only be integrated within the parallel layers and the reinforcement can only be efficiently designed for a two-dimensional load case. Multi-axial non-planar MEX with Co-fiber reinforcement has the potential to produce components for complex three-dimensional load cases and to reduce or even control anisotropy. Alsharhan & Centea et al. (2017) addresses this hypothesis in their work and developed a multi-axial MEX setup to investigate this. Practical studies that support the hypotheses were carried out in the work of Shang & Tian et al. (2020), Zhang & Zhang et al. (2019) and Fang & Zhang et al. (2024).

2.3.5 Evaluation of Robotic Multi-Axis MEX

Due to the higher degrees of freedom, the multi-axis MEX offers many advantages compared to the traditional three-axis planar MEX. For example, surface roughness and anisotropy can be reduced, mechanical properties improved and the need for support structures avoided or reduced. If the multi-axis MEX is realized with a six-axis industrial robot and equipped with a DES, further advantages can be achieved. Thanks to the large build space in comparison to the footprint of the robot and the high achievable material output with DES, large-volume thermoplastic components can be produced quickly and with the advantages of multi-axial printing. The direct processing of granulate with screw extruders offers not only a higher material output but also a higher availability of materials and lower material costs compared to the filaments commonly used for conventional FDM printers. However, controlling the material output is generally more difficult than with filaments, especially if the print head is not kept constantly vertical. Further disadvantages result from the increased complexity of path planning due to the additional degrees of freedom and collision risks. Theoretically, Co-fiber reinforcement with multi-axial MEX systems has considerable advantages compared to conventional three-axis planar systems but has only been investigated to a limited extent. Furthermore, there are very few studies on the consolidation of multi-axial Co-fiber reinforcement in MEX.

2.4 Conclusion from the State of the Art

The advantages of combining highly formable DiCoFRP with CoFRP were explained at the beginning of this chapter. Their combined characteristics allow the economical production of lightweight FRP components with high strength and stiffness and a high degree of design freedom. In order to achieve the maximum reinforcement effect and exploit the potential of CoDiCoFRP, a high degree of bonding between the material systems must be achieved. This includes reducing voids and maximizing autohesion through sufficient impregnation, consolidation and solidification. This can be accomplished using pre-impregnated materials such as UD-tapes and controlled consolidation and solidification processes with optimized process parameters for the material system.

The combination of conventional manufacturing processes such as compression molding and thermoforming allows the economical production of CoDiCoFRP in large quantities. However, due to the high costs and effort involved in the production of tools and molds, these manufacturing techniques are not suitable for the economical production

of individualized components. Approaches in which components are reinforced with Co-fibers (UD-tapes) after compression molding using the ATL process theoretically offer at least the potential for subsequent individualization. However, complex individual structures of the DiCo part cannot be realized as its shape is predetermined by the mold.

As shown in Chapter 2.2, MEX offers the potential to produce highly customized CoDi-CoFRP. Due to the low availability of pre-impregnated Co-fibers, limited component sizes and material output rates with the FDM printers used, these systems are only suitable for small components for very low quantities. The mainly used conventional planar 3D printing of parallel layers does not provide optimal reinforcement for 3D load paths and increases anisotropy. Furthermore, these systems have low degrees of bonding and further defects and drawbacks due to the lack of pressure during processing. Current research efforts show that the void content and autohesion can be significantly improved with dedicated consolidation, but none of the approaches are yet mature during processing. The analysis of the state-of-the-art shows that semi-in-situ and in-situ approaches with compaction rollers have the highest potential for economical automation of the consolidation process.

As shown in Chapter 2.3, due to the high output rates and the direct processing of various granulates, MEX DES are suitable for the rapid production of customized DiCo-FRP. Combined with six-axis industrial robots, large-volume DiCoFRP can be produced quickly with the advantages of multi-axial 3D printing. However, compared to conventional MEX, Co-fiber reinforcement is researched even less, with several research gaps. In addition, path planning is significantly more complex due to the increased complexity of the required paths and kinematics.

The resulting further research gaps and needs can be summarized in five main research questions and are listed below. In the further course of the thesis, these research questions will be systematically addressed and answered. The resulting expanded and more specific objective and an overall approach are discussed in the following chapter.

From the analysis of the state of the art and the motivation for a subsequent individualization and individual production of CoDiCoFRP with a high output rate and automation level, the following research questions arise:

1. What or how does a manufacturing process look like that enables the individualization and individual production of large CoDiCoFRP with a high output rate? Which process steps are required for the customized production of CoDiCo components?
2. What or how does a prototypical and experimental production plant look like in order to study the processes and explore their potential?
3. How should the individual process steps and in particular the consolidation process be carried out to maximize the degree of bonding between the Co and DiCo parts?
4. How can optimal consolidation process parameters for the newly developed processes be determined for selected material systems in compliance with boundary conditions?
5. What mechanical properties can the CoDiCoFRP achieve based on standardized tests for a selected material system?

3 Objective and Approach

Based on the previous detailed analysis of the current state of the art, the identified research gaps and the derived research questions, the following section first defines the precise objective and then describes the approach for achieving the objective.

3.1 Objective

The overall objective is to develop a manufacturing process and system that allows the subsequent individualization and individual production of CoDiCoFRP with a high output rate. Robot-based multi-axial MEX DES are to be used for the flexible forming of the DiCo areas to ensure large component sizes with high material output and maximum design freedom. Due to the good impregnation and good automatability of UD-tapes, as shown in the analysis of the state of the art, UD-tapes are to be used for the Co-fiber reinforcement. For the consolidation of DiCo and CoFRP, approaches from ATL systems are to be adapted and applied to the field of additive manufacturing with MEX systems. In addition to the development of a suitable process for the hybridization of the material systems, a prototypical experimental setup is to be developed for experiments and studies. This is intended in particular to optimize and evaluate the consolidation and hybridization process using a selected material system. In addition to hardware development and material and process studies, kinematic analyses have to be conducted and digital process chains need to be developed.

Since, as described in Chapter 2.2, consolidation for Co-fiber reinforcement in MEX is still immature and is crucial for the hybridization of Co and DiCoFRP, the scientific research focus of this thesis is mainly on improving the consolidation process.

3.2 Approach

The approach and work packages used in this thesis to achieve the described objectives are summarized in Figure 3-1. In Chapter 4 based on the function analysis system technique, required functions and associated subsystems are derived that are necessary for the system and process to be developed. Existing reference systems from the state of the art are taken into account in accordance with the theory of product generation engineering (PGE) (Albers & Rapp et al. 2018) in order to determine which subsystems can be newly developed or adapted from reference systems for the objectives described above. For the subsystems and associated functions with the highest new

development effort according to the PGE, empirical investigations and thermal simulations are carried out. These include the examination of various materials and an influence analysis according to Ishikawa. In addition to the identification of a suitable process, at the end of Chapter 4, an increased understanding of the process as well as requirements for the experimental system to be developed are available.

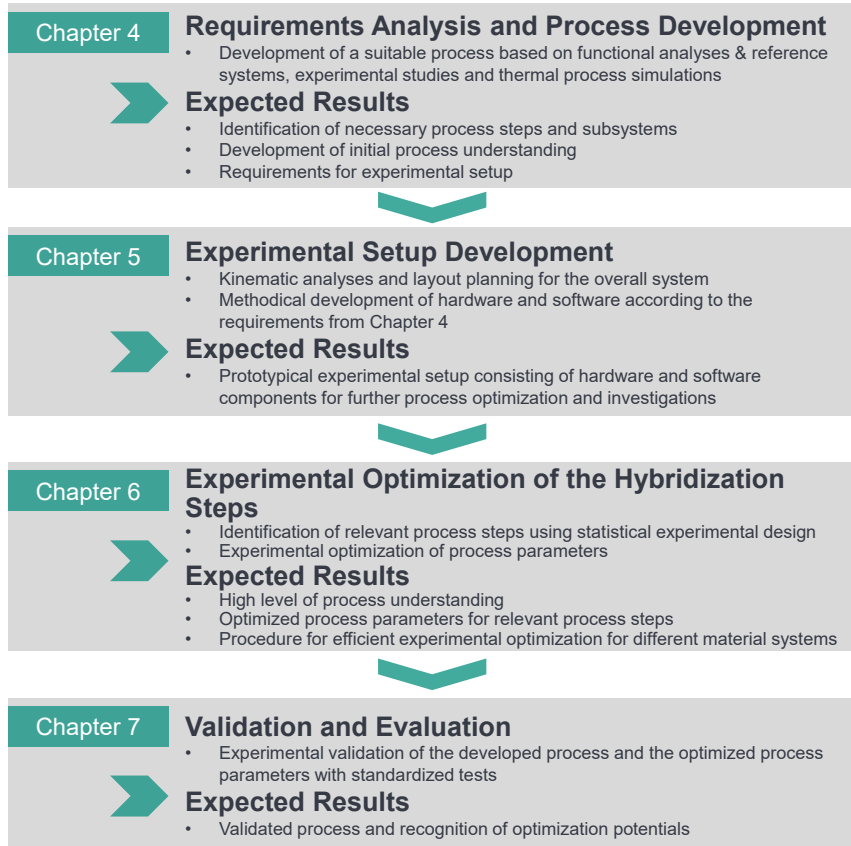


Figure 3-1: Procedure and approach to achieve the objective

The further development of the experimental production setup is carried out in Chapter 5, which is based on the SPALTEN methodology (Albers & Burkhardt et al. 2005). This is a universal problem-solving methodology that is suitable for methodical product de-

velopment but can also be applied to completely different problems such as the development of a new manufacturing process. The application of the SPALTEN method in Chapter 5 is not explained or elaborated in more detail, as it is not relevant to the overall understanding of the thesis. It should only be pointed out that, in accordance with the SPALTEN method, several concepts were developed for the various subsystems, which were evaluated based on a utility value analysis and experimental investigations. The solutions for the subsystems presented in Chapter 5 are based on the concept with the highest rating. The individual concepts are not discussed further.

In Chapter 6, the process developed in Chapter 4 is analyzed experimentally with statistical methods using the experimental system developed in Chapter 5. Relevant process steps and associated process parameters are optimized experimentally for a selected material system.

Chapter 7 validates the developed process and the associated experimental system. For this purpose, samples and demonstrators are produced using the results from Chapter 6 and strength and comparative values are determined using standardized tests such as DIN 527-4 and ASTM D5868-01 in order to determine the degree of fulfillment of the newly developed process. Problems and opportunities of the new process and the experimental setup can be identified.

4 Requirements Analysis and Process Development

The primary objective of Chapter 4 is to identify the necessary process steps and how they are combined into a hybridization process for the subsequent individualization and individual production of CoDiCoFRP. This also includes the identification of necessary subsystems. To achieve this, the required functions and subsystems are determined in Chapter 4.1. Chapter 4.2 then identifies relevant process parameters and requirements. The reference systems identified in the analysis and assessment of the state of the art (see Chapter 2) serve as the basis for Chapters 4.1 and 4.2. In Chapter 4.3, different hybridization process variants and individual process steps are investigated and evaluated experimentally. Further process investigations are carried out in Chapter 4.4 using thermal simulations. In addition to the identified process and subsystems, requirements for the experimental setup which is developed in Chapter 5 are also being derived.

4.1 Identification of Functions and Subsystems

Based on the Function Analysis System Technique (FAST) according to (VDI 2803), the main functions for the production of CoDiCoFRP according to the objectives are identified, as can be seen in Figure 4-1.

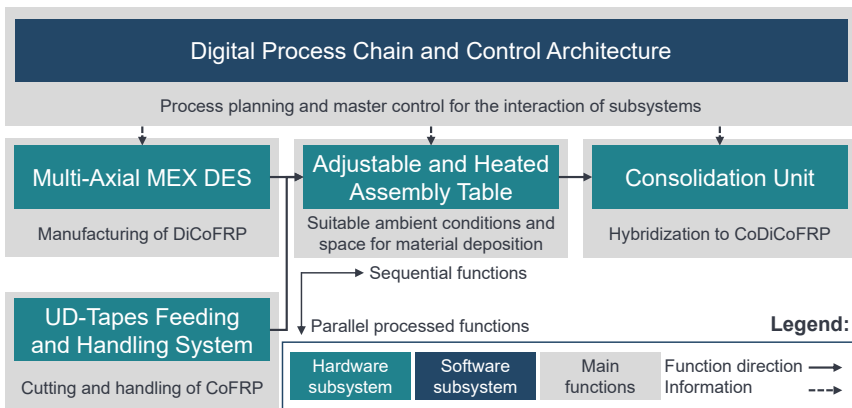


Figure 4-1: Required main functions and subsystems visualized with a diagram-based on FAST

The main function is the manufacturing of the Co and DiCoFRP, the provision of a suitable work space, and the hybridization of the Co and DiCo components to form a Co-

DiCoFRP. In parallel, a master control system coordinates the main functions, consisting of a Digital Process Chain and Control Architecture. Based on the theories of PGE, suitable reference systems have been identified from the analysis of the state of the art as subsystems to fulfill the main functions. A multi-axial MEX DES (cf. Chapter 2.3.1) can be used to manufacture the DiCoFRP component. A handling and feeding system is required for the provision and preparation of the CoFRP. Both mentioned subsystems do not have to be newly developed and can be transferred from the state of the art with minor adaptations. The Robotic Swing Folding described in Chapter 2.1.3.3 is used for the subsystem responsible for handling and feeding the CoFRP in the form of UD-tapes. The Consolidation Unit, the Adjustable and Heated Assembly Table and the Digital Process Chain and Control Architecture are adjustment constructions according to the PGE theory. This means, that some functionalities can be adopted from reference systems from the state of the art, but must be strongly adjusted for their new purpose. The Consolidation Unit is the subsystem requiring the most development effort, as the new hybridization process uses this Consolidation Unit. ATL systems (cf. Chapter 2.1.3.1) as well as in-situ and semi-in-situ approaches for Co-fiber reinforcement in MEX (cf. Chapter 2.2.3) are used as reference systems. The Adjustable and Heated Assembly Table uses conventional heated 3D printer beds as reference systems. Various reference systems for robot offline programming and component slicing are used and combined for the development of the digital process chain.

Based on the functions and subsystems identified according to the FAST analysis and the analysis of reference systems from the state of the art, the general target system is shown in Figure 4-2. As the Consolidation Unit requires the highest development effort, its exact design is still relatively vague compared to the other subsystems. It is only certain that, like ATL systems, it requires at least one heat source and a compaction roller or similar. The Assembly Table also requires a suitable heating source and possibly additional kinematic degrees of freedom to ensure cooperation with the other systems and to provide suitable boundary conditions for the processes. In the course of the work, the target system is further defined and developed step by step on the basis of findings from various studies.

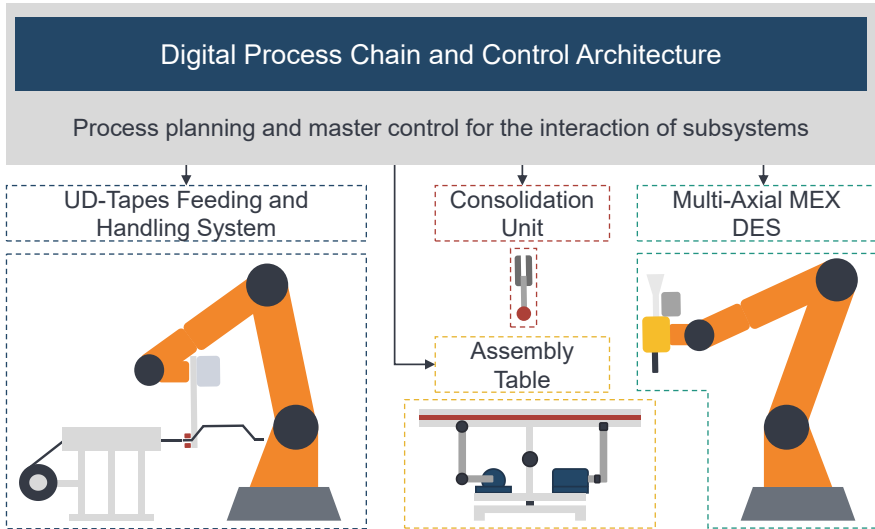


Figure 4-2: Overview and configuration of the conceptual target system consisting of the main subsystems

A detailed explanation of the methodical development of the subsystems Consolidation Unit, Adjustable and Heated Assembly Table and the Digital Process Chain and Control Architecture can be found in Chapter 5. This is preceded in the following Chapter 4.2 by a detailed requirements analysis and definition of the boundary conditions for the development. Chapter 4.3 describes the systematic development of the process (function) for the hybridization of Co and DiCoFRP based on experiments and simulations, which defines further requirements for the subsystems. The final Section 4.4 of this Chapter summarizes the findings and requirements of the newly developed hybridization process for the individualization and individual production of CoDiCoFRP. Based on this, the target system, the experimental production system, is precisely defined.

4.2 Identification of Process Parameters and Requirements

Figure 4-3 shows all identified controllable and non-controllable process parameters that can influence the intended manufacturing process. The identification is based on the analysis of the identified reference systems from the state of the art described in the previous Section 4.1 and partly from preliminary studies conducted in (A_Davide 2021; A_Kill 2022; A_Buschulte 2022).

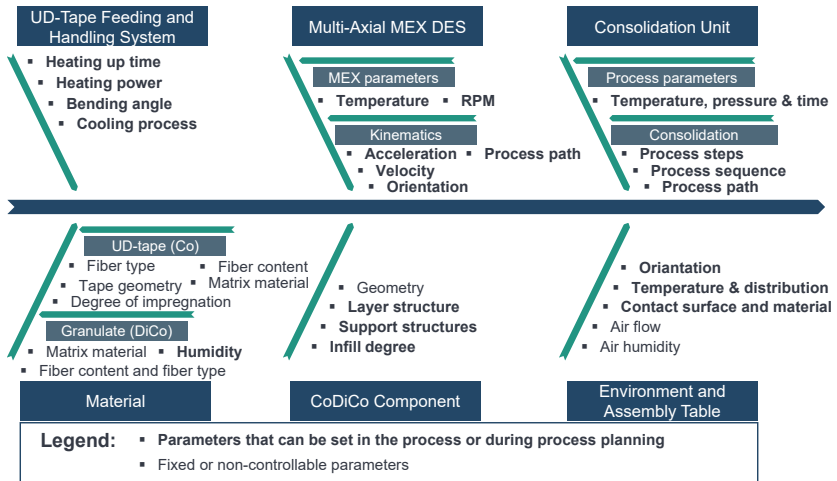


Figure 4-3: Ishikawa diagram of controllable and non-controllable influencing parameters

As can be seen in Figure 4-3, most of the parameters can be controlled by the respective subsystem. Process parameters of the CoDiCo components that depend on the individual geometry (e.g. support structure or infill degree) are set during process planning with the Digital Process Chain subsystem. The most common process parameter is temperature. Temperature and many other process parameters are highly material specific. In order to be able to quantify the requirements for the individual subsystems and their individual processes, a pre-selection of a suitable representative material system is necessary. The results of the selection are presented in the following section.

4.2.1 Material Selection

To ensure that the developed subsystems and their specific processes are suitable to meet the requirements of real applications, a technically relevant and widely used FRP material system is selected. For the matrix material of the CoDiCoFRP, PA6 is chosen, as it is currently one of the most widely used and relevant engineering thermoplastics. PA6 has good mechanical properties for a thermoplastic material, such as adequate strength, stiffness and impact strength and is often reinforced with carbon or glass fibers to further improve its thermomechanical properties (Karsli & Aytac 2013, p. 270). The disadvantage of PA6 becomes apparent during processing, as it should be dried before processing due to its high hydrophilic behavior, which means that other thermoplastics

are usually preferred in the field of AM MEX, although PA6 is still commonly used (Kumar & Sadasivuni et al. 2022, p. 168–170). Since the welding of different thermoplastics with each other is only possible to a very limited extent, especially with PA6 (Hopmann & Michaeli 2017, p. 258), PA6 is selected for the matrix materials of the Co and DiCo parts. In order to maximize strength and stiffness, pre-impregnated UD-tapes made of carbon fibers (CF) are selected for the Co part. UD-tapes made of PA6 and CF are generally very common and are offered by various suppliers. For the DiCo part, glass fibers (GF) and carbon fibers could be used, which offer different advantages and disadvantages. Based on the pre-study presented in Chapter 4.3.1 and the achieved mechanical properties during hybridization to form CoDiCoFRP, the material system is selected for further analyses. Table 4-1 shows an overview of all material systems analyzed in this thesis and their most important properties. The materials selected for the main study are used in the experiments from Chapter 6 onwards.

Table 4-1: Overview of material properties (based on ¹(Matsuo & Hojo et al. 2019) and manufacturer's data sheets ²(Spectrum Group 2021), ³(3DXTECH 2022a) and ⁴(3DXTECH 2022b))

Manufacturer and product type	Pre-study			Main study	Main & pre-study
	Spectrum Nylon PA6 ²	Amidex PA6 GF30 ³	CarbonX Fiber Nylon ⁴	PRO-plast PA6 CF30	Tencate Cetex TC910 ¹
Fiber		DiCo	DiCo	DiCo	Co
Fiber material	No fiber reinforcement	Glass	Carbon	Carbon	Carbon
Fiber volume fraction		30 %	< 30 %	30 %	43 %
Semi-finished product	Filament	Filament	Filament	Granulate	UD-tape
Matrix	PA6	PA6	PA6	PA6	PA6
Density	1.05 g/cm ³	1.3 g/cm ³	1.17 g/cm ³	1.28 g/cm ³	1.45 g/cm ³
Thickness	1.75 mm	1.75 mm	1.75 mm	N/A	0.16 mm
E-Modulus	2.3 GPa	4.2 GPa	3.8 GPa	Not specified	100 GPa
Tensile Strength	Not specified	62.8 MPa	63 MPa	Not specified	1900 MPa
Recommended process temperature	250 - 270 °C	270 °C	275 °C	Not specified	249 - 271 °C

4.2.2 Process Requirements

As described in Chapter 4.1, the subsystems *Consolidation Unit*, *Adjustable and Heated Assembly Table* and the *Digital Process Chain and Control Architecture* must be newly developed or existing solutions must be significantly adapted from the state of the art. For this purpose, the requirements for the new hybridization process of Co and DiCo-FRP must be precisely defined. The requirements quantified in Table 4-2 result from

the relevant process parameters identified (cf. Figure 4-3) and the material system analysis carried out in the previous section. As the Digital Process Chain and Control Architecture subsystem is hierarchically above the other subsystems (cf. Figure 4-1), the requirements defined in the table for the Adjustable and Heated Assembly Table and the Digital Process Chain and Control Architecture subsystems also apply to it. Since the new hybridization process and the associated experimental setup should be suitable for all thermoplastic FRP and not just for the chosen PA6, the ranges of the process parameters have been selected accordingly.

Table 4-2: Description and quantification of process parameter requirements for the hybridization of Co and DiCoFRP

Subsystem	Process parameter/feature	Description and quantification
Consolidation Unit	Consolidation temperature range	80 - 400 °C
	Consolidation pressure range	For homogeneous pressure distribution 0.1 - 3 MPa; For approximately linear load 3 - 30 MPa
	Consolidation time	No upper limit, less than 1 s should be achievable
	Consolidation paths	Non-planar multi-axial paths with gradients of at least 45°
Adjustable and Heated Assembly Table	Heated bed/Assembly Table temperature	Homogeneous temperature distribution in the range of 60 - 200 °C
	Tilting of the heated bed/Assembly Table	Up to 60 ° around its own x- and y-axis relative to the horizontal position, 360 ° around the z-axis
	Designed for high loads	Based on consolidation pressure and safety factors, up to 300 N can occur on the surface
	Material compatibility	The contact surface must ensure very good adhesion for the Co- and DiCo materials

4.3 Process Development and Analysis

As described at the beginning of this chapter (cf. Figure 4-1), the Consolidation Unit is the subsystem with the highest development effort. There is currently no flexible process for the hybridization of DiCoFRP produced using the MEX process and CoFRP from UD-tapes. For this reason, the systematic identification of a suitable hybridization process is presented in this section. In Chapter 4.3.1, four different hybridization strategies for the integration of UD-tapes (Co-fiber) in the MEX process are investigated with a simple test setup for pre-studies. Hybridization strategies are composed of different combinations of process steps. The influence of different DiCo material systems

is also analyzed and a material selection is made for the main investigations from Chapter 6 onwards. The identified hybridization strategies are further investigated in Chapter 4.3.2 with the help of thermal simulations and effect analyses for a better process understanding. For the interaction of the different subsystems and the definition of suitable kinematics, a kinematic analysis is carried out in Chapter 5.1, as this is a part of the development of the experimental setup.

4.3.1 Experimental Investigation of Hybridization Strategies

Different hybridization strategies have been developed and tested in (A_Kill 2022; A_Buschulte 2022) to identify one or more suitable hybridization processes including relevant process steps for the integration of UD-tapes into the MEX process. In the following section, the hybridization strategies and their process steps are explained based on the production procedure of the test specimens for the experiments. The various experiments carried out to investigate the hybridization strategies are presented in the following Chapters 4.3.1.2 and 4.3.1.3.

4.3.1.1 Definition of Hybridization Strategies and Specimen Production

As shown in Figure 4-4, the hybridization strategies S1 – S5 result from the combination of different process steps. The main process steps are *Consolidation I*, *Consolidation II*, *Overprinting* and *Point Welding* for securing the UD-tape after positioning. Consolidation I refers to a consolidation directly on the UD-tape, whereas Consolidation II involves an additional MEX layer on the UD-tape due to previous Overprinting.

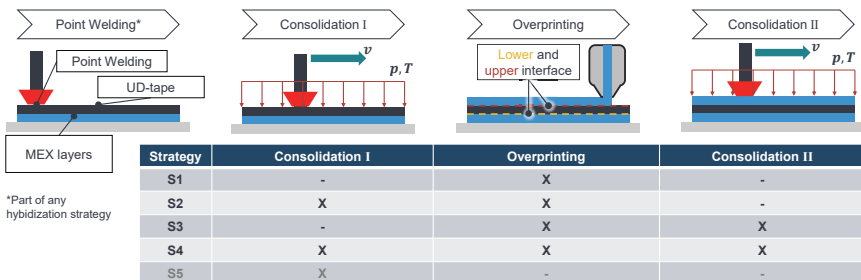


Figure 4-4: Hybridization strategies for integrating UD-tapes into the MEX process

Description of the Hybridization Strategies and Individual Process Steps

For S1 to S4, it is assumed that the Co-fibers (UD-tape) are located inside the component in a sandwich structure. This results in a lower and upper interface between the UD-tape and the 3D-printed layers using MEX. If the UD-tapes should be on the surface of the component, only the Consolidation I process step is needed, resulting in S5. Consolidation I and Consolidation II are very similar to the ATL processes described in Chapter 2.1.3.1. In principle, Consolidation I can be repeated for the different strategies to stack several UD-tapes and increase the fiber content. Consolidation II is carried out after the UD-tape has been overprinted with a layer using the MEX process. Except for the local Point Welding of the UD-tape, all process steps contribute to bonding the interfaces between the UD-tape and the printed layers.

In S1, the hybridization and bonding of the upper and lower interfaces in theory takes place through the heat input of the extruded material during Overprinting. As this step is carried out at very low pressure, there is little consolidation. Compared to S1, S2 also involves targeted consolidation of the lower interface, using the step Consolidation I. In S3, targeted consolidation of the upper interface takes place with Consolidation II. The lower interface is also consolidated but to a much lesser extent due to heat loss. S4 involves targeted consolidation of both the upper and lower interfaces, using Consolidation I and II. S5 is a variation of S4 where there is no Overprinting. As the influence of Consolidation I can be determined by experiments with S1 to S4, no separate experiments are carried out for S5.

Production of Test Specimens

To produce test specimens to evaluate the hybridization strategies including different material systems, an initial prototypical setup was created as shown in Figure 4-5. The setup consists of a modified FDM printer and allows the flexible production of different shaped test specimens. A simplified consolidation unit is positioned offset from the extruder nozzle. The simplified consolidation unit is freely movable in height and has interchangeable consolidation irons. An additional controller can be used to set the temperature of the consolidation unit. By exchanging weights in combination with the different surfaces of the irons, the consolidation pressure can be adjusted. The theoretical consolidation time can be controlled via the velocity of the printer axes, which together with the consolidation path can be controlled via the G-code.

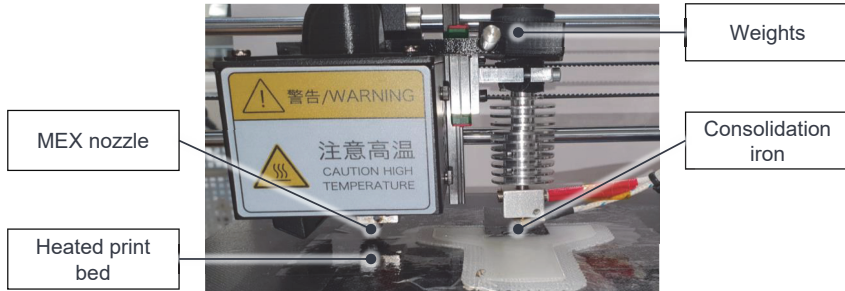


Figure 4-5: First prototypical experimental setup consisting of a modified FDM printer for the investigation of the hybridization strategies

Identification of suitable Process Parameters

With the help of the first prototypical setup, suitable process parameters can be determined iteratively. As described during the material selection in Chapter 4.2.1, glass and carbon fibers are analyzed for the DiCo part. In order to better determine the influence of the DiCo-fibers, unreinforced PA6 is also used as a reference. Table 4-3 shows the process parameters identified for the different material systems.

Table 4-3: Experimentally determined process parameters for the hybridization of the UD-tapes with the different material systems of the MEX layers

Process parameter	PA6	DiCo PA6 GF	DiCo PA6 CF
Temperature extruder	230 °C	245 °C	245 °C
Temperature heated bed	85 °C	90 °C	75 °C
Temp. Consolidation I	180 °C	204 °C	217 °C
Temp. Consolidation II	140 °C	170 °C	180 °C
Pressure Consolidation I	1.5 MPa	1.5 MPa	1.5 MPa
Pressure Consolidation II	0.5 MPa	0.5 MPa	0.5 MPa
Consolidation velocity	1.5 mm/s	1.5 mm/s	1.5 mm/s

The temperatures for the extruder and the heated bed are as recommended by the manufacturer for the respective material. To ensure that the consolidation process had sufficient time for the formation of intimate contact and for autohesion (cf. 2.1.2.2), the velocity was set to the minimum possible with the setup. With these two temperatures and the speed as boundary conditions, the process parameters temperature and pressure for Consolidation I and II were determined iteratively as shown in Figure 4-6. For this purpose, several lanes with a varying combination of parameters were consolidated on one component. In accordance with the one-factor-at-a-time experimental design,

only one of the two process parameters was increased step by step at a time. This continued until significant damage occurred. For Consolidation I, this means severe deformation and scraping of the matrix layer from the UD-tape. For Consolidation II, the same requirements apply to the printed MEX layer on the UD-tape.

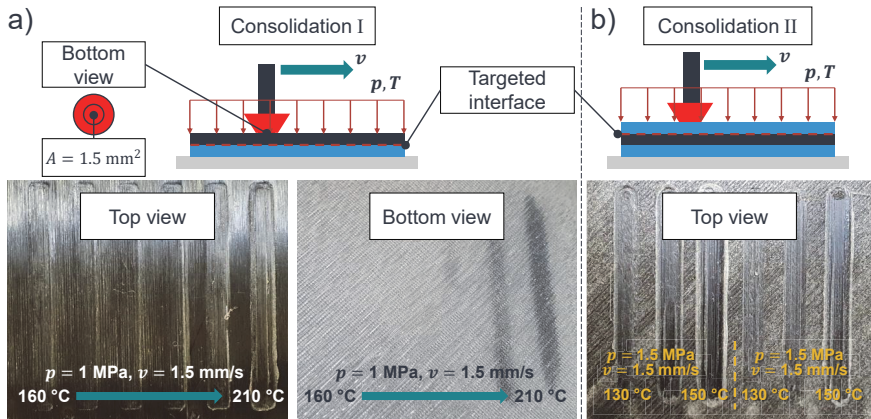


Figure 4-6: Experimental iterative identification of suitable process parameters for Consolidation I and II using PA6 for the MEX layers

As can be seen in Table 4-3, Consolidation II is carried out at significantly lower temperatures and pressures than Consolidation I for all material systems, as otherwise the first MEX layer on the UD-tape would suffer considerable damage. This damage, in the form of severe deformation, causes problems when printing subsequent layers. This can also be partly traced back to the form of the consolidation iron. This is considered in the development of the subsystem Consolidation Unit in Chapter 5.2.1.

In the following two sections, the hybridization strategies S1 to S4 and the three material systems with the identified process parameters are examined and evaluated using different experiments.

4.3.1.2 Interface Studies

As described in Chapter 2.1.2.2, there must be a high degree of bonding D_b in the interface areas of an FRP in order to achieve the maximum reinforcement effect of Co-fibers. The degree of bonding is correlated with the maximum transmissible shear stresses between the fiber-matrix interface. For this reason, the maximum transmissible

shear stresses of the individual hybridization strategies are used in order to compare and evaluate them.

Specimen Geometry

Based on (DIN EN 1465; Baranowski & Schlotthauer et al. 2022, p. 9), a suitable test specimen for the tensile shear test was determined in (A_Buschulte 2022) as shown in Figure 4-7. As can be seen in Figure 4-7 a), the sandwich structure of the test specimen provides an upper and lower interface between the UD-tape and the respective MEX layer, which makes it suitable for testing strategies S1 - S4. In addition to the mechanical tests, the test specimens are also scanned using computed tomography (CT), to qualitatively determine the void content in the region of interest (ROI, see Figure 4-7 b)). The void content allows conclusions about the degree of intimate contact D_{ic} which has a direct influence on the resulting degree of bonding D_b .

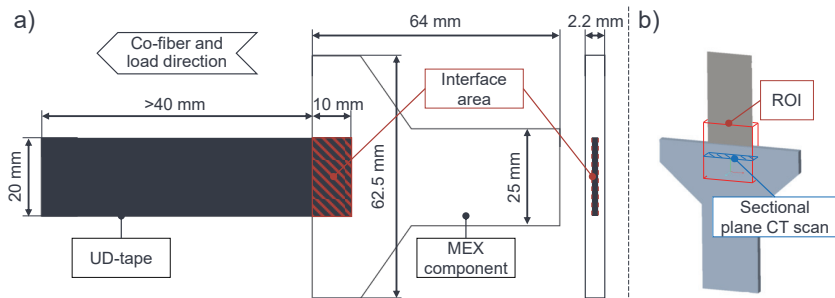


Figure 4-7: Test specimen: a) Geometric dimensions and interface area crucial for the tensile shear test; b) ROI for the CT scans (based on (DIN EN 1465; A_Buschulte 2022; Baranowski & Schlotthauer et al. 2022, p. 9))

Computed Tomographic Analysis

The aim of CT analysis is to provide a conclusion about the degree of intimate contact D_{ic} which correlates with the void content in the interfaces. For this purpose, samples as shown in Figure 4-7 were produced using the hybridization strategies S1-S4 for the three material systems described in Chapter 4.2.1.

CT scans were conducted in (A_Kreusel 2022) with a Zeiss Metrotom 800 device. The CT scans allow the upper and lower interface areas to be analyzed independently for the four hybridization strategies, which is not directly possible with the following mechanical tests. Using generated CT reconstructions, it is possible to detect voids in the

area surrounding the two interfaces and thus evaluate the formation of intimate contact. For void detection and analysis, the procedure of Du Plessis & Sperling et al. (2018) was adapted and performed using VG Studio Max 3.4.5 software. In the first step a ROI was defined, which is the area surrounding the two interfaces (see Figure 4-7 b)). For this purpose, the tape was identified using region growing, then bordered at a distance of 1 mm. In the next step, the voids within this ROI were detected by setting a threshold and ultimately evaluated using VG Studio's advanced (classic) surface determination algorithm and the porosity analysis algorithm "from defect ROI" (Matkovic & Höger et al. 2023). An exemplary result of the CT scans can be seen in Figure 4-8 on the left.

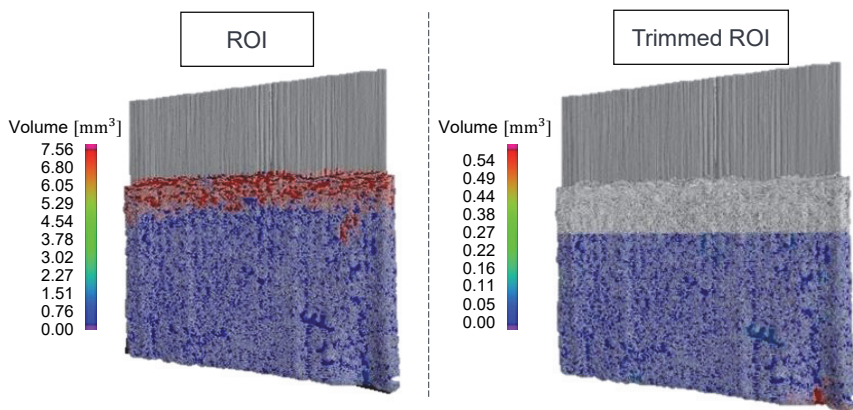


Figure 4-8: Volume of detected voids in the ROI and the trimmed ROI (based on (A_Kreusel 2022))

The volume of the voids can be identified using the color scale. Blue dots indicate many small voids. At the transition area where the UD-tape hangs out of the component, the algorithm identifies a large void, which is shown in red. In fact, there are actually many medium-sized voids, but they are connected by individual small channels and are therefore identified as one. As a very high and heavily fluctuating void content was always found in the transition area to the exposed UD-tape, this area is cut off in all analyses, as shown in the trimmed ROI in Figure 4-8. This ensures that not too many outliers are included in the measured data for determining the void content. The reason for the increased void content is due to a drop in temperature at the transition area. In (A_Tritschler 2023) a thermal simulation to determine the temperature curve during the

consolidation of the samples was set up. It is shown, that the temperatures of the interface drop by approx. 10 °C at the edge area compared to component areas further inwards. This is due to the UD-tape hanging out of the component, which acts as a heat sink due to its good thermal conductivity and relatively large surface area. This effect is considered in the main study in Chapters 6 and 7 by using an adapted test specimen. Further thermal simulations in more detail are discussed in Chapter 4.3.2.

Figure 4-9 shows the detected voids described by this method within a sectional plane in the ROI (cf. Figure 4-7 b)), with the MEX material layer PA6 GF as an example.

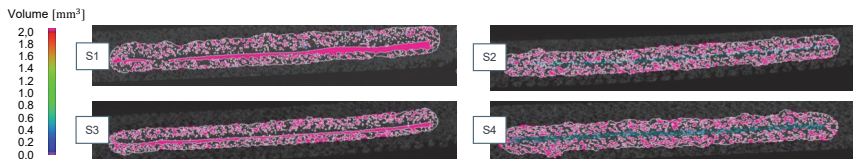


Figure 4-9: Voids detected with CT scans within a sectional plane in the ROI for PA6 GF for hybridization strategies S1 - S4 (Matkovic & Höger et al. 2023)

The colored areas show the detected voids in the ROI. Due to the selected scale and the limited resolution, whereby individual voids are summarized, most voids appear to have a volume greater than 2 mm³. For S1 and S3, a clear air gap can be recognized along the lower interface. This is due to the fact that in both cases no Consolidation I took place, and thus no intimate contact could be established. For the upper interface, there appears to be a relatively high degree of intimate contact D_{ic} that develops when the UD-tape is overprinted. In the case of S2 and S4, it can be seen that there is no air gap at the lower interface and therefore Consolidation I ensures the development of a relatively high degree of intimate contact.

In order to obtain a quantifiable statement from the CT scans, it is checked whether there is a correlation between the degree of intimate contact and the void content. For this purpose, at first one sample per strategy and material system was examined in order to be able to evaluate this approach. The void content within the ROI for the three material systems analyzed can be seen in Table 4-4.

Table 4-4: Voids detected with CT scans within a sectional plane in the ROI for PA6 GF

Material	Void content				PCC
	S1	S2	S3	S4	
PA6	16.15 %	11.96 %	13.76 %	17.03 %	0.04
PA6 GF	32.28 %	32.99 %	34.82 %	32.67 %	-0.15
PA6 CF	31.67 %	23.99 %	30.52 %	18.19 %	-0.98

A positive and negative correlation between two data series can be quantified based on the Pearson correlation coefficient (PCC). For the unreinforced PA6 and PA6 GF with $|\text{PCC}| \approx 0$, there is no to very little correlation between the reachable mean shear stress of S1 - S4 interfaces (explained below, cf. Figure 4-10) and the void content in the ROI. In the case of PA6 CF with $\text{PCC} \approx -1$, there is a strong negative correlation. This means that the maximum transmissible shear stress of the interface increases with decreasing void content in the ROI. Due to the very high time required for CT scans and the deviations in PCC between the individual material systems, the void content in the ROI is not used any further to quantify the interface of the individual hybridization strategies. Nevertheless, the qualitative evaluation and comparison of the CT scans can be used to make statements about the formation of an intimate contact.

Tensile Shear Test

The aim of the tensile shear test is to obtain a quantitative value in order to be able to make a statement about the degree of bonding D_b . For this purpose, mechanical tests are used to determine the transferable shear stresses of the interface for the four hybridization strategies and the three material systems. The specimen type from Figure 4-7 was produced using the hybridization strategies and process parameters shown in the previous Section 4.3.1.1. Based on (DIN EN 1465) the tensile shear tests were carried out for a defined sample size for each hybridization strategy.

To estimate the sample size n_i of the shear stress tests per hybridization strategy, Equation 4-1 based on (Kleppmann 2020, p. 30) is used.

$$N_i = 2 \cdot n_i \approx 60 \cdot \left(\frac{\sigma_i}{\Delta\mu_{i,j}} \right)^2 \quad 4-1$$

Within the test $\Delta\mu_{i,j}$ is the effect that should be detected with high probability between the hybridization strategy number i and j . In this context, $\Delta\mu_{i,j}$ is defined as the difference between the mean values of the maximum shear stress between two hybridization

strategies, where the indices i and j represent the strategies being compared. σ_i is the standard deviation of the respective hybridization strategy i for which the number of samples is calculated. The total number of samples required to compare two strategies is $N_i = 2 \cdot n_i$.

As there were no reference values for σ_i and $\Delta\mu_{i,j}$, in the first step five samples of each hybridization strategy were produced with unreinforced PA6 for the MEX layers in order to have reference values for Equation 4-1. The highest number of samples required results in $n_2 \approx 12$ with $\sigma_2 = 200.41$ MPa and $\Delta\mu_{2,3} = 318.47$ MPa. Based on this estimation, the tests were repeated accordingly for the three matrix material systems PA6, PA6 GF and PA6 CF. The results can be seen in Figure 4-10.

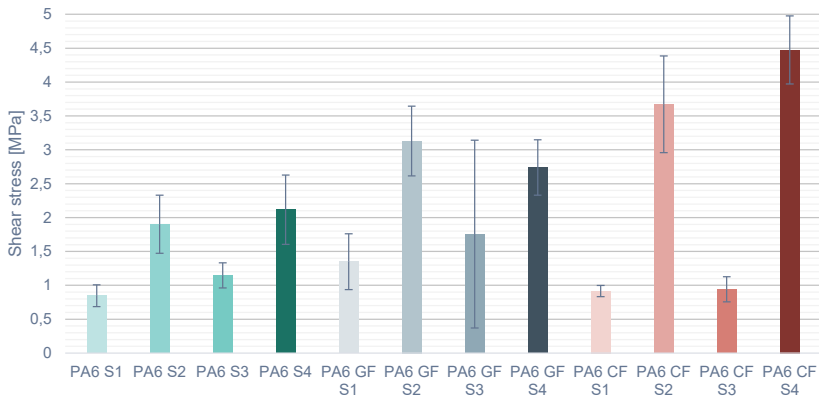


Figure 4-10: Mean shear stress and standard deviation of the individual hybridization strategies and material systems (Matkovic & Höger et al. 2023)

Evaluation of the Interface Studies and Tensile Shear Tests

Figure 4-10 shows the mean shear stresses and standard deviations achieved for the individual strategies and material systems. With S1, no controlled consolidation takes place and the weak bond is created only by the heat input of the MEX process during Overprinting without any significant pressure. This results in an air gap in the lower interface as shown with the CT scan in Figure 4-9 S1, which shows that no intimate contact is formed. For all 3 material systems PA6, PA6 GF and PA6 CF, when comparing S1 and S2, it can be seen that Consolidation I already causes a significant increase in shear strength and thus an increase in the degree of bonding. This correlates with

the CT scan in Figure 4-9 S2, showing the absence of an air gap and thus the formation of an intimate contact. Consolidation alone after Overprinting for S3 causes only a small increase in shear strength when compared with S1. For S3, the CT scans show that, as for S1, there is an air gap at the lower interface. Therefore, the Consolidation II after Overprinting cannot form an intimate contact at the lower interface. S4 shows the highest shear strengths for PA6 and PA6 CF matrix material systems due to the use of Consolidation I and II. The slightly lower shear strength for PA6 GF S4 compared to S2 may be due to a lower specimen quality, due to starting wear of the extruder and nozzle. The samples for PA6 GF S3 were the last to be produced and a nozzle wear of the extruder due to the abrasive effect of the short fibers could be observed, resulting in the highest standard deviation.

Overall, the comparison between S3 and S1, as well as the comparison between S4 and S2, shows that Consolidation II after Overprinting causes only a small increase in shear strength and only for two of the three material systems. This can probably be attributed to a too-low Consolidation II temperature (cf. Table 4-3). This temperature had to be lower to prevent the MEX layer on the UD-tape from softening too much and ultimately being damaged during consolidation. Regardless of the strategy, Figure 4-10 shows a clear upward trend in shear strength when comparing the material systems. This can be traced back to the different thermal properties of the material systems. In general, fiber-reinforced filaments have a higher thermal conductivity and heat capacity. This seems to have a positive influence during consolidation due to better heat transfer from the consolidation iron to the interface. (Matkovic & Höger et al. 2023)

The tests show that at least Consolidation I is required, as in S2. A second consolidation (Consolidation II), as in S4 after Overprinting, seems to give only small improvements, but this can be attributed to non-ideal process parameters and the non-ideal consolidation iron. The necessary adjustments and optimization to the Consolidation Unit are shown in Chapter 5.2.1, which are used to determine the optimum process parameters in Chapter 6. In addition, adjustments to the sample shape are made in Chapters 6 and 7 to avoid the influence of the high void content as shown in the CT scan in Figure 4-8 and to perform separate optimization of Consolidation I and II. In principle, S2 and S4 are suitable methods for achieving good adhesion between the UD-tape and the MEX layers. In the next section, tensile tests are carried out to validate whether the desired strengthening effect could actually be achieved with UD-tape integration and hybridization strategies S2 and S4. The results are discussed in the following section.

4.3.1.3 Investigation of the Reinforcement Effect

To validate the reinforcement effect of S2 and S4, tensile tests were carried out in (A_Kill 2022) for the three matrix material systems PA6, PA6 GF, and PA6 CF based on the standard (DIN EN ISO 527-4).

Specimen Geometry

Figure 4-11 shows the test specimen geometry using as an example the semi-transparent PA6 material system with a single 6 mm wide UD-tape. Samples without tapes (w.t.) were also produced in order to be able to have a comparison for the reinforcement effect of integrating the UD-tape with S2 and S4. Following the recommendation of the used standard, five repetitions were carried out for each test.

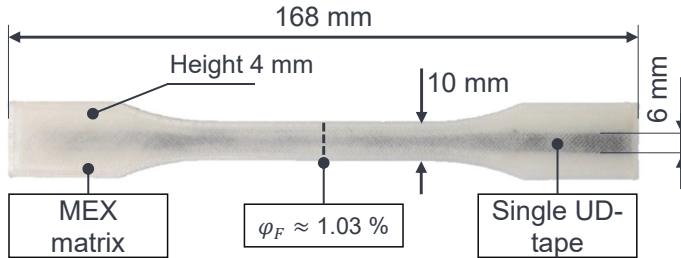


Figure 4-11: FRP specimen made of PA6 matrix with integrated UD-tape and a fiber volume fraction of $\varphi_F = 1.032\%$ (based on (DIN EN ISO 527-4))

Results of the Tensile Tests

The results of the tensile tests are shown in Figure 4-12. A comparison of S2 and S4 with the reference tensile tests without integrated tape shows that reinforcement was achieved for all material systems. The relative reinforcement effect is the highest for the non-reinforced matrix material PA6, at slightly less than 200 %. For the two DiCo matrix materials reinforced with GF and CF, the relative reinforcement effect is overall lower at under 100 %. S4 has a slightly higher reinforcement effect than S2 for PA6 CF and PA6 GF. For the purely PA6 it is the other way around, with S2 achieving a higher reinforcement effect than S4. This could be due to non-optimized process parameters during Consolidation II, which damages the overprinted layer of the UD-tape. This then

has an effect on the strength of the entire tensile specimen. In absolute terms, the highest tensile strengths are achieved with PA6 CF S4, which also corresponds to the highest shear stresses achieved in the previous section (cf. Figure 4-10).

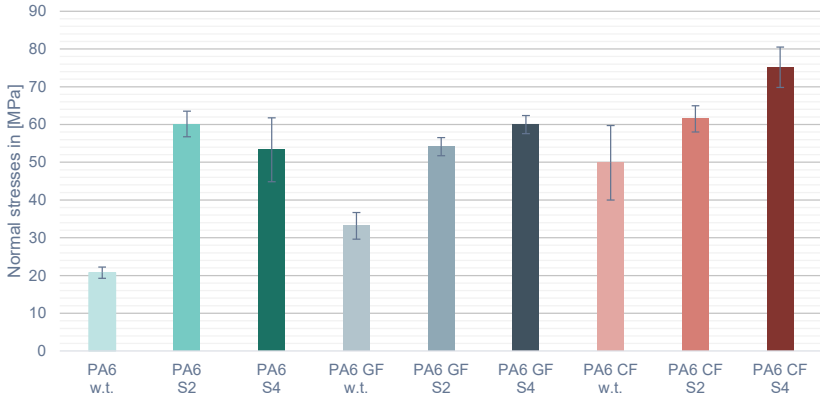


Figure 4-12: Average tensile strengths and standard deviations achieved based on (DIN EN ISO 527-4) for hybridization strategies S2 and S4 for all material systems; Results for specimens without UD-tape (w.t.) reinforcement as reference

Evaluation of the Reinforcement Effect

In general, the results show that S2 and S4 are suitable hybridization strategies. In order to better compare the results with other state-of-the-art processes, the degree of fulfillment D_f , as shown in Equation 4-2 (Baumann 2020, p. 121–122), is used. D_f specifies the percentage of the theoretical maximum tensile strength $R_{FRP,||,th}$ that the FRP has achieved, with $R_{FRP,||,re}$ being the actual strength achieved. This allows the comparison of different material systems with different fiber volume fractions.

$$D_f = \frac{R_{FRP,||,re}}{R_{FRP,||,th}} \cdot 100 \% \quad 4-2$$

$R_{FRP,||,th}$ is calculated using Equation 2-2 from the model of Voigt (1889). The material properties required for the calculation are listed in Table 4-5. The fiber volume fraction φ_F required for the calculation of D_f is sample-specific and must be calculated.

Table 4-5: Material properties required for the calculation of $R_{FRP,||,th}$ of the tensile specimens (based on ¹(Matsuo & Hojo et al. 2019) and manufacturer's data sheets ²(Spectrum Group 2021), ³(3DXTECH 2022a) and ⁴(3DXTECH 2022b))

E_M PA6 ²	E_M PA6 GF ³	E_M PA6 CF ⁴	E_F ¹	R_F ¹	φ_F
2300 Mpa	4200 Mpa	3800 Mpa	230 GPa	4674 Mpa	1.032 %

With a thickness of 0.16 mm and a fiber volume fraction of 43 % for the UD-tape, the cross-sectional area of the fibers in the specimen is $A_f = 0.16 \text{ mm} \cdot 6 \text{ mm} \cdot 43/100 = 0.413 \text{ mm}^2$. Based on Equation 4-3 and a cross-sectional area of the FRP test specimen of $A_{FRP} = 40 \text{ mm}^2$, this results in a fiber volume fraction of $\varphi_F = 1.032 \text{ %}$.

$$\varphi_F = \frac{A_f}{A_{FRP}} \cdot 100 \text{ %} \quad 4-3$$

The fiber volume fraction of the tensile specimens is relatively low compared to the state of the art, as only one UD-tape was integrated. With Co-fiber integration in MEX, the fiber volume fraction is often in the range of 10 - 20 %, and in exceptional cases even up to 50 % (Baumann 2020, p. 121–122). Since theoretically as many UD-tapes as desired can be layered before Overprinting in S2 and S4, the fiber volume fraction can be increased to almost 43 %, which corresponds to that of the UD-tape.

The theoretical tensile strengths $R_{FRP,||,th}$ calculated with Equation 2-2 as well as the calculated degrees of fulfillment D_f for S2 and S4 with Equation 4-2 for all three material systems are listed in Table 4-6.

Table 4-6: Calculated theoretical tensile strengths $R_{FRP,||,th}$ and degree of fulfillment D_f for all material systems, S2 and S4

FRP Materials	Theoretical tensile strength $R_{FRP, ,th}$	Degree of fulfillment D_f	
		S2	S4
PA6 + UD-tape	94.49 MPa	64 %	56 %
PA6 GF + UD-tape	132.71 MPa	41 %	45 %
PA6 CF + UD-tape	124.66 MPa	49 %	60 %

Processes for continuous fiber integration in MEX from the state of the art achieve D_f values in the range of 19 - 62 %. The D_f values achieved here for S2 and S4 in the range of 41 - 64 % show the applicability of the hybridization strategies, especially as the consolidation unit and the process parameters are not optimized as described. The analysis of PA6 GF and PA6 CF shows that higher values for D_f are achieved with S4

than with S2. In contrast, the purely PA6 is an outlier, as the absolute highest value for D_f is achieved with S2. As already mentioned, this is probably due to the process parameters not being fully optimized. The quality of the parameters used for the different material systems is therefore subject to fluctuations and PA6 S2 is an outlier.

Warpage Analysis of Tensile Test Specimens

In addition to determining the tensile strength, the specimens are suitable for providing a qualitative evaluation of material warpage. Figure 4-13 (left) shows the tensile test specimens from the side view. As can be seen by comparing the PA6 specimen with and without UD-tape, hybridization with Co-fibers causes extreme distortion of the specimens.

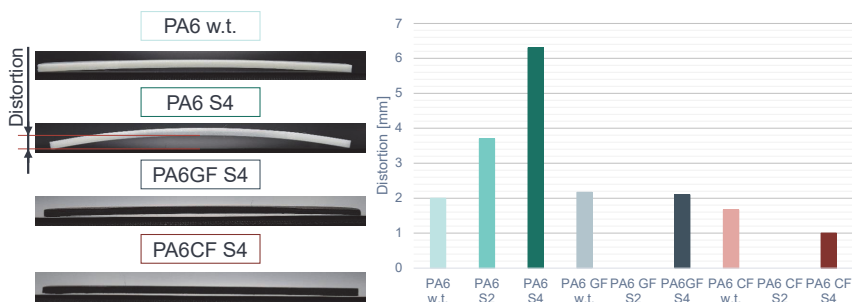


Figure 4-13: (Left) Distortion of the tensile specimens from the side view: PA6 without UD-tape (w.t.) as reference for S4 of PA6, PA6 GF and PA6 CF; (Right) Average deformation of five analyzed specimens

The distortion occurs after the samples are removed from the heated bed and have time to cool down. Due to the characteristics of the MEX FDM process, the PA6 sample without tape has already a slight deformation. Significant higher warpage of the PA6 samples with UD-tape reinforcement (S2 and S4) can be attributed to the differing coefficients of thermal expansion (CTE) of the Co-fibers and the PA6 MEX matrix. PA6 has a positive CTE, which causes it to contract as it cools down. In contrast, the carbon Co-fibers have a negative CTE in the direction of the fibers, which causes them to elongate when cooled down. In theory, the distortion therefore decreases when the CTE of the printed MEX matrix and the Co-fibers are more similar. This can be observed in Figure 4-13 on the right for the PA6 GF and PA6 CF MEX matrix. The DiCo-fibers in the MEX matrix bring the CTE closer together and thus reduce distortion. The average deformation is lowest for PA6 GF S2 and PA6 CF S2. As deformations of less than 1

mm could not be measured with the measurement setup, therefore no exact measured values are available for these.

4.3.1.4 Evaluation of the Hybridization Strategies

Based on the interface studies, hybridization strategies S2 and S4 were identified as suitable processes for the individual production and subsequent individualization of Co-DiCoFRP for further investigations and developments. The main process steps are *Point Welding* to secure UD-tapes, *Overprinting* and *Consolidation I and II*. An experimental system for the automated execution of these process steps is developed in Chapter 5.

S4 demonstrates slightly better results with DiCo MEX materials (PA6 GF and CF) compared to S2, suggesting that the additional Consolidation II can enhance the reinforcement effect when hybridizing Co and DiCoFRP under specific conditions. For this reason, optimal process parameters for Consolidation I and II are being analyzed in the main studies in Chapter 6. Due to the lowest distortion when using carbon DiCo-fibers in the MEX matrix, PA6 CF was determined to be the most suitable material for further investigations of the new hybridization process.

As the tests were only carried out with a simple prototype setup for only small component dimensions, thermal simulations are carried out in the following section. This further increases the understanding of the process. Based on this, the requirements for the experimental setup to be developed can be further defined.

4.3.2 Thermal Simulations and Analysis of Consolidation I and II

Production of the specimens described in the previous section was carried out under constant boundary conditions and for a constant and small geometry. The intended process for hybridization of CoDiCoFRP should be applicable for individual components, which means that boundary conditions and component geometries do not remain constant. Temperature is one of the process parameters that is critical to successful hybridization (cf. Chapter 4.2) and is sensitive to changing boundary conditions and geometries. Since any geometry is theoretically conceivable, it must be ensured that the identified hybridization strategies S2 and S4 and thus Consolidation I and II can also be carried out under changing conditions. For this reason, an effect analysis based on thermal simulations is carried out in the next section for stationary analyses in order

to identify the geometric factors that have the greatest influence on temperature. Results of dynamic simulations are presented in the subsequent section, where the temperature changes during Consolidation I and II are simulated, and it is shown how these can be regulated in a stable manner with changing geometries. The conclusions are directly applied to the design of the experimental setup in Chapter 5.

All thermal simulations were carried out using the finite element method (FEM) in COMSOL Multiphysics 6.1 in (A_Tritschler 2023). As hundreds of geometric factor combinations were required, the LiveLink interface to MATLAB was used. This allows simulations with different parameterized geometries to be started and evaluated automatically. In the individual simulation models set up, heat transfer takes place via conduction, convection and radiation, each based respectively on the Fourier formula, Newton's cooling law and the Steffan-Blotzmann law (Cengel 2007, p. 374–391). Comsol Multiphysics couples the heat flows into an equation to determine the resulting temperatures.

4.3.2.1 Stationary Effect Analysis of Consolidation I and II

The aim of the stationary analyses is to identify the geometric factors that have the greatest influence on the temperature in the relevant Co and DiCoFRP interface areas. Factors are changed and combined at certain factor levels in the simulations. To determine the effect of the factors on the temperature, the resulting temperatures in the interface area are analyzed using interaction diagrams.

Assuming that the extruded material has time to cool down between the MEX process step, i.e. printing and consolidation, a stationary state is reached in which the temperature distribution in the component remains constant. This stationary state is regarded as the starting point for the respective consolidation and its sensitivity to changing geometric dimensions is analyzed in the next step.

Model Development of the Stationary Simulation

The model setup in COMSOL which is parameterizable with MATLAB for the stationary simulations is shown in Figure 4-14. The variable factors are labelled in green and their factor levels for Consolidation I are listed in Table 4-8 and for Consolidation II in Table 4-9. Constant boundary conditions such as the ambient temperature are shown in grey.

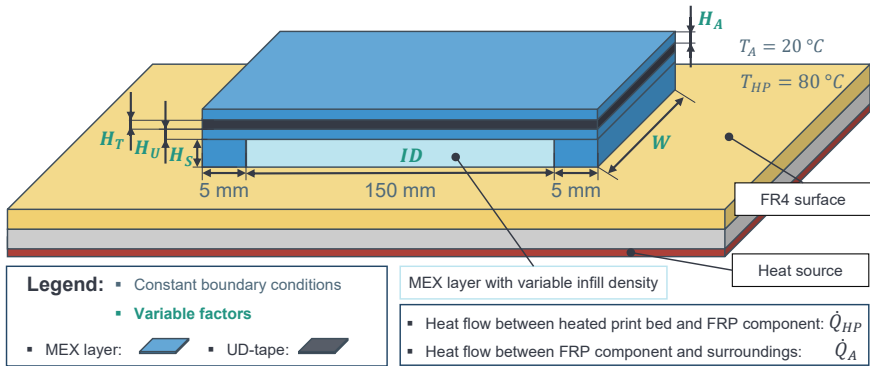


Figure 4-14: Principle setup of the parameterizable model in COMSOL for the stationary simulations with variable factors and constant boundary conditions

The environment in the simulation model itself is regarded as an ideal blackbody radiator with an ambient temperature of $T_A = 20\text{ °C}$. All heat flows (conduction, convection and radiation) occurring between the CoDiCoFRP component and the surroundings (ambient) are summarized here as \dot{Q}_A for the sake of simplicity. The heated bed is the only heat source in the stationary simulations and the heat flows between the heated bed and the component can be summarized as \dot{Q}_{HP} . The stationary state is reached when the combined heat flows over the limits of the CoDiCoFRP component cancel each other out which results in $\dot{Q}_{HP} - \dot{Q}_A = 0$.

The mesh resolution for the FEM was selected adaptively, which means that the areas of interest – the lower interface of the UD-tape for Consolidation I and the upper interface for Consolidation II – have a significantly higher resolution than the rest of the geometry. The overall mesh resolution was additionally reduced step by step in a convergence analysis to identify the roughest possible resolution at which plausible results are obtained. This made it possible to simulate hundreds of factor combinations with acceptable simulation times.

Material properties required for the thermal simulations are listed in Table 4-7. These are either obtained directly from the manufacturer's data and from literature data for similar material systems (Matsuo & Hojo et al. 2019; Behzad & Sein 2007), or calculated using Equation 4-4. The equation is a simplified mixing rule for FRP composites to de-

termine the resulting thermal property γ from the individual properties γ_i of the components and is based on (Behrens 1968). The resulting mass of the entire FRP composite is m_{FRP} , where m_i is the mass of the component i in the FRP composite.

$$\gamma = \sum_{i=1}^n \frac{m_i}{m_{FRP}} \cdot \gamma_i \quad 4-4$$

Equation 4-4 was used to determine the thermal capacity and conductivity of the DiCoFRP PA6 CF and the CoFRP (UD-tape), the results are shown in Table 4-7. FR4 is a flame-retardant grade 4, glass-reinforced epoxy laminate material, which is used as the surface material of the heated bed as shown in Figure 4-14. This surface material is used for the main experimental setup as described in Chapter 5 and ensures good adhesion of the CoDiCoFRP.

Table 4-7: Material properties used for the thermal simulations (based on (Matsuo & Hojo et al. 2019; Behzad & Sein 2007; A_Tritschler 2023))

Material	Thermal capacity	Thermal conductivity	Material density	Emissivity
PA6 CF	1403 J/(Kg·K)	5.261 W/(K·m)	1.263 g/cm ³	0.98
FR4	600 J/(Kg·K)	5.261 W/(K·m)	1.850 g/cm ³	0.85
UD-tape	1106 J/(Kg·K)	17 in fiber and 10.3 W/(K·m) perpendicular to fiber direction	1.45 g/cm ³	0.98

Experimental Design and Factor Level Combinations

Table 4-8 shows all factor levels that are combined and simulated for the effect analysis of Consolidation I. As there is no printed MEX layer on the UD-tape in Consolidation I, H_A is constantly 0 mm. This results in $3^5 = 243$ factor combinations.

Table 4-8: Factor levels for the stationary thermal effect simulation of Consolidation I

Factor	Factor levels		
Width W	20 mm	60 mm	100 mm
Height of the support structure H_S	2 mm	20 mm	40 mm
Height directly under the UD-tape H_U	2 mm	5 mm	10 mm
Height above the UD-tape H_A		Constant 0 mm	
Infill density ID of the support structure	100 %	60 %	20 %
Hight of UD-tape H_T , quantified using number of tapes	1	2	3

The factor levels were determined based on previous simulations as well as from empirical values and estimations. For example, an infill degree $ID = 20\%$ is a typical value

in the field of FDM printing. As the developed process is to be used in particular for structural components, solid material with $ID = 100\%$ is also considered.

Figure 4-15 a) shows an example of the simulation and geometry generated for the factor level combination with one of the smallest dimensions and b) the simulation and geometry generated for the combination with the largest dimensions.

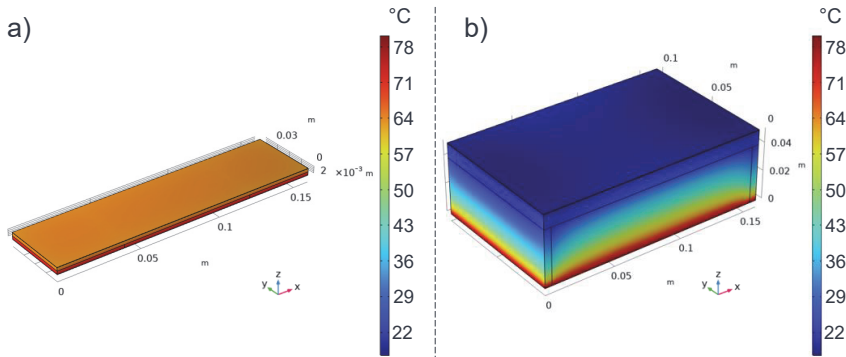


Figure 4-15: Thermal simulation results for the stationary case of Consolidation I for: a) $W = 30\text{ mm}, H_S = 2\text{ mm}, H_U = 2\text{ mm}, H_A = 0\text{ mm}, ID = 100\%$ and $H_T = 1$; b) $W = 100\text{ mm}, H_S = 40\text{ mm}, H_U = 10\text{ mm}, H_A = 0\text{ mm}, ID = 20\%$ and $H_T = 3$ (based on (A_Tritschler 2023))

It can be clearly seen that b) with a surface temperature of approx. $20\text{ }^\circ\text{C}$ is significantly cooler than a) with approx. $60\text{ }^\circ\text{C}$. A more detailed evaluation and analysis are provided below. Table 4-9 shows the factor levels for the stationary simulations for the effect analysis of Consolidation II.

Table 4-9: Factor levels for the stationary thermal effect simulation of Consolidation II

Factor	Factor levels		
Width W	Constant 40 mm		
Height of the support structure H_S	2 mm	20 mm	40 mm
Height directly under the UD-tape H_U	2 mm	5 mm	10 mm
Height above the UD-tape H_A	1 mm	2 mm	10 mm
Infill density ID support structure	100 %	60 %	20 %
Height of the UD-tape H_T , quantified using number of tapes	1	2	3

In contrast to the simulations of Consolidation I, for Consolidation II the UD-tape is overprinted before consolidation, which means that the height H_A of the MEX matrix

layer above the tape is not equal to 0 mm. As the results of the effect analysis of Consolidation I below show, the width W has no significant influence on the temperature, this factor was kept constant for Consolidation II. This again results in $3^5 = 243$ factor combinations.

Results of the Stationary Simulations for Consolidation I and II

Interaction plots were created for the evaluation and visualization of each of the 243 thermal simulations of Consolidation I and II. Figure 4-16 shows the interaction plot for Consolidation I, based on the simulated mean temperatures in the center of the lower interface (interface under the UD-tape).

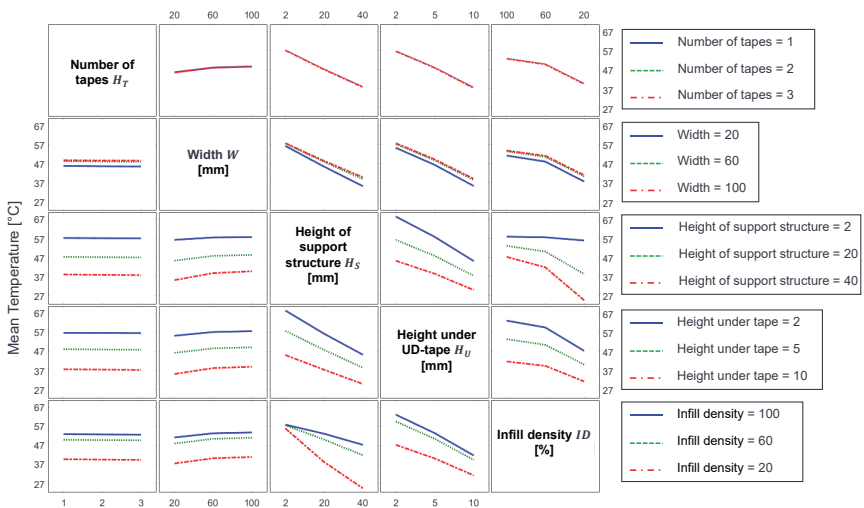


Figure 4-16: Two-factor interaction plot for the temperature reached at the center of the lower interface for the stationary simulation of Consolidation I (based on (A_Tritschler 2023))

The interactions between two factors can be observed within a box using the courses of the interpolated lines in relation to each other. In the first row, the boxes show the interaction of the factor *number of tapes* H_T , with the four other factors. In all four boxes, it can be seen that the lines for 1, 2 and 3 UD-tapes are mostly on top of each other. This means that the number of tapes has hardly any effect on the temperature. The second row shows the interaction of the Width W with the other factors. Only a small effect can be seen here for the different factor levels on the temperature.

In the third row in Figure 4-16, it can be seen that a temperature difference of 20 °C - 30 °C can be observed for the factor *height of support structure* H_S between the factor levels 2 mm and 40 mm, which means that there is a significant effect. In the fifth column from the left in the row for the *height of the support structure* H_S , a strong interaction with the factor *infill density* ID can be recognized by the non-parallel lines. As most of the lines in most of the boxes are largely parallel to each other, relatively few interactions can be observed. Generally, the interaction diagram qualitatively shows that the *height under the tape* H_U and the *height of the support structure* H_S have the highest effect on the mean temperature. The strongest interaction occurs between the *infill density* ID and *height of support structure* H_S . For the *width* W hardly any effect can be observed and was therefore kept constant at 40 mm in Consolidation II and not analyzed in more detail.

Figure 4-17 shows the interaction plot for Consolidation II. In comparison to Consolidation I, the *height of the material above the UD-tape* H_A instead of the *width* W is considered as a variable factor.

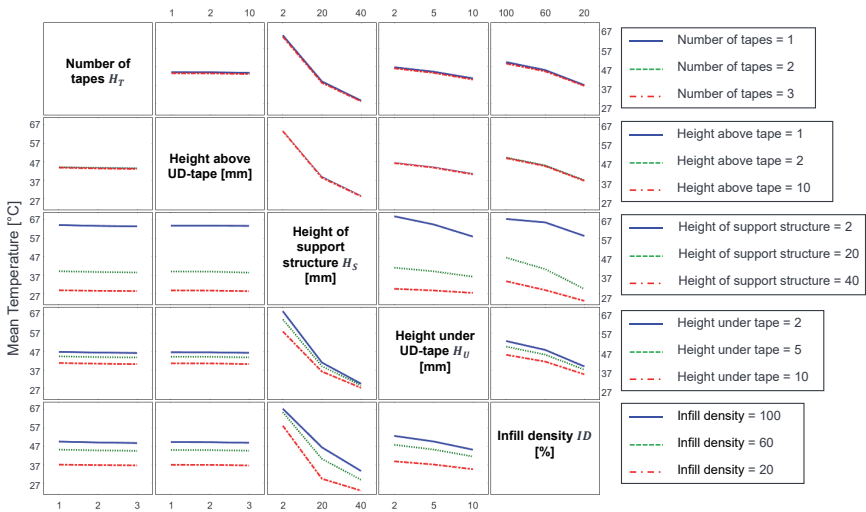


Figure 4-17: Two-factor interaction plot for the temperature reached at the center of the upper interface for the stationary simulation of Consolidation II (based on (A_Tritschler 2023))

The simulated mean temperature in the center of the upper interface is considered the target value. In general, similar interactions and effects can be observed as with Consolidation I. For the stationary case, the *number of tapes* H_T and the *height above the tape* H_A have hardly any influence on the temperature in the upper interface. The greatest effects and interactions can be seen for the *height of the support structure* H_S , the *height under the tape* H_U and the *infill density* ID .

Evaluation of the Stationary Simulations for Consolidation I and II

The analyses of the simulation results for the mean temperatures with changing geometric factors show that in the interfaces for Consolidation I and II fluctuating temperatures occur for the stationary case. This means that the consolidation process parameters, in particular the temperatures, must be dynamically adapted to changing conditions. The following section therefore examines with simulations how the changing conditions can be compensated for with a dynamic temperature control. Because the factors *height of the support structure* H_S , the *height under the tape* H_U and the *infill density* ID have shown the highest effect and interaction for Consolidation I and II, they are also considered as relevant factors in the dynamic simulations. To simplify the simulations, they are summarized as one factor. Although the factors the *number of tapes* H_T and the *height above the tape* H_A have no significant effect on the stationary simulations, they are nevertheless considered in the dynamic simulations, as they are in direct contact with the heat sources of the Consolidation Unit and a higher effect is expected.

Validation of the Simulation Models

The simulation models described were validated with experiments carried out subsequently with the real experimental setup. The experimental setup is described in Chapter 6. Individual extreme cases were compared for this purpose. Three components were printed with the factor levels 2 mm, 20 mm and 40 mm for the height of the support structure H_S and height above the tape $H_A = 0$ mm. The smallest value was used for all other factor levels (cf. Table 4-8). After sufficient time to reach the stationary state, the surface temperatures were measured with a pyrometer. The temperature deviations from the simulation model were approx. ± 10 °C. As the results of the thermal simulations are only used for qualitative conclusions, the quality of the model is more than sufficient. For this reason, the following simulations were set up according to the same principle with the same material parameters.

4.3.2.2 Dynamic Thermal Simulation of Consolidation I and II

Based on the conclusions drawn from the thermal simulations for the stationary case in the previous section, a dynamic analysis is carried out in the following sections. An appropriate dynamic heating concept to compensate for the changing conditions is determined based on the thermal simulations. This ensures that the temperatures in the interfaces are as constant as possible during consolidation. The simulations were carried out in parallel with the development of the Consolidation Unit in Chapter 5.2.1 and were incorporated directly into the design.

Model Development of the Dynamic Thermal Simulation

The basic setup for the dynamic simulations in COMSOL is shown in Figure 4-18. Compared to the stationary simulation in the previous section, two additional heat sources are available which move with constant velocity over the FRP composite. Since Chapter 4.3.1 showed that a heated iron can cause damage to the matrix material, it was decided to switch to a roller. As the PA6 is in a molten state during consolidation, a relatively large contact surface is formed between the roller and the component. To recreate this, the contact area of the roller is flattened accordingly. The second heat source is a general radiant heater, which is assumed to be able to constantly preheat the area just in front of the roller to 230 °C. Such radiant heaters are often used for the reference ATL system described in Chapter 2.1.3.1. Chapter 5.2.1.2 describes how such a radiant heater can be implemented in combination with a dynamic control loop.

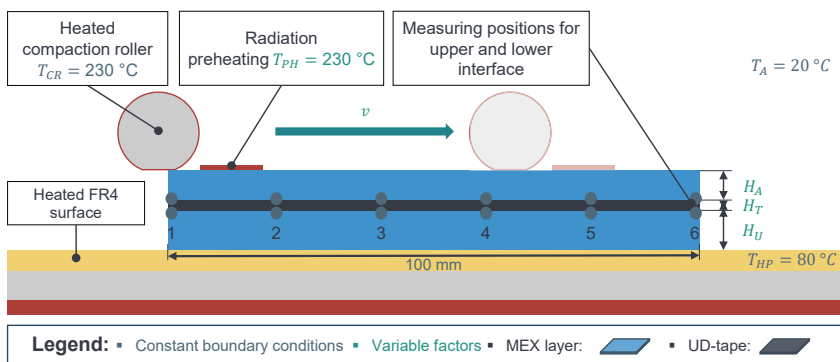


Figure 4-18: Principle setup of the time-dependent model in COMSOL for the dynamic simulations with variable factors and constant boundary conditions

The radiant heater ensures that the temperatures in the interfaces are as constant as possible, even with changing conditions, so that uniform consolidation can take place. Compensation for temperature fluctuations by adaptive temperature control of the compaction roller itself is not technically possible, as the roller can only change temperature slowly due to its thermal inertia caused by its mass. The material properties, which are the same as for the stationary simulations from the previous section, can be found in Table 4-7. The heated roller is made of steel and has a diameter of 10.5 mm and a width of 2 mm.

Experimental Design and Factor Levels

The levels of the variable factors for Consolidation I and II are listed in Table 4-10. As described in the evaluation in the previous section, the variable factors below the tape were summarized in factor H_U for simplification, as the general height below the tape has the greatest effect on the temperatures in the interface area. The width of the component in the simulations is a constant 80 mm due to its small effect. For Consolidation I, there is no printed layer on the UD-tape, which means that $H_A = 0$. For Consolidation II, this factor is variable.

Table 4-10: Factor level combinations for the time-dependent dynamic simulations for Consolidation I and II

Factor	Factor levels			
	Consolidation I		Consolidation II	
Height directly under the UD-tape H_U	1 mm	100 mm	1 mm	100 mm
Consolidation velocity v	1 mm/s	10 mm/s	1 mm/s	10 mm/s
Height above the tape H_A	Constant 0 mm		1 mm	3 mm
Radiant preheating T_{PH}	230 °C	Non	230 °C	Non
Height of the UD-tape H_T , quantified using number of tapes	1	3	Constant 1	

In the measuring positions 1 - 6 in Figure 4-18 – in the case of Consolidation I in the lower interface, for Consolidation II in the upper interface, each in the center across the width – the temperatures are recorded during the respective consolidation process. The heated roller and the preheated area move at a constant velocity over the component surface. Figure 4-19 shows how the temperatures in the measuring points differ with preheating and without preheating for Consolidation I and an exemplary factor combination. In general, it can be seen that with preheating the desired temperature of 230 °C is reached more closely and that it is maintained for a longer time.

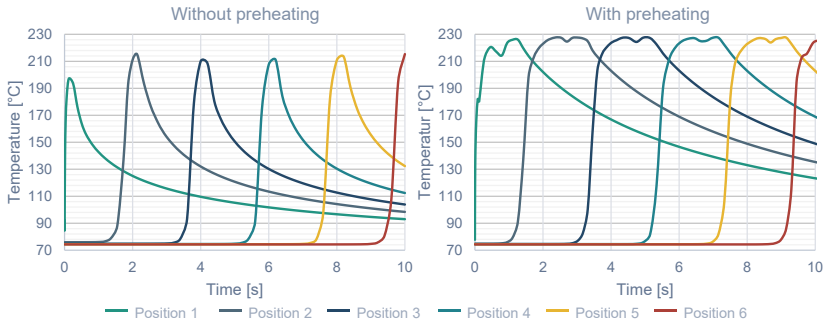


Figure 4-19: Temperature curves at measuring positions 1 to 6 for Consolidation I with and without preheating for $H_U = 1 \text{ mm}$, $v = 10 \text{ mm/s}$ & $H_T = 3$ (based on (A_Tritschler 2023))

Figure 4-20 shows the different temperature curves for Consolidation II with and without preheating for a selected factor combination. For this factor combination, the desired temperature of 230 °C is not reached even with preheating, showing the insulating effect of the MEX layer on the UD-tape. An evaluation of all factor combinations for Consolidation I and II is provided in the following section.

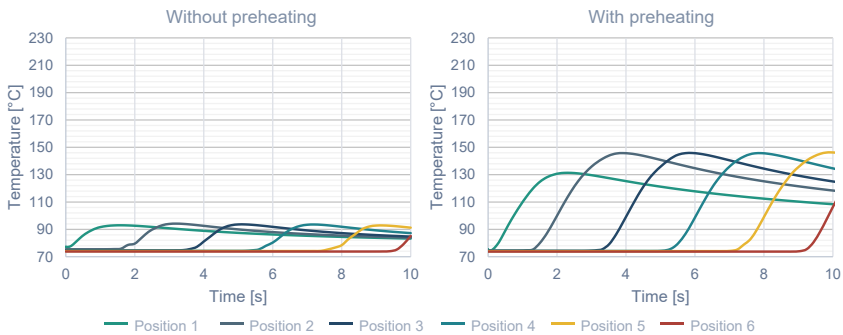


Figure 4-20: Temperature curves at measuring points 1 to 6 for Consolidation II with and without preheating for $H_U = 1 \text{ mm}$, $v = 10 \text{ mm/s}$ & $H_A = 3 \text{ mm}$ (based on (A_Tritschler 2023))

Results and Evaluation of the Dynamic Simulations for Consolidation I and II

For each of the four variable factors, there are two factor levels, (cf. Table 4-10) resulting in $2^4 = 16$ combinations for Consolidation I and II. Radiation preheating is one of

the factors with the factor levels being *with preheating* ($T_{PH} = 230 \text{ }^\circ\text{C}$) and *without preheating*. Figure 4-21 on the right shows the influence of preheating for Consolidation I. The remaining $2^3 = 8$ factor level combinations are listed in the table on the left.

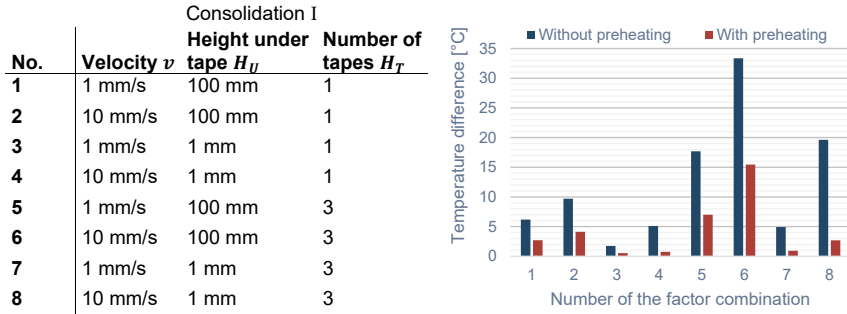


Figure 4-21: Influence of radiation preheating during Consolidation I: (Left) Numbering of the 8 simulated factor level combinations; (Right) Average temperature difference of measuring points 1 - 6 from the target temperature of 230 °C with and without radiation preheating (based on (A_Tritschler 2023))

The bar chart on the right shows the average temperature differences of measurement points 1 - 6 (cf. Figure 4-18) from the target temperature of 230 °C during Consolidation I for the remaining 8 factor combination. A comparison of the mean temperature differences clearly shows that they are significantly lower with radiation preheating. On average, radiant preheating reduces the temperature difference across the 8 factor combinations by 65%. Factor level combinations No. 5 and 6 show that the combination of a high component and the use of three multiple UD-tapes makes it more difficult to achieve the targeted temperature in the interface area. With No. 6, even with preheating, there is an average deviation of 15 °C from the desired 230 °C. The formation of intimate contact and autohesion is therefore very slow or does not take place sufficiently during consolidation to ensure that a high degree of bonding is achieved. The simultaneous consolidation of several tapes is therefore only possible with very small component heights and low consolidation velocities, as can be seen from factor combination No. 7. Since large component sizes are assumed and the velocity should not be unnecessarily slow due to production times, it is not advisable to consolidate several tapes at the same time. If several tapes need to be stacked in one area of a component, the UD-tapes must be consolidated individually one after the other.

As for Consolidation I, the mean temperature differences with and without radiation preheating were determined also for Consolidation II. The average differences for the respective factor level combinations are shown in Figure 4-22.

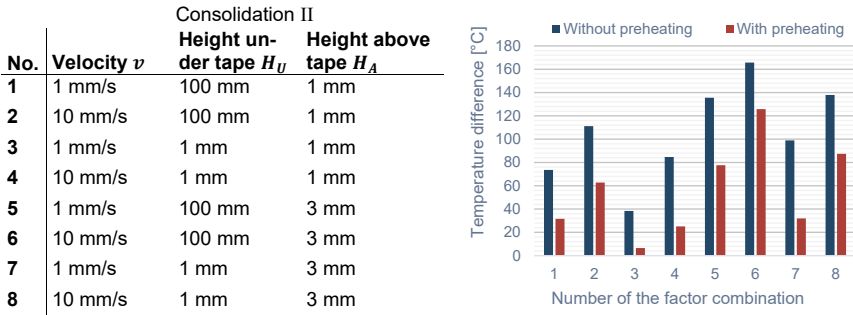


Figure 4-22: Influence of radiation preheating during Consolidation II: (Left) Numbering of the 8 simulated factor level combinations; (Right) Average temperature difference of measuring points 1 - 6 from the target temperature of 230 °C with and without radiation preheating (based on (A_Tritschler 2023))

It can be seen that preheating reduces the temperature difference to the target temperature by an average of 47%. Overall, the differences are significantly higher than with Consolidation I. This is due to the fact that the printed MEX layer over the tape has an insulating effect and the heat from the heating roller and the radiant heating can only flow poorly into the area of the upper interface. The printed MEX layer above the UD-tape should therefore be as thin as possible, i.e. only one regular layer height of MEX. Considering the factor combinations No. 1 - 4, it can be seen that the mean temperature difference to 230 °C is only sufficiently small for No. 3 in order to ensure the formation of a high degree of bonding. This result also correlates with the empirical experiments. As shown in the pre-tests of the different hybridization strategies (cf. Chapter 4.3.1) and in the final tests in Chapter 6.2, the effect of Consolidation II on the degree of bonding for the material systems tested is only limited.

Figure 4-23 illustrates the temperature distribution for a snapshot of the time-dependent simulation of Consolidation I for factor combination No. 8 according to Figure 4-21. As can be seen in the comparison between a) and b), the heat input is significantly higher with radiant preheating.

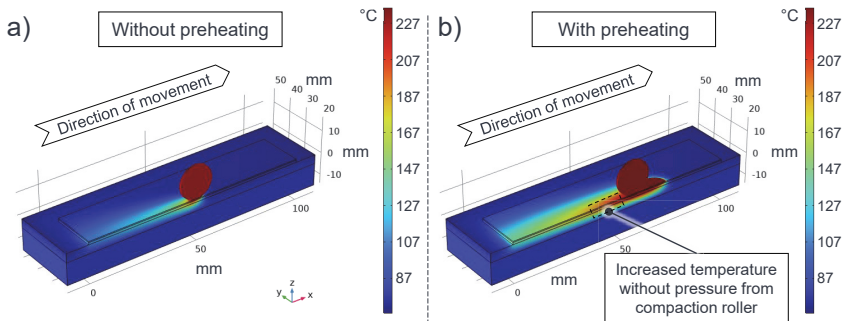


Figure 4-23: Momentary snapshot of the temperature distribution for factor combination No. 8 of Consolidation I, sectional view along half the component width: a) Temperature distribution without radiation preheating; b) Temperature distribution with radiation preheating (based on (A_Tritschler 2023))

Due to the higher thermal energy input in the area around the compaction roller as a result of preheating, the area behind the roller cools down more slowly. As the thermo-plastic remains in the molten state for a longer period of time without the compaction roller applying pressure, unwanted deconsolidation can occur, causing air pockets (voids) to expand. In order to achieve controlled solidification as described in Chapter 2.1.2.2, the pressure should be maintained for a short time during the cooling phase. For this reason, an additional compaction roller is added behind the heated compaction roller in the design of the Consolidation Unit in the experimental setup in Chapter 5.2.1.

The dynamic simulations of the time-dependent temperature curves in the interface areas for different factor combinations show that radiation preheating is very effective. This makes it easier to achieve the target temperature for consolidation in the interface area, even under changing conditions. The simulations show that only one UD-tape can be processed at a time during Consolidation I. If more UD-tapes are to be layered, Consolidation I must be carried out several times. According to the simulation, Consolidation II is difficult due to the insulating effect of the printed MEX layer over the UD-tape. The desired temperatures in the interface area can only be achieved for low layer heights above the UD-tape and only under certain conditions. A more precise quantification is made based on the simulations in the following section. The practical applicability of Consolidation II is explained in more detail in Chapter 6.2 using a design of experiments (DoE). The actual implementation and control concept of the theoretical radiant preheating system used here in the simulation is presented in Chapter 5.2.1.2.

4.3.2.3 Adaptive Preheating for Height Differences

The aim of this section is to investigate if and how radiant preheating can be used to compensate for changing height differences of components during Consolidation I and II, which would result in changing temperatures in the interface areas. The simulations in the previous section have fundamentally and qualitatively shown that radiant preheating is suitable for equalizing temperature fluctuations due to changing conditions. To simplify matters, 230 °C was defined as the target temperature in the interface area and the radiant preheating was also set to 230 °C. In order to minimize the effort required to identify optimum process parameters (temperature and pressure of the compaction roller and velocity) for the consolidation experiments in Chapter 6, the optimal process parameters are identified under constant conditions, i.e. a fixed factor combination. In concrete terms, this means that the experimental tests are all carried out for a constant height of the component for example. The simulations carried out in this section are intended to show that optimum process parameters identified for one condition (height), can also be used under other conditions/factor combinations using radiant preheating. This proof significantly reduces the amount of experiments required to identify optimum process parameters, as these only have to be carried out for one height of specimens.

Results of Adaptive Preheating for Consolidation I

Based on the simulation model in the previous section (cf. Figure 4-18), reference simulations were carried out for Consolidation I. The process parameters with $T_{HP} = 80$ °C, $T_{CR} = 230$ °C, $T_{PH} = 175$ °C, $H_T = 1$, $v = 5$ mm/s and $H_U = 3$ mm were selected for the reference simulation, which is based on values used in the experiments in Chapter 6. The temperature for the radiant preheating T_{PH} is a constant 175 °C. Figure 4-24 shows the comparison of the temperatures reached in the interface area positions 1- 6 during Consolidation I for the reference height $H_U = 3$ mm and for an exemplary simulation with $H_U = 100$ mm. The maximum temperatures reached in Figure 4-24 in the measuring position 1 - 6 at height $H_U = 3$ mm and for an exemplary simulation at $H_U = 100$ mm were only found to deviate by 2 - 5 °C. Similar results were achieved for other heights as well. Temperature differences are so small that the experimentally identified process parameters for Consolidation I do not need to be adjusted for other conditions. This is due to the fact that the radiant heater heats the area in front of the roller (cf. Figure 4-24 temperature curves for position 4) so quickly that the approx. 175 °C is always reached

and constant thermal boundary conditions are always present for the heated roller before it consolidates the area.

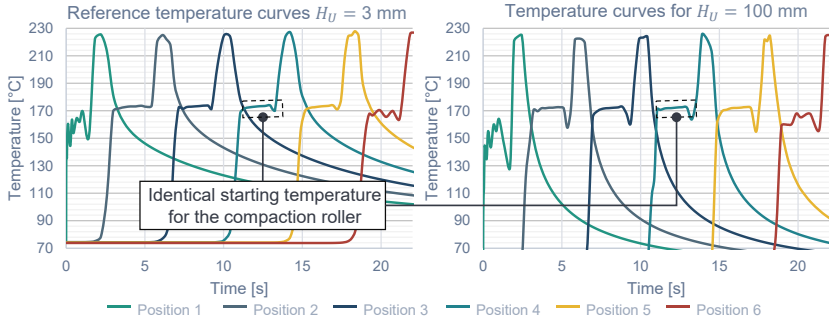


Figure 4-24: Comparison of the temperature curves at measuring positions 1 to 6 for Consolidation I for $T_{HP} = 80\text{ }^{\circ}\text{C}$, $T_{CR} = 230\text{ }^{\circ}\text{C}$, $T_{PH} = 175\text{ }^{\circ}\text{C}$, $H_T = 1$ and $v = 5\text{ mm/s}$: Reference simulation with $H_U = 3\text{ mm}$ and a simulation with $H_U = 100\text{ mm}$

Results of Adaptive Preheating for Consolidation II

Simulative comparisons were carried out for Consolidation II using the same approach as for Consolidation I. Results showed, that the number of UD-tapes has no significant influence on the temperature curves of the upper interface and the height H_U of the component under the UD-tape has only a minor effect. However, the height H_O of the printed MEX layer above the UD-tape has a considerable influence. This is related to the insulating effect of the layer as described with Figure 4-22 in the previous section. To ensure that the same starting temperatures are always present in the interface area before Consolidation II with the compaction roller, the radiation heater must increase the preheating temperature with increasing H_U and H_O . A functional correlation was determined using iterative simulation based on the model in Figure 4-18. For different increasing combinations of H_U and H_O in the range of $H_U \in [3\text{ mm}; 100\text{ mm}]$ and $H_O \in [0^+ \text{ mm}; 1.5\text{ mm}]$, the preheating temperature T_{PH} of the radiant heating was increased until the maximum temperatures in the measuring points 1 - 6 in the interface corresponded to around 2-5 $^{\circ}\text{C}$ deviation of the reference simulation. With a linear function for H_U , which has only a small influence on the temperature, and a third-degree polynomial function for the influence of H_O , the regression function in Equation 4-5 is obtained. $T_{PH}(H_U, H_O)$ describes, as a function of H_U and H_O , which temperature must be set for

the radiant preheating so that the same maximum temperatures are reached in the interface as for the reference.

$$T_{PH}(H_U, H_O) = - \left(0.033 \frac{^{\circ}\text{C}}{\text{mm}^4} \cdot H_U + 8.234 \frac{^{\circ}\text{C}}{\text{mm}^3} \right) \cdot H_O^3 + \left(0.099 \frac{^{\circ}\text{C}}{\text{mm}^3} \cdot H_U + 34.703 \frac{^{\circ}\text{C}}{\text{mm}^2} \right) \cdot H_O^2 + \left(0.115 \frac{^{\circ}\text{C}}{\text{mm}^2} \cdot H_U + 11.737 \frac{^{\circ}\text{C}}{\text{mm}} \right) \cdot H_O + 0.025 \frac{^{\circ}\text{C}}{\text{mm}} \cdot H_U + 231.176 \text{ } ^{\circ}\text{C} \quad 4-5$$

$H_U \in [3 \text{ mm}; 100 \text{ mm}]; H_O \in [0^+ \text{ mm}; 1.5 \text{ mm}]$

Figure 4-25 shows the curves of T_{PH} over H_O for selected H_U . It can be seen that from a layer height of $H_O = 1.1 \text{ mm}$, preheating temperatures of $300 \text{ } ^{\circ}\text{C}$ are already required in some cases.

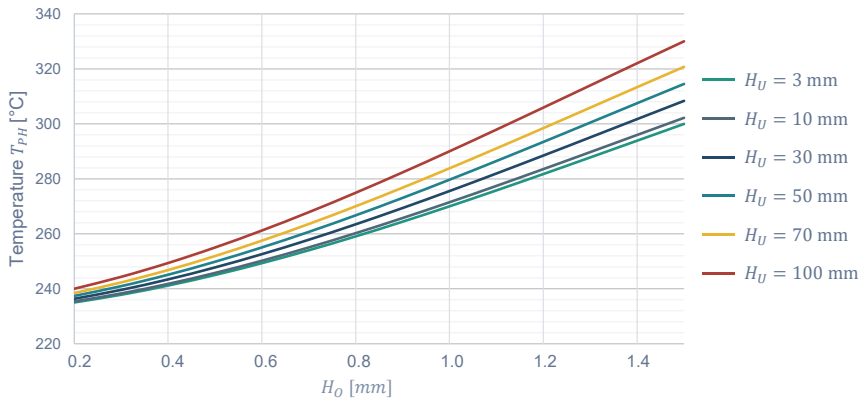


Figure 4-25: Visualization of Equation 4-5: Temperature T_{PH} set as a function of H_U and for selected H_O in order to achieve the specified reference temperature in the interface area for Consolidation II

Such high temperatures are not feasible in practice as the thermoplastic PA6 used begins to decompose at $300 \text{ } ^{\circ}\text{C}$ and above. The experiences with experiments in Chapter 6 show that the developed radiant heater cannot guarantee homogeneous heat distribution on uneven components, which can lead to locally significantly higher temperatures than set. The radiant heater must therefore be operated with a safety factor well below $300 \text{ } ^{\circ}\text{C}$. This means that the height H_O of the layer above the UD-tape must be set very low. However, this is technically very difficult to realize with the MEX direct extrusion system used, as it is designed for high material outputs and layer heights. **Based on the results obtained here, it is assumed that Consolidation II will have no effect under the given boundary conditions and for the selected material system. The hypothesis is tested experimentally in Chapter 6.2.**

4.3.2.4 Evaluation of the Thermal Simulations

The thermal simulations carried out in the previous sections show that complex temperature control is required due to the variable geometry that is possible with 3D printing. As shown with the dynamic simulations, radiant preheating is suitable to adapt to changing conditions as it can be controlled dynamically. However, the simulations have also shown that Consolidation II is unlikely to have any effect under these conditions. In addition to the radiant preheating and the heated compaction roller, the simulations show that a solidification roller is also required to carry out the necessary thermal management during processing. As a result, the Consolidation Unit cannot be designed rotationally symmetrical, which means that it must be orientated in the process direction during consolidation.

4.4 Conclusion and Definition of the Target System

Based on a FAST analysis, the main functions and subsystems required for the set objective were identified in Chapter 4.1. According to the theories of PEG, the *Consolidation Unit* and the *Adjustable and Heated Assembly Table* were identified as the subsystems with the highest new development effort. The general overall process requirements identified are listed and described in Chapter 4.2. As no flexible process for the hybridization of DiCoFRP produced using the MEX process and CoFRP from UD-tapes is currently available, numerous experimental pre-tests and simulations were carried out in Chapter 4.3. Two suitable hybridization processes (S2 and S4) were identified consisting of the main process steps: *Point Welding* to secure UD-tapes, *Overprinting* and *Consolidation I and II*. In addition to identifying suitable hybridization processes, the requirements for an experimental prototype production setup are thus defined in more detail. Based on the identified subsystems, the identified process requirements, and the newly developed hybridization process, a clearer target system compared to the first conceptual target system (cf. Figure 4 2) for the prototype experimental setup can be defined. This includes the hardware arrangement and functionality of the subsystems, as illustrated in Figure 4-26.

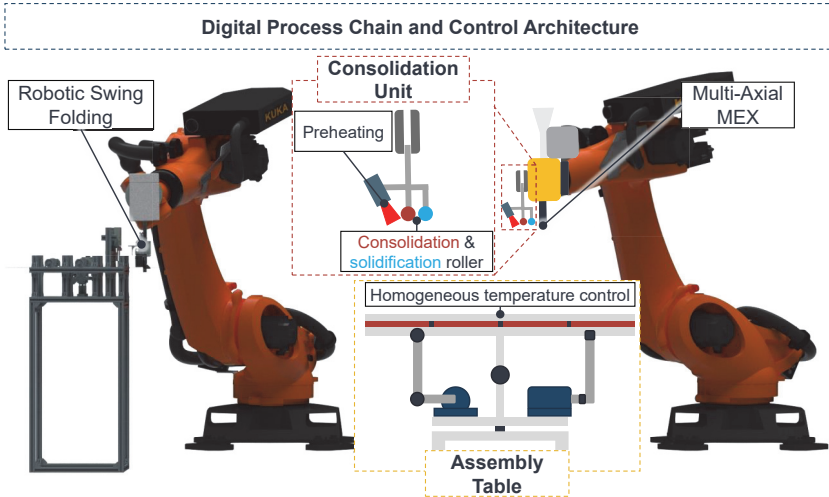


Figure 4-26: Overview and configuration of the target system consisting of the main subsystems with the Consolidation Unit, the Assembly Table and the Digital Process Chain and Control Architecture as subsystems still to be developed

The Robotic Swing Folding described in Chapter 2.1.3.1 is used for the subsystem responsible for handling and feeding the CoFRP in the form of UD-tapes. A multi-axial MEX DES setup (cf. Chapter 2.3) for 3D printing is suitable for the processing of DiCoFRP. As the Co and DiCoFRP should be produced simultaneously to reduce production time and synchronization is required for hybridization, two standard six-axis robots with an overlapping workspace are needed, as shown in Figure 4-26. As the Robotic Swing Folding already exists as a functioning reference system and uses a KUKA KR180 R2500 extra industrial six-axis robot, the same robot model is used for the MEX DES and the Consolidation Unit. Within this workspace is the Assembly Table which provides homogeneous temperature control and appropriate orientation adjustments of the build area for the hybridization.

As the process steps of MEX DES 3D printing, Consolidation (I and II) and Point Welding take place immediately after each other for the hybridization strategies identified in Chapter 4.3.1, it was concluded that the Consolidation Unit should be combined with a single-screw extruder for MEX DES to create a hybrid end-effector as shown in Figure 4-26. In accordance with the classification in Chapter 2.2.3, in-situ or semi-in-situ con-

consolidation can thus be realized without the need for post-processing and/or an autoclave. In order to be able to better study the consolidation of the CoDiCoFRP, a semi-in-situ consolidation is specified for the target system. This allows MEX DES 3D printing and consolidation to be examined independently. As the thermal simulations in the previous Chapter 4.3.2 have shown, the Consolidation Unit requires a preheating system and a solidification roller in addition to the consolidation roller (see Figure 4-26).

A further detailed description of the developed subsystems and the overall system is provided in the remaining sections of Chapter 5. The developed experimental system is used in Chapter 6 to investigate and optimize the identified individual process steps of hybridization.

5 Experimental Setup Development

The required subsystems, relevant process steps and experimental and simulative analyses were carried out in the previous Chapter 4 to define the target system. Results and derived requirements are used in this chapter, which deals with the development of the experimental setup. First, a kinematic analysis for the overall system and the subsystems is carried out in Chapter 5.1 in order to obtain a suitable kinematic layout for the newly developed process. The individual subsystems developed are presented in Chapter 5.2. The actual development process of the individual subsystems, which was carried out using the SPALTEN methodology and the PGE analysis, is not described further. The focus is on explaining the relevant functions of the subsystems that influence the developed process. Individual functions are analyzed and validated with the help of experiments. The last subchapter 5.3 contains a brief summary.

5.1 Kinematic Analysis

The target system defined in Chapter 4.4 contains three individual kinematic systems consisting of two six-axis industrial robots (KUKA KR180 R2500 extra) and an additional kinematic system for the Assembly Table. One aim of the kinematic analysis is to optimize the layout of the robot cell with regard to the workspace based on a reachability analysis and at the same time to gain a better understanding of the kinematics. In Chapter 5.1.1, a kinematic analysis is first carried out for the use of the Consolidation Unit subsystem as the end-effector of one of the industrial robots. The aim is to determine whether an additional axis is required due to the identified directional dependency in the consolidation process (see Chapter 4.3.2.2). Chapter 5.1.2 focuses on the kinematics of the Assembly Table subsystem and how this is optimally positioned in the layout of the robot cell. It also examines whether additional axes are required to maximize the workspace. In Chapter 5.1.3, a generic analysis of the overall system is carried out in order to identify a theoretically optimal layout.

The *Multi-Axial MEX DES* and *UD-Tapes Feeding and Handling System* (Robotic Swing Folding) subsystems are not analyzed separately in terms of kinematics, as they are taken from the state of the art and the kinematic correlations are known. However, they are included in the kinematic analysis of the overall system with their given kinematic boundary conditions. The kinematic analyses were carried out in (A_Larsch 2024).

5.1.1 Kinematic Analysis of the Consolidation Unit

In the thermal simulations in Chapter 4.3.2.2, it was shown that during consolidation a temperature gradient is required along the process direction in order to achieve controlled consolidation and solidification. The preheated surface must point in the direction of movement as shown in Figure 5-1 a). This means that the Consolidation Unit cannot be built up rotationally symmetrically. The Consolidation Unit (end-effector) must therefore be orientated around the z-axis of the tool coordinate system depending on the process direction, which is determined by the path of the surface to be consolidated. As this is probably only possible in a limited workspace with the six-axis of the used industrial robot, the need for a seventh rotary axis is examined below. For this purpose, a part of the concept of the Consolidation Unit with a theoretical additional axis was designed as shown in Figure 5-1 b) and a kinematic model was set up including the industrial robot.

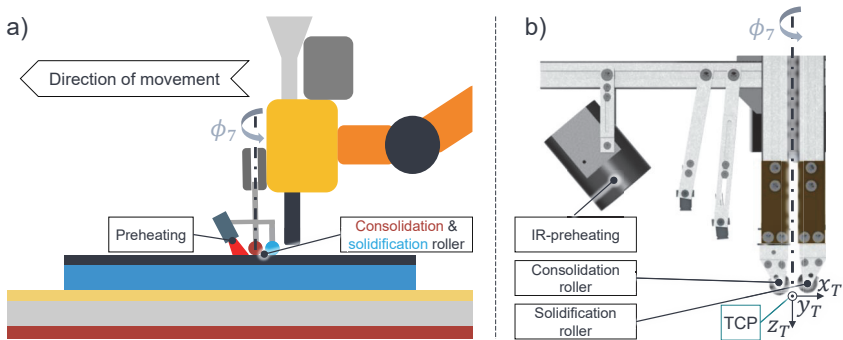


Figure 5-1: a) Conceptually illustrated Consolidation Unit and its orientation in the direction of movement during consolidation; b) Possible implementation of a part of the Consolidation Unit with an additional seventh rotational axis

In order to investigate which workspace can be achieved with the industrial robot with six and seven axes, the dexterous workspace was determined in (A_Larsch 2024) for simplified assumptions and reachability analyses were conducted. Figure 5-2 shows the results of the reachability analyses, the background of which was explained in Chapter 2.3.2.

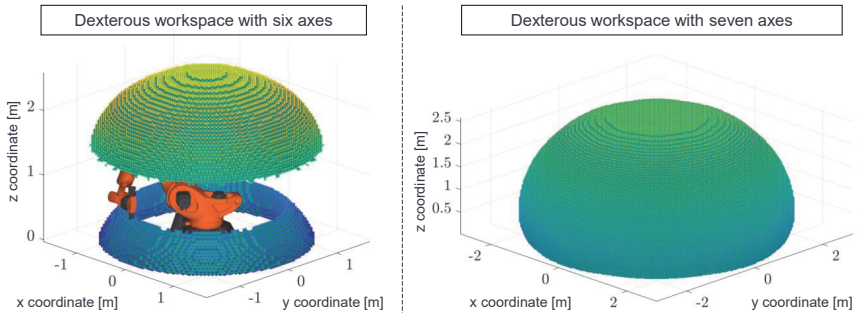


Figure 5-2: Achievable dextrous workspace for a Kuka KR180 R2500 extra for defined orientations of the end-effector: (Left) Use of the usual six axes; (Right) equipped with an additional seventh axis of rotation in the end-effector (based on (A_Larsch 2024))

All points that the end-effector or the TCP can reach with specified orientations using the standard six-axis industrial robot KUKA KR 180 R2500 extra are shown on the left. For reasons of simplification and reduction of computing time, only planar consolidation is assumed, i.e. the TCP is always orientated perpendicular to the x-y plane. As the TCP must be orientated depending on the process direction, points are only considered to be reachable if the TCP can be rotated 360° around the z-direction at these points. The resulting non-contiguous usable dextrous workspace is shown on the left in Figure 5-2. The actually usable dextrous workspace is reduced even further if it is considered that there must be an overlap with the workspace of the second robot system for handling the UD-tapes. Consolidation of large-volume components is therefore not possible with only six axes.

Figure 5-2 on the right shows the dextrous workspace using an additional axis of rotation. In the kinematic modeling, the end-effector has an additional axis of rotation around its z-axis (cf. Figure 5-1 b)), which means that the orientation of the TCP can be continuously rotated by 360° for each pose of the robot. The additional axis makes it possible to achieve the full workspace that the industrial robot itself normally provides in the six-axis state. For this reason, the Consolidation Unit is equipped with an additional axis of rotation. The implementation is described in Chapter 5.2.1.

5.1.2 Kinematic Analysis of the Assembly Table

This section analyses the influence of additional kinematic degrees of freedom on the Assembly Table and its positioning relative to the two industrial robots. Figure 5-3 shows the initial setting for the kinematic analysis.

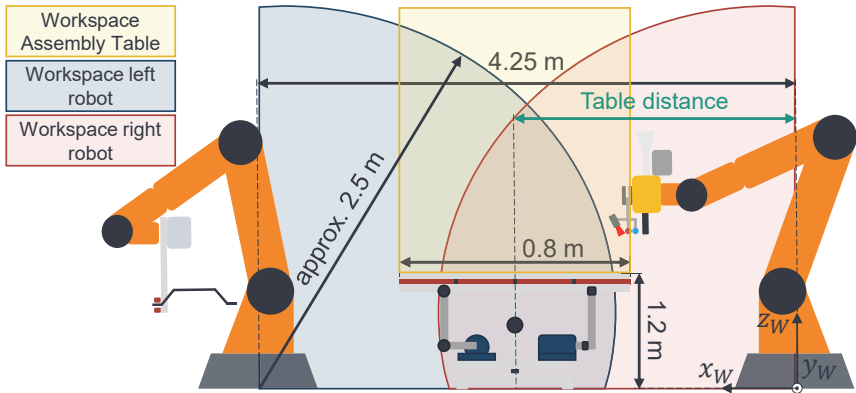


Figure 5-3: Simplified illustration of the setup for the kinematic analysis to determine the resulting workspace as a function of the positioning of the Assembly Table including additional axes

The two industrial robots have a fixed distance of 4.25 m and the Assembly Table can be moved variably along the connecting line between the robots. For simplification, it is assumed that the table has a height of 1.2 m and an edge length of 0.8 m. The position of the table is defined by the distance to the world coordinate system along the x-direction. In this case, the world coordinate system is located at the origin of the right-hand robot. In simplified terms, the workspace of the collaborative system is considered to be the intersection of the three individual workspaces. To determine the workspaces of the two robots, a reachability analysis is carried out in the same way as in the previous section. For the robot with the Consolidation Unit as the end-effector, it is assumed that it has the required seventh additional axis. The workspace of the assembly area is the volume above the table surface. Above a height of approx. 2.5 m, this is cut off, as this is the reachable height of the robots. In addition to the variable movement, the table also has two degrees of freedom. It can be tilted from -30° to 30° around the y-axis and rotated 360° around the z-axis.

Figure 5-4 shows the resulting workspace as a function of the table position and the addition of the two rotational degrees of freedom of rotating and tilting. For no additional DOF, the ideal position is approx. 2 m relative to the right-hand robot. With the addition of further DOFs, the optimum position shifts almost completely to the center between the two robots. With the additional freedom to tilt, the workspace increases only relatively slightly from 0.31 m³ to approx. 0.42 m³. The ability to rotate the table around the z-axis significantly increases the volume to approx. 0.71 m³.

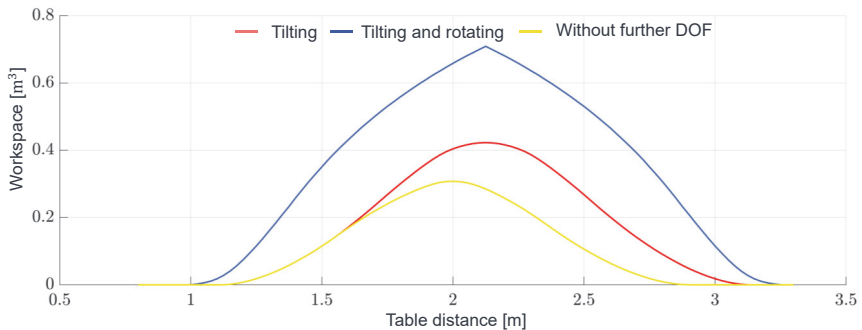


Figure 5-4: Resulting workspace depending on the positioning of the Assembly Table and additional degrees of freedom (based on (A_Larsch 2024))

Ultimately, tilting only increases in the workspace slightly. The degree of freedom of rotation increases the volume considerably, as the rotation around the z-axis ensures that both robots can reach each end of the Assembly Table at any time.

The resulting shape of the usable workspace with a volume of approximately 0.71 m³ is shown in Figure 5-5. It can be clearly seen that the workspace is limited by the edge length of 0.8 m of the table and the maximum reach of the robot (approximately 2.5 m). The workspace also exhibits a clear rotational symmetry, which can be attributed to the additional rotational axis of the table. This results in a greater possible component height along the edges of the table, compared to the center of the table. As discussed briefly in the following section, the volume can be further increased by adjusting the kinematic structure, although it should be noted how the shape of the workspace changes further in the process. Due to the indentation in the workspace above the center of the table, only constant component heights of 0.9 m can be achieved over the entire surface of the table. Component heights of up to approx. 1.2 m are possible at the edges. The edge length of the table of 0.8 m can theoretically be fully utilized.

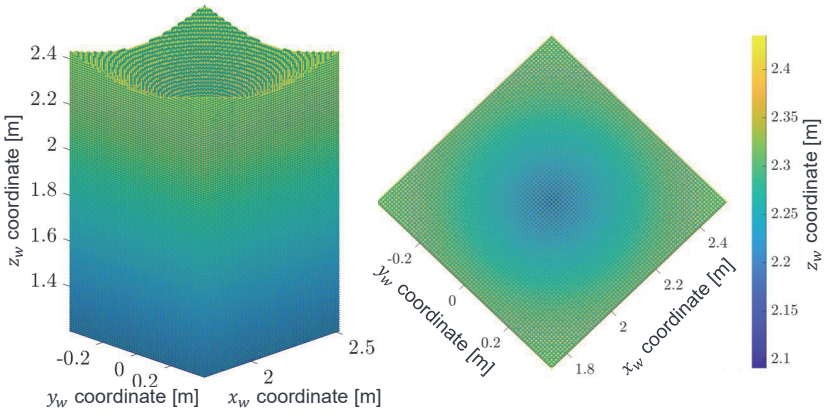


Figure 5-5: Usable workspace based on the world coordinate system as shown in Figure 5-3 with a rotatable and tiltable Assembly Table (based on (A_Larsch 2024))

The previous kinematic analyses were carried out for a fixed distance between the robots and a constant edge length of the printing table in order to investigate the influence of additional DOF in the Assembly Table. In the following section, a general analysis is carried out with variable spacing and dimensions of the Assembly Table in order to determine an ideal layout of the robot cell.

5.1.3 Kinematic Analysis of the Entire System

Based on the setup as shown in Figure 5-3, Figure 5-6 shows the workspace as a function of a variable distance between the two robots and a variable edge length of the print table. As described in the previous section, the Assembly Table has a rotational degree of freedom of 360° around the z-axis. The results were achieved by iteratively increasing the distance between the robots and the edge length of the Assembly Table while it was centered between the robots. Figure 5-6 shows that the workspace grows continuously as the distance between the robots and the edge length of the heated bed increases. However, this statement is practically limited. From a robot distance of approx. 5.5 m, the workspace continues to increase, but can only be used to a limited extent. The robots no longer reach the center of the Assembly Table with their end-effector, which means that the setup can only be used for certain component shapes. Based on the fact that the table can rotate 360° , only donut-shaped components would be possible if the distance is too large between the robots.

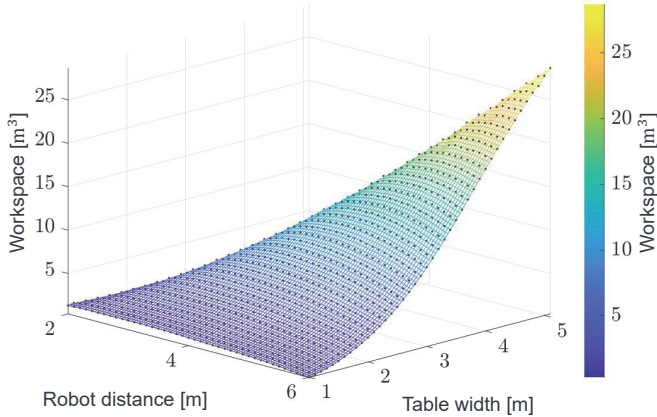


Figure 5-6: Resulting workspace depending on the robot distance and the positioning of the Assembly Table with a rotational degree of freedom around the z-axis (A_Larsch 2024)

For the general case, the best layout is achieved if the distance between the robots is selected so that both robots can just reach the center of the Assembly Table with their end-effector. In this case, this is a distance of approx. 5.5 m. The edge lengths of the printing table can be selected so that the Assembly Table can still rotate without colliding with the robots. Further smaller optimizations could be achieved by varying the table height, but this was not pursued further due to the extremely high computational effort of adding an additional variable.

From the overall kinematic analysis, it can be summarized that an additional rotational axis is required in the end-effector for the consolidation process. To maximize the workspace of this system of collaborative robots, the Assembly Table should be equipped with an additional rotational axis around the z-axis. The implementation of the additional rotational degrees of freedom is described in the following sections. The theoretically optimal layout consisting of the maximum distance between the robots is not realized in practice due to the excessive effort involved in repositioning the robots. The edge length of the printing table is set at 0.8 m for practical reasons, such as good accessibility during experiments where manual work is required. This also ensures that the Assembly Table has enough room for tilting between the robots. The following section provides an overview of the overall system before explaining the subsystems in detail.

5.2 System Overview, Development and Functionality

Based on the generically identified subsystems in Chapter 4.1, the definition of the target system in Chapter 4.4 and the kinematic analyses carried out in the previous Chapter 5.1, an overview of the experimental setup developed can be seen in Figure 5-7.

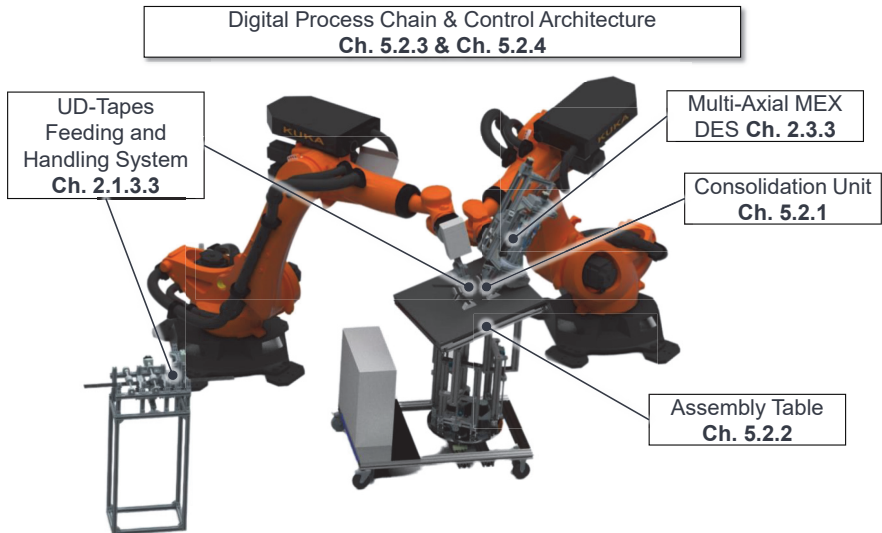


Figure 5-7: Overview of the entire experimental setup and the subsystems

The functionality of the newly developed subsystems *Consolidation Unit*, *Adjustable and Heated Assembly Table* and the *Digital Process Chain & Control Architecture* are analyzed in more detail in the following subchapters.

As described in Chapter 3.2, the SPALTEN methodology was used for the development of the subsystems. The individual steps of the methodology and the resulting alternative solutions for the subsystems are not described in detail in this thesis. The functionality of the developed subsystems is described to the extent necessary for understanding the process. Experimental results regarding machine-process-component interactions are presented for the individual subsystems.

5.2.1 Development and Testing of the Consolidation Unit

The Consolidation Unit was developed based on the requirements identified and the preliminary tests carried out in Chapter 4. In (A_Kleinwort 2022) several alternative solutions (concepts) were designed according to the SPALTEN methodology (Albers & Burkhardt et al. 2005) and individual subsystems were experimentally tested and evaluated based on a utility analysis. The implemented concept can be seen in Figure 5-8 and is presented in the following sections and the main functionalities are explained.

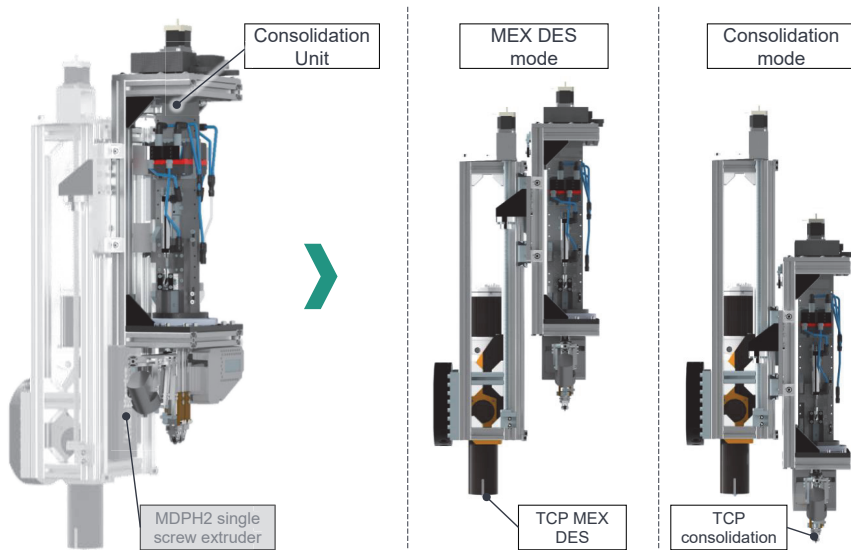


Figure 5-8: Hybrid end-effector for MEX DES and consolidation; switch between MEX DES and consolidation mode by raising and lowering the Consolidation Unit

As determined in the definition of the target system in Chapter 4.4, the Multi-Axial MEX DES subsystem and the Consolidation Unit were combined in one hybrid end-effector. By raising and lowering the unit, it is possible to quickly switch between MEX DES and consolidation mode. The main process steps for the hybridization of Co and DiCoFRP, as defined in Chapter 4.3, include Point Welding, Overprinting, and Consolidation I and II. The consolidation mode is utilized for both Consolidation I and II process steps, as well as for Point Welding. In addition to general 3D printing, MEX DES mode is used for the Overprinting process step during hybridization. Further details on the execution of the process steps with the hybrid end-effector are explained in Chapter 5.2.4.1.

As both MEX DES 3D printing and consolidation have multi-axial paths, the Consolidation Unit moves between the two modes so far that the risk of collision with produced FRP components is minimized. For this purpose, the Consolidation Unit was designed in such a way that the parts of the end-effector are located within a 45° cone around the respective TCP. For the MEX DES mode, the TCP is located at the tip of the nozzle of the single-screw extruder and for the consolidation mode between the two compaction rollers.

For MEX DES 3D printing, a single-screw extruder MDPH2 from Massive Dimension is installed in the hybrid end-effector. This enables output quantities of approx. 1 kg/h and extrusion temperatures of approx. 450 °C. For the control of the single screw extruder, a programmable logic controller (PLC) from Beckhoff is used. As the MEX DES subsystem is not a new development but is only being applied, it will not be explained further. An overview of other subsystems and parts of the hybrid end-effector and Consolidation Unit is shown in Figure 5-9. The subsystems represent a grouping of the parts according to their main function. In this way, a distinction can be made between the main function of *motion & force control* and *temperature control*. Controlled motion and positioning are performed by two independent stepper motors. Stepper motor 1 is used to raise and lower the Consolidation Unit as described previously to switch between the modes. The end positions of the Consolidation Unit are defined by tactile limit switches. Stepper motor 2 is used to rotate the two compaction rollers from 0-359°. This is the seventh axis, which, as shown in Chapter 5.1.1, is necessary due to the required rotation along the process direction. As identified in the preliminary study in Chapter 4.3.2.2, an additional solidification roller is required in addition to the heated consolidation roller. The mechanical set-up is identical for both rollers, allowing a symmetrical set-up. The rollers can be exchanged quickly, allowing wider rollers to be used, for example. As a result, larger areas with less complex shapes can be consolidated more quickly. In order to apply a defined force or pressure with the rollers, two pressure regulators and a double-acting pneumatic cylinder are used for each roller. In addition to applying and regulating the force, this setup also allows balancing and performing short linear movements. The second subsystem has the main function of temperature control. In addition to heating the consolidation roller, the secondary function is to preheat the UD-tape with an IR-heater.

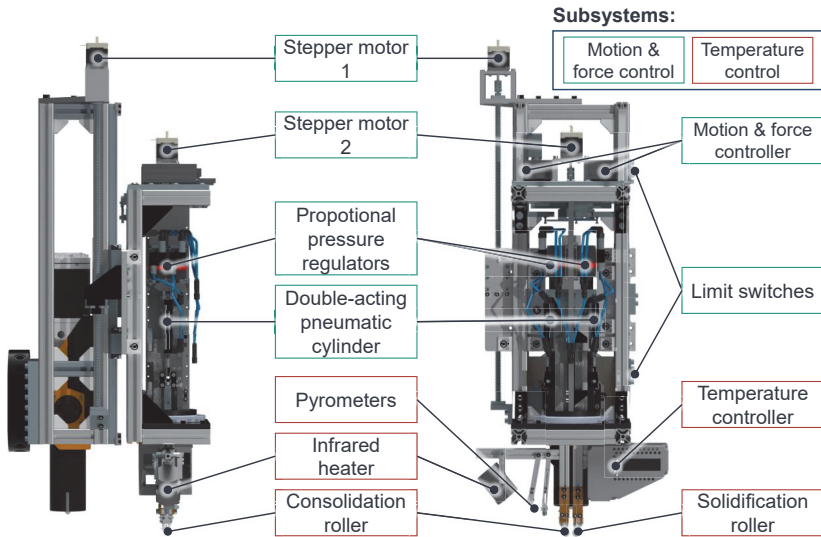


Figure 5-9: Main parts and subsystems of the Consolidation Unit

Both subsystems are operated by one controller each of which is connected to the robot controller via a bus system and parallel wiring. As described in more detail in subsequent Chapter 5.2.3, the control architecture is decentralized, which means that the Consolidation Unit can be operated autonomously. The operation of the force and temperature control is described in more detail in the following two sections.

5.2.1.1 Motion and Force Control

As mentioned in the previous section, the force control for each roller consists of 2 proportional pressure regulators and a double-acting pneumatic cylinder that is connected to the respective roller. The pressure regulators are Aircom PRE1-U06, which output a pressure proportional to the applied voltage. For this model, 1 V is proportional to 1 bar output pressure. If the input pressure is high enough, the regulators can output up to 6 bar. The output pressure is regulated 43 times per second, which enables relatively fast control of the force. As shown in Figure 5-10 on the left, one regulator is connected to the upper chamber and one to the lower chamber of the double-acting cylinder.

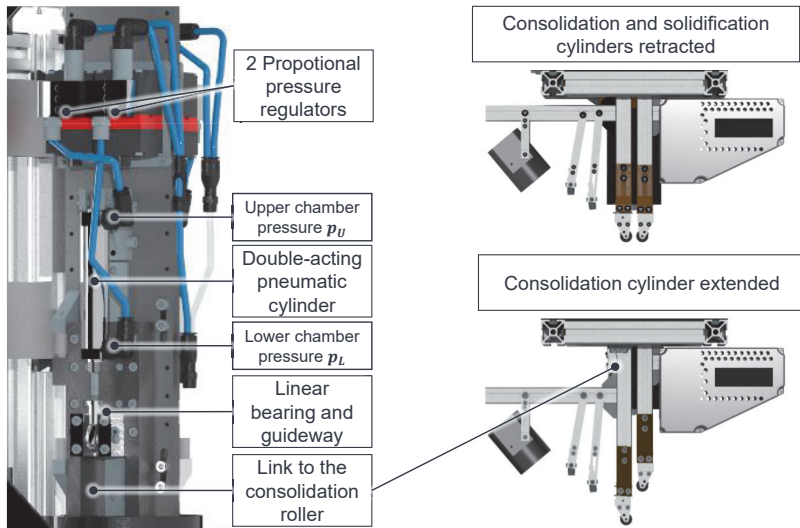


Figure 5-10: Main components for the pneumatic force control of the Consolidation Unit

The cylinder is an Airpel M16D50.0-U with extremely low internal friction. As shown in (A_Kleinwort 2022), low friction is necessary for precise force control. With an input pressure of 6 bar in the upper chamber, the cylinder can apply up to 119 N of force. The force resulting at the respective roller is the result of the force of the cylinder and the force due to the own weight of the installed parts as well as existing friction. One roller on an aluminum profile and one cylinder are each attached to the same linear guide, which enables force transmission. The guides are mounted on ball bearings, which significantly reduces friction and also guides linear movements. Due to a travel distance of 50 mm per cylinder and thus roller, this design enables the consolidation of uneven surfaces. The pressure in the chambers is automatically readjusted during retraction due to surface roughness, allowing constant force control of the rollers. As shown in Figure 5-10 on the right, the setup can also be used to quickly retract or extend the rollers together or individually. This enables, for example, Point Welding of the UD-tapes on the printed components by holding the tape in place with the solidification roller after the hot consolidation roller retracts and until the melted interface has solidified again.

The voltage control of the proportional pressure regulator and the control of the stepper motors 1 and 2 (cf. Figure 5-9), including the built-in brakes and sensors, is carried out via a microcontroller designed for the task. The microcontroller consists of a custom-printed circuit board with various sensors, which is mounted as a shield on an Arduino MEGA.

Force Calculation

As described in the following Chapter 5.2.3, the control architecture is decentralized. With this architecture, the controller receives the control variables from a higher-level control system and is responsible for autonomous execution. This functionality is particularly evident in multi-axial consolidation, as can be seen in Figure 5-11, where the Consolidation Unit is generally not orientated constantly to the direction of gravity, which means that the weight force of the moving parts does not point completely and constantly to the surface normal. As a result, the pressure in the double-acting pneumatic cylinder must be adjusted depending on the orientation of the Consolidation Unit.

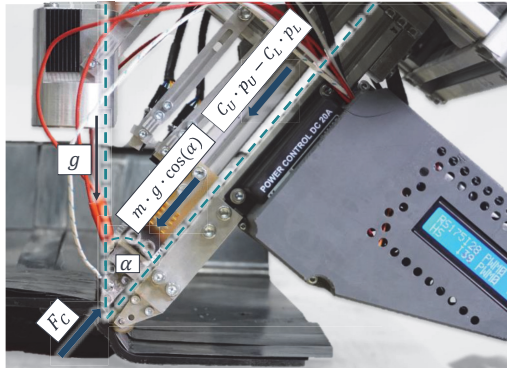


Figure 5-11: Force equilibrium and resulting contact force F_C as a function of the angle α of the Consolidation Unit and the applied pressures p_U and p_L

The approximate resulting contact force F_C that a roller applies perpendicular to a surface can be seen in Equation 5-1. As there is very little friction overall due to the ball bearings and cylinders used, the frictional force is neglected. Since the rollers and other moving parts only move slowly during operation, the inertia force can also be neglected. p_U and p_L are the pressures applied in the upper and lower chamber respectively and C_U and C_L are the effective piston areas in the respective chamber.

$$F_C \approx C_U \cdot p_U - C_L \cdot p_L + m \cdot g \cdot \cos(\alpha) \quad 5-1$$

The resulting weight force of the roller and the other moving parts is calculated as a function of the angle α between the consolidation roller and the direction of gravity as $F_W(\alpha) = m \cdot g \cdot \cos(\alpha)$. $F_W(\alpha)$ represents a disturbance that is canceled out by the pressure control in the chambers. Since the Consolidation Unit is orientated maximally perpendicular to the gravitational direction during operation, it follows that $\alpha \leq 90^\circ$. By pressurizing the lower chamber, $F_W(\alpha)$ can therefore be cancelled out by fulfilling Equation 5-2.

$$C_L \cdot p_L - m \cdot g \cdot \cos(\alpha) = 0 \quad 5-2$$

So that the microcontroller can calculate the required pressure p_L in a continuous loop to compensate for the weight force, a gyroscope type BNO055 is installed on the PCB which provides the angle α of the Consolidation Unit. This allows the desired consolidation or contact force F_C to be set according to Equation 5-3 by setting p_U .

$$F_C \approx C_U \cdot p_U \quad 5-3$$

As described in Chapter 2.1.3.1., reference ATL systems from the state of the art for consolidation only work with force control due to the difficulty of determining the pressure distribution in the contact area of the roller, even though the consolidation pressure is the decisive process parameter. Since the rollers in the Consolidation Unit developed here can be changed according to the requirements, it is not sufficient to consider the force as a process parameter. The following section therefore presents a simple approach for determining equivalent stresses when using different rollers.

Consolidation and Solidification Pressure

For the experiments presented in Chapter 6, rollers of different dimensions and materials are considered for consolidation and solidification. Rollers with a width of 5 mm were selected due to the relatively small sample dimensions. The heated consolidation roller is made of steel and has ball bearings. As a result of the high stiffness, it is possible to achieve high stresses as shown in the following calculation. The non-heated solidification roller has a covering made of silicone. This allows a lower pressure to be applied over a large area and relatively homogeneously.

In order to be able to compare and exchange different rollers, a simple static modeling of the pressure distribution as in (Cheng & Zhao et al. 2018, p. 1420) based on Hertzian

contact theory is used. According to (Popov 2016, p. 63–69; Kirchner 2007, p. 664–665), neglecting friction yields the replacement E-modulus E^* as shown in Equation 5-4 for the contact of a cylindrical and a plane elastic body. E_1 and E_2 are the respective modules of elasticity of the components in contact and μ_1 and μ_2 are their poisson's ratios.

$$E^* = \frac{2 \cdot E_1 \cdot E_2}{(1 - \mu_1^2) \cdot E_2 + (1 - \mu_2^2) \cdot E_1} \tag{5-4}$$

The material properties and geometric dimensions for the consolidation and solidification rollers used in Chapter 6 are listed in the table in Figure 5-12.

Roller	E_1	E_2	μ_1	μ_2	l_{eff}	r
Consolidation	2 GPa	210 GPa	0.45	0.3	5 mm	7 mm
Solidification	2 GPa	10 MPa	0.45	0.3	5 mm	8 mm

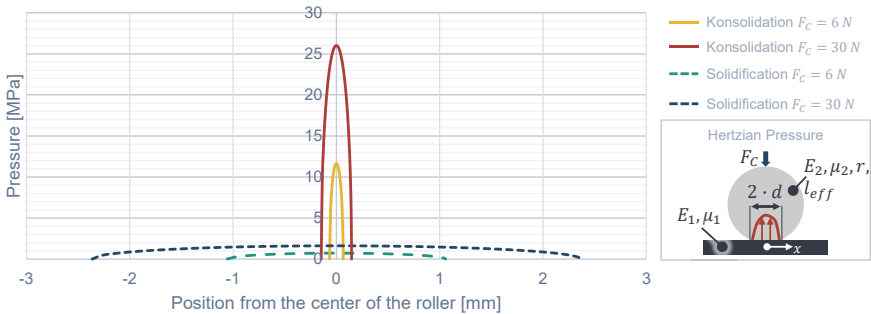


Figure 5-12: Calculated pressure distribution along the width of a consolidation and solidification roller in contact with PA6 CF for 6 N and 30 N contact force

As the process is carried out at high temperatures, the E-module of PA6 with CF decreases significantly. To the author's knowledge, there is no reliable data on the material properties for the considered temperature range. The temperature distribution in the material below the rollers during consolidation is also extremely inhomogeneous (see Figure 4-23 in Chapter 4.3.2.2). The values for E_1 and μ_1 are therefore only based on estimates for PA6 with 30 % GF in the melting range (Bottenbruch & Alewelt 1996 as cited in Wurzer 2021, p. 30). E_2 and μ_2 is dependent on the material used for the respective roller.

The width $2 \cdot d$ (see Figure 5-12 bottom right) of the contact surface can be calculated for an applied contact force F_C using the respective replacement E-module and the effective length l_{eff} and the radius r of the respective rollers with Equation 5-5.

$$2 \cdot d = 2 \cdot \sqrt{\frac{8 \cdot F_C \cdot r}{\pi \cdot l_{eff} \cdot E^*}} \quad 5-5$$

Equation 5-6 allows the maximum equivalent compressive stress in the contact surface to be calculated as a function of the contact force and the related geometric dimensions.

$$p^*_{max} = \frac{2 \cdot F_C}{\pi \cdot l_{eff} \cdot d} \quad 5-6$$

By using Equation 5-7, the pressure distribution $p(x)$ along the contact width can be calculated based on Hertzian modeling.

$$p(x) = p^*_{max} \cdot \sqrt{1 - \left(\frac{x}{d}\right)^2} \quad 5-7$$

The calculated pressure distribution for the contact force range of 6 - 30 N (cf. experimentally identified process windows in Chapter 6.1) is shown for both the consolidation and the solidification roller in the graph in Figure 5-12. It can clearly be seen that the rigid steel consolidation roller produces a line load and the softer silicone consolidation roller produces a relatively homogeneous surface load. Due to the simplified modeling assumptions described above, this is not the actual stress but only a technical equivalent stress. When replacing with wider or narrower rollers (changing l_{eff}), as is planned depending on the application, this modeling is very suitable for calculating equivalent pressures or the associated contact force F_C . The experimental investigation of the influence of the contact force during consolidation and solidification in Chapter 6 can therefore be transferred to other roller dimensions.

The calculated equivalent pressures for consolidation with up to over 25 MPa at $F_C = 30$ N are significantly higher than those of the state of the art with comparable ATL processes. This is because not only flat UD-tapes are consolidated in this thesis, but a consolidation and hybridization between UD-tapes and a relatively rough MEX 3D printed surface has to be achieved. The high pressures are therefore required to smooth

out the surface roughness and create an intimate contact before autohesion (cf. Chapter 2.1.2.2) can take place. Experiments with heat-resistant pressure measuring foils (FUJIFILM PRESCALE High Temperature, Super Low Pressure) between the printed MEX layer and a UD-tape during Consolidation I, as seen in Figure 5-13 (bottom left), show how the intimate contact can only form at high pressures within a suitable process window.

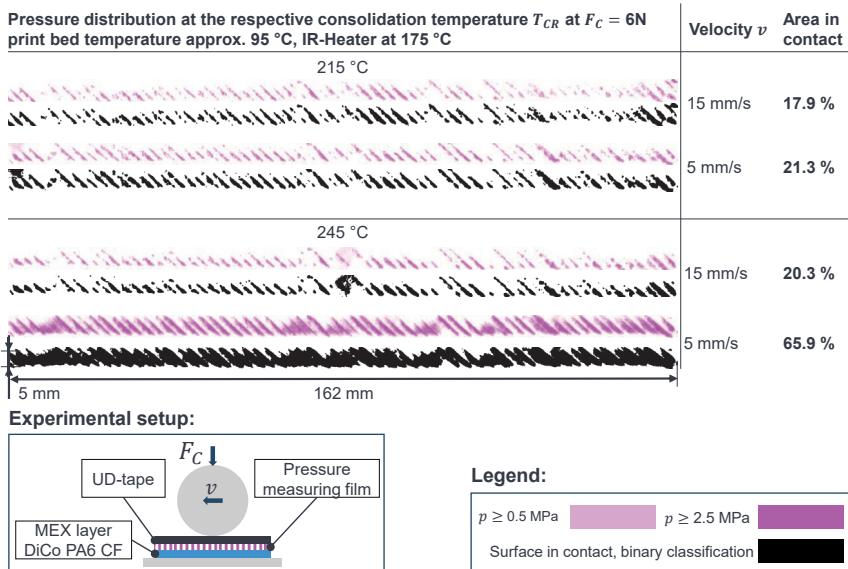


Figure 5-13: Measured pressure distribution and analyzed area in contact in the lower interface after Consolidation I

The pressure distribution in purple clearly shows the paths in which the melted material is deposited during MEX DES. The pressures measured, represented by the different shades of purple, can only be analyzed qualitatively, as the temperatures are higher than those for which the films are designed (220 °C). Of course, the pressure measuring foils also are a significant disturbance, simply because they act as an insulating layer in the interface area, which hinders consolidation. To the author's knowledge, there are no better pressure measuring foils available for this application. However, a conversion to a black and white binary image provides information on the percentage of the contact area that has been flattened, which is directly correlated with the degree of intimate

contact (cf. Chapter 2.1.2.2). At a temperature of $T_{CR} = 215 \text{ }^\circ\text{C}$ of the consolidation roller, it can be seen that the reduction of the consolidation velocity v from 15 mm/s to 5 mm/s, and thus the increase in the consolidation time, does not result in a significant increase in the relative contact area. Only in a suitable process window such as $T_{CR} = 245 \text{ }^\circ\text{C}$, $F_c = 6 \text{ N}$ and $v = 5 \text{ mm/s}$ does a noticeable flattening take place with 65.9 % of the area in contact.

In addition to increasing the understanding of the process with regard to force control and the required pressure distribution during consolidation, these results show the influence of the different temperatures. The temperature control is explained in more detail in the next section.

5.2.1.2 Temperature Control

The heating system consists of two closed control loops, one for the consolidation roller and one for the IR-preheating, that are controlled by a shared temperature controller. As shown in Figure 5-14, the temperature control is located on the side of the solidification roller and the heat sources and sensors are on the side of the heated consolidation roller.

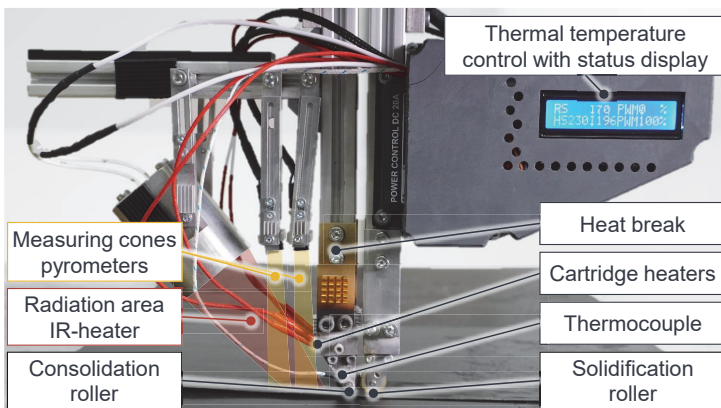


Figure 5-14: Overview of the setup of the temperature control for the IR-preheating and consolidation roller

The consolidation roller is heated via two 24 V heating cartridges and the temperature at the axle bearing of the roller is measured with a thermocouple. A correction function to compensate for the temperature difference between the roller surface and the axle

bearing was determined experimentally. A heat break consisting of ceramics with low thermal conductivity coefficients and heat sinks is installed to prevent an unwanted upward flow of heat into the rest of the end-effector. The maximum heat output has been limited to 60 W by the software for safety reasons. The heating power was more than sufficient for the experiments carried out in Chapter 6 for the relatively small consolidation roller. If larger consolidation rollers are used, the heating power limit can be increased to 100 W. The implementation of the radiant preheating simulated in Chapter 4.3.2.2 is carried out with a control loop consisting of an IR-heater and two pyrometers (MLX90614). The pyrometers measure the temperature of the surface in front of the consolidation roller as shown in the figure. The IR-heater with a focal length of approx. 100 mm and a heat output of up to 150 W can preheat the area in front of the roller in a highly dynamic manner.

The temperature controller has a screen that displays the most important variables such as the actual and set temperature. Like the motion and force controller described in the previous section, the temperature controller consists of a custom microcontroller based on an Arduino Nano. Like the motion and force controller, the temperature controller can act autonomously due to the decentralized control architecture. A more detailed description of the exact control architecture can be found in the subsequent Chapter 5.2.3.

Both control loops are based on a digital PID controller whose controller parameters were set experimentally in (A_Söder 2023) according to the Ziegler-Nichols tuning method. As shown in the simulations in Chapter 4.3.2, the thermal boundary conditions can fluctuate greatly due to different geometries. For example, the uppermost MEX 3D layer and therefore the interface area to be consolidated can be significantly cooler for high components than for low ones. The control loop for the consolidation roller is robust against such varying boundary conditions due to the relatively high thermal capacity. As shown in (A_Söder 2023), the control loop for IR-preheating is only robust for a small preheating temperature and consolidation velocity range under varying boundary conditions. In order to ensure a constant controller quality during preheating, the control loop for IR-preheating has different PID control parameter sets depending on the selected preheating temperature and consolidation velocity.

The overall control of the Consolidation Unit has been designed to work in combination with the Adjustable and Heated Assembly Table subsystem. This subsystem is explained in more detail in the following section.

5.2.2 Development and Testing of the Assembly Table

As described in Chapter 4.1, the main function of the subsystem Adjustable and Heated Assembly Table is to provide a suitable workspace and ambient conditions for the deposition and assembly of the different components and materials. In order to achieve this, the Assembly Table must provide a suitable heated printing bed for the multi-axial MEX DES of DiCoFRP and create suitable conditions for hybridization with CoFRP (UD-tapes) including the consolidation steps. An overview of the developed subsystem Assembly Table can be seen in Figure 5-15 a).

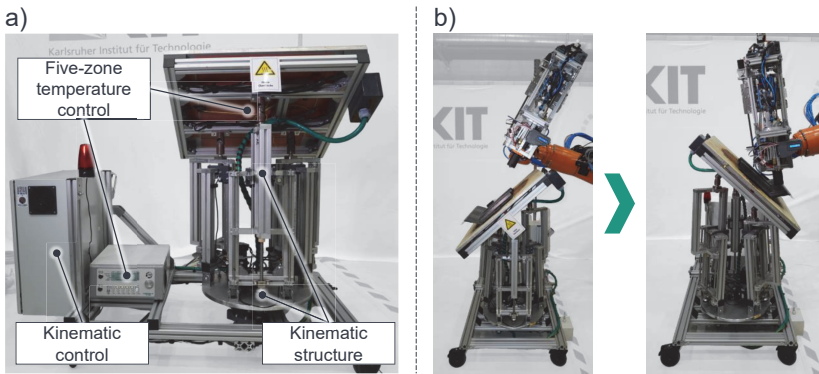


Figure 5-15: Overview Assembly Table: a) Subsystems five-zone temperature control, kinematic structure & control; b) Use of additional kinematic axis to ensure accessibility here, for example, with a rotation of 180° around its own z-axis

The main functions are precise orientation and homogeneous temperature control of the 800 mm · 800 mm heated bed. The heated bed consists of a three-layer structure. In the middle layer, there is an aluminum plate which, on the one hand, has to absorb the relatively high forces during consolidation, but also enables a homogeneous temperature distribution due to its good thermal conductivity. The bottom layer consists of silicone heating mats. The top layer is the contact surface of the component and can be quickly replaced or removed depending on the material or application. If a component is manufactured from scratch entirely on the heated bed, i.e. MEX 3D printed, extremely good adhesion must be ensured, especially as additional forces can act on the component during consolidation. For this purpose, the contact surface can be replaced depending on the material being processed. Since PA6 is processed as the base material in the context of this thesis, the contact surface is made of FR4. However, if

the system and the process are used for the customization of prefabricated LFT components, for example, the contact surface is not necessarily required. In this case, the prefabricated components must be secured mechanically using clamps.

To fulfill its function, the Assembly Table consists of two further subsystems *kinematic structure & control* and *five-zone temperature control*. The functionality of the two subsystems and the requirements that led to their development are explained in the following two sections.

5.2.2.1 Kinematic Structure

The kinematic analysis in Chapter 5.1 showed that the Assembly Table requires a rotational axis around its own z-axis for the reachability during hybridization. An additional axis of rotation around its own x- and y-axis also helps with accessibility, but the main function of these two axes is to support multi-axial MEX DES 3D printing. Figure 5-15 b) shows how, for example, tilting the table with an additional 180 ° rotation around the z-axis makes the multi-axis non-planar MEX (cf. Chapter 2.2.3) possible. One difficulty with multi-axial printing is that the direction of material extrusion is not constant to the direction of gravity. Figure 5-16 shows the material output rate for PA6 with 30 % CF at 280 °C as a function of the angle of the single-screw extruder to the direction of gravity at different rotational speeds, specified in revolutions per minute (RPM).

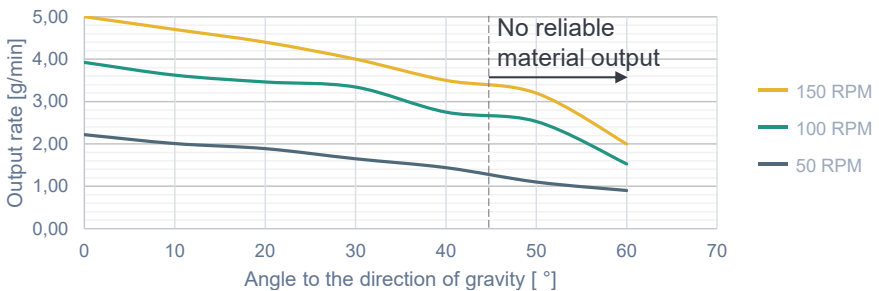


Figure 5-16: Measured output rate for PA6 with 30 % CF at 280 °C as a function of the angle of the single-screw extruder Massive Dimension MDPH2 for different RPM

The output rate is non-linear over the angle and not proportional to the RPM. In addition, the output rate depends on the material and temperature. The measurements were carried out in 5 ° steps up to 70 ° for one minute each. Before each step, the extruder was returned to the vertical position (0 ° to the direction of gravity) in order to have the

same starting conditions. From approx. 45° , the granulate flows irregularly into the extruder screw, resulting in strong fluctuations in the output rate over a longer period of time. From approx. 60° , the granulate does not flow by itself from the filling area of the extruder into the screw. The output rate can therefore no longer be determined above 60° , as the granulate can only be extruded which is in the screw.

Only for small angles over a short period of time, the material output rate during multi-axial MEX 3D printing can be considered constant. Since the aim of this work is to develop a process for large-volume components, the output rate has to be constant over a longer period of time. However, in order to achieve the highest possible tilt of the extruder relative to the build direction during 3D printing, the Assembly Table must also be tilted. The output rate for tilting angles up to 30° from the extruder is considered constant for simplification. In order to be able to print at 90° relative to the build direction, the kinematics for the heated bed are designed to enable tilting of up to 60° around the x- and y-axis.

In addition to the required kinematic adjustability, the Assembly Table must be rigid due to the contact forces that occur during consolidation. At the same time, the risk of collision between this kinematic and the two other kinematics (industrial robots) must be minimized. In (A_Hinze 2022), various kinematic concepts were analyzed and evaluated according to the requirements.

The kinematic structure of the Assembly Table that fulfills the above-mentioned requirements and was selected and implemented is shown in Figure 5-17 a). Based on the principle of three degrees of freedom (Tsai 1999), a parallel kinematic structure was chosen. Three linearly extendable axes are each connected via joints to a moving (frame for heated bed) and fixed platform. By extending the axis in a targeted manner, it is possible to rotate around the x- and y-axis (cf. Figure 5-17 b)). In addition, height adjustment in the z-direction is possible. In this design, the lower fixed plate has an additional rotary axis, which enables a rotation around the z-axis.

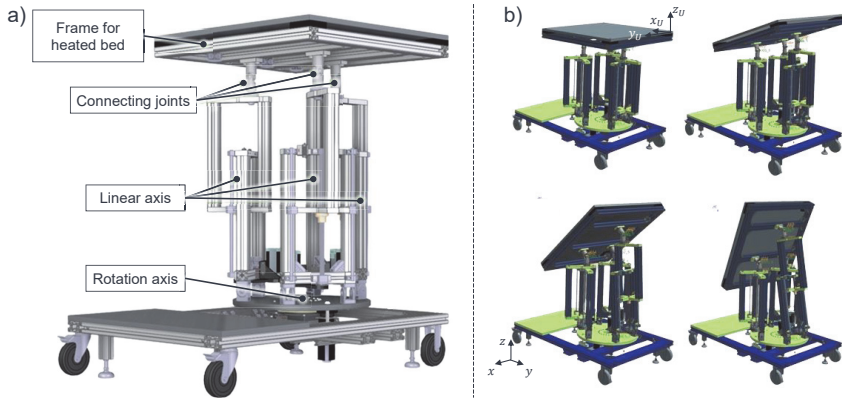


Figure 5-17: a) Overview of the kinematic structure of the Assembly Table; b) Rotation around the y-axis from 0-60 ° by extending one linear axis (based on (A_Hinze 2022))

Since the heated bed is the shared work surface of the two industrial robots, the same user coordinate system (x_U, y_U, z_U , cf. Chapter 2.3.1) with origin in one of the corners of the heated bed is defined for both. A tilt or rotation by the kinematic therefore always corresponds to a change in the user coordinate system.

The three motors for the extendable linear axes and the motor for the rotation axis around z are closed-loop stepper motors and are controlled via a PLC Controllino mega. As with the Consolidation Unit (see Chapter 5.2.1), the control architecture is decentralized and is explained in more detail in the subsequent Chapter 5.2.3. In the following section, the control of the temperature of the heated bed is explained.

5.2.2.2 Five-Zone Temperature Control

A five-zone temperature control system was implemented in order to achieve a homogeneous temperature distribution on the heated bed surface. This consists of five silicone heating mats, each equipped with a thermocouple, mounted on the underside of the aluminum layer. In the center is a large 600 mm · 600 mm heating mat and four smaller heating mats along the four edges. This ensures that the edge area, which cools down more quickly, is heated relatively strongly and therefore the temperature distribution is more homogeneous. A Thermoplay TH-M6 temperature controller is used to control the silicon heating mats, which can automatically determine suitable settings for the PID controllers for the different zones. No temperature changes are planned during the

production of the components and the alternation of the different processes (MEX and consolidation) as this would have several disadvantages. In addition to a considerable increase in production time due to waiting times, temperature fluctuations can contribute to additional distortion of the components. As explained in Chapters 4.3.2.3 and 5.2.1.2, the IR-heater is used for local preheating during consolidation, which means that the heated bed temperature does not need to be adjusted when switching between the MEX and consolidation process steps. The temperature control is therefore not integrated into the rest of the control architecture but must be switched on and started separately when the system is started.

5.2.3 Development of the Control Architecture

A simplified overview of the control architecture including the Communication protocols of the experimental setup can be seen in Figure 5-18.

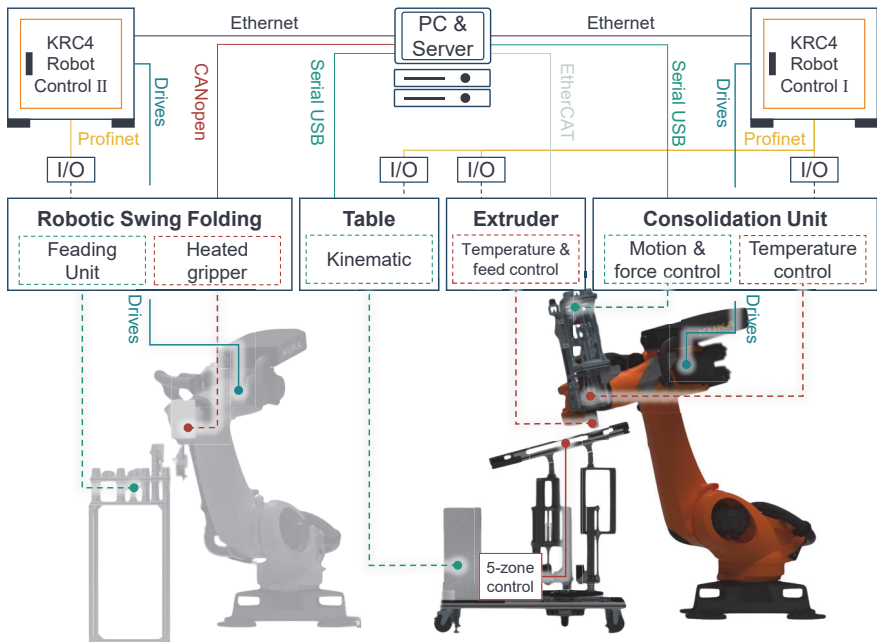


Figure 5-18: Overview of the control architecture and communication protocols

The main program created by the user on the PC is transferred to Robot Control I and processed by it. In addition to the robot paths, the main program contains various sub-programs that are responsible for synchronizing and controlling the other subsystems. Basically, the main program is structured like a typical machine numeric control (NC) code and is processed line by line. If, for example, the MEX system is to be used, i.e. 3D printing is to be carried out, the corresponding signal is sent to the extruder via Profinet and parallel-wired input/output (I/O) interface to start it. The control of the single-screw extruder has to be pre-parameterized by the PC. By this, for example, the temperature and the feed rate in RPM are preset depending on the material and the selected velocity of the robot. A similar principle applies to the temperature control of the Consolidation Unit. For the kinematic control of the Adjustable and Heated Assembly Table subsystem and the motion and force control of the Consolidation Unit, 8-bit communication is established via 8 parallel I/O wiring. This allows 256 different control signals to be sent from Robot Control I to the respective subsystem. As a result, for example, the Assembly Table can be moved to the desired orientation or the additional rotary axis of the Consolidation Unit can be rotated accordingly. As the control architecture is decentralized, the commands to be executed are controlled by the respective control unit of the corresponding subsystem. The control units of the subsystems were specified in the previous sections.

Since the main program is read in and processed by Robot Control I and the corresponding signals and instructions are distributed to the subsystems, Robot Control I is considered the master of the entire control architecture. Although the Robotic Swing Folding executes its program completely independently, its controller Robot Control II communicates with Robot Control I as a client via the server. Robot Control I uses the server to transmit the starting commands to Robot Control II for preparing and positioning the UD-tapes. Robot Control I thus ensures the synchronization of the entire experimental setup. The main program is generated using a digital process chain, which is explained in more detail in the following section.

5.2.4 Development of the Digital Process Chain

The digital process chain includes all manual and automated steps required to generate the main program described in the previous section and to parameterize the controllers of the subsystems. Before the logic and the procedure for planning and creating the

main program are explained in Section 5.2.4.2, the main manufacturing process steps are explained below.

5.2.4.1 Process Steps

In Chapter 4, the four main process steps Point Welding, Overprinting and Consolidation I and II were identified for the hybridization of Co and CoDiCoFRP. Further process steps are required for the individual production or subsequent individualization of CoDiCoFRP. For a better overview during process planning, some process steps are summarized. Due to the identical process sequence, Consolidation I and II can be summarized and referred to as consolidation in this section. In addition, consolidation always includes solidification, as the solidification roller is used in parallel to the consolidation roller (see Figure 5-14). Solidification is therefore not always explicitly mentioned below. Overprinting is carried out using the MEX process, which can also be used for the general 3D printing of parts of the composite. These two processes are summarized under MEX. The UD-tapes are prepared and handled using Robotic Swing Folding. Point Welding to secure the UD-tape is carried out in conjunction with the consolidation roller and the Robotic Swing Folding. As only the subordinate placement function of Robotic Swing Folding is used for Point Welding, these two process steps cannot be summarized. As can be seen in Figure 5-19, there are the four summarized main process steps *Robotic Swing Folding*, *MEX*, *Point Welding* and *Consolidation*, which can be combined in any desired quantity and sequence.

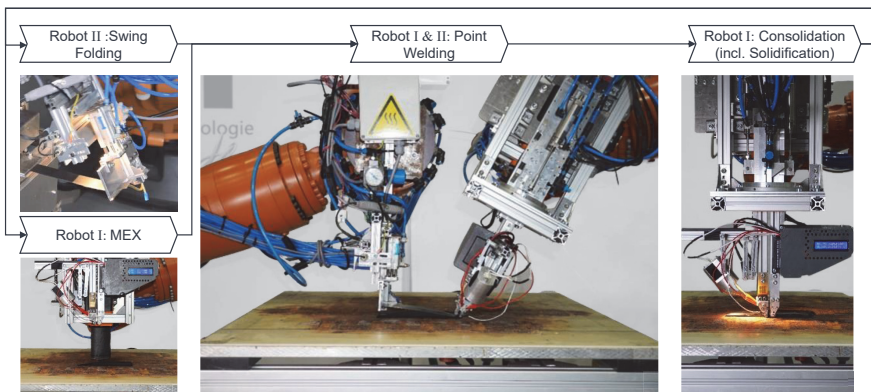


Figure 5-19: The four main process steps and an example process sequence

How these four main process steps are combined depends firstly on whether an individual component is to be manufactured completely from scratch or whether a partially prefabricated component is only to be individualized subsequently. Other important influencing factors are the component geometry and the desired Co and DiCo composition.

The current process sequence shown in Figure 5-19 illustrates a typical process sequence for the individual production of a component from scratch. First, the MEX DES is used to start printing the base body, which can consist of a DiCo material. At the same time, the Robotic Swing Folding process can already start with the production of preforms (see Chapter 2.1.3.1 and (Kupzik 2022) for further details). Once the base body has been printed to the desired layer and the preform made from UD-tape (Co part) is prepared, hybridization can take place to create a CoDiCo component. Hybridization consists of the process steps of Point Welding and Consolidation. During Point Welding, the preform is partially deposited at the desired location using Robot II and fixed in place with one or more welding points using the Consolidation Unit of Robot I. Robot II can then move away with the gripper for the preform and the hybridization can be completed by using the Consolidation Unit of Robot I. Subsequently, the main process steps can be carried out as often as required in a loop.

All main process steps include further subprocess steps. As the focus in Chapter 6 is on methodologically optimizing the consolidation process (incl. solidification), its subprocess steps are explained below. As shown in Figure 5-20, Consolidation consists of an initialization step and the actual consolidation process.

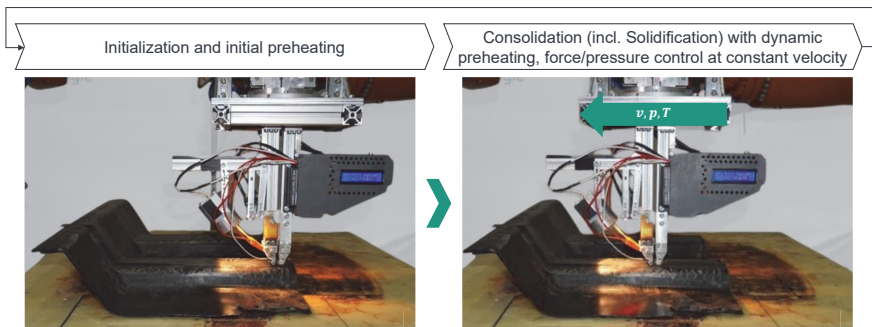


Figure 5-20: The two subprocess steps of the main process step Consolidation

Initialization includes heating the consolidation roller and activating the force control (see Chapter 5.2.1). To save time, the initialization takes place at the start of the overall process. Before the actual consolidation process can be carried out at a constant movement, the IR-heater must initially preheat the component surface in front of the consolidation roller. Once the desired temperature has been reached, the Consolidation Unit moves over the component at a constant velocity and consolidation and solidification force/pressure, while dynamic preheating (see Chapter 4.3.2.3) ensures constant thermal boundary conditions. When the end of the path to be consolidated is reached, the consolidation roller retracts first and the solidification roller remains extended until it has also reached the end. The separate extension and retraction mechanisms of the two rollers are explained in Figure 5-10. The process steps are carried out in a loop with an offset along the width of the UD-tape until the entire area to be consolidated is covered.

The main process steps are combined to form an overall process by creating and merging corresponding subprograms. How the subprograms and the main program are created is explained in the following section.

5.2.4.2 Digital Process Planning

The following section describes the digital process planning procedure for the production of an individual CoDiCoFRP component from the ground up. In principle, the digital process steps for the subsequent individualization of a partially prefabricated component follow the same procedure and are not described separately due to their similarity. As shown in Figure 5-21, digital process planning consists of the four main digital process steps *segmentation*, *merging*, *collision control and post-processing* and *parameterization via GUI/PC*. The digital process steps are run through manually by the user and at the end the main program is generated, which can be executed by the robot control I (cf. Figure 5-18). Some of the individual steps can be automated using proprietary software. Which software is used in each case is explained in more detail below.

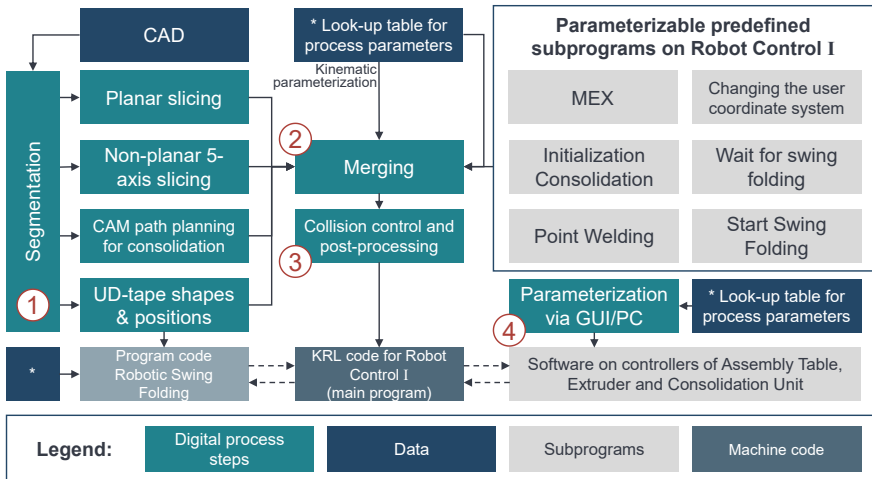


Figure 5-21: Digital process steps and further building blocks for planning an entire manufacturing process

Step 1 – Segmentation

In the first step, the component is geometrically segmented in a CAD software. The segmentation and thus the selection of the suitable segment type is carried out manually within a CAD environment in the course of this thesis and thus requires expert knowledge from the user. As shown in Figure 5-22, a distinction can be made between the four different segment types *planar slicing*, *non-planar five-axis slicing*, computer-aided manufacturing (CAM) *path planning for consolidation* and *UD-tape shapes & positions*.



Figure 5-22: Four different segment types visualized using the example of a generic component to be manufactured from scratch

The segment types determine which main process steps are required and what digital processing is needed. The segment type also determines whether it is a DiCo-fiber reinforced area (using MEX) or a Co-fiber reinforced area (integration of UD-tapes).

Table 5-1 shows which main process step (cf. Figure 5-19) is required for the production of which segment type. The further digital process steps required for processing the respective segment type are explained in more detail below.

Table 5-1: Main process step to be executed based on the segment type

Segment type	Planar slicing	Non-planar five-axis slicing	CAM path planning for consolidation	UD-tape shapes & positions
Main process step	(three-axis) MEX	(five-axis) MEX	Consolidation (incl. solidification)	Robotic Swing Folding and Point Welding

Planar and Non-Planar Five-Axis Slicing

For segments that are 3D printed, i.e. produced using the main process step MEX, slicers are used that automatically generate a tri-axial planar G-code. If a smoother surface is required, e.g. because the next layer consists of a UD-tape preform and a smooth interface with a low void content is required, the G-code can be converted to a non-planar five-axis G-code. This is explained in more detail in the following Section 5.2.4.3.

CAM Path Planning for Consolidation

The main process step Consolidation is required for the hybridization and creation of CoDiCo-fiber reinforced areas. Any CAM software that allows the generation of movement commands via surface information can be used to generate the G-code. The path commands are created using five cartesian axes, i.e. no specifications are made for the rotation of the TCP (center point between the consolidation and solidification rollers, see Figure 5-8) around its own z-axis. The targeted use of the seventh axis of the Consolidation Unit (see Chapter 5.2.1) takes place in the digital process step 3 (see below) during post-processing. During post-processing, the seventh axis is aligned so that the non-symmetrical Consolidation Unit always points correctly towards the direction of movement.

UD-Tape Shapes & Positions

In addition to deriving paths for the segments to be 3D printed using the MEX process and the segments to be consolidated, the segmentation also determines which area contains UD-tapes in the form of preforms. Preliminary FEM based topology optimization can be used to determine where the UD-tapes need to be placed for an optimum

reinforcement effect, however this was not a part of the studies in this thesis. The position and shape of the UD-tape preforms are therefore taken for granted. Furthermore, a method for deriving the preforms shapes for Robotic Swing Folding was developed in (Kupzik 2022). The shape and position of the UD-tapes also determine how the main process step Point Welding is carried out, as this mainly depends on the positioning of the UD-tapes. The positions for placing the tapes are inserted in the main program and thus transferred to Robot Control I and II for execution (cf. Figure 5-18).

Step 2 – Merging

In step 2 (cf. Figure 5-21), after segmentation, the individual paths are merged into a continuous main program according to the sequence of the required main process steps. During merging, standardized subprograms are also added, which are already available on Robot Control I and can be executed with a single command line. One subprogram is, for example, the initialization of the consolidation process step, which was explained in the previous section. The subprograms must be parameterized, in the case of consolidation this means specifying the preheating temperature, the consolidation temperature, the consolidation velocity and the consolidation force/pressure. Parameterization is carried out depending on various factors, such as the characteristics of the used materials. Process parameters are either based on values from literature or must first be determined experimentally. However, only the kinematic values are parameterized during the merging process, e.g. the consolidation velocity. The other parameters such as the temperature values are parameterized in step 4.

Step 3 – Collision Control and Post-Processing

After merging, a G-code-based main program is available, which must be converted into the robot-specific programming language during post-processing in the third step. In this case, it is converted into the KUKA robot language (KRL). RoboDK software from RoboDK Inc. is used for the conversion. For this purpose, a digital twin of the setup was created, which allows the program to be checked for any errors or collisions before it is sent to Robot Control I to be executed on the real system.

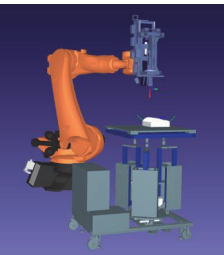
As step 3 in Figure 5-21 involves post-processing, which includes collision checking and conversion of the G-code into a robot-specific program, the G-code can theoretically be created using any slicer or suitable CAM software. One of the advantages of using suitable CAM software is that it can also be used directly to create the paths for the consolidation process. Conventional slicers for 3D printing are not suitable for this,

as they offer too few or no options for adapting the paths to the geometric boundary conditions of the Consolidation Unit. In the context of this work, for example, the CAM software Mastercam was considered in combination with the extension APlus from CA-Manufacturing Solutions Inc. The advantage of this software combination is that it is suitable for the hybridization of different processes and offers integrated segmentation functionalities like a simple geometric division of the component and selection of different process steps and tools. An alternative approach in the form of open-source software for segmentation and generating non-planar five-axis G-code from three-axis code is discussed in the subsequent Section 5.2.4.3

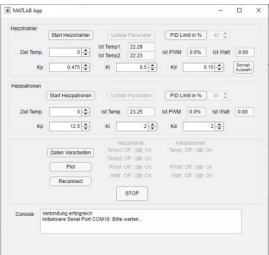
Step 4 – Parameterization via GUI/PC

As shown in Figure 5-21 and described in the previous section, Robot Control I executes the main program and acts as the master in the control architecture. To ensure that all subsystems are ready for use and synchronization can take place, the subsystems must be parameterized before the overall process is started. This is done via the PC using custom graphical user interfaces (GUI) in combination with look-up tables for the settings. Each subsystem has its own GUI. Figure 5-23 shows an example of the GUI and the integrated look-up table for parameterizing the temperature control of the Consolidation Unit. In addition, part of the digital twin of the overall system is displayed in RoboDK. The CAD models imported into RoboDK are greatly simplified to speed up post-processing and collision control in particular.

Collision control and post-processing in RoboDK



GUI for parameterizing the temperature control of the Consolidation Unit



Integrated look-up table for parameterizing and setting the IR-preheater

C: 180°C		1 mm/s				3 mm/s				5 mm/s				10 mm/s								
A	50	45	40	35	30	25	20	15	10	5	0	45	40	35	30	25	20	15	10	5	0	
22°C	0.475	0.5	0.55	0.675	0.5	0.55	0.675	0.5	0.55	0.675	0.5	0.55	0.675	0.5	0.55	0.675	0.5	0.55	0.675	0.5	0.55	0.675
50°C	0.1	0.5	0.15	0.15	0.5	0.15	0.2	0.5	0.15	0.2	0.5	0.15	0.2	0.5	0.15	0.2	0.5	0.15	0.2	0.5	0.15	0.2
80°C	0.1	0.5	0.15	0.15	0.5	0.15	0.2	0.5	0.15	0.2	0.5	0.15	0.2	0.5	0.15	0.2	0.5	0.15	0.2	0.5	0.15	0.2

C: 180°C		1 mm/s				3 mm/s				5 mm/s				10 mm/s								
A	50	45	40	35	30	25	20	15	10	5	0	45	40	35	30	25	20	15	10	5	0	
22°C	3	1.25	0.2	2	1.1	0.3	0.75	1.1	0.2	2	3	0.4										
50°C	2	1.25	0.2	1.75	1.1	0.2	2	1.1	0.2	2	0.4											
80°C	2	1.25	0.2	1.75	1.1	0.2	2	1.1	0.2	2	1.7	0.1										

Figure 5-23: (Left) Digital twin for post-processing and collision control with RoboDK; (Center) GUI and integrated (Right) look-up table for parameterizing the temperature control of the Consolidation Unit subsystem

Overall, the current state of digital process planning is very complex and requires a lot of user input. Although this offers the flexibility to create freely shaped and assembled

components, which is particularly necessary in experimental operation, this process is prone to errors. Collision control at the end of process planning therefore ensures that there are no collisions between the subsystems. However, collision control with any newly printed areas of the component is not possible with the current setup, as the material discharge is not simulated. Since an identified collision or error in the main program can only be identified at the end of process planning, this means that the previous process steps, in particular segmentation, must be repeated iteratively to eliminate the error. To avoid this time-consuming procedure as far as possible, the process limits due to the shape of the end-effector are already considered during segmentation. For example, only gradients of a maximum of 45° are tolerated during consolidation. Various tool-dependent limit values can be set in the CAM software mentioned above to ensure that the generated paths are as collision-free as possible during slicing.

In the following section, the application of an open-source slicer is presented in which non-planar three-axis paths can be generated with collision avoidance. Through adaptation and subsequent process steps, this slicer is suitable for the segmentation into planar and non-planar areas as described above. Furthermore, a subsequent transformation of non-planar three-axis paths into non-planar five-axis paths is possible

5.2.4.3 Non-Planar Three-Axis to Five-Axis Transformation

The segmentation process and the generation of non-planar five-axis G-code are explained below using the example of Overprinting a curved UD-tape surface. The process was developed, refined and tested in (A_Teboul 2022). As can be seen in Figure 5-24, in the first step, the area of the surface to be overprinted is exported as a standard triangle language (STL) file from a CAD environment. At the same time, the entire component, referred to here as the main body, is also exported as an STL file. Slicing is carried out using the open-source software called Slic3r with an extension from Ahlers & Wasserfall et al. (2019) for three-axis non-planar printing of surfaces. In addition to various settings for the non-planar surface, the extension also offers settings for collision avoidance. As the extension was designed for standard three-axis FDM printers, the settings options relate to the dimensions of such 3D printers. If the MEX DES robot is also only used for three-axis printing, the settings can also be adapted to the dimensions of the single-screw extruder end-effector. However, if non-planar five-axis printing is carried out, the settings for collision avoidance can no longer be used and are deactivated.

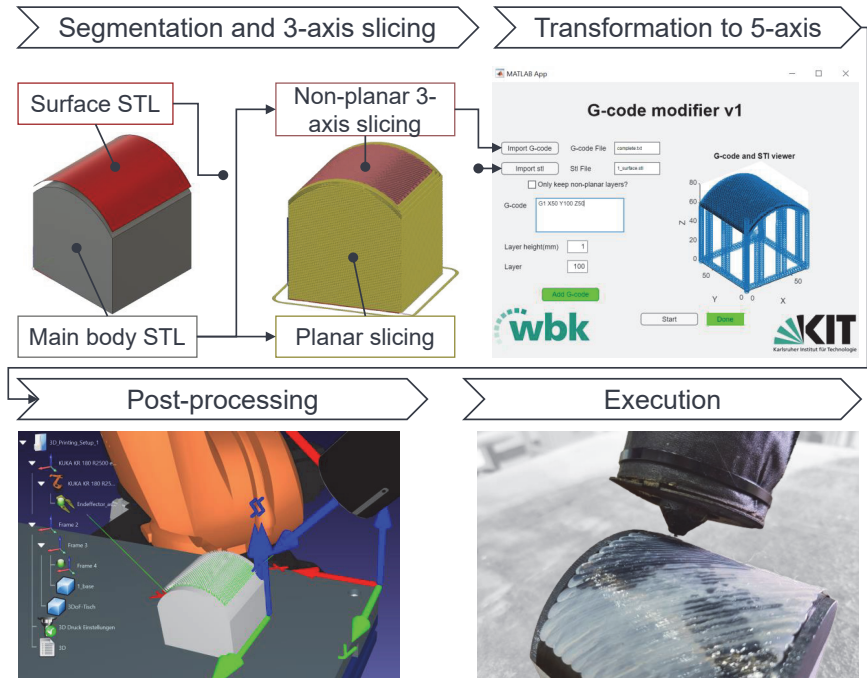


Figure 5-24: Segmentation and non-planar three- to five-axis transformation for the Overprinting, as explained in the example of overprinting curved surfaces

After slicing a non-planar three-axis G-code is available. This is loaded into a GUI with the previously extracted surface STL file, which outputs a non-planar five-axis G-code that can be read by RoboDK. The main functions of the GUI *planar and non-planar G-code separation, STL normal extraction and G-code matching and construction of five-axis G-code with IJK Vectors* are explained below. The exact programming is explained in more detail in (A_Teboul 2022).

Planar and Non-Planar G-Code Separation

Since only the non-planar layers of the part need to be converted to five-axis G-code, it is important to separate them from the planar G-code before processing to save computation time. This was achieved by writing a simple loop that scans through the extracted G-code points and checks whether three neighboring points all have different z -values, indicating non-planar motion. For planar G-code, only two neighboring points

can have a different z-value, especially during a layer change, but for non-planar motion, the z-value is constantly changing to adapt to the slope of the part's surface. (A_Teboul 2022)

STL Normal Vector Extraction and G-Code Matching

STL files describe a surface with many facets, each described by three vertices and a surface normal vector. In the first step, the data is extracted from the imported surface STL file. In the second step, a matching between the facets and the non-planar G-code points from the previous separation takes place. This is achieved by essentially applying an algorithm from Rodriguez-Padilla & Cuan-Urquizo et al. (2021), in which points of a trajectory are projected onto a non-planar tessellated surface. As a result, the G-code points are matched to a corresponding facet and the linked normal vector is extracted.

Construction of Five-Axis G-Code with IJK Vectors

In the last step, the information of the normal vector for each point has to be implemented into the G-code. For better compatibility with RoboDK, the IJK tool vector convention is used to supplement the orientation of the normal vector to the x, y and z coordinates of the G-code. The IJK tool vector convention is an alternative to the usual specification of the 5-axes orientation of the TCP using a combination of two of the three rotational A, B and C axes. As the orientation of the TCP is specified via a vector and not via additional rotational axes, this notation is machine-independent. This is particularly useful as the conventions for naming the ABC-axes usually differ between traditional machine tools and robots.

Once the transformation to five-axis G-code has been completed with the GUI, the G-code can be loaded into RoboDK and processed further, as shown in Figure 5-24. As described in the previous section, post-processing for KRL and a collision check take place. The last step in the figure shows the actual execution. The curved UD-tape surface was overprinted with transparent, unreinforced PA6. It can be clearly seen that non-planar five-axis printing produces a very smooth surface, which is not possible with three-axis non-planar processes, as the wall of the nozzle would collide with the discharged material at steep angles (see Figure 2-20).

5.3 Conclusion

Based on the new process developed in Chapter 4, a corresponding experimental setup was developed and critical subsystems were analyzed and validated experimentally. An overview of the final setup can be seen in Figure 5-25.

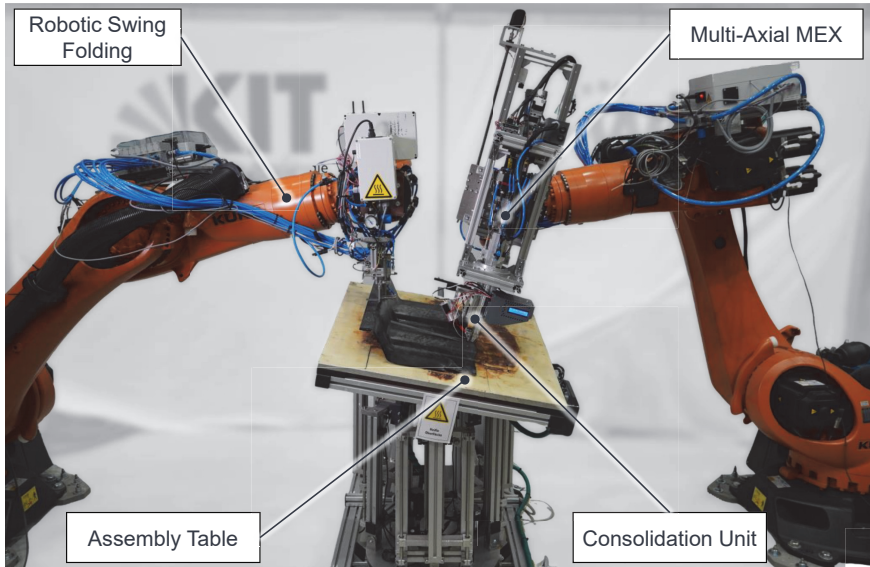


Figure 5-25: Prototypical experimental production system for subsequent individualization and individual production of CoDiCoFRP

The prototypical and experimental production system allows an individualization and individual production of CoDiCoFRP. During the development of the experimental setup, the influence of changing geometric boundary conditions (e.g. different CoFRP proportions and other component shapes and sizes) was considered. For this purpose, based on the results of thermal simulations (see Chapter 4.3.2), a heating system with IR-heating was installed at the Consolidation Unit. For a more homogeneous temperature distribution, a five-zone temperature control was installed as part of the Assembly Table. Since the experimental setup was set up in a climate-controlled laboratory, it can be assumed that few interfering factors and constant boundary conditions can be expected with regard to the heating system. If a production system is set up according to

the same design, it cannot be assumed that an elaborate climate control system is installed in the production hall in an industrial environment, which can lead to strong fluctuations and disturbances. To address this, the system can be enclosed and equipped with an air conditioning system.

Furthermore, if the component sizes and shapes vary greatly, constant boundary conditions can no longer be assumed. Although this is partially compensated for by IR-heating, this only applies to the consolidation processes. In MEX, no preheating is used, which means that there may be strong temperature fluctuations in the component and that layer adhesion is not constant. To address this, more intelligent slicers can be used and developed that consider different rates of cooling in different components and thus adapt the path planning and possibly the temperatures during extrusion to the shape.

In summary, the resulting flexibility from the kinematic freedom and the open process control is used in Chapter 6 for the development of a methodical experimental optimization of the hybridization process for non-specific material systems.

6 Experimental Optimization of the Hybridization Steps

The objective of this chapter is to show the methodical procedure for identifying optimized process parameters for the hybridization and integration of UD-tapes into the MEX process. The focus here is on the process steps Consolidation I and II as well as Overprinting, which are the main steps of different hybridization strategies as presented in Chapter 4.3.1. The Point Welding process step does not require optimization and is therefore not examined any further. The experimental production system described in Chapter 5 is used for the entire tests and production of specimens.

The methodological procedure for the identification of optimum process parameters is carried out using the material system determined in Chapter 4.3.1.3 as an example (PA6 CoDiCo CF system, see material parameters in Table 4-1, main study). In addition to the methodological approach developed and the optimized process parameters identified for the PA6 CF system, the process understanding for the individualization and individual production of CoDiCoFRP is improved.

Table 6-1 shows the relevant process parameters for the experimental optimization and analysis of Consolidation I and II. As usual in statistical design of experiments, the individual process parameters are referred to below by the synonym factor.

Table 6-1: Constant and variable process parameters/factors for the experimental analysis and optimization of Consolidation I and II

Process parameter	Constant		Variable - Aim of optimization		
	T_{PH}	T_{HP}	T_{CR}	v	F_C
Description	Surface IR-preheating temperature	Temperature heated bed	Temperature of consolidation roller	Velocity of consolidation and solidification roller	Contact force roller perpendicular to the surface
Range	175 °C	100 °C	215 - 275 °C	1 - 20 mm/s	6 - 30 N

The value ranges of the factors are adapted for the material systems under consideration and are based on the findings from Chapter 4, literature and manufacturer specifications as well as brief preliminary tests that are not explained in detail here. MEX layers generated for the samples of Consolidation I and II are carried out at an extrusion temperature of $T_E = 280$ °C, and an extruder rotational speed of $U_E = 68$ RPM. For the infill pattern, monotonous straight lines with 45 ° to the longitudinal direction of the samples and 100 % density are used. The velocity of the robot and thus of the extruder is

constant $v_E = 40$ mm/s. All tests were carried out with a nozzle diameter of $d_E = 1.5$ mm on the extruder and a layer height of $L_H = 1$ mm.

As described in Chapter 5.2.1.1, the contact force F_C can be converted into technical equivalent stresses for a more generalized result. In all tests, the consolidation roller and the solidification roller are operated with the same contact force. Due to the different materials and dimensions of the two rollers, this results in the two different equivalent stresses $p^*_{max,CR}$ and $p^*_{max,SR}$. For the sake of simplicity, only the contact force is therefore given in the following sections. The associated stresses for the contact forces F_C considered in the experiments were calculated using Equation 5-6 and can be seen in Table 6-2.

*Table 6-2: Calculated technical equivalent stress $p^*_{max,CR}$ and $p^*_{max,SR}$ for the consolidation and solidification rollers for relevant contact forces F_C*

F_C	6 N	12 N	18 N	24 N	30 N
$p^*_{max,CR}$	11.76 MPa	16.62 MPa	20.3 MPa	23.34 MPa	26.18 MPa
$p^*_{max,SR}$	0.72 MPa	1.02 MPa	1.25 MPa	1.45 MPa	1.62 MPa

6.1 Optimization of Consolidation I

The objective is to identify optimized process parameters for Consolidation I under consideration of boundary conditions and to develop a better understanding of the overall process. Optimized process parameters are considered to be those that achieve the highest degree of bonding D_b (cf. Chapter 2.1.2.2) in the interface between the MEX layer and the UD-tape, as this results in a high reinforcement effect of the composite. As described in Chapter 4.3.1.2 and applied in the pre-studies, D_b correlates with the transferable shear stresses in the interface area. To determine the transferable shear stresses for varying process parameters/factors, tensile shear tests are carried out in the following Chapters 6.1.2 - 6.1.4. The specimen production and evaluation were carried out in (A_Beck 2024).

Specimen Design, Production and Test Procedure

Compared to the specimen shape used in Chapter 4.3, the shape was adapted based on the findings of the pre-studies to be able to better analyze Consolidation I and II. The new test specimen is based on (ASTM D5868-01) and can be seen in Figure 6-1.

Definition of the Optimization Objective

Before the aforementioned tests can be carried out, a suitable process window and factor levels are determined for the statistical design of experiments in the following Chapter 6.1.1. In addition, a mathematical damage model is set up as a function of the variable factors. During the optimization search in Chapter 6.1.4, the damage model and the process window limits prevent process parameters/factors to being used that cause damage to the component. This is illustrated in Figure 6-2 using the example of the two process factors consolidation velocity v and consolidation roller temperature T_{CR} .

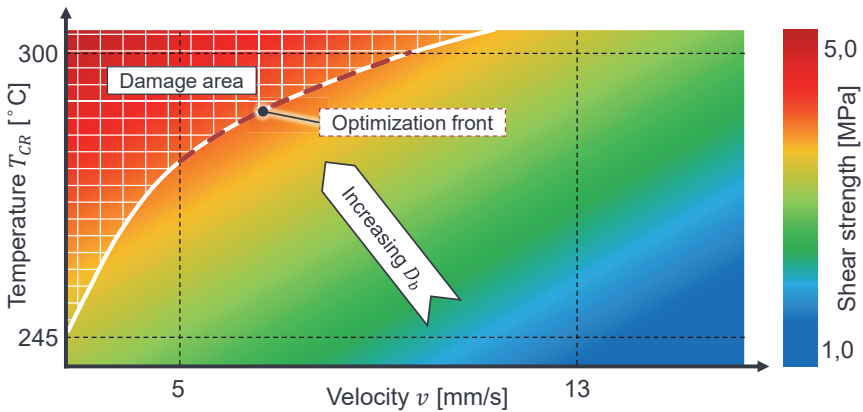


Figure 6-2: Illustration of the optimum search: Factor variation according to the consolidation model and compliance with the limits of the process window and the damage model

The consolidation model, which is derived in Chapter 6.1.3, specifies that the shear strength and thus the degree of bonding D_b increases with increasing temperature and decreasing velocity. An optimum is achieved along a front where components are not damaged and other boundary conditions are met by the limits of the process window. Determination of the damage model and the associated process window is explained in the following section.

6.1.1 Process Window Identification and Damage Modeling

For the three variable factors consolidation roller temperature T_{CR} , contact force F_C and velocity v , upper and lower limits were defined based on literature data from comparable processes, manufacturer data and individual test runs. Due to the high range of the values, five factor levels with constant intervals were selected for sufficient resolution. In order to consider the interaction between the factors, they are all combined with each other, resulting in $5^3 = 125$ combinations.

Experimental Execution

The 125 combinations were tested on the component (600 mm edge length) shown in Figure 6-3 with 100 mm long consolidation tracks, according to the procedure and boundary conditions of Consolidation I as shown in Figure 6-1.

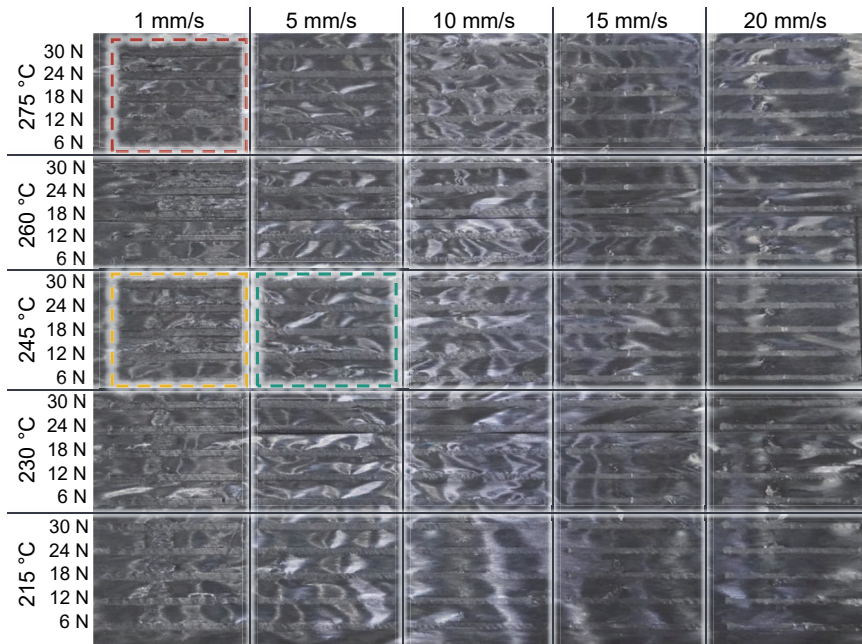


Figure 6-3: 100 mm long consolidation tracks carried out with all 125-factor level combinations of the consolidation roller temperature T_{CR} , contact force F_C and velocity v based on the process sequence of Consolidation I

The component consists of three MEX layers made of PA6 DiCo CF with a total height of 3 mm and one layer of UD-tape on top of it. As shown in the figure, the component can be divided into 25 cells. Within a cell, the factors temperature T_{CR} and velocity ν remain constant, whereas the factor of the contact force F_c is gradually increased from 6 N to 30 N.

Close-ups of the selected cells from Figure 6-3 can be seen in Figure 6-4. For the evaluation of the 125 factor level combinations, a catalog of defects was created as shown in the same figure, which evaluates the consolidation results with a value from 1 to 10.

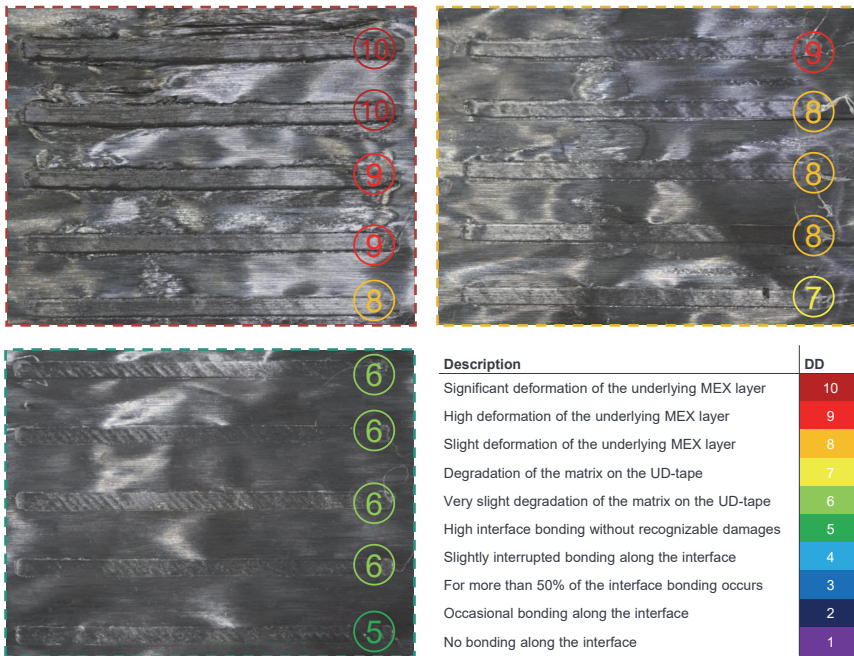


Figure 6-4: Close-up of selected consolidation tracks from Figure 6-3 and defect catalog with damage values for Consolidation I

If there is significant damage characterized by severe deformation of the MEX layers, the factor level combination is given a damage degree (DD) of 10. For values below 5, no damage is recognizable, but interruptions in the bonding at the interface between the UD-tape and the MEX layer are noticeable. With a value of 1, there is no bonding

at all. A value of 5 indicates the best consolidation result. The interface is fully consolidated and there are no interruptions in the bonding. A value of 6 - 7 means that slight damage (degradation) can be partially observed on the upper matrix layer of the UD-tape without deforming the MEX layer underneath. A value of 7 is therefore defined as the maximum acceptable damage limit. The value 4 is used as the lower limit, at which an almost complete bonding can be observed.

Evaluation of the Process Window Identification

An evaluation of all consolidation tracks from Figure 6-3 according to the error catalog can be found in Figure 0-1 in the Appendix. The factor levels as input variables and their corresponding damage values as output variables result in the regression function $S_{D,C1}(T_{CR}, F_C, v)$ in Equation 0-1 in the Appendix. A multidimensional polynomial of the third degree serves as the basis for the regression function. The damage model in the form of the regression function allows the damage values to be estimated as a function of factor values for which no experimental data is available.

Figure 6-5 on the right shows the output of the damage model for the analyzed factor level combinations in three-dimensional factor space. A comparison with the actual values on the left shows good accuracy with an average discrepancy of 0.3.

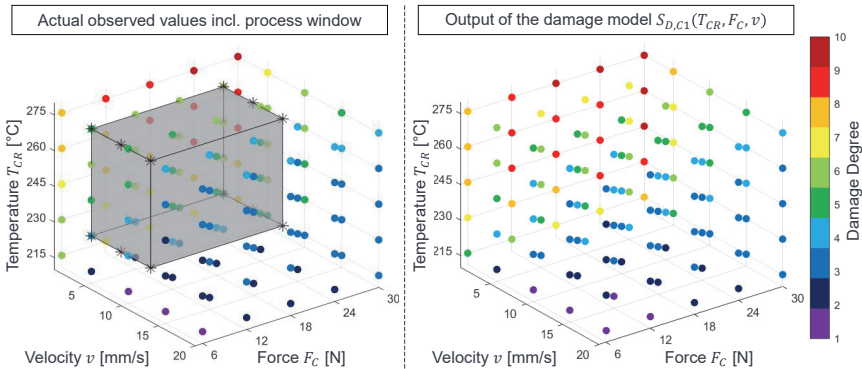


Figure 6-5: (Left) 3D representation of the damage actually observed for all factor level combinations of the tracks in Consolidation I incl. process window; (Right) calculated damage values based on modeling with regression function

The damage values for the factor level combinations and other aspects result in the process window for Consolidation I of the material system under consideration, represented by the grey box in Figure 6-5 on the left. As can be seen, the process window

mainly contains areas with damage values 4 - 6, i.e. where complete consolidation with continuous bonding without major damage is to be expected. The upper and lower values for the process window are shown in Table 6-3.

Table 6-3: Process window limits for Consolidation I of PA6 CoDiCo CF material system

Factor	Lower limit	Upper limit
Consolidation roller temperature T_{CR}	230 °C	275 - 300 °C
Contact force F_C	6 N	24 N
Velocity v	1 - 5 mm/s	13 mm/s

These limits serve as values for the factor levels of the experimental design in the following section. Values of individual factors may exceed these limits during optimization in Section 6.1.4 if, in combination with the values for the other factors, the value remains below 7 according to the damage model $S_{D,C1}(T_{CR}, F_C, v)$. The lower limit for the consolidation velocity v is regarded as a fixed limit value. This should not be set below 5 mm/s in order to guarantee an appropriate production time, even if the damage model allows it. For the consolidation roller temperature $T_{CR} = 300$ °C is the absolute upper limit and must not be exceeded, as the used PA6 starts to decompose above this temperature. For the contact force F_C , a lower value than the upper limit selected here should always be aimed for. Although relatively solid components can be assumed for the large-volume components considered in this study, if thin-walled areas and/or overhangs are consolidated, the forces selected here could cause damage.

The obtained damage model prevents unwanted damage, such as deformation of the MEX layer, but is only suitable for making qualitative statements about the degree of bonding D_b . In the following sections, a statistical design of experiments is therefore carried out with experimentally determined tensile shear strengths in order to quantitatively determine the degree of bonding D_b and optimize process parameters/factors.

6.1.2 Analysis of Global Variance

In the following, an analysis of variance (ANOVA) and statistical design of experiments are used to determine the significance, the effect and the interactions of the factors consolidation roller temperature T_{CR} , contact force F_C and velocity v on the target variable. The target variable is the maximum shear stress $\tau_{max,C1} = F_{max,C1}/A_C$ of the interface under consideration, as shown in the description of the test specimen in Figure 6-1, which occurs at the highest measured force $F_{max,C1}$ during the tensile tests. Tensile

tests are carried out with a ZwickRoell 10 kN RetroLine tensile machine based on the ASTM D5868-01 standard.

Experimental Design

The factor level combinations of the experiments are shown in Table 6-4. These are based on the process window limits defined in the previous section.

Table 6-4: Factor levels for the analysis of Consolidation I for the material system PA6 CoDiCo CF

Factor	First factor level (-)	Second factor level (0)	Third factor level (+1)
Temperature T_{CR}	230 °C	275 °C	-
Contact force F_c	6 N	24 N	-
Velocity v	5 mm/s	9 mm/s	13 mm/s

As a non-linear correlation is assumed for the consolidation velocity v based on experience from the previous experiments, three factor levels are used here. For the other two factors, only two factor levels are used in order to keep the experimental effort reasonable. This results in $n_f = 2^2 \cdot 3^1 = 12$ factor level combinations for a full factorial experiment.

The number of samples N_{C1} required can be estimated according to Kleppmann (2020, p. 29–30) using Equation 6-1.

$$N_{C1} = n_f \cdot n_{C1} \approx 60 \cdot \left(\frac{\sigma_{C1}}{\Delta\mu_{C1}} \right)^2 \quad 6-1$$

In order to obtain an estimate of the expected standard deviation σ_{C1} , the results of the preliminary tests for PA6 CF S2 are used (cf. Chapter 4.3.1.2, Figure 4-10). It is therefore assumed that $\sigma_{C1} = 0.7137$ MPa. For the effect $\Delta\mu_{C1}$ to be detected, an estimate is made. Shear stresses of 5 MPa are expected during the tensile shear tests. The technically relevant recognizable effect is set at 10 % of the expected maximum shear stress, which results in $\Delta\mu_{C1} = 0.5$ MPa. This results in a total number of samples of $N_{C1} = 122$. With $n_f = 12$, the number of samples per factor level combination is $n_{C1} = 10.2 \approx 11$.

Production of the samples for the individual factor level combinations was randomized. This means that the 11 samples per factor combination were not produced simultaneously in one production step. In one production step, up to 5 samples were produced

for 3 different factor level combinations. These results of the designed experiment are presented and evaluated below.

Results and Statistical Evaluation

The mean maximum shear stress $\bar{\tau}_{max,C1}$ for all 12 factor level combinations at 11 repetitions, including the standard deviation and variance, can be seen in Table 6-5. For a better overview, particularly good values are highlighted in dark green and particularly poor values in dark red.

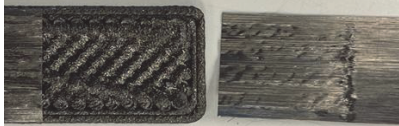


Table 6-5: Mean maximum shear stress $\bar{\tau}_{max,C1}$ based on ASTM D5868-01 from Consolidation I PA6 CoDiCo CF (based on (A_Beck 2024))

T_{CR}	F_C	v	Combination number	Mean value $\bar{\tau}_{max,C1}$	Standard deviation	Variance
230 °C	6 N	5 mm/s	1	0,921 MPa	0,266 MPa	0,071 (MPa) ²
		9 mm/s	2	0,492 MPa	0,269 MPa	0,072 (MPa) ²
		13 mm/s	3	0,269 MPa	0,162 MPa	0,026 (MPa) ²
	24 N	5 mm/s	4	3,35 MPa	0,714 MPa	0,510 (MPa) ²
		9 mm/s	5	1,357 MPa	0,495 MPa	0,245 (MPa) ²
		13 mm/s	6	0,927 MPa	0,653 MPa	0,427 (MPa) ²
275 °C	6 N	5 mm/s	7	3,662 MPa	0,572 MPa	0,327 (MPa) ²
		9 mm/s	8	2,948 MPa	0,832 MPa	0,693 (MPa) ²
		13 mm/s	9	0,468 MPa	0,158 MPa	0,025 (MPa) ²
	24 N	5 mm/s	10	4,06 MPa	0,749 MPa	0,562 (MPa) ²
		9 mm/s	11	2,851 MPa	0,941 MPa	0,886 (MPa) ²
		13 mm/s	12	1,462 MPa	0,871 MPa	0,758 (MPa) ²

As expected, the highest values for $\bar{\tau}_{max,C1}$ and therefore the highest degree of bonding D_b occur at the highest consolidation roller temperature T_{CR} and contact force F_C as well as the lowest velocity v . A general trend can be recognized that higher standard deviations can be seen at higher contact force. This could be due to slight damage to the UD-tape. According to the previously introduced damage model, these factor level combinations have an increased damage value but are still accepted. It could also be the case that at higher forces, the force control quality is not the same as at lower forces, due to the compressibility of the air used. Possible improvements to the Consolidation Unit are therefore discussed in the final outlook of the thesis.

A visual evaluation of the samples after failure in the tensile test has shown that 3 modes of failure generally occur. Examples of this can be seen in Table 6-6, the numbering and corresponding factor level combination are listed in Table 6-5.

Table 6-6: Failure modes and corresponding factor level combination (based on (A_Beck 2024))

Failure mode	Combination no.	Image
Interface failure	1, 2, 3, 5, 6, 9, 12	
Fiber breakage/in-interface failure	4, 7, 8, 10, 11	
Interlaminar MEX layers failure	7, 10 (For $U_E = 68$ RPM)	

Complete interface failure occurs for the factor level combinations with a $\bar{\tau}_{max,C1}$ of significantly less than 2.8 MPa (e.g. numbers 1 - 3). This indicates that the degree of bonding is not sufficient. For factor level combinations with approximately 2.8 MPa $< \bar{\tau}_{max,C1} < 3.4$ MPa (e.g. numbers 4, 8, and 11), fiber breakage is increasingly observed. This indicates a high degree of bonding, as the fibers break before debonding and are therefore strongly utilized. In the third failure mode, no failure occurs in the interface under consideration, but a failure occurs between the second and third MEX layers. As this type of failure indicates a very high degree of bonding, but no useful values can be calculated for $\bar{\tau}_{max,C1}$, such samples are regarded as outliers. This type of failure occurred sporadically and randomly for factor level combinations number 7 and 10, i.e. for those with the highest $\bar{\tau}_{max,C1}$ values. In order to obtain 11 reliable samples in each case, the extruder was slightly over-extruding at $U_E = 75$ RPM (instead of $U_E = 68$ RPM) during MEX layer production to ensure better adhesion between the layers. This measure changes the results to mainly fiber breakage and partial interface failure for the factor level combination 7 and 10.

For further statistical evaluation, it is checked whether the measured results of the tests have a normal distribution, as this, in particular, is a requirement for the following significance analysis. Figure 6-6 therefore shows the histogram (left) and probability plot

(right) of the test results for $\bar{\tau}_{max,C1}$ from Consolidation I. Like the histogram, the probability plot allows the assumption of a normal distribution of the measurement results, even if slight deviations from the normal distribution of measurements can be observed.

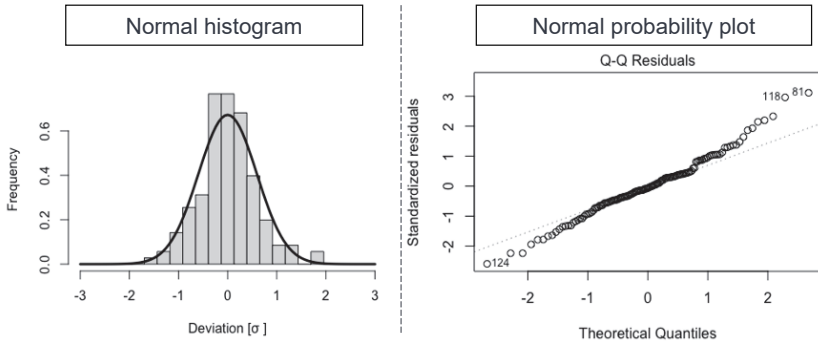


Figure 6-6: Histogram and probability plot for $\bar{\tau}_{max,C1}$ show that a normal distribution for Consolidation I can be assumed (based on (A_Beck 2024))

As a normal distribution is present, a significance test is performed for the measured results for $\bar{\tau}_{max,C1}$. In order to analyze whether the effects found with the experiments are significant, a null hypothesis is set up and a significance level is selected. In this case, the usual value of 5 % is selected. The null hypothesis states that the effect does not influence the target variable $\bar{\tau}_{max,C1}$. Significance level describes the probability that the null hypothesis will be falsely rejected. With this null hypothesis and the selected significance level, an effect could be assumed with a probability of 5 % that is not actually present. If the p-value is below the significance level, the null hypothesis can be rejected and the effect is significant. The significance values (p-values) calculated for the experiments of Consolidation I are shown in Table 6-7.

Table 6-7: Significance analysis of the factors and their combinations for Consolidation I PA6 CoDiCo CF (based on (A_Beck 2024))

	T_{CR}	F_C	ν	$T_{CR}:F_C$	$T_{CR}:\nu$	$F_C:\nu$	$T_{CR}:F_C:\nu$
p-value	$< 2 \cdot 10^{-16}$	$1.13 \cdot 10^{-12}$	$< 2 \cdot 10^{-16}$	$5.47 \cdot 10^{-5}$	$9.31 \cdot 10^{-9}$	0.000969	$6.93 \cdot 10^{-5}$
Significance	***	***	***	***	***	***	***

For a p-value below 0.05, the effect of the factor is significant. If the p-value is below 0.001, this is labeled in the last column with " *** ", which means that it is highly significant. The significance value is well below the significance level 0.05 for all factors and

their combinations. The null hypothesis can therefore be rejected and it can be concluded that all factors have significant effects on $\bar{\tau}_{max,C1}$ and therefore on the degree of bonding D_b .

In addition to the significance analysis, the main effects are calculated based on the calculated maximum mean shear stresses $\bar{\tau}_{max,C1}$ from Table 6-5 and are shown in Figure 6-7.

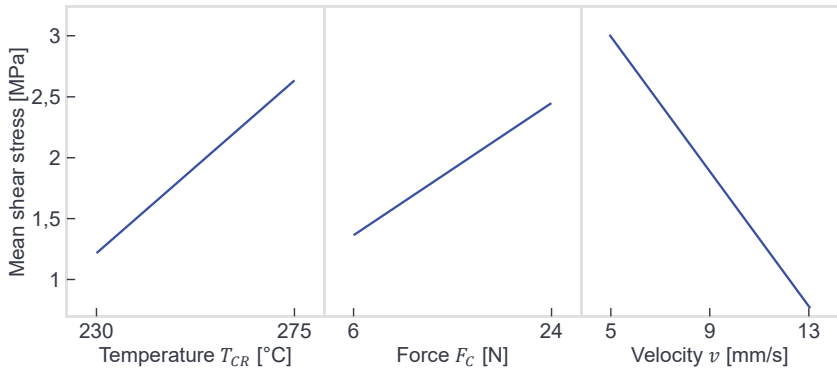


Figure 6-7: Main effect diagrams of Consolidation I PA6 CoDiCo CF

As expected from the significance analysis, all factors show a noticeable effect. Velocity has the greatest effect in the defined process window. That means, that at higher consolidation velocity v , $\bar{\tau}_{max,C1}$ and thus D_b decrease significantly. The assumed non-linear relationship between v and the maximum mean shear stress $\bar{\tau}_{max,C1}$ cannot be confirmed in this diagram. An increase in consolidation roller temperature T_{CR} or contact force F_C also causes an increase in D_b . However, the effect of the force is smaller.

Figure 6-8 shows the interactions between the factors. All factors have interactive effects, whereby both weakening and partially strengthening effects can be observed. It is noticeable that the increase in contact force F_C at high consolidation roller temperature T_{CR} has only a small effect on $\bar{\tau}_{max,C1}$. This can also be seen when comparing factor level combination numbers 7 and 10 in Table 6-5, where the increase in F_C from 6 N to 24 N only results in a relatively small increase in $\bar{\tau}_{max,C1}$.

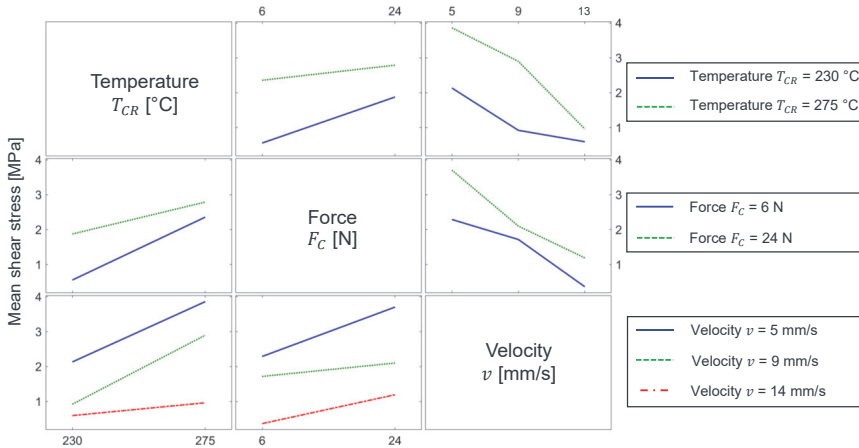


Figure 6-8: Interaction diagrams of Consolidation I PA6 CoDiCo CF (based on (A_Beck 2024))

The diminishing effect of the contact force F_C on $\bar{\tau}_{max,C1}$ as the consolidation temperature roller T_{CR} rises can be seen more clearly in Figure 6-9.

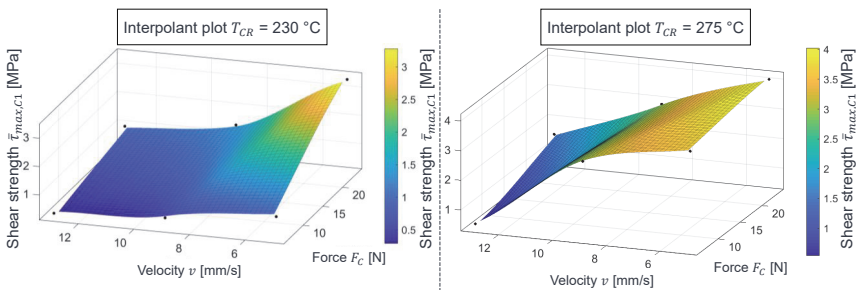


Figure 6-9: Spline-interpolant plots of $\bar{\tau}_{max,C1}$ for $T_{CR} = 230 \text{ }^\circ\text{C}$ and $275 \text{ }^\circ\text{C}$

The figure shows two simple plots of $\bar{\tau}_{max,C1}$ from Table 6-5 as an interpolation function over the contact force F_C and velocity v for $T_{CR} = 230 \text{ }^\circ\text{C}$ and $275 \text{ }^\circ\text{C}$ respectively. At $230 \text{ }^\circ\text{C}$, an increase in force at $v = 5 \text{ mm/s}$ results in a noticeable increase of $\bar{\tau}_{max,C1}$. The comparison with the plot for $275 \text{ }^\circ\text{C}$ shows that an increase in force at $v = 5 \text{ mm/s}$ has only a very small effect. This correlation is essential for the optimization in Chapter 6.1.4, as reducing the force in this range can reduce the damage (see damage model in Chapter 6.1.1) without significantly reducing $\bar{\tau}_{max,C1}$.

As a result of the statistically validated experiments, a better understanding of the process is available and the significance, effects and interactions of the individual factors are known. This understanding of the process is applied to the optimization of process parameters/factors in Chapter 6.1.4. Before the optimization is carried out, a consolidation model is created in the following chapter based on the data obtained.

6.1.3 Consolidation I Modeling

Equation 6-2 shows the consolidation model, which provides an estimate of the achievable shear stress $\tau^*_{max,C1}(T_{CR}, F_C, v)$ depending on the selected process variables/factors.

$$\begin{aligned} \tau^*_{max,C1}(T_{CR}, F_C, v) &= -17.3103 \text{ MPa} + 0.0805 \frac{\text{MPa}}{^\circ\text{C}} \cdot T_{CR} + 0.3614 \frac{\text{MPa}}{\text{N}} \cdot F_C + 0.7618 \frac{\text{MPa}}{\frac{\text{mm}}{\text{s}}} \cdot v \\ &- 0.001 \frac{\text{MPa}}{^\circ\text{C} \cdot \text{N}} \cdot T_{CR} \cdot F_C - 0.0038 \frac{\text{MPa}}{^\circ\text{C} \cdot \frac{\text{mm}}{\text{s}}} \cdot T_{CR} \cdot v - 0.0041 \frac{\text{MPa}}{\text{N} \cdot \frac{\text{mm}}{\text{s}}} \cdot F_C \cdot v \\ &- 0.0014 \frac{1}{(\frac{\text{mm}}{\text{s}})^2} \cdot v^2 \end{aligned} \quad 6-2$$

$$T_{CR} \in [215 \text{ }^\circ\text{C}; 300 \text{ }^\circ\text{C}]; F_C \in [6 \text{ N}; 30 \text{ N}]; v \in [2 \text{ mm/s}; 13 \text{ mm/s}];$$

A multidimensional polynomial function serves as the basis for the regression function, which is fitted using least squares with the data from the experiments in Table 6-5. A first-degree polynomial is used for the consolidation roller temperature T_{CR} and the contact force F_C and a second-degree polynomial is used to model the influence of the velocity. Due to the relatively small amount of learning data of only 12 factor combinations, including their associated output variables, the model is very simple and produces acceptable results with an average deviation of 0.41 MPa compared to the training data.

A visualization of the output of the model is shown in Figure 6-10. The model has poor model quality in areas with factor combinations that cause a low energy input (low force and temperature at high velocity). For $\tau^*_{max,C1}(210 \text{ }^\circ\text{C}, 4 \text{ N}, 14 \text{ mm/s}) \approx -0.81 \text{ MPa}$ is calculated, which is not feasible from a purely physical point of view. For factor combination ranges with high energy input, the model provides reasonable outputs up to a certain limit. The limit values for the factors given in Equation 6-2 consider the range of application of the model.

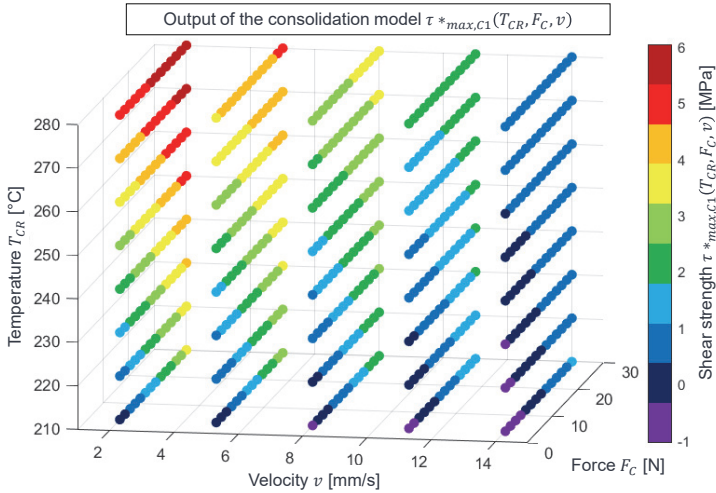


Figure 6-10: Output of the consolidation model $\tau^{*max,C1}(T_{CR}, F_C, v)$ for Consolidation I PA6 CoDiCo CF

The consolidation model alone is not suitable for finding optimized process parameters/factor values with regard to maximum shear stress due to its simplicity in the form of the low polynomial degree, owing to relatively little measurement data. Eventual local maxima cannot be determined in this way, only the global optimization direction. As described in Figure 6-2, the consolidation model, in combination with the process window and considering the damage model, enables the efficient identification of optimized parameters. The procedure for this is described in the next section.

6.1.4 Experimental Optimization of Consolidation I

With the previously introduced consolidation model $\tau^{*max,C1}(T_{CR}, F_C, v)$, considering the maximum acceptable damage limit $S_{D,C1}(T_{CR}, F_C, v) < 7$ and the relevant limits from the defined process window, the search for optimal process parameters for Consolidation I can be described with Equation 6-3.

$$\begin{aligned} & \max_{T_{CR}, F_C, v} \left(\tau^{*max,C1}(T_{CR}, F_C, v) \right) \\ & \text{subject to: } S_{D,C1}(T_{CR}, F_C, v) < 7, \\ & 230 \text{ }^\circ\text{C} \leq T_{CR} \leq 300 \text{ }^\circ\text{C}, 6 \text{ N} \leq F_C \leq 24 \text{ N}, v \geq 5 \text{ mm/s} \end{aligned} \tag{6-3}$$

In principle, this optimization problem could be solved purely mathematically, but in reality, this would lead to only limited optimization of the process parameters/factors. As mentioned in the previous section, the consolidation model does not include any potential local maxima in the process window under consideration. As an alternative to mathematical optimization, the statistical design of experiments offers sequential optimization methods. These generally provide a dynamic test plan, which is iteratively adapted after experiments have been carried out and new results are available. Examples of such experimental optimization procedures are the method of the steepest ascent or evolutionary algorithms (Kleppmann 2020, p. 295–300). However, as these can lead to relatively complex experimental designs and have to be adapted to the constraints given here, such as compliance with the damage limit, these optimization methods are considered too complex for this case. The method used here to determine optimized process parameters can be regarded as a hybrid approach. Using the generated mathematical models, obtained process knowledge is used and only necessary experiments are carried out to determine optimized process parameters. This means that fewer experiments are required compared to purely sequential optimization methods. The aforementioned considerations are incorporated into the optimization steps described below.

Optimization Steps

1. Based on the analysis of the main effects in Chapter 6.1.2 (cf. Figure 6-7), the factor with the highest effect is selected. Considering the defined process window (see Chapter 6.1.1, Table 6-3), this factor is set so that $\tau_{*max,C1}$ is maximized. In the present case, this results in $v = 5$ mm/s.
2. The factor with the smallest effect according to the main effect diagram is minimized (cf. Figure 6-7), considering the limit of the process window. The intention behind this is that the factor with the second largest effect, the temperature T_{CR} , can thus be increased further, considering the allowed limits based on the damage model. As shown in Figure 6-9 in Chapter 6.1.2, increasing the force F_C at high temperatures has only a minor effect. This observation is utilized here. It also ensures that the process parameters/factors identified with a low contact force F_C , can also be used for thin-walled components, as described in Chapter 6.1.1. Finally, two relatively low values for F_C are selected to take account of any non-linear effects. In this case, this means that $F_{C,1} = 6$ N and $F_{C,2} = 15$ N.

3. With the damage model and the previously defined values for $F_{C,i}$ and $v = 5$ mm/s, the maximum permissible value for T_{CR} can be determined using $S_{D,C1}(T_{CR}, F_{C,i}, 5 \text{ mm/s}) = 7$. This results in $T_{CR,1} = 292 \text{ }^\circ\text{C}$ and $T_{CR,2} = 280 \text{ }^\circ\text{C}$.

4. In the last step before an experimental verification, the theoretically achievable shear stresses are calculated using the consolidation model. This results in:

$$\tau^*_{max,C1,1} (292 \text{ }^\circ\text{C}, 6 \text{ N}, 5 \text{ mm/s}) = 4.59 \text{ MPa}$$

$$\tau^*_{max,C1,2} (280 \text{ }^\circ\text{C}, 15 \text{ N}, 5 \text{ mm/s}) = 4.24 \text{ MPa}$$

Since both theoretically calculated values are higher than the actual highest experimentally measured value $\bar{\tau}_{max,C1} = 4.06 \text{ MPa}$ for $275 \text{ }^\circ\text{C}$, 24 N and 5 mm/s (cf. Table 6-5), the associated process parameters are considered suitable for searching an optimum.

5. As the quality of the consolidation model is limited, experiments are carried out in the final step for the factor combinations found in order to verify them. This is done according to the same procedure as in Chapter 6.1.2, based on the ASTM D5868-01 standard (cf. Figure 6-1) to identify experimentally the maximum tensile shear stresses of the interfaces. In each case, 11 repetitions are carried out.

Evaluation of the Optimization Results

The experimental results of the two optimized factor combinations can be seen in Table 6-8 under numbers 2 and 3.

Table 6-8: Comparison of optimized and non-optimized factor combinations

No.	T_{CR}	F_C	v	Calculated $\tau^*_{max,C1}$	Mean value $\bar{\tau}_{max,C1}$	Standard deviation
1	275 °C	6 N	5 mm/s	3.65 MPa	3.662 MPa	0.572 MPa
2	292 °C	6 N	5 mm/s	4.59 MPa	4.03 MPa	0.475 MPa
3	280 °C	15 N	5 mm/s	4.24 MPa	3.846 MPa	0.410 MPa
4	275 °C	24 N	5 mm/s	4.4 MPa	4.06 MPa	0.749 MPa

Numbers 1 and 4 are shown here as a reference from the previous experiments (cf. Table 6-5). It can be seen that the values $\tau^*_{max,C1}$ calculated according to the consolidation model do not correspond exactly with the experimentally determined values $\bar{\tau}_{max,C1}$, but the tendency is correct. A comparison of the optimized results of number 2 and the previously determined highest values of number 4 provides practically identical values for $\bar{\tau}_{max,C1}$ given the relatively high standard deviations. Since the optimized process parameters/factors of number 2 require a much lower force F_C and this was one

of the objectives of the optimization, the result can be considered a significant improvement.

The optimization is hereby concluded. Presumably, higher values for $\bar{\tau}_{max,c1}$ could be found by further iterations of the described hybrid optimization procedure, but since the value for $\bar{\tau}_{max,c1}$ seems to converge slightly above 4 MPa, the additional effort is not considered appropriate. In principle, a further increase of $\bar{\tau}_{max,c1}$ is possible if this has the highest priority. For this purpose, the limit value for v can be removed, which, however, results in considerably increased production times. When going through the 5 steps of the hybrid optimization procedure, with the difference that in step 2 $F_c = 6$ N and $T_{CR} = 275$ °C are specified, the damage model yields $v = 2.6$ mm/s. In the experimental execution this results in $\bar{\tau}_{max,c1} = 4.318$ MPa with a standard deviation of 0.671 MPa.

Optimal Process Parameters for Consolidation I

Based on the systematic analysis of Consolidation I, starting with the definition of the process window, the creation of a damage model, the statistical analysis of the factors and the derivation of a consolidation model, optimized process parameters were identified, considering the boundary conditions. **For the validation tests in Chapter 7, the factor values $F_c = 6$ N, $T_{CR} = 292$ °C and $v = 5$ mm/s shown in Table 6-8 are used.** In the following section, Consolidation II is analyzed according to a similar approach.

6.2 Optimization of Consolidation II

The objective is to identify optimized process parameters for Consolidation II under consideration of boundary conditions and to develop a better understanding of the overall process. The basic procedure is the same as for Consolidation I described in Chapter 6.1 and is therefore not described in detail here.

Specimen Design, Production and Test Procedure

The same specimen shape and test standard ASTM D5868-01 as for Consolidation I are used to determine the maximum shear stress in the interface. The difference to Consolidation I lies in the production of the specimens. As can be seen in Figure 6-11,

the structure of the specimen is turned upside down during the manufacturing in Consolidation II compared to Consolidation I (cf. Figure 6-1).

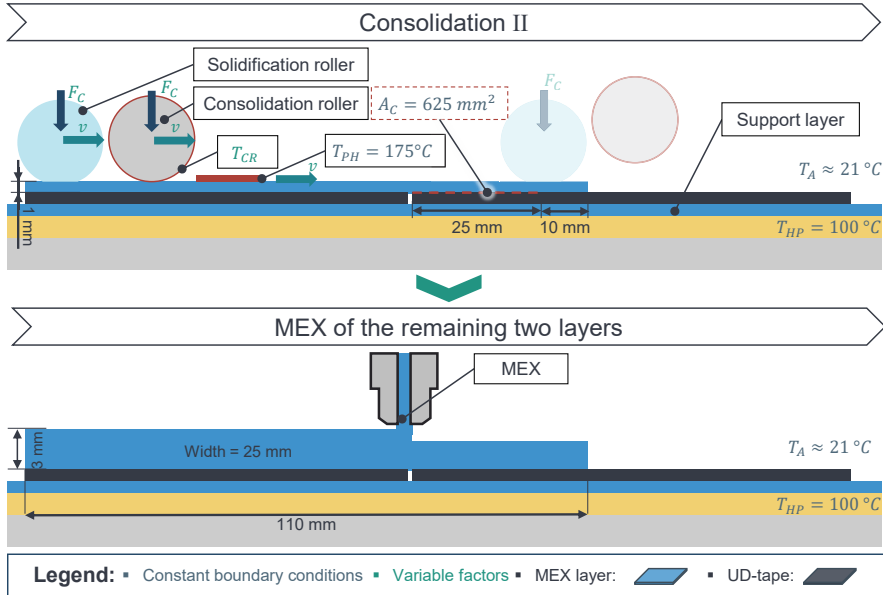


Figure 6-11: Sample dimensions based on (ASTM D5868-01) for the tensile shear tests; Constant and variable factors and motion sequence during Consolidation II

The two UD-tapes are first attached to a support layer, which is not part of the specimen but is only used for the manufacturing process. After that the two UD-tapes are overprinted with a 1 mm layer using the MEX process. Consolidation II then follows the same procedure as Consolidation I. In the final step, two more layers are printed using the MEX process as shown to obtain the desired sample shape.

Based on the results of the preliminary tests in Chapter 4.3.1.2 (shown in Figure 4-10) for an almost identical PA6 CoDiCo CF material system, it is reasonable to assume that Consolidation II will only have a minor effect. For this reason, after identifying a suitable process window in Chapter 6.2.1, only a shortened variance analysis is carried out to determine whether there is a significant effect of Consolidation II at all. As it shown in the subsequent section that no sufficient effect could be identified, the analysis and further optimization of the process parameters for Consolidation II was discontinued. The relevant results leading to this conclusion are explained below.

6.2.1 Process Window Identification and Damage Modeling

The process window for Consolidation II was determined in the same way as for Consolidation I (cf. Chapter 6.1). For the three variable factors consolidation roller temperature T_{CR} , contact force F_C and velocity v , upper and lower limits were defined based on literature data from comparable processes, manufacturer data and individual test runs. Due to the high range of the values, five factor levels with constant intervals were selected for sufficient resolution. In order to consider the interaction between the factors, they are all combined with each other, resulting in $5^3 = 125$ combinations.

Experimental Execution

The 125 combinations were tested on the component (600 mm edge length) shown in Figure 6-12 with 100 mm long consolidation tracks, according to the procedure and boundary conditions of Consolidation II as shown in Figure 6-11.

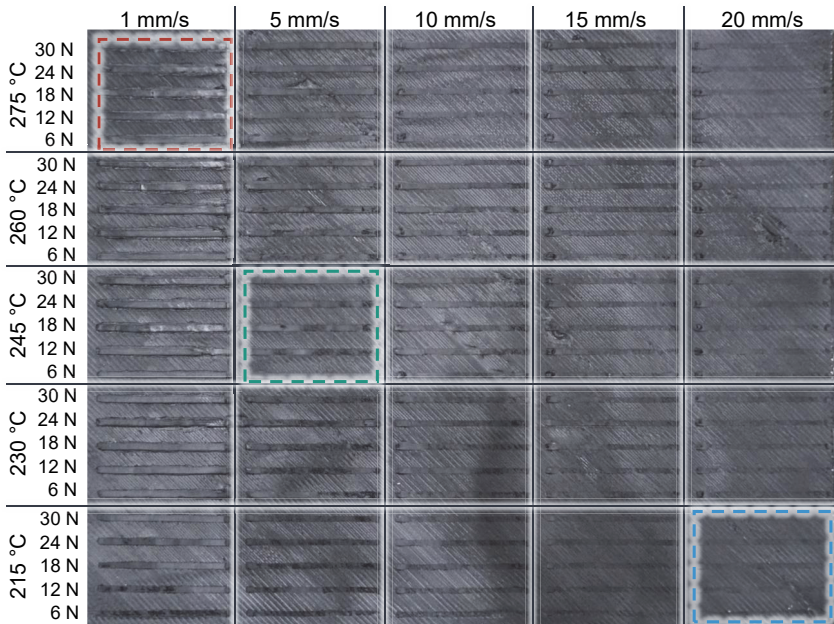


Figure 6-12: 100 mm long consolidation tracks carried out with all 125 factor level combinations of the consolidation roller temperature T_{CR} , contact force F_C and velocity v based on the process sequence of Consolidation II

Compared to Consolidation I, the component is produced upside down. As can be seen in the figure and equivalent to the first step shown in Figure 6-11, a 1 mm upper MEX layer was printed on a UD-tape and then consolidated. A catalog of defects was created according to the same procedure as for Consolidation I. This is shown in Figure 6-13.

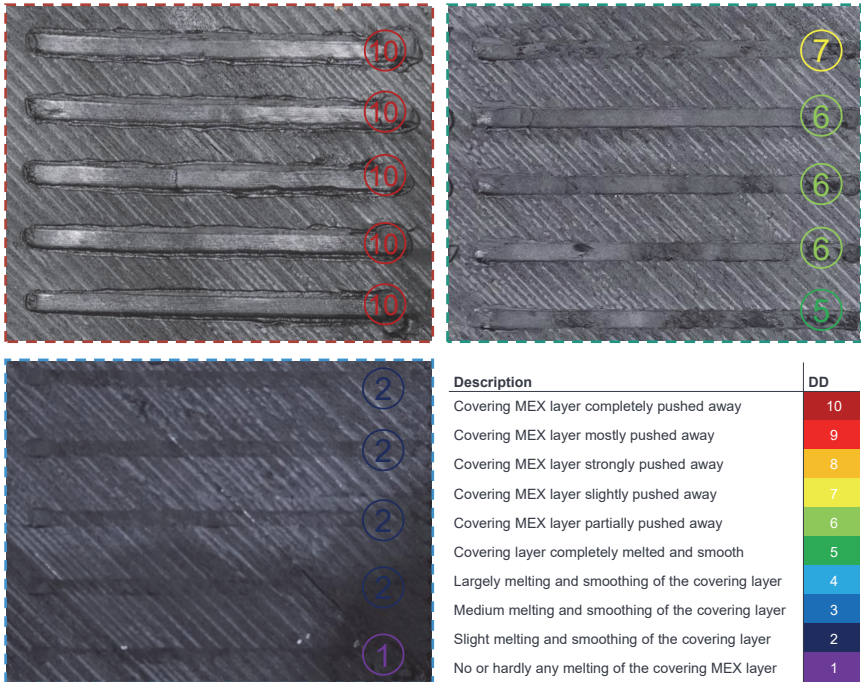


Figure 6-13: Close-up of selected consolidation tracks and defect catalog with damage degree for Consolidation II

Overall, it can be seen that damage occurs more quickly compared to Consolidation I because consolidation takes place directly on the MEX layer without any UD-tape in between. It should be mentioned that a very good adhesion of the MEX layer to the UD-tape can be observed with all process parameters. An evaluation of all 125 consolidation tracks can be found in Figure 0-2 in the Appendix.

Evaluation of the Process Window Identification

A three-dimensional visualization of the damage as a function of the process parameters/factors can be seen on the left in Figure 6-14. A comparison with the process window for Consolidation I in Figure 6-5 shows that the process window for Consolidation II is somewhat smaller. This is due to the fact that Consolidation II only shows signs of consolidation from approx. 245 °C onwards.

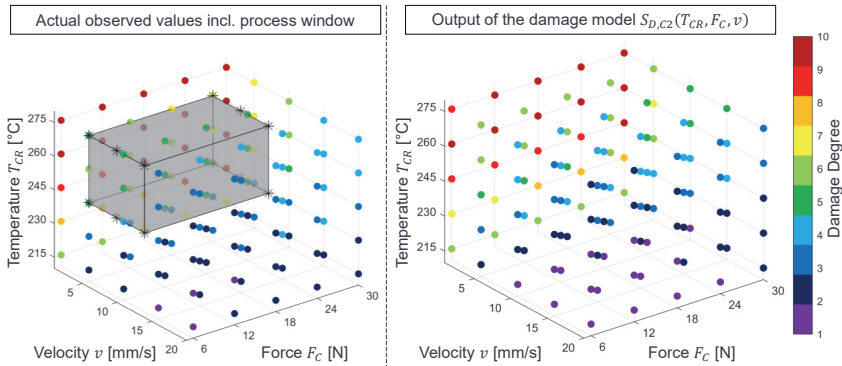


Figure 6-14: (Left) Three-dimensional representation of the damage actually observed for all factor level combinations of the tracks in Consolidation II incl. process window; (Right) Calculated damage values based on modeling with regression function

Considering the same boundary conditions as for Consolidation I, the upper and lower limits for the factors are shown in Table 6-9. As with Consolidation I, the consolidation roller temperature T_{CR} can generally be increased up to 300 °C, as PA6 only starts to decompose from this point onwards if no damage is to be expected in combination with the other factors. The velocity can also be reduced to $v = 1$ mm/s if no damage is to be expected. However, as this prolongs the process extremely, a lower limit of 5 mm/s is set.

Table 6-9: Process window limits for Consolidation II of PA6 CoDiCo CF material system

Factor	Lower limit	Upper limit
Consolidation roller temperature T_{CR}	245 °C	275 - 300 °C
Contact force F_c	6 N	24 N
Velocity v	1 - 5 mm/s	13 mm/s

For the sake of completeness, the damage model $S_{D,C2}(T_{CR}, F_C, v)$ for Consolidation II was determined and is shown on the right in Figure 6-14. As no optimization is carried out for Consolidation II, the damage model is no longer used. $S_{D,C2}(T_{CR}, F_C, v)$ is created analog to $S_{D,C1}(T_{CR}, F_C, v)$ and is based on a multidimensional polynomial regression function of the third degree. Since $S_{D,C2}(T_{CR}, F_C, v)$ is not used any further, it is not discussed in detail.

The result of the process window identification, shown in Table 6-9, could be used to determine suitable factor levels setting up a full factorial test plan and statistical evaluation, as for Consolidation I. However, as described in the following section, this was not carried out after no significant effect of Consolidation II was found.

6.2.2 Analysis of Variance

Since the results in Chapter 4.3.1.2 suggested that Consolidation II possibly does not have a significant effect on the transferable shear stress in the interface, this is verified experimentally. The achievable maximum shear stresses $\bar{\tau}_{max,C2}$ of consolidated and non-consolidated specimens as shown in Figure 6-11 based on the ASTM D5868-01 standard are compared for this purpose.

Experimental Design

A factor level combination with the values $F_C = 24$ N, $T_{CR} = 275$ °C and $v = 5$ mm/s was used for the consolidated samples. According to the process window and the damage model, these values are on the edge of damaging the composite and should therefore lead to good consolidation result. To estimate the required number of samples per test series, the Equation 4-1 introduced in Chapter 4.3.1.2 and comparative values for the expected standard deviation $\sigma = 0.429$ MPa, from Figure 4-10 for PA6 CF S3, are used. As for Consolidation I, the effect to be recognized is set to $\Delta\mu = 0.5$ MPa. This results in a total number of samples of $N = 44$, i.e. 22 repetitions per test series (consolidated and non-consolidated).

Results and Statistical Evaluation

The results for the mean shear stresses $\bar{\tau}_{max,C2}$ obtained in the interface area are shown in Table 6-10.

Table 6-10: Mean maximum shear stress $\bar{\tau}_{max,C2}$ based on ASTM D5868-01 from Consolidation II PA6 CoDiCo CF (based on (A_Beck 2024))

T_{CR}	F_C	v	Mean value $\bar{\tau}_{max,C2}$	Standard deviation	Variance
Without Consolidation II			2.72 MPa	0.222 MPa	0.049 (MPa) ²
275 °C	24 N	5 mm/s	2.61 MPa	0.43 MPa	0.185 (MPa) ²

At first glance, the consolidation even appears to have a slightly negative effect on the shear stress with a reduction of $\bar{\tau}_{max,C2}$ by 0.11 MPa. However, this value could be purely coincidental, as the number of samples analyzed is based on the assumption that an effect of $\Delta\mu = 0.5$ MPa should be detected and not just 0.11 MPa. In order to avoid having to produce further samples, a significance analysis is carried out below.

Before the significance analysis is carried out, it is checked whether there is a normal distribution for the results of $\bar{\tau}_{max,C2}$. As shown in the histogram and the probability plot in Figure 6-15, a normal distribution can be assumed and significance test can be performed.

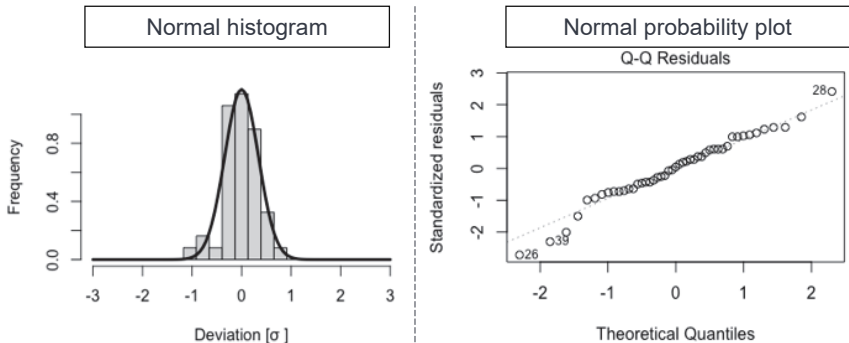


Figure 6-15: Histogram and probability plot for $\bar{\tau}_{max,C2}$ show that a normal distribution for Consolidation II can be assumed (based on (A_Beck 2024))

The null hypothesis is defined with the claim that Consolidation II has no influence on the target value of the maximum mean shear stress $\bar{\tau}_{max,C2}$, with the significance level set at 0.05. A significance test of the results yields a p-value of 0.241. Thus, the significance value is above the significance level of 0.05 of the null hypothesis. Consequently, the null hypothesis is confirmed and there are no significant, relevant differences between consolidated and non-consolidated samples.

Optimal Process Parameters for Consolidation II

From the results it can be concluded that Consolidation II does not improve the degree of bonding D_b within the selected process window. However, it is assumed that by opening the lower limit of the velocity v , the degree of bonding could still be improved.

A positive effect could possibly be achieved by reducing v up to the damage threshold. However, as this is only to be expected with an extreme reduction of v , the production times would be disproportionately long for a presumably only minor positive effect. Therefore, no investigations were carried out in this regard.

From the results, it can be further concluded that, at least for the PA6 CoDiCo CF material system under consideration, Consolidation II does not lead to any significant improvement in the degree of bonding D_b under the given boundary conditions. However, this statement cannot be generalized for all material systems. As the preliminary tests in Chapter 4.3.1.2 have shown, Consolidation II had a higher effect on other material systems. The Consolidation II process could also presumably deliver better effects under other boundary conditions. For example, a reduction in the height of the MEX layer above the UD-tape that is present during Consolidation II could have a positive influence. This could yield in a better heat transfer to the relevant interface. Alternatively, the preheating temperature of the IR-heater could be increased. Based on the thermal simulations in Chapter 4.3.2.3 (see Figure 4-25), the preheating temperature T_{PH} should be set to approx. 275 °C at this MEX layer height above the UD-tape. However, as described in the beginning of Chapter 6, this was only set to $T_{PH} = 175$ °C due to focusing problems with curved and rough surfaces of the specimens, which can lead to local temperature jumps and therefore damage to the materials. The further development of the control concept of the IR-heater could solve this problem, whereby Consolidation II could theoretically also be used for higher MEX layer heights.

A positive effect that can be observed in these experiments is the relatively high value of $\bar{\tau}_{max,C2} \approx 2.70$ MPa (see Table 6-10), which results from the Overprinting alone. The following section therefore examines whether a higher degree of bonding D_b between the UD-tape and the MEX layer can be achieved by adjusting the extrusion parameters during the MEX process while Overprinting the UD-tape.

6.3 Optimization of Overprinting

As described in Chapter 4.3.1 (see Figure 4-4), Overprinting is a main process step of the hybridization strategies S1 - S4 and is therefore used when the UD-tape should be covered with MEX-layers. The results from the previous section for Consolidation II show no effect in the defined process window, at least for the material system under consideration and the given boundary conditions. Therefore, the following section examines whether the shear strength and thus the degree of bonding D_b can be increased by adjusting the extrusion parameters in the MEX process.

As shown in Chapter 6.1.3, the temperature, the force - or more specifically the pressure - and the consolidation velocity all have a significant effect on the degree of bonding D_b . The movement velocity of the single-screw extruder during Overprinting would have to be reduced to expect a positive effect on D_b . In order not to increase the manufacturing time unnecessarily, this option is not considered. The temperature of the extruder can only be changed slowly due to the high thermal inertia. Increasing the temperature only for one overprinting layer of the UD-tape is highly inefficient due to the additional heating and cooling phase. Increasing the pressure in the MEX process can be achieved by varying different process variables without significantly increasing the production time. For the following investigation, an attempt is therefore made to increase the degree of bonding D_b by increasing the pressure during material extrusion.

In the MEX process, the process parameters extrusion Temperature T_E , rotational extruder speed U_E , extruder velocity v_E , the layer height L_H and generally the trajectory, i.e. the print pattern, influence the pressure that is created in the material in the outlet area of the nozzle. The pressure can be adjusted most effectively by changing U_E . In the following section, the actual effect of this on the considered material system and the given boundary conditions are examined.

6.3.1 Pressure Build-Up During Over-Extrusion

In order to ensure that a significant increase in pressure is actually possible by changing rotational extruder speed U_E , i.e. over-extrusion, corresponding tests were carried out with pressure measurement films (FUJIFILM PRESCALE High Temperature, Super Low Pressure). The results can be seen in Figure 6-16.

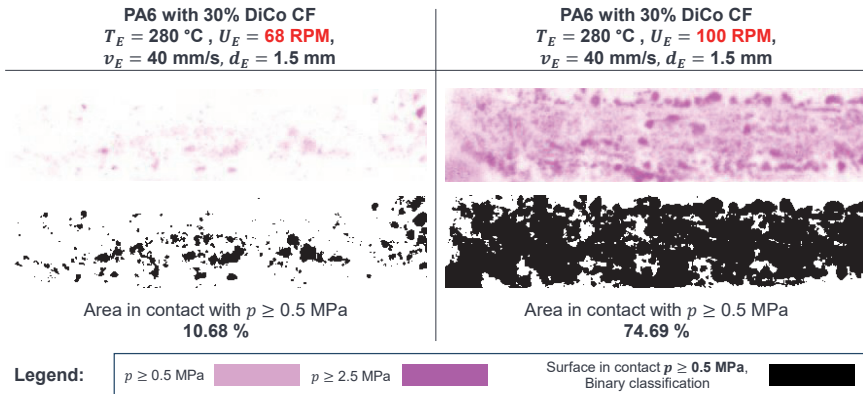


Figure 6-16: Comparison of the resulting pressure when Overprinting measurement films at 68 RPM and 100 RPM

Monotonous straight lines with 45° to the longitudinal direction of the samples and 100 % density were extruded on the print measurement film with a layer height of 1 mm and a heated bed temperature of $T_{HP} = 100\text{ °C}$ using the MEX process on approx. 50 mm · 10 mm areas. This was carried out with otherwise constant process parameters once at $U_E = 68\text{ RPM}$, which corresponds to the ideal rotational speed for a good printing result, and at $U_E = 100\text{ RPM}$, which corresponds to considerable over-extrusion. The rotational speed could be increased even further, but over-extrusion leads to problems such as decreasing dimensional accuracy, and is therefore not increased any further. Other relevant parameters are listed in the Figure 6-16.

The comparison of the discoloration of the pressure measurement films in Figure 6-16 for $U_E = 100\text{ RPM}$ and $U_E = 68\text{ RPM}$ shows a noticeable effect. With the pressure-measuring film pressures from 0.5 MPa on can be detected. For $U_E = 68\text{ RPM}$, this is only the case for 10.68 % of the overprinted area according to a binary analysis. The binary evaluation converts the scan of the pressure measurement film into a black and white image and checks what percentage of the surface is discolored. At $U_E = 100\text{ RPM}$, however, a pressure greater than 0.5 MPa is detected for 74.69 % of the area. The more intensive discoloration of the pressure measurement film also indicates pressures of theoretically more than 2.5 MPa. However, the pressure measurement foils are only intended for an application range of up to 220 °C and the extruder temperature

was set at $T_E = 280$ °C. Therefore, the intensity of the discoloration cannot be used to make any reliable statements about the actual pressure that has occurred.

6.3.2 Effect Analysis of Over-Extrusion

As the increase of U_E for the given boundary conditions and the material system under consideration actually leads to an increase in pressure during Overprinting, the effect on the degree of bonding is examined below. For the tests, the maximum mean shear stress $\bar{\tau}_{max,OP}$ based on the ASTM D5868-01 standard is used, as in Consolidation I and II. The specimens are basically produced in the same way as for Consolidation II (see Chapter 6.2, Figure 6-11), but without the use of the consolidation. The first MEX layer, i.e. the Overprinting of the UD-tape, is printed with $U_E = 100$ RPM and the two following layers with $U_E = 68$ RPM.

Experimental Design

Comparison samples are produced at $U_E = 68$ RPM throughout. The results without consolidation in Chapter 6.2.2 are used here, as these were produced under these required conditions. Equation 4-1 is used to estimate the number of samples. The effect to be recognized is set to $\Delta\mu = 0.5$ MPa, as in Consolidation I and II. The standard deviation $\sigma = 0.222$ MPa is taken from the results for $U_E = 68$ RPM without consolidation (see Chapter 6.2.2, Table 6-10). This results in the total number of samples $N = 11.616 \approx 12$, and the number of samples per rotational speed variant $n = 6$. However, as 22 samples were already produced and analyzed for $U_E = 68$ RPM in the previous tests, 22 samples are also produced for $U_E = 100$ RPM.

Results and Evaluation

The results for the maximum mean shear stress $\bar{\tau}_{max,OP}$ based on the ASTM D5868-01 standard are shown in Table 6-11. An increase in $U_E = 68$ RPM produces a recognizable effect of an increase in $\bar{\tau}_{max,OP}$ of approx. 0.5 MPa. A significance analysis is not carried out due to the noticeable higher number of repetitions than actually necessary. The effect is therefore not considered to be random.

Table 6-11: Mean maximum shear stress $\bar{\tau}_{max,OP}$ from Overprinting PA6 Co CF with PA6 DiCo CF based on ASTM D5868-01

U_E	Mean value $\bar{\tau}_{max,OP}$	Standard deviation	Variance
68 RPM	2.72 MPa	0.222 MPa	0.049 (MPa) ²
100 RPM	3.23 MPa	0.31 MPa	0.076 (MPa)²

Presumably, increasing the speed, also in combination with changing other process parameters, could result in a further increase in $\bar{\tau}_{max,OP}$. However, since the actual print quality already decreases at $U_E = 100$ RPM, increasing the rotational speed is associated with further disadvantages. In addition to the geometric inaccuracy within the layer with the over-extrusion, this error is transferred to other subsequent layers. Besides further geometric deviations, damage can also occur due to increased material accumulation which then can collide with the nozzle.

Optimal Process Parameters for Overprinting

Overprinting with $U_E = 100$ RPM is considered to be largely optimized and is used for the final validation tests in the following Chapter 7 for sample production.

6.4 Conclusion of the Experimental Optimizations

Based on a systematic experimental investigation, optimized parameters for the newly developed hybridization process of PA6 CoDiCo CF material system were determined with the aid of the experimental system developed. In addition to simultaneously gaining an understanding of the process, an efficient procedure for determining optimized process parameters was identified for Consolidation I in particular, which can also be transferred to other material systems. Investigations into Consolidation II have shown that this has no effect under the given boundary conditions. Overprinting was optimized and it was shown that Overprinting can also lead to an increase in the degree of bonding of the interface through targeted over-extrusion. In order to validate the results of the optimization, final validation tests are carried out in the following Chapter 7 using the process parameters obtained.

7 Validation and Evaluation

As the newly developed process and the associated experimental system should enable the individualization and individual production of CoDiCoFRP with a high output rate and automation level, the validation is subdivided. With the commissioning of the experimental setup in Chapter 5 and the production of test components in Chapter 6, it has already been shown that individual production, i.e. production according to the basic principle of additive manufacturing, is possible. Therefore, for individual production, only the results of the process parameter optimization are further validated in the following Chapter 7.1. For this purpose, the achieved reinforcement effect and its improvement are analyzed. The subsequent Chapter 7.2, examines whether the optimized process parameters obtained can be transferred to the subsequent individualization of thermoplastic components made from a similar material system. In addition, a simple demo component is produced to demonstrate the possibilities of subsequent individualization.

7.1 Validation of the Optimized Process Parameters

In order to obtain quantitative values for the reinforcement effect and to validate the newly developed hybridization process for CoDiCo material systems, tensile tests are carried out using the (DIN EN ISO 527-4) standard. The tests are carried out in such a way that it is simultaneously shown that the optimizations of the process parameters carried out in Chapter 6 lead to an increase in the mechanical properties.

Design of Experiments

The specimen shape used is based on Type B from the (DIN EN ISO 20753) standard and has a length of 80 mm and a width of 10 mm. Due to investigations of varying Co-fiber content and layer structures, different component heights are used. The samples are produced based on the hybridization strategy S2 (see Chapter 4.3.1.2, Figure 4-4). This means that the Co-fiber portion, i.e. UD-tape, is located in the middle of the sample and is surrounded by MEX layers. Thus, the process steps Consolidation I and Overprinting are used in the sample, which means that both can be examined simultaneously. The process parameters relevant to the two process steps used to produce the samples are shown in Table 7-1.





Table 7-1: Relevant optimized process parameters of the experiments carried out in this chapter for the process steps Consolidation I and Overprinting

	Process parameter	Description	Value
Consolidation I	T_{PH}	Surface IR-preheating temperature	175 °C
	T_{HP}	Temperature heated bed	100 °C
	T_{CR}	Temperature of consolidation roller	292 °C
	v	Velocity of consolidation and solidification roller	5 mm/s
	F_C	Contact force roller perpendicular to the surface	6 N
Overprinting	T_{HP}	Temperature heated bed	100 °C
	T_E	Temperature single screw extruder	280 °C
	v_E	Velocity of the Extruder during material direct extrusion	40 mm/s
	U_E	Single screw extruder rotational speed	100 RPM
	L_H	Layer height during material direct extrusion	1 mm

These process parameters are based on the results of the experimental optimization in the previous chapter. Except for the Overprinting of UD-tapes at $U_E = 100$ RPM, the layers are printed with the extruder at $U_E = 68$ RPM. For the print pattern, monotone straight lines at 45 ° to the longitudinal direction of the samples at 100 % density are used for all layers. The same material system was used as in Chapter 6. PA6 with 30% DiCo CF was used for the matrix consisting of the MEX layers. The Co component consists of the UD-tapes with PA6 matrix and 43 % CF fiber volume content (see Table 4-1, Chapter 4.2.1). This yields a PA6 CoDiCo CF material system.

Table 7-2 shows the four different layer structures investigated as well as the resulting heights and the resulting percentage of Co-fiber volume fraction φ_F .

Table 7-2: Different layer structures for the specimens based on (DIN EN ISO 20753) as well as relevant properties and mechanical characteristics

	Type 1	Type 2	Type 3	Type 4
Layer structure				
Height	4 mm	4.16 mm	5.32 mm	4.32 mm
Co φ_F	0 %	1.65 %	2.59 %	3.19 %
E_{th}	3.724 GPa	7.470 GPa	9.580 GPa	10.930 GPa
$R_{FRP, ,th}$	61.3 MPa ($=R_{FRP, ,re}$)	151.5 MPa	194.6 MPa	222.1 MPa

The Co-fiber content φ_F is calculated in the same way as in Chapter 4.3.1.3 using Equation 4-3. This allows the calculation of the theoretical E-modulus $E_{FRP,||,th}$ based on Equation 2-1 and subsequently the calculation of the theoretical tensile strength





$R_{FRP,||,th}$ based on Equation 2-2. Specimen structure type 1 without Co-fibers (UD-tape) serves as a reference for determining the reinforcement effect and because no Co-fibers are integrated, the theoretical strength also corresponds to the real measured strength. Equation 4-1 from Chapter 4.3.1.2 is used to estimate the number of samples for comparing two types to each other with relative statistical certainty. Normal stresses of 150 MPa are expected. The technically relevant recognizable effect is set at 10 % of the expected normal stress, which results in $\Delta\mu = 15$ MPa. To estimate the standard deviation, five samples each of type 1 and 2 were pre-tested using the tensile test. The larger standard deviation of $\sigma = 8.9$ MPa was obtained for type 2. This standard deviation results in a number of $n = 10.56 \approx 11$ repetitions per sample type.

For type 2, the test series is carried out an additional time with the non-optimized process parameters for Consolidation I with $T_{CR} = 275$ °C, $F_C = 6$ N and $v = 9$ mm/s and Overprinting at $U_E = 68$ RPM. According to the findings in Chapter 6, these lead to a lower transmissible shear stress in the interface area, which should ultimately lead to poorer utilization of the Co-fibers and poorer reinforcement effect. The aim of this additional test is to show that optimizing the process parameters actually leads to an increase in strength.

Evaluation and Results

The results of the achieved tensile strengths $R_{FRP,||,re}$ and the associated standard deviations σ are shown in Table 7-3.

Table 7-3: Achieved tensile strengths $R_{FRP,||,re}$ and standard deviations σ based on (DIN EN ISO 527-4) and the resulting degree of fulfillment D_F for specimen types 1- 4

	Type 2 non-opt.	Type 2 optimized	Type 3	Type 4
Layer structure				
$R_{FRP, ,re}$	82.2 MPa	97.0 MPa	131.1 MPa	117.6 MPa
σ	8.81 MPa	9.16 MPa	5.79 MPa	11.57 MPa
D_F	57 %	64 %	67 %	53 %

In order to obtain a quantitative statement about the reinforcement effect, the degree of fulfillment D_F is determined using Equation 4-2, as in Chapter 4.3.1.3. This indicates how much of its theoretical strength $R_{FRP,||,th}$ the FRP has achieved. The theoretical strengths for all 4 types are listed in Table 7-3. For all types 1 - 4 and for type 2 with non-optimized parameters, the results are shown in Figure 7-1.

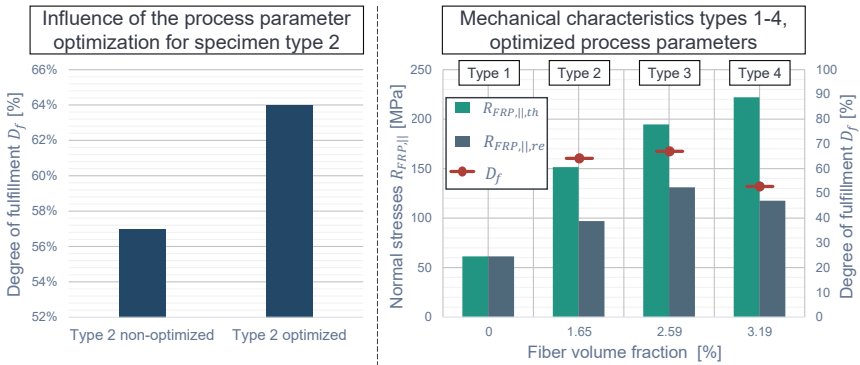

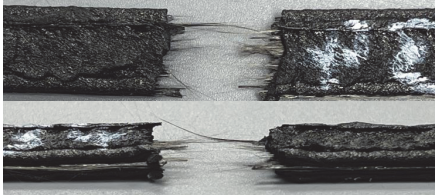


Figure 7-1: (Left) Degree of fulfillment for optimized and non-optimized process parameters using specimen type 2; (Right) Mechanical characteristics for specimen type 1 - 4 for optimized process parameters (based on (A_Beck 2024))

With the non-optimized process parameters, the result for type 2 is $R_{FRP,||,re} = 82.2$ MPa and $D_F = 57$ %. The comparison with the value for the optimized parameters of type 2 $R_{FRP,||,re} = 97$ MPa and $D_F = 64$ % shows a noticeable difference. It can therefore be concluded that optimizing the process parameters as described in Chapter 6 leads to an increase in the reinforcement effect.

The results for specimen types 1 - 4 produced with the optimized process parameters are shown in Figure 7-1 on the right. In addition to the theoretical strength $R_{FRP,||,th}$ and the actual strength $R_{FRP,||,re}$ from the mean values of the tensile tests according to (DIN EN ISO 527-4), the resulting degree of fulfillment D_F is shown. A degree of fulfillment $D_F = 64$ % is achieved for type 2 (optimized). As shown in the illustration in Table 7-3, only one UD-tape was used, as a result of which the Co-fiber volume fraction φ_F is only 1.65 %. For the investigation of higher fiber volume fractions, the specimens of type 3 and 4 each have two UD-tapes. Type 4 shows an increase in strength $R_{FRP,||,re}$ compared to type 2, but the degree of fulfillment D_F is noticeably lower at 53 % compared to 64 %. The second UD-tape was applied by Consolidation I onto the first UD-tape. This results in a very high fiber volume fraction in a relatively small area, which is approx. 43 % (the same as the Co-fiber volume fraction of the UD-tape itself). It is assumed that the matrix, the MEX layer made of PA6 DiCo CF, cannot transfer the forces sufficiently into the Co-fibers of the UD-tape due to the relatively small interface area. This assumption is confirmed by the mode of failure shown in Table 7-4.

Table 7-4: Classification of specimen types 1 - 4 produced with optimized process parameters according to the most frequent mode of failure (based on (A_Beck 2024))

Failure mode	Sample type	Image
Delamination	Type 4	
Fiber breakage	Type 2 Type 3	

With type 4, delamination mainly occurs, i.e. the MEX matrix layer detaches from the UD-tape. For types 2 and 3, fiber breakage occurs for the most part and delamination occurs only occasionally. The forces are therefore better transferred from the surrounding matrix MEX layer to the UD-tape with types 2 and 3, which means that the Co-fibers of the UD-tape are better utilized, which leads to fiber breakage. The highest degree of fulfillment of $D_F = 67\%$ is achieved with specimen type 3. Here, there are also two UD-tapes within the specimen, but there is an additional MEX layer between the two UD-tapes. Compared to type 4, there is therefore a larger interface area between the Co-fibers of the UD-tape and the matrix made of MEX layers. The forces are therefore better transferred to the Co-fibers in type 3 and the reinforcement effect of the Co-fibers is better utilized.

Conclusion for the Optimized Process Parameter

The values achieved for the degree of fulfillment of $D_F = 64\%$ for type 2 and $D_F = 67\%$ for type 3 are above the state of the art (cf. analysis in Chapter 4.3.1.3). The process developed and experimental setup in the context of this work is therefore suitable for individual production of reinforced CoDiCoFRP. Comparison between non-optimized process parameters and optimized parameters for the production of type 2 specimens shows that optimizing the process parameters results in an increase from $D_F = 57\%$ to $D_F = 64\%$. The process for optimizing the process parameters carried out and developed in Chapter 6 has thus been validated.

7.2 Validation of Subsequent Individualization

In addition to the individual production of FRP according to the principle of additive manufacturing, the objective defined in Chapter 3.1 is also the subsequent individualization of FRP components. This generally refers to the subsequent individualization of thermoplastic components that are produced using conventional manufacturing processes. The individualization can include the application of UD-tapes according to different load cases or the MEX 3D printing of individual structures onto the component. This is interesting for components that are produced in large quantities but may have slightly different variants. With conventional manufacturing processes, in such cases either several slightly different press molds have to be produced at great expense, or expensive flexible press tools are required.

The following sections therefore examine whether a component from an exemplary conventional manufacturing process can be subsequently individualized using the developed system and process. First, the application of Consolidation I is examined in Chapter 7.2.1. Subsequently, in Chapter 7.2.2, a demo component is used to show that further subsequent individualization is possible with the MEX process.

The LFT-D process, explained in Chapter 2.1.3.2, is used as a reference for a conventional manufacturing process for the production of large-volume FRP components with DiCo long fibers. PA6 with CF is also used as the material system in order to be able to transfer the previous findings as far as possible.

7.2.1 Application of Consolidation I for Subsequent Individualization

Figure 7-2 shows an LFT sheet with an edge length of 300 mm and a thickness of 3 mm produced using the LFT-D process.

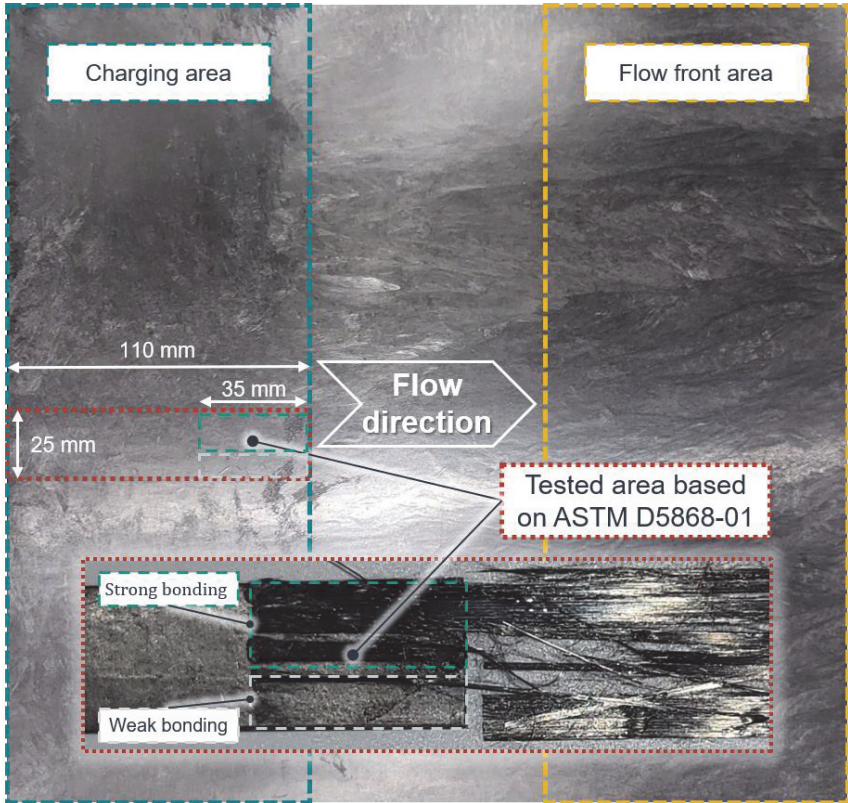


Figure 7-2: Based on (ASTM D5868-01) analyzed areas of an LFT sheet made of PA6 DiCo long CF

For the production of the LFT sheet PA6 and DiCo long carbon fibers were used. Compared to the material used for MEX DES 3D printing in the previous chapters, the fibers are noticeably longer. The fibers in the granulate used for the MEX DES process have a length in the millimeter range or even shorter, whereas the fibers in the LFT-D process used here can be in the centimeter range. This results in noticeably different thermal

properties, particularly in terms of thermal conductivity. The average fiber volume fraction in the LFT sheet under consideration is approx. 20 % by volume, but varies greatly within the component. In the charging area, i.e. where the LFT plastificate is inserted in the mold (cf. Figure 7-2 on the left), the fiber volume percentage is usually the highest. Along the flow front, which is formed when the press is closed and the plastificate is displaced, the fiber volume percentage decreases. In addition, the fiber volume percentage also fluctuates perpendicular to the flow front because the inserted plastificate already has an uneven internal fiber distribution. Figure 7-2 also shows that the fibers are mostly aligned along the flow direction.

Design of Experiments

To examine whether the Consolidation I process for hybridizing MEX layers and UD-tapes can also be used for LFT sheets, samples were produced in accordance with the (DIN EN ISO/ASTM 52900) standard using the same principle as in Chapter 6.1 (see Figure 6-1) for MEX layers. As shown in Figure 7-2 as an example, 110mm · 25 mm areas were cut out and the samples for the shear tests were produced based on the standard. This was carried out in parallel for the charging area and for the area in which the flow front aligned the fibers more evenly. As for the experiments in Chapter 6.1.2, 11 samples were produced for each area. The process parameters used are shown in Table 7-5. These were determined using an iterative approach by increasing them step by step until recognizable damage was detected.

Table 7-5: Process parameters used for the Consolidation I process with LFT specimens

Process parameter	T_{PH}	T_{HP}	T_{CR}	v	F_c
Description	Surface IR preheating temperature	Temperature heated bed	Temperature of compactions or consolidation roller	Velocity of consolidation and solidification roller	Contact force roller perpendicular to the surface
Value	175 °C	150 °C	275 °C	2.5 mm/s	6 N

In comparison to Chapter 6.1, these are not optimized process parameters, but a high degree of bonding can generally be expected along the damage limit. The main difference to consolidation with MEX layers is the noticeable higher heated bed temperature $T_{HP} = 150$ °C. $T_{HP} = 100$ °C chosen for MEX layers is a compromise in order to have suitable boundary conditions for MEX 3D printing. These restrictions do not apply here. In addition, the consolidation velocity v had to be reduced from 5 mm/s to 2.5 mm/s

compared to the MEX layers in order to achieve a subjectively satisfactory consolidation result. The 5 mm/s was selected as the lower limit when consolidating MEX layers in order to avoid unnecessarily prolonging the entire production process. This limitation was not set here, as only a few consolidation steps are assumed in the subsequent individualization and the total time required is therefore reduced.

Evaluation and Results

The results for the maximum mean shear stress $\bar{\tau}_{max,C1S}$ resulting from Consolidation I for subsequent individualization can be seen in Table 7-6.

Table 7-6: Results of the shear tests based on (DIN EN ISO 20753) for Consolidation I of LFT sheets

Mechanical characteristics	Charging area	Flow front area
$\bar{\tau}_{max,C1S}$	2.58 MPa	4.175 MPa
Standard deviation	1.19 MPa	1.18 MPa

It is evident that there is a considerable difference between the specimens in the two areas of the LFT sheet. This is due to the explained strongly fluctuating fiber volume fraction between the two areas, as well as the different fiber orientations, which result in different thermal properties. However, there are also strong fluctuations within the areas, as can be seen from the very high standard deviations. The 11 samples per area are spread vertically to the direction of flow in the respective area. As can be seen on the example specimen in Figure 7-2, that even in the small interface area there can be strong fluctuations in the bonding achieved. In the area with weak bonding, the UD-tape showed almost no bonding in the tensile tests, whereas the other area led to increased fiber breakage due to the good bonding.

Figure 7-3 illustrates how subsequent individualization is carried out with Consolidation I for more complex components. The Robotic Swing Folding developed by Kupzik (2022) produces the near net shape preforms from UD-tapes and places them on the component. These are then consolidated with the Consolidation Unit. Inclines of 45° - 60° are possible.

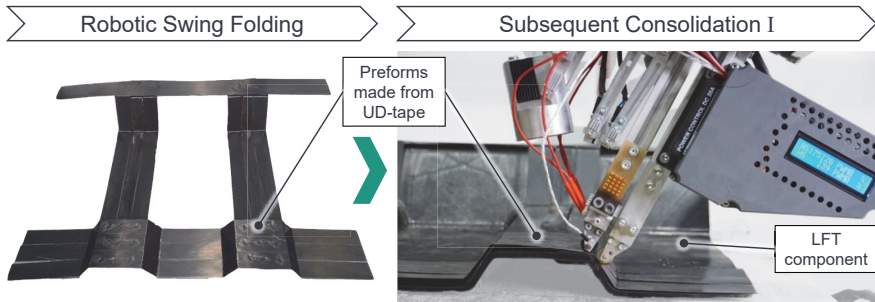


Figure 7-3: Three-dimensional subsequent reinforcement of LFT components with preformed UD-tapes using Robotic Swing Folding

Conclusion for the Subsequent Individualization and Reinforcement

In general, the results show that Consolidation I is also suitable for the subsequent individualization of components manufactured using conventional methods. However, the process parameters must be adapted compared to consolidation with MEX layers despite the similar material system. Additional problems arise due to the selected LFT-D process, which leads to uneven fiber distribution in the production of such sheets. It's likely that larger LFT components could yield more consistent consolidation results with smaller fluctuations, as they allow for longer flow paths and achieve a more uniform fiber distribution. Presumably, the subsequent individualization with Consolidation I of components produced with other selected conventional processes is easier. This could be the case with injection molding, where shorter DiCo-fibers are typically employed for reinforcement. Consequently, thermal properties similar to layers produced with the MEX process can be expected.

The process parameters determined for Consolidation I for subsequent individualization are used in combination with the additive MEX process in the following section, to demonstrate further individualization possibilities.

7.2.2 Additive Subsequent Individualization

In the previous section, it was shown that subsequent individualization in the case of local reinforcements using Consolidation I is possible with the developed experimental

system and process. This section will highlight the further potential of subsequent individualization through the use of the MEX DES.

Design of Experiments

Figure 7-4 shows an LFT sheet that has been subsequently individualized with functional three-dimensional structures using the MEX DES 3D printing.

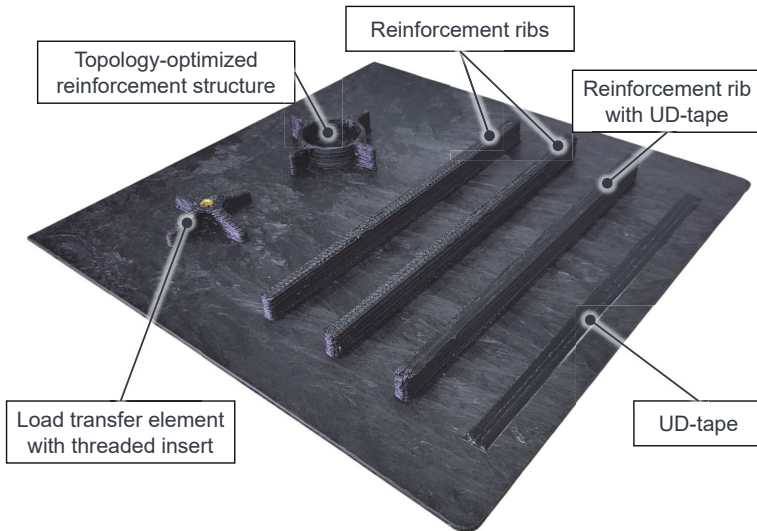


Figure 7-4: Subsequently customized LFT sheet using MEX DES 3D printing and Consolidation I

The LFT sheet was placed on the assembly area of the experimental system and the heated bed temperature was set to $T_{HP} = 100\text{ }^{\circ}\text{C}$. The extruder temperature was set to $T_E = 280\text{ }^{\circ}\text{C}$. Tests have shown that over-extrusion is necessary to ensure good adhesion between the LFT sheet and the MEX interface. The relationship between extruder speed U_E , over-extrusion and pressure build-up during direct extrusion was explained in Chapter 6.3. For this reason, the first layer of all structures was extruded at $U_E = 100\text{ RPM}$. All further layers were extruded at 68 RPM . The layer height is $L_H = 1\text{ mm}$.

Evaluation and Results

Figure 7-4 shows examples of structures for individualization. In addition to the manufacturing of simple reinforcement ribs, more complex topology-optimized structures can

also be printed. This makes it theoretically possible to customize components for different load cases. Due to the high output rate of the MEX DES, individualizations can be carried out in a time-efficient manner. In addition to reinforcement and stiffening structures, load transfer elements, for example, can also be printed. As shown in the figure, there is an additional thread insert in the load transfer element. Furthermore, customization with MEX DES 3D printing can also be combined with the consolidation process and UD-tape reinforcement as desired. An example of this can be seen in the figure using a rib that has also been reinforced with UD-tape.

Conclusion for the Additive Subsequent Individualization

From a geometric point of view, there are theoretically no limits to subsequent customization, especially because the experimental setup is also suitable for five-axis non-planar 3D printing. This means that even noticeably more complex components can be subsequently overprinted. **Additive subsequent individualization is therefore feasible.**

7.3 Conclusion of the Validation and Evaluation

The objective of this chapter was to validate the developed experimental system and the newly developed process with regard to the two fields of application of the subsequent individualization and individual production of CoDiCoFRP. Chapter 7.1 shows that a noticeable reinforcement of individually manufactured components, i.e. 3D printed components, is possible. For this purpose, tensile tests were carried out and the degrees of fulfillment D_F determined. In order to show that subsequent individualization and reinforcement are possible, tests were carried out in Chapter 7.2 with LFT components, which were selected as representatives of components produced using conventional manufacturing processes. The results showed that the process parameters must be adjusted to the properties resulting from the specific manufacturing process and that limitations are likely to be expected. In general, however, subsequent individualization is possible. The experimental system and process developed have therefore been validated for both fields of application.

8 Summary and Outlook

This chapter summarizes the research work in this thesis. The outlook presents improvement measures for a series application and possible future work.

8.1 Summary

Conventional manufacturing processes allow the economical production of DiCoFRP in large quantities. Process approaches for combining the advantages of Co and DiCo material systems into CoDiCoFRP exist, but are still immature, especially for thermoplastic material systems. Overall, these processes are not suitable for the production of individual components due to high tool costs. This work therefore shows how flexible production systems consisting of robotic kinematics and additive processes can be combined to enable subsequent individualization and individual production of CoDiCoFRP with a high output rate.

Based on the literature review in Chapter 2, conventional manufacturing processes and additive manufacturing processes for CoDiCoFRP were analyzed. In addition to identifying research gaps and questions, reference systems were identified and used to develop the new process and the experimental system. Based on the defined research questions, an objective and approach were defined in Chapter 3 in order to answer these. From the analysis of the state of the art and the motivation for a subsequent individualization and individual production of CoDiCoFRP with a high output rate and automation level, the following research questions were identified, which were systematically addressed in individual chapters.

1. What and how does a manufacturing process look like that enables the individualization and individual production of large CoDiCoFRP with a high output rate? Which process steps are required for the customized production of CoDiCo components?

Based on a FAST analysis according to VDI 2803, the required functions and associated subsystems were identified at the beginning of Chapter 4 order to identify a suitable process. The functions and associated subsystems were classified according to the PGE theory, which made it possible to better estimate and formalize the development effort. According to the theory, the Consolidation Unit and the Adjustable and Heated Assembly Table required the most development effort. For the other subsystems and

functions, it was possible to make greater use of reference systems from the state of the art. For example, a MEX DES was chosen for the flexible production of the DiCo part and the Robotic Swing Folding developed by Kupzik (2022) for the provision and handling of the Co part (UD-tapes). The function or process of hybridization of CoDiCo material systems of the subsystem Consolidation Unit was classified with the highest development effort according to the theory of PGE. Extensive preliminary investigations were carried out in the following Chapters 4.2 and 4.3 to identify a suitable hybridization process. In Chapter 4.2, process requirements were first determined using an Ishikawa diagram and reference systems. Subsequently, different hybridization processes were analyzed and evaluated with the help of experiments based on standards in Chapter 4.3.1. The hybridization processes were further investigated using thermal simulations in Chapter 4.3.2. The identified subsystems and associated function, main process steps Point Welding, Overprinting, Consolidation I and Consolidation II as well as a first initial understanding of the process served as the basis for the manufacturing process that enables the individualization and individual production of large CoDiCoFRP with high output rates.

2. What and how does a prototypical and experimental production plant look like in order to study the processes and explore their potential?

Suitable subsystems have already been pre-selected in chapter 4 and the requirements for the various process steps and functions have been defined. The individual subsystems that had to be newly developed for a prototypical experimental setup were presented in Chapter 5. These were developed based on the SPALTEN methodology. Before the functionality and special features of the individual subsystems developed were presented, a kinematic analysis was carried out at the beginning of Chapter 5.1. This allowed the arrangement of the overall experimental production system to be optimized and the required additional axes of subsystems to be identified. The established control architecture and the developed digital process chain were presented at the end of Chapter 5. In combination with the other subsystems, this represents the experimental production system. The system provides the necessary flexibility to allow further research into the newly developed process with different material systems.

3. How should the individual process steps and in particular the consolidation process be carried out to maximize the degree of bonding between the Co and DiCo parts?
4. How can optimal consolidation process parameters for the newly developed processes be determined for selected material systems in compliance with boundary conditions?

Based on the process knowledge and defined process steps from Chapter 4 as well as the experimental setup developed in Chapter 5, experiments were carried out in Chapter 6. The process steps Consolidation I and II as well as Overprinting were experimentally investigated and optimized for the selected material system PA6 CoDiCo CF. Various test standards were used for the investigations and to gain a better understanding of the consolidation process. The results were evaluated and analyzed using various statistical methods, such as significance analyses. Consolidation II was identified as ineffective, for the given boundary conditions and the considered material system. Consolidation I, on the other hand, was optimized using a hybrid approach based on process modeling and sequential experimental search. In the case of Overprinting, it was experimentally determined that over-extrusion leads to a higher degree of bonding. In addition to optimized process parameters for the hybridization and consolidation of the selected material system, a procedure for process parameter optimization was developed, which can also be transferred to other material systems.

5. What mechanical properties can the CoDiCoFRP achieve based on standardized tests for a selected material system?

In order to quantify the reinforcement effect and to validate the process parameters determined in Chapter 6, standardized tensile tests were carried out in Chapter 7.1 based on DIN 527-4. The degree of fulfillment D_F was determined in order to improve comparability, particularly as the absolute values of the tensile tests are heavily dependent on the Co-fiber content. A maximum degree of fulfillment of 67 % was determined. This roughly corresponds to the highest values that can currently be achieved with additive MEX processes with continuous fiber reinforcement from the state of the art.

In addition to determining the mechanical properties in Chapter 7.1, further validation tests were carried out in Chapter 7.2. These tests focused on the subsequent individualization of components manufactured using conventional production methods. The LFT-D process was chosen as a representative conventional manufacturing process. It was demonstrated that subsequent individualization is possible, but that adjustments to the resulting component properties using the conventional manufacturing process are necessary. These results, in combination with the developed experimental set-up in Chapter 5 and the experimental optimization in Chapter 6, ultimately validated the overall objective. A process and a prototype system were successfully developed for a subsequent individualization and individual production of CoDiCoFRP with a high output rate and automation level.

Further investigations and, in particular, optimization of the process for other material systems can be carried out. Further developments need to be carried out on the hardware, particularly for use in a serial operation for the subsequent individualization of components. A brief outlook is provided below.

8.2 Outlook

As part of this thesis, a process and experimental setup for the individual production and subsequent individualization of CoDiCoFRP with a high output rate and degree of automation was developed. The materials investigated were selected for the process due to their prevalence and availability on the market and their advantageous properties. When designing the hardware for the experimental setup, flexibility for future research was considered. The test setup is therefore suitable for investigating other material systems consisting of other fiber types and thermoplastics. In principle, all fiber types including natural fibers can be tested in combination with all thermoplastics. This means that in the future, the system can be used to manufacture individual components with other material systems, i.e. according to the principle of additive manufacturing from scratch. Examples of applications here could be customized bucket seats for the racing sector or for premium vehicles.

Furthermore, the system is suitable for investigations into the subsequent individualization of components manufactured using a wide variety of classic manufacturing processes for thermoplastics such as injection molded components. Investigations into the subsequent customization of LFT components can be continued. Existing LFT-D processes that enable the hybridization of DiCoFRP with UD-tapes during compression

molding have very expensive tools. Subsequent individualized reinforcement with UD-tapes can simplify the tools and reduce costs. The UD-tapes can also be placed optimized for other load cases. Further geometric customization is possible with the MEX DES. For example, vehicle components that have minor geometric differences in a vehicle series due to different equipment or motorization can still be produced with the same mold.

For use in series production, the digital process chain in particular would have to be developed further, as it currently requires a lot of manual input from the user for complex components. CAM systems with extensions for additive manufacturing and which allow hybrid process planning could be adapted for this purpose.

The LFT-D process was used to demonstrate and validate the subsequent individualization of components manufactured using conventional processes. In principle, the subsequent consolidation and overprinting of such LFT components is possible, but an approach still needs to be developed as to how fluctuating material properties, in particular fluctuating fiber volume fractions in the component, can be considered.

In general, the prototype hardware of the system can be further developed in order to be able to produce even more complex component shapes. In particular, the Consolidation Unit subsystem could be made more compact in further iterations. Direct integration of the consolidation and solidification rollers along adapted nozzles of the extruder would be conceivable. For this purpose, more compact voice coil motors could be used for the actuation instead of the currently complex pneumatic system. Further dimensioning around the required contact forces would be necessary for this. This could further improve the quality of force control and possibly reduce the higher standard deviations at higher consolidation forces (see Chapter 6.1.2). It may also be considered whether the temperature control can be further optimized together with the force control. For example, applying vibrations could further improve the consolidation. In combination with ultrasonic welding, the heating concept could therefore also be further optimized.

The overall system and control architecture could be simplified if another industrial robot were used for the kinematics of the Adjustable and Heated Assembly Table. However, there could be disadvantages due to the serial kinematics, which are less rigid than the parallel kinematics currently used. With the process knowledge now available, particu-

larly with regard to the necessary contact forces, a more precise dimensioning and assessment of the suitability of such a third industrial robot could be carried out. Alternatively, the overall structure could be simplified if only largely planar production in three-axis operation is sufficient or desired. In this case, the additional axes of the Adjustable and Heated Assembly Table could be generally omitted.

Furthermore, the experimental setup consisting of two cooperating industrial robots and a supporting kinematic system (Assembly Table) can be used universally and is not limited to the processing of thermoplastic materials. For this purpose, only the end-effectors need to be exchanged and the robot path planning adapted to the new process. It thus follows the basic concept of value stream kinematics, in which entire production flows are realized using uniform standard kinematics based on industrial robots (Mühlbeier & Gönzheimer et al. 2021). In consideration of volatile markets, increasing demand for customized products in small quantities and decreasing product life cycles, such flexible kinematic systems can meet the requirements for future production systems.

List of Own Publications

The publications listed below were created during the author's work as a research assistant at the wbk Institute of Production Science.

Baranowski, M.; **Matkovic, N.**; Kleim, S.; Friedmann, M.; Fleischer, J.; Springmann, M.; Middendorf, P.; Schäfer, A.; Waldhof, M. & Parspour, N. (2023), „Additive-Subtractive Process Chain for Highly Functional Polymer Components“, *International Journal of Mechanical Engineering and Robotics Research*, p. 339–346, DOI: 10.18178/ijmerr.12.6.339-346.

Mehner, M.; **Matkovic, N.**; Mühlbeier, E.; Mayer, D.; Fleischer, J. & Verl, A. (2023), „Evaluation of external control of KUKA Industrial Robots for laboratory and prototype environments“. *ISR Europe 2023. 56th International Symposium on Robotics, in cooperation with Fraunhofer IPA*. Stuttgart, Germany, September 26-27, 2023, Editors: Verl, A. & Kraus, W., VDE Verlag, Berlin, Germany, p. 278–284. ISBN: 978-3-8007-6140-1.

Matkovic, N.; Höger, K.; Friedmann, M.; Stamer, F.; Fleischer, J. & Lanza, G. (2023), „Identification of hybridization strategies for combining fused filament fabrication with unidirectional tape reinforcement“, *Composites Communications*, 38, DOI: 10.1016/j.coco.2022.101484.

Matkovic, N.; Kupzik, D.; Steidle-Sailer, C.; Friedmann, M. & Fleischer, J. (2022), „Novel Robot-Based Process Chain for the Flexible Production of Thermoplastic Components with CFRP Tape Reinforcement Structures“, *Procedia CIRP*, 106, p. 21–26, DOI: 10.1016/j.procir.2022.02.149.

Mühlbeier, E.; Oexle, F.; Gerlitz, E.; **Matkovic, N.**; Gönneheimer, P. & Fleischer, J. (2022), „Conceptual control architecture for future highly flexible production systems“, *Procedia CIRP*, 106, p. 39–44, DOI: 10.1016/j.procir.2022.02.152.

Springmann, M.; **Matkovic, N.**; Schäfer, A.; Waldhof, M.; Schlotthauer, T.; Friedmann, M.; Middendorf, P.; Fleischer, J. & Parspour, N. (2022), „Flexible and High-Precision Integration of Inserts by Combining Subtractive and Non-Planar Additive Manufacturing of Polymers“, *Key Engineering Materials*, 926, p. 268–279, DOI: 10.4028/p-ed900k.

Baranowski, M.; **Matkovic, N.**; Friedmann, M. & Fleischer, J. (2021), „3D-Druck für die Mobilität von morgen : Additiv-subtraktiver Prozess mit Inline-Prozessregelung für

hochfunktionale Kunststoffbauteile“, *wt Werkstattstechnik online*, 111 (11-12), p. 807–811, DOI: 10.37544/1436-4980-2021-11-12-37.

Matkovic, N.; Götz, M.; Kupzik, D.; Nieschlag, J.; Coutandin, S. & Fleischer, J. (2021), „Additives Roboter-Extrusions-System“, *VDI-Z*, 163 (01-02), p. 55–57, DOI: 10.37544/0042-1766-2021-01-02-55.

References

References according to the scheme (A_<surname> <year>) refer to student theses that were supervised by the author of this thesis in terms of content and organization.

(A_Garcia-Vasquez 2023)

Garcia-Vasquez, N. (2023), *Classification and evaluation of additive manufacturing of thermoplastic composites for fused deposition modeling*. Bachelor's thesis, Karlsruhe Institute of Technology, Karlsruhe, Germany, wbk Institute of Production Science. Guidance by: Matkovic, N.

(A_Davide 2021)

Davide, W. (2021), *Conceptual design, construction and virtual implementation of a consolidation unit as end effector of an industrial robot*. Master's thesis, Karlsruhe Institute of Technology, Karlsruhe, Germany, wbk Institute of Production Science. Guidance by: Matkovic, N.

(A_Söder 2023)

Söder, J. (2023), *Design of a heating System for fibre reinforcement 3D Printing with an Industrial Robot*. Master's thesis, Karlsruhe Institute of Technology, Karlsruhe, Germany, wbk Institute of Production Science. Guidance by: Matkovic, N.

(A_Hinze 2022)

Hinze, T. (2022), *Development and putting into operation of a moving print bed for the additive manufacturing of continuous fiber-reinforced components using articulated robots*. Master's thesis, Karlsruhe Institute of Technology, Karlsruhe, Germany, wbk Institute of Production Science. Guidance by: Matkovic, N.

(A_Kreusel 2022)

Kreusel, A. (2022), *Development of a methodology for the quality assurance of additive fibre-reinforced plastic components using computed tomography*. Bachelor's thesis, Karlsruhe Institute of Technology, Karlsruhe, Germany, wbk Institute of Production Science. Guidance by: Höger, K. and Matkovic, N.

(A_Kleinwort 2022)

Kleinwort, M. (2022), *Development of an end-effector for continuous fiber reinforcement of additively manufactured thermoplastic components using unidirectional tapes*. Master's thesis, Karlsruhe Institute of Technology, Karlsruhe, Germany, wbk Institute of Production Science. Guidance by: Matkovic, N.

(A_Teboul 2022)

Teboul, A. (2022), *Digital process chain development for non-planar additive manufacturing with 5DOF robotic arm*. Bachelor's thesis, Karlsruhe Institute of Technology, Karlsruhe, Germany, wbk Institute of Production Science. Guidance by: Matkovic, N.

(A_Kill 2022)

Kill, H. (2022), *Experimental investigation of short-fiber-reinforced thermoplastics for the hybridization of UD-tapes using the FFF-process*. Bachelor's thesis, Karlsruhe Institute of Technology, Karlsruhe, Germany, wbk Institute of Production Science. Guidance by: Matkovic, N.

(A_Buschulte 2022)

Buschulte, S. (2022), *Experimental investigation on the hybridization of UD-tapes using the FFF-method*. Bachelor's thesis, Karlsruhe Institute of Technology, Karlsruhe, Germany, wbk Institute of Production Science. Guidance by: Matkovic, N.

(A_Beck 2024)

Beck, E. (2024), *Experimental optimization of the consolidation process in continuous fiber reinforcement using unidirectional tapes in the FFF process*. Bachelor's thesis, Karlsruhe Institute of Technology, Karlsruhe, Germany, wbk Institute of Production Science. Guidance by: Matkovic, N.

(A_Larsch 2024)

Larsch, J. (2024), *Influence of additional kinematic freedoms on workspace expansion in multi-robot-systems*. Bachelor's thesis, Karlsruhe Institute of Technology, Karlsruhe, Germany, wbk Institute of Production Science. Guidance by: Matkovic, N.

(A_Tritschler 2023)

Tritschler, N. (2023), *Simulative sensitivity and parameter study of the consolidation process in fiber reinforcement in the FFF process*. Bachelor's thesis, Karlsruhe Institute of Technology, Karlsruhe, Germany, wbk Institute of Production Science. Guidance by: Matkovic, N.

(3DXTECH 2022a)

3DXTECH (2022), *Technical Data Sheet: AmideX™. PA6-GF30 3D Printing Filament*. URL: <https://www.3dxttech.com/products/> [Accessed: 01.08.2022].

(3DXTECH 2022b)

3DXTECH (2022), *Technical Data Sheet: CarbonX™. Carbon Fiber Nylon (Gen3) 3D Printing Filament*. URL: <https://www.3dxtech.com/products/> [Accessed: 01.08.2022].

(Agarwal & Kuchipudi et al. 2018)

Agarwal, K.; Kuchipudi, S. K.; Girard, B. & Houser, M. (2018), „Mechanical properties of fiber reinforced polymer composites: A comparative study of conventional and additive manufacturing methods“, *Journal of Composite Materials*, 52 (23), p. 3173–3181, DOI: 10.1177/0021998318762297.

(Ahlers & Wasserfall et al. 2019)

Ahlers, D.; Wasserfall, F.; Hendrich, N. & Zhang, J. (2019), „3D Printing of Non-planar Layers for Smooth Surface Generation“. *2019 IEEE 15th International Conference on Automation Science and Engineering (CASE)*. Vancouver, BC, Canada, August 22-25, 2019, Editors: Cappelleri, D., Dimarogonas, D. V., Dotoli, M., Fanti, M. P., Lutz, P., Seatzu, C. & Xie, X., IEEE, New York City, United States, p. 1737–1743. ISBN: 978-1-7281-0356-3, DOI: 10.1109/COASE.2019.8843116.

(Akhoundi & Behravesh et al. 2020)

Akhoundi, B.; Behravesh, A. H. & Bagheri Saed, A. (2020), „An innovative design approach in three-dimensional printing of continuous fiber–reinforced thermoplastic composites via fused deposition modeling process: In-melt simultaneous impregnation“, *Proceedings of the Institution of Mechanical Engineers, Part B: Journal of Engineering Manufacture*, 234 (1-2), p. 243–259, DOI: 10.1177/0954405419843780.

(Albers & Burkhardt et al. 2005)

Albers, A.; Burkhardt, N.; Meboldt, M. & Saak, M. (2005), „SPALTEN Problem Solving Methodology in the Product Development“. *Engineering design and the global economy. 15th International Conference on Engineering Design - ICED 05*. Melbourne, Australia, August 15-18, 2005, Editor: Samuel, A. E., The Design Society, Melbourne, Australia. ISBN: 978-085825788-7, DOI: 10.5445/IR/1000007075.

(Albers & Rapp et al. 2018)

Albers, A.; Rapp, S.; Heitger, N.; Wattenberg, F. & Bursac, N. (2018), „Reference Products in PGE – Product Generation Engineering: Analyzing Challenges Based

on the System Hierarchy“, *Procedia CIRP*, 70, p. 469–474, DOI: 10.1016/j.procir.2018.02.046.

(Ali & Kurokawa et al. 2023)

Ali, M. H.; Kurokawa, S.; Shehab, E. & Mukhtarkhanov, M. (2023), „Development of a large-scale multi-extrusion FDM printer, and its challenges“, *International Journal of Lightweight Materials and Manufacture*, 6 (2), p. 198–213, DOI: 10.1016/j.ijlmm.2022.10.001.

(Ali & Yan et al. 2023)

Ali, Z.; Yan, Y.; Mei, H.; Cheng, L. & Zhang, L. (2023), „Impact of fiber-type and autoclave-treatment at different temperatures on the mechanical properties and interface performance of various fiber-reinforced 3D -printed composites“, *Polymer Composites*, 44 (6), p. 3232–3244, DOI: 10.1002/pc.27314.

(Alsharhan & Centea et al. 2017)

Alsharhan, A. T.; Centea, T. & Gupta, S. K. (2017), „Enhancing Mechanical Properties of Thin-Walled Structures Using Non-Planar Extrusion Based Additive Manufacturing“. *12th International Manufacturing Science and Engineering Conference collocated with the JSME/ASME 2017 6th International Conference on Materials and Processing*. Los Angeles, California, USA, June 4-8, 2017, The American Society of Mechanical Engineers, New York, USA. ISBN: 978-0-7918-5073-2, DOI: 10.1115/MSEC2017-2978.

(Amirkhosravi & Pishvar et al. 2018)

Amirkhosravi, M.; Pishvar, M. & Altan, M. C. (2018), „A New Approach to Apply Consolidation Pressure in Composite Manufacturing by Using Neodymium Iron Boron Magnets“. *Americas Conference of the Polymer Processing Society*. November 5-9, 2018. Boston, Massachusetts, USA.

(Andreu & Kim et al. 2022)

Andreu, A.; Kim, S.; Dittus, J.; Friedmann, M.; Fleischer, J. & Yoon, Y.-J. (2022), „Hybrid material extrusion 3D printing to strengthen interlayer adhesion through hot rolling“, *Additive Manufacturing*, 55, DOI: 10.1016/j.addma.2022.102773.

(ASTM D5868-01)

ASTM D5868-01 (2023), *Test Method for Lap Shear Adhesion for Fiber Reinforced Plastic (FRP) Bonding*, ASTM International, West Conshohocken, PA, USA.

(Bakhshi & Hojjati 2020)

Bakhshi, N. & Hojjati, M. (2020), „Effect of compaction roller on layup quality and defects formation in automated fiber placement“, *Journal of Reinforced Plastics and Composites*, 39 (1-2), p. 3–20, DOI: 10.1177/0731684419868845.

(Baranowski & Schlotthauer et al. 2022)

Baranowski, M.; Schlotthauer, T.; Netzer, M.; Gönzheimer, P.; Coutandin, S.; Fleischer, J. & Middendorf, P. (2022), „Hybridization of Fused Filament Fabrication Components by Stereolithographic Manufactured Thermoset Inserts“. *Recent Advances in Manufacturing Engineering and Processes. ICMEP - The 10th International Conference on Manufacturing Engineering and Processes*. Singapore, March 11-14, 2021, Editor: Agarwal, R. K., Springer Singapore, Singapore, p. 3–14. ISBN: 978-981-16-3933-3, DOI: 10.1007/978-981-16-3934-0_1.

(Baranowski & Scholz et al. 2024)

Baranowski, M.; Scholz, J.; Kößler, F. & Fleischer, J. (2024), „Systematic Development of a Novel Laser-Sintering Machine with Roving Integration and Sustainability Evaluation“, *Machines*, 12 (5), DOI: 10.3390/machines12050336.

(Baumann 2020)

Baumann, F. (2020), *Additive Fertigung von endlosfaserverstärkten Kunststoffen mit dem ARBURG Kunststoff-Freiform Verfahren*. Doctoral dissertation, Karlsruhe Institute of Technology, Shaker Verlag, Düren, Germany. ISBN: 978-3-8440-7234-1.

(Baumann & Scholz et al. 2017)

Baumann, F.; Scholz, J. & Fleischer, J. (2017), „Investigation of a New Approach for Additively Manufactured Continuous Fiber-reinforced Polymers“, *Procedia CIRP*, 66, p. 323–328, DOI: 10.1016/j.procir.2017.03.276.

(Behrens 1968)

Behrens, E. (1968), „Thermal Conductivities of Composite Materials“, *Journal of Composite Materials*, 2 (1), p. 2–17, DOI: 10.1177/002199836800200101.

(Behzad & Sein 2007)

Behzad, T. & Sein, M. (2007), „Finite element modeling of polymer curing in natural fiber reinforced composites“, *Composites Science and Technology*, 67 (7-8), p. 1666–1673, DOI: 10.1016/j.compscitech.2006.06.021.

(Blok & Woods et al. 2017)

Blok, L. G.; Woods, B.; Yu, H.; Longana, M. L. & Potter, K. P. (2017), „3D printed composites—Benchmarking the state-of-the-art“. 21st International Conference on Composite Materials, Xi'an, China, August 20-25, 2017, p. 1–9.

(Böhlke & Henning et al. 2020)

Böhlke, T.; Henning, F.; Hrymak, A. N.; Kärger, L.; Weidenmann, K. & Wood, J. T. (2020), *Continuous-Discontinuous Fiber-Reinforced Polymers. An Integrated Engineering Approach*, Carl Hanser Verlag, Munich, Germany. ISBN: 978-1-56990-692-7.

(Bottenbruch & Alewelt 1996)

Bottenbruch, L. & Alewelt, W. (1996), *Technische Thermoplaste, Polyamide, Kunststoff Handbuch* ¾, Carl Hanser Verlag, Munich, Germany. ISBN: 978-3446163706.

(Bourban & Bernet et al. 2001)

Bourban, P.-E.; Bernet, N.; Zanetto, J.-E. & Månson, J.-A. E. (2001), „Material phenomena controlling rapid processing of thermoplastic composites“, *Composites Part A: Applied Science and Manufacturing*, 32 (8), p. 1045–1057, DOI: 10.1016/S1359-835X(01)00017-3.

(Caminero & Chacón et al. 2018)

Caminero, M. A.; Chacón, J. M.; García-Moreno, I. & Reverte, J. M. (2018), „Inter-laminar bonding performance of 3D printed continuous fibre reinforced thermoplastic composites using fused deposition modelling“, *Polymer Testing*, 68, p. 415–423, DOI: 10.1016/j.polymertesting.2018.04.038.

(Cengel 2007)

Cengel, Y. (2007), *Introduction to Thermodynamics and Heat Transfer + EES Software*, McGraw-Hill Science, New York, USA. ISBN: 978-0077235659.

(Chacón & Caminero et al. 2019)

Chacón, J. M.; Caminero, M. A.; Núñez, P. J.; García-Plaza, E.; García-Moreno, I. & Reverte, J. M. (2019), „Additive manufacturing of continuous fibre reinforced thermoplastic composites using fused deposition modelling: Effect of process parameters on mechanical properties“, *Composites Science and Technology*, 181, DOI: 10.1016/j.compscitech.2019.107688.

(Chawla 2019)

Chawla, K. K. (2019), *Composite Materials. Science and Engineering*, Springer International Publishing, Cham, Switzerland. ISBN: 978-3-030-28982-9.

(Cheng & Zhao et al. 2018)

Cheng, J.; Zhao, D.; Liu, K.; Wang, Y. & Chen, H. (2018), „Modeling and impact analysis on contact characteristic of the compaction roller for composite automated placement“, *Journal of Reinforced Plastics and Composites*, 37 (23), p. 1418–1432, DOI: 10.1177/0731684418798151.

(Colton & Muzzy et al. 1992)

Colton, J.; Muzzy, J.; Birger, S.; Yang, H. & Norpoth, L. (1992), „Processing parameters for consolidating PEEK/carbon fiber (APC-2) composites“, *Polymer Composites*, 13 (6), p. 421–426, DOI: 10.1002/pc.750130604.

(Davis & Gramann et al. 2003)

Davis, B. A.; Gramann, P.; Osswald, T. A. & Rios, A. (2003), *Compression molding*, Carl Hanser Verlag, Munich, Germany. ISBN: 3-446-22166-2.

(Denavit & Hartenberg 1955)

Denavit, J. & Hartenberg, R. S. (1955), „A Kinematic Notation for Lower-Pair Mechanisms Based on Matrices“, *Journal of Applied Mechanics*, 22 (2), p. 215–221, DOI: 10.1115/1.4011045.

(Dickson & Barry et al. 2017)

Dickson, A. N.; Barry, J. N.; McDonnell, K. A. & Dowling, D. P. (2017), „Fabrication of continuous carbon, glass and Kevlar fibre reinforced polymer composites using additive manufacturing“, *Additive Manufacturing*, 16, p. 146–152, DOI: 10.1016/j.addma.2017.06.004.

(DIN EN 1465)

DIN EN 1465:2009-07 (2009), *Klebstoffe - Bestimmung der Zugscherfestigkeit von Überlappungsklebung*, Beuth Verlag, Berlin, Germany.

(DIN EN ISO 527-4)

DIN EN ISO 527-4:2023-07 (2023), *Plastics - Determination of tensile properties - Part 4: Test conditions for isotropic and orthotropic fibre-reinforced plastic composites*, Beuth Verlag, Berlin, Germany.

(DIN EN ISO 20753)

DIN EN ISO 20753:2019-02 (2019), *Plastics - Test specimens*, Beuth Verlag, Berlin, Germany.

(DIN EN ISO/ASTM 52900)

DIN EN ISO/ASTM 52900:2022-03 (2022), *Additive Fertigung - Grundlagen - Terminologie*, Beuth Verlag, Berlin, Germany.

(Drzal & Rich et al. 1983)

Drzal, L. T.; Rich, M. J. & Lloyd, P. F. (1983), „Adhesion of Graphite Fibers to Epoxy Matrices: I. The Role of Fiber Surface Treatment“, *The Journal of Adhesion*, 16 (1), p. 1–30, DOI: 10.1080/00218468308074901.

(Du Plessis & Sperling et al. 2018)

Du Plessis, A.; Sperling, P.; Beerlink, A.; Tshabalala, L.; Hoosain, S.; Mathe, N. & Le Roux, S. G. (2018), „Standard method for microCT-based additive manufacturing quality control 1: Porosity analysis“, *MethodsX*, 5, p. 1102–1110, DOI: 10.1016/j.mex.2018.09.005.

(Ehrenstein 2006)

Ehrenstein, G. W. (2006), *Faserverbund-Kunststoffe. Werkstoffe - Verarbeitung - Eigenschaften*, Carl Hanser Verlag, Munich, Germany. ISBN: 978-3-446-22716-3.

(Elkaseer & Müller et al. 2020)

Elkaseer, A.; Müller, T.; Rabsch, D. & Scholz, S. G. (2020), „Impact of Nonplanar 3D Printing on Surface Roughness and Build Time in Fused Filament Fabrication“. *Sustainable Design and Manufacturing 2020, Proceedings of the 7th International Conference on Sustainable Design and Manufacturing (KES-SDM 2020)*. Singapore, Editors: Scholz, S. G., Howlett, R. J. & Setchi, R., Springer Singapore, Singapore, p. 285–295. ISBN: 978-981-15-8130-4, DOI: 10.1007/978-981-15-8131-1_26.

(Elsner & Eyerer et al. 2012)

Elsner, P.; Eyerer, P. & Hirth, T. (2012), *Kunststoffe. Eigenschaften und Anwendungen*, Springer Berlin Heidelberg, Berlin, Heidelberg, Germany. ISBN: 978-3-642-16173-5.

(Engelhardt & Ehard et al. 2019)

Engelhardt, R.; Ehard, S.; Wolf, T.; Oelhafen, J.; Kollmannsberger, A. & Drechsler,

K. (2019), „In Situ Joining of Unidirectional Tapes on Long Fiber Reinforced Thermoplastic Structures by Thermoplastic Automated Fiber Placement for Scientific Sounding Rocket Applications“, *Procedia CIRP*, 85, p. 189–194, DOI: 10.1016/j.procir.2019.09.015.

(Fang & Zhang et al. 2020)

Fang, G.; Zhang, T.; Zhong, S.; Chen, X.; Zhong, Z. & Wang, C. C. L. (2020), „Reinforced FDM: Multi-axis filament alignment with controlled anisotropic strength“, *ACM Transactions on Graphics*, 39 (6), p. 1–15, DOI: 10.1145/3414685.3417834.

(Fang & Zhang et al. 2024)

Fang, G.; Zhang, T.; Huang, Y.; Zhang, Z.; Masania, K. & Wang, C. C. (2024), „Exceptional mechanical performance by spatial printing with continuous fiber: Curved slicing, toolpath generation and physical verification“, *Additive Manufacturing*, 82, DOI: 10.1016/j.addma.2024.104048.

(Fleischer 2021)

Fleischer, J. (2021), *Intrinsische Hybridverbunde für Leichtbautragstrukturen. Grundlagen der Fertigung, Charakterisierung und Auslegung*, Springer Vieweg, Berlin, Germany. ISBN: 978-3-662-62832-4.

(Fleischer & Gebhardt 2013)

Fleischer, J. & Gebhardt, J. (2013), „Lokale Verstärkungen schnell erzielen“, *Maschinen Markt Composites World*, 4, p. 15–17.

(Fleischer & Teti et al. 2018)

Fleischer, J.; Teti, R.; Lanz, a. G.; Mativenga, P.; Möhring, H.-C. & Caggiano Alessandra (2018), „Composite materials parts manufacturing“, *CIRP Annals - Manufacturing Technology*, 67, p. 603–626, DOI: 10.1016/j.cirp.2018.05.005.

(Frigeni 2023)

Frigeni, F. (2023), *Industrial robotics control. Mathematical models, software architecture, and electronics design*, Apress, New York, USA. ISBN: 978-1-4842-8988-4.

(Gevatter & Grünhaupt 2006)

Gevatter, H.-J. & Grünhaupt, U. (2006), *Handbuch der Mess- und Automatisierungstechnik in der Produktion. 3D Printing, Rapid Prototyping, and Direct Digital*

Manufacturing, Springer Berlin Heidelberg, Berlin, Heidelberg, Germany. ISBN: 978-3-540-21207-2.

(Gibson & Rosen et al. 2015)

Gibson, I.; Rosen, D. & Stucker, B. (2015), *Additive Manufacturing Technologies*, Springer New York, New York, USA. ISBN: 978-1-4939-2112-6.

(Goh & Dikshit et al. 2018)

Goh, G. D.; Dikshit, V.; Nagalingam, A. P.; Goh, G. L.; Agarwala, S.; Sing, S. L.; Wei, J. & Yeong, W. Y. (2018), „Characterization of mechanical properties and fracture mode of additively manufactured carbon fiber and glass fiber reinforced thermoplastics“, *Materials & Design*, 137, p. 79–89, DOI: 10.1016/j.matdes.2017.10.021.

(Grand View Research 2023)

Grand View Research (2023), *Composites Market Size, Share & Trends Analysis Report By Product Type (Carbon Fiber, Glass Fiber), By Manufacturing Process (Layup, Filament, Injection Molding, Pultrusion), By End-use, By Region And Segment Forecasts, 2023 - 2030*. URL: <https://www.grandviewresearch.com/industry-analysis/composites-market#> [Accessed: 10.03.2024].

(Gröschel & Drummer 2014)

Gröschel, C. & Drummer, D. (2014), „The Influence of Moisture and Laminate Setup on the De-Consolidation Behavior of PA6/GF Thermoplastic Matrix Composites“, *International Polymer Processing*, 29 (5), p. 660–668, DOI: 10.3139/217.2976.

(He & Jiang et al. 2022)

He, Y.; Jiang, J.; Qu, W. & Ke, Y. (2022), „Compaction pressure distribution and pressure uniformity of segmented rollers for automated fiber placement“, *Journal of Reinforced Plastics and Composites*, 41 (11-12), p. 427–443, DOI: 10.1177/07316844211054166.

(He & Wang et al. 2020)

He, Q.; Wang, H.; Fu, K. & Ye, L. (2020), „3D printed continuous CF/PA6 composites: Effect of microscopic voids on mechanical performance“, *Composites Science and Technology*, 191, DOI: 10.1016/j.compscitech.2020.108077.

(Henning & Moeller 2020)

Henning, F. & Moeller, E. (2020), *Handbuch Leichtbau. Methoden, Werkstoffe, Fertigung*, Carl Hanser Verlag, Munich, Germany. ISBN: 978-3-446-45638-9.

(Hetrick & Sanei et al. 2022)

Hetrick, D. R.; Sanei, S. H. R. & Ashour, O. (2022), „Void Content Reduction in 3D Printed Glass Fiber-Reinforced Polymer Composites through Temperature and Pressure Consolidation“, *Journal of Composites Science*, 6 (5), p. 128, DOI: 10.3390/jcs6050128.

(Hirsch & Scholz et al. 2024)

Hirsch, P.; Scholz, S.; Borowitzka, B.; Vyhnał, M.; Schlimper, R.; Zschehyge, M.; Kotera, O.; Stipkova, M. & Scholz, S. (2024), „Processing and Analysis of Hybrid Fiber-Reinforced Polyamide Composite Structures Made by Fused Granular Fabrication and Automated Tape Laying“, *Journal of Manufacturing and Materials Processing*, 8 (1), p. 25, DOI: 10.3390/jmmp8010025.

(Holschuh & Becker et al. 2012)

Holschuh, R.; Becker, D. & Mitschang, P. (2012), „Verfahrenskombination für mehr Wirtschaftlichkeit des FVK-Einsatzes im Automobilbau“, *Lightweight Design*, 5 (4), p. 14–19, DOI: 10.1365/s35725-012-0106-3.

(Hopmann & Michaeli 2017)

Hopmann, C. & Michaeli, W. (2017), *Einführung in die Kunststoffverarbeitung*, Hanser, Munich, Germany. ISBN: 978-3-446-45355-5.

(Hopmann & Ophüls et al. 2019)

Hopmann, C.; Ophüls, M.; Schulz, M. & Janssen, H. (2019), „Individualisierte Fertigung von faserverstärkten Hybridbauteilen“, *Lightweight Design*, 12 (4), p. 64–71, DOI: 10.1007/s35725-019-0038-2.

(Hopmann & Wilms et al. 2021)

Hopmann, C.; Wilms, E.; Beste, C.; Schneider, D.; Fischer, K. & Stender, S. (2021), „Investigation of the influence of melt-impregnation parameters on the morphology of thermoplastic UD-tapes and a method for quantifying the same“, *Journal of Thermoplastic Composite Materials*, 34 (9), p. 1299–1312, DOI: 10.1177/0892705719864624.

(Huang & Fu et al. 2021)

Huang, S.; Fu, Q.; Yan, L. & Kasal, B. (2021), „Characterization of interfacial properties between fibre and polymer matrix in composite materials – A critical review“, *Journal of Materials Research and Technology*, 13, p. 1441–1484, DOI: 10.1016/j.jmrt.2021.05.076.

(Jiang & He et al. 2019)

Jiang, J.; He, Y. & Ke, Y. (2019), „Pressure distribution for automated fiber placement and design optimization of compaction rollers“, *Journal of Reinforced Plastics and Composites*, 38 (18), p. 860–870, DOI: 10.1177/0731684419850896.

(Jiang & Newman et al. 2021)

Jiang, J.; Newman, S. T. & Zhong, R. Y. (2021), „A review of multiple degrees of freedom for additive manufacturing machines“, *International Journal of Computer Integrated Manufacturing*, 34 (2), p. 195–211, DOI: 10.1080/0951192X.2020.1858510.

(Karsli & Aytac 2013)

Karsli, N. G. & Aytac, A. (2013), „Tensile and thermomechanical properties of short carbon fiber reinforced polyamide 6 composites“, *Composites Part B: Engineering*, 51, p. 270–275, DOI: 10.1016/j.compositesb.2013.03.023.

(Katayama 2013)

Katayama, S. (2013), *Handbook of laser welding technologies*, Woodhead Publishing, Cambridge, UK. ISBN: 978-0-85709-264-9.

(Khan & Mitschang et al. 2010)

Khan, M. A.; Mitschang, P. & Schledjewski, R. (2010), „Identification of some optimal parameters to achieve higher laminate quality through tape placement process“, *Advances in Polymer Technology*, 29 (2), p. 98–111, DOI: 10.1002/adv.20177.

(Kirchner 2007)

Kirchner, E. (2007), *Leistungsübertragung in Fahrzeuggetrieben. Grundlagen der Auslegung, Entwicklung und Validierung von Fahrzeuggetrieben und deren Komponenten*, Springer Berlin Heidelberg New York, Berlin, Heidelberg, Germany, New York, USA. ISBN: 978-3-540-35292-1.

(Kleppmann 2020)

Kleppmann, W. (2020), *Versuchsplanung. Produkte und Prozesse optimieren*, Carl Hanser Verlag, Munich, Germany. ISBN: 978-3-446-46146-8.

(Krajangsawasdi & Blok et al. 2021)

Krajangsawasdi, N.; Blok, L. G.; Hamerton, I.; Longana, M. L.; Woods, B. K. S. & Ivanov, D. S. (2021), „Fused Deposition Modelling of Fibre Reinforced Polymer Composites: A Parametric Review“, *Journal of Composites Science*, 5 (1), p. 29, DOI: 10.3390/jcs5010029.

(Krčma & Paloušek 2022)

Krčma, M. & Paloušek, D. (2022), „Comparison of the effects of multiaxis printing strategies on large-scale 3D printed surface quality, accuracy, and strength“, *The International Journal of Advanced Manufacturing Technology*, 119 (11-12), p. 7109–7120, DOI: 10.1007/s00170-022-08685-4.

(Kropka & Muehlbacher et al. 2017)

Kropka, M.; Muehlbacher, M.; Neumeyer, T. & Altstaedt, V. (2017), „From UD-tape to Final Part – A Comprehensive Approach Towards Thermoplastic Composites“, *Procedia CIRP*, 66, p. 96–100, DOI: 10.1016/j.procir.2017.03.371.

(Kumar & Sadasivuni et al. 2022)

Kumar, A. P.; Sadasivuni, K. K.; AlMangour, B. & Majid, M. S. A. b. (2022), *High-Performance Composite Structures: Additive Manufacturing and Processing*, Springer Singapore, Singapore. ISBN: 978-981-16-7376-4.

(Kupzik 2022)

Kupzik, D. (2022), *Robotic Swing Folding of three-dimensional UD-tape-based Reinforcement Structures*. Doctoral dissertation, Karlsruhe Institute of Technology, Shaker Verlag, Düren, Germany. ISBN: 978-3-8440-8716-1.

(Lee & Springer 1987)

Lee, W. I. & Springer, G. S. (1987), „A Model of the Manufacturing Process of Thermoplastic Matrix Composites“, *Journal of Composite Materials*, 21 (11), p. 1017–1055, DOI: 10.1177/002199838702101103.

(Leichtbau BW GmbH 2015)

Leichtbau BW GmbH (2015), *Studie Additive Manufacturing im Leichtbau. Strategische und betriebswirtschaftliche Herausforderungen und Perspektiv*, Leichtbau

BW GmbH, Stuttgart. URL: https://www.funk-maschinenbau.de/wp-content/uploads/LeichtbauBW_Studie.pdf, [Accessed: 08.06.2024].

(Link 2022)

Link, T. (2022), *Prozessspezifische Einflussgrößen auf die Morphologie kontinuierlich faserverstärkter thermoplastischer Halbzeuge und deren Auswirkungen auf die mechanischen Eigenschaften*. Doctoral dissertation, Karlsruhe Institute of Technology, Fraunhofer Verlag, Stuttgart, Germany. ISBN: 978-3-8396-1961-2.

(Mark & Woodruff et al. 2017)

Mark, G. T.; Woodruff, R. B.; Parangi, A. L.; Benhaim, D. S. & Sklaroff, B. T. (2017), *Multilayer fiber reinforcement design for 3D printing, US Patent US10603841B2*. URL: <https://patents.google.com/patent/us9815268b2/en> [Accessed: 08.06.2024].

(Matkovic & Götz et al. 2021)

Matkovic, N.; Götz, M.; Kupzik, D.; Nieschlag, J.; Coutandin, S. & Fleischer, J. (2021), „Additives Roboter-Extrusions-System“, *VDI-Z*, 163 (01-02), p. 55–57, DOI: 10.37544/0042-1766-2021-01-02-55.

(Matkovic & Höger et al. 2023)

Matkovic, N.; Höger, K.; Friedmann, M.; Stamer, F.; Fleischer, J. & Lanza, G. (2023), „Identification of hybridization strategies for combining fused filament fabrication with unidirectional tape reinforcement“, *Composites Communications*, 38, DOI: 10.1016/j.coco.2022.101484.

(Matkovic & Kupzik et al. 2022)

Matkovic, N.; Kupzik, D.; Steidle-Sailer, C.; Friedmann, M. & Fleischer, J. (2022), „Novel Robot-Based Process Chain for the Flexible Production of Thermoplastic Components with CFRP Tape Reinforcement Structures“, *Procedia CIRP*, 106, p. 21–26, DOI: 10.1016/j.procir.2022.02.149.

(Matsuo & Hojo et al. 2019)

Matsuo, T.; Hojo, M. & Kageyama, K. (2019), „Influence of gripping method on tensile properties of unidirectional thermoplastic CFRP – Round-robin activity for international standardization in Japan“, *Journal of Composite Materials*, 53 (28-30), p. 4161–4171, DOI: 10.1177/0021998319855419.

(Matsuzaki & Ueda et al. 2016)

Matsuzaki, R.; Ueda, M.; Namiki, M.; Jeong, T.-K.; Asahara, H.; Horiguchi, K.; Nakamura, T.; Todoroki, A. & Hirano, Y. (2016), „Three-dimensional printing of continuous-fiber composites by in-nozzle impregnation“, *Scientific reports*, 6, DOI: 10.1038/srep23058.

(Mauricio Guajardo-Trevino & Ahuett-Garza et al. 2022)

Mauricio Guajardo-Trevino, A.; Ahuett-Garza, H.; Orta-Castanon, P.; Daniel Urbina-Coronado, P.; Saldana, C. & Kurfess, T. R. (2022), „Effects of deposition - strategy - induced raster gaps and infill voids on the compressive strength of 3D printed isogrid structures“, *Manufacturing Letters*, 31, p. 15–19, DOI: 10.1016/j.mfglet.2021.12.001.

(Mehdikhani & Gorbatikh et al. 2019)

Mehdikhani, M.; Gorbatikh, L.; Verpoest, I. & Lomov, S. V. (2019), „Voids in fiber-reinforced polymer composites: A review on their formation, characteristics, and effects on mechanical performance“, *Journal of Composite Materials*, 53 (12), p. 1579–1669, DOI: 10.1177/0021998318772152.

(Mele & Pisaneschi et al. 2022)

Mele, M.; Pisaneschi, G.; Campana, G.; Zucchelli, A. & Ciotti, M. (2022), „Effect of selected process parameters on dimensional accuracy in Arburg Plastic Freeforming“, *Rapid Prototyping Journal*, 28 (9), p. 1677–1689, DOI: 10.1108/RPJ-05-2021-0109.

(Mori & Maeno et al. 2014)

Mori, K.; Maeno, T. & Nakagawa, Y. (2014), „Dieless Forming of Carbon Fibre Reinforced Plastic Parts Using 3D Printer“, *Procedia Engineering*, 81, p. 1595–1600, DOI: 10.1016/j.proeng.2014.10.196.

(Mühlbeier & Gönninger et al. 2021)

Mühlbeier, E.; Gönninger, P.; Hausmann, L. & Fleischer, J. (2021), „Value Stream Kinematics“. *Production at the leading edge of technology. Proceedings of the 10th Congress of the German Academic Association for Production Technology (WGP)*. Dresden, Germany, September, 23–24, 2020, Editors: Behrens, B.-A., Brosius, A., Hintze, W., Ihlenfeldt, S. & Wulfsberg, J. P., Springer Berlin Heidelberg, Berlin, Heidelberg, Germany, p. 409–418. ISBN: 978-3-662-62137-0, DOI: 10.1007/978-3-662-62138-7_41.

(Nakagawa & Mori et al. 2017)

Nakagawa, Y.; Mori, K. & Maeno, T. (2017), „3D printing of carbon fibre-reinforced plastic parts“, *The International Journal of Advanced Manufacturing Technology*, 91 (5-8), p. 2811–2817, DOI: 10.1007/s00170-016-9891-7.

(Narnhofer & Schledjewski et al. 2013)

Narnhofer, M.; Schledjewski, R.; Mitschang, P. & Perko, L. (2013), „Simulation of the Tape-Laying Process for Thermoplastic Matrix Composites“, *Advances in Polymer Technology*, 32 (S1), 705-713, DOI: 10.1002/adv.21312.

(Neitzel & Mitschang et al. 2014)

Neitzel, M.; Mitschang, P. & Breuer, U. (2014), *Handbuch Verbundwerkstoffe. Werkstoffe, Verarbeitung, Anwendung*, Carl Hanser Verlag, Munich, Germany. ISBN: 978-3-446-43696-1.

(Ning & Cong et al. 2015)

Ning, F.; Cong, W.; Qiu, J.; Wei, J. & Wang, S. (2015), „Additive manufacturing of carbon fiber reinforced thermoplastic composites using fused deposition modeling“, *Composites Part B: Engineering*, 80, p. 369–378, DOI: 10.1016/j.compositesb.2015.06.013.

(Oberlercher & Laux et al. 2023)

Oberlercher, H.; Laux, M.; Heim, R.; Berndt, A.; Amancio-Filho Sergio T. & Riemelmoser, F. O. (2023), „In-situ consolidation of additively manufactured continuous fiber reinforced material: Technical approach and results“. *The 26th International ESAFORM Conference on Material Forming - 2023*. Kraków, Poland, April 19-21, 2023, Editors: Madej, L., Sitko, M. & Perzynski, K., Materials Research Forum LLC, Millersville, PA, USA, p. 85–92, DOI: 10.21741/9781644902479-10.

(O'Connor & Dowling 2019)

O'Connor, H. J. & Dowling, D. P. (2019), „Low-pressure additive manufacturing of continuous fiber-reinforced polymer composites“, *Polymer Composites*, 40 (11), p. 4329–4339, DOI: 10.1002/pc.25294.

(Oztan & Karkkainen et al. 2019)

Oztan, C.; Karkkainen, R.; Fittipaldi, M.; Nygren, G.; Roberson, L.; Lane, M. & Celik, E. (2019), „Microstructure and mechanical properties of three dimensional-printed continuous fiber composites“, *Journal of Composite Materials*, 53 (2), p. 271–280, DOI: 10.1177/0021998318781938.

(Pandelidi & Bateman et al. 2021)

Pandelidi, C.; Bateman, S.; Piegert, S.; Hoehner, R.; Kelbassa, I. & Brandt, M. (2021), „The technology of continuous fibre-reinforced polymers: a review on extrusion additive manufacturing methods“, *The International Journal of Advanced Manufacturing Technology*, 113 (11-12), p. 3057–3077, DOI: 10.1007/s00170-021-06837-6.

(Penumakala & Santo et al. 2020)

Penumakala, P. K.; Santo, J. & Thomas, A. (2020), „A critical review on the fused deposition modeling of thermoplastic polymer composites“, *Composites Part B: Engineering*, 201, DOI: 10.1016/j.compositesb.2020.108336.

(Popov 2016)

Popov, V. (2016), *Kontaktmechanik und Reibung. Von der Nanotribologie bis zur Erdbebendynamik*, Springer Vieweg, Berlin, Heidelberg, Germany. ISBN: 978-3-662-45974-4.

(Prashanth & Subbaya et al. 2017)

Prashanth, S.; Subbaya, K. M.; Nithin, K. & Sachhidananda, S. (2017), „Fiber Reinforced Composites - A Review“, *Journal of Material Science & Engineering*, 06 (03), DOI: 10.4172/2169-0022.1000341.

(Raspall & Velu et al. 2019)

Raspall, F.; Velu, R. & Vaheed, N. M. (2019), „Fabrication of complex 3D composites by fusing automated fiber placement (AFP) and additive manufacturing (AM) technologies“, *Advanced Manufacturing: Polymer & Composites Science*, 5 (1), p. 6–16, DOI: 10.1080/20550340.2018.1557397.

(Rodriguez-Padilla & Cuan-Urquizo et al. 2021)

Rodriguez-Padilla, C.; Cuan-Urquizo, E.; Roman-Flores, A.; Gordillo, J. L. & Vázquez-Hurtado, C. (2021), „Algorithm for the Conformal 3D Printing on Non-Planar Tessellated Surfaces: Applicability in Patterns and Lattices“, *Applied Sciences*, 11 (16), p. 7509, DOI: 10.3390/app11167509.

(Schlotthauer & Nolan et al. 2021)

Schlotthauer, T.; Nolan, D. & Middendorf, P. (2021), „Influence of short carbon and glass fibers on the curing behavior and accuracy of photopolymers used in stereolithography“, *Additive Manufacturing*, 42, DOI: 10.1016/j.addma.2021.102005.

(Schürmann 2007)

Schürmann, H. (2007), *Konstruieren mit Faser-Kunststoff-Verbunden*, Springer Berlin Heidelberg, Berlin, Heidelberg, Germany. ISBN: 978-3-540-72189-5.

(Shaik & Schuster et al. 2022)

Shaik, Y. P.; Schuster, J.; Katherapalli, H. R. & Shaik, A. (2022), „3D Printing under High Ambient Pressures and Improvement of Mechanical Properties of Printed Parts“, *Journal of Composites Science*, 6 (1), p. 16, DOI: 10.3390/jcs6010016.

(Shang & Tian et al. 2020)

Shang, J.; Tian, X.; Luo, M.; Zhu, W.; Li, D.; Qin, Y. & Shan, Z. (2020), „Controllable inter-line bonding performance and fracture patterns of continuous fiber reinforced composites by sinusoidal-path 3D printing“, *Composites Science and Technology*, 192, DOI: 10.1016/j.compscitech.2020.108096.

(Shi & Mizuno et al. 2022)

Shi, J.; Mizuno, M.; Bao, L. & Zhu, C. (2022), „A Facile Molding Method of Continuous Fiber-Reinforced Thermoplastic Composites and Its Mechanical Property“, *Polymers*, 14 (5), DOI: 10.3390/polym14050947.

(Siciliano & Khatib 2016)

Siciliano, B. & Khatib, O. (2016), *Springer Handbook of Robotics*, Springer International Publishing, Basel, Switzerland. ISBN: 978-3-319-32550-7.

(Spectrum Group 2021)

Spectrum Group (2021), *Technical data sheet Spectrum Filaments. Nylon PA6 Low Warp Filament*. URL: <https://spectrumfilaments.com/de/filament/> [Accessed: 01.06.2021].

(Stokes-Griffin & Matuszyk et al. 2012)

Stokes-Griffin, C. M.; Matuszyk, T. I.; Compston, P. & Cardew-Hall, M. J. (2012), „Modelling the Automated Tape Placement of Thermoplastic Composites with In-Situ Consolidation“. *Sustainable Automotive Technologies 2012: Proceedings of the 4th International Conference*, Editors: Subic, A., Wellnitz, J., Leary, M. & Koopmans, L., Springer Berlin Heidelberg, Berlin, Heidelberg, Germany, p. 61–68. ISBN: 978-3-642-24144-4, DOI: 10.1007/978-3-642-24145-1_9.

(Thomas & Kuruville et al. 2013)

Thomas, S.; Kuruville, J.; Malhotra, S. K.; Goda, K. & Sreekala, M. S. (2013), *Polymer composites. Vol. 1: Macro- and microcomposites*, Wiley-VCH, Weinheim, Germany. ISBN: 978-3-527-32624-2.

(Tian & Liu et al. 2016)

Tian, X.; Liu, T.; Yang, C.; Wang, Q. & Li, D. (2016), „Interface and performance of 3D printed continuous carbon fiber reinforced PLA composites“, *Composites Part A: Applied Science and Manufacturing*, 88, p. 198–205, DOI: 10.1016/j.compositesa.2016.05.032.

(Tsai 1999)

Tsai, L.-W. (1999), *Robot analysis. The mechanics of serial and parallel manipulators*, J. Wiley, New York, USA. ISBN: 978-0-471-32593-2.

(Ueda & Kishimoto et al. 2020)

Ueda, M.; Kishimoto, S.; Yamawaki, M.; Matsuzaki, R.; Todoroki, A.; Hirano, Y. & Le Duigou, A. (2020), „3D compaction printing of a continuous carbon fiber reinforced thermoplastic“, *Composites Part A: Applied Science and Manufacturing*, 137, p. 105985, DOI: 10.1016/j.compositesa.2020.105985.

(van de Werken & Hurley et al. 2019)

van de Werken, N.; Hurley, J.; Khanbolouki, P.; Sarvestani, A. N.; Tamijani, A. Y. & Tehrani, M. (2019), „Design considerations and modeling of fiber reinforced 3D printed parts“, *Composites Part B: Engineering*, 160, p. 684–692, DOI: 10.1016/j.compositesb.2018.12.094.

(van Der Klift & Koga et al. 2016)

van Der Klift, F.; Koga, Y.; Todoroki, A.; Ueda, M.; Hirano, Y. & Matsuzaki, R. (2016), „3D Printing of Continuous Carbon Fibre Reinforced Thermo-Plastic (CFRTP) Tensile Test Specimens“, *Open Journal of Composite Materials*, 06 (01), p. 18–27, DOI: 10.4236/ojcm.2016.61003.

(VDI 2803)

VDI 2803:2019-01 (2019), *Function analysis - Fundamentals and method*, Beuth Verlag, Berlin, Germany.

(Vedernikov & Minchenkov et al. 2022)

Vedernikov, A.; Minchenkov, K.; Gusev, S.; Sulimov, A.; Zhou, P.; Li, C.; Xian, G.;

Akhatov, I. & Safonov, A. (2022), „Effects of the Pre-Consolidated Materials Manufacturing Method on the Mechanical Properties of Pultruded Thermoplastic Composites“, *Polymers*, 14 (11), DOI: 10.3390/polym14112246.

(Voigt 1889)

Voigt, W. (1889), „Ueber die Beziehung zwischen den beiden Elasticitätsconstanten isotroper Körper“, *Annalen der Physik*, 274 (12), p. 573–587, DOI: 10.1002/andp.18892741206.

(Wang & Ju et al. 2019)

Wang, F.; Ju, F.; Rowe, K. & Hofmann, N. (2019), „Real-time control for large scale additive manufacturing using thermal images“. *2019 IEEE 15th International Conference on Automation Science and Engineering (CASE)*. Vancouver, BC, Canada, August 22-25, 2019, Editors: Cappelleri, D., Dimarogonas, D. V., Dotoli, M., Fanti, M. P., Lutz, P., Seatzu, C. & Xie, X., IEEE, New York City, United States, p. 36–41. ISBN: 978-1-7281-0356-3, DOI: 10.1109/COASE.2019.8843264.

(Weber 2009)

Weber, W. (2009), *Industrieroboter. Methoden der Steuerung und Regelung*, Fachbuchverlag Leipzig im Carl Hanser Verlag, Leipzig, Germany. ISBN: 978-3-446-41031-2.

(Werner & Aburaia et al. 2021)

Werner, J.; Aburaia, M.; Raschendorfer, A. & Lackner, M. (2021), „MeshSlicer: A 3D-Printing software for printing 3D-models with a 6-axis industrial robot“, *Proceedia CIRP*, 99, p. 110–115, DOI: 10.1016/j.procir.2021.03.018.

(Wickramasinghe & Do et al. 2020)

Wickramasinghe, S.; Do, T. & Tran, P. (2020), „FDM-Based 3D Printing of Polymer and Associated Composite: A Review on Mechanical Properties, Defects and Treatments“, *Polymers*, 12 (7), DOI: 10.3390/polym12071529.

(Willemstein 2021)

Willemstein, N. (2021), *Integration of an In-Situ Consolidation Mechanism into the Fused Deposition Modeling Process for Low Porosity Continuous Fiber-Reinforced Thermoplastic Structures*. Doctoral dissertation, University of Twente, Enschede, Netherlands.

(Wu & Geng et al. 2015)

Wu, W.; Geng, P.; Li, G.; Di Zhao; Zhang, H. & Zhao, J. (2015), „Influence of Layer Thickness and Raster Angle on the Mechanical Properties of 3D-Printed PEEK and a Comparative Mechanical Study between PEEK and ABS“, *Materials*, 8 (9), p. 5834–5846, DOI: 10.3390/ma8095271.

(Wurzer 2021)

Wurzer, S. (2021), *Viskoelastische Eigenschaften von Polyamid unter Feuchtigkeitseinfluss*. Master's thesis, Montanuniversität Leoben, Leoben, Austria, Lehrstuhl für Werkstoffkunde und Prüfung der Kunststoffe.

(Yang & Pitchumani 2002)

Yang, F. & Pitchumani, R. (2002), „Interlaminar contact development during thermoplastic fusion bonding“, *Polymer Engineering & Science*, 42 (2), p. 424–438, DOI: 10.1002/pen.10960.

(Yassin & Hojjati 2018)

Yassin, K. & Hojjati, M. (2018), „Processing of thermoplastic matrix composites through automated fiber placement and tape laying methods“, *Journal of Thermoplastic Composite Materials*, 31 (12), p. 1676–1725, DOI: 10.1177/0892705717738305.

(Zhang & Fang 2017)

Zhang, J. & Fang, X. (2017), „Challenges and key technologies in robotic cell layout design and optimization“, *Proceedings of the Institution of Mechanical Engineers, Part C: Journal of Mechanical Engineering Science*, 231 (15), p. 2912–2924, DOI: 10.1177/0954406216642473.

(Zhang & Zhang et al. 2019)

Zhang, K.; Zhang, W. & Ding, X. (2019), „Multi-axis additive manufacturing process for continuous fibre reinforced composite parts“, *Procedia CIRP*, 85, p. 114–120, DOI: 10.1016/j.procir.2019.09.022.

(Zhang & Zhou et al. 2020)

Zhang, J.; Zhou, Z.; Zhang, F.; Tan, Y.; Tu, Y. & Yang, B. (2020), „Performance of 3D-Printed Continuous-Carbon-Fiber-Reinforced Plastics with Pressure“, *Materials (Basel, Switzerland)*, 13 (2), DOI: 10.3390/ma13020471.

(Zhuang & Zou et al. 2023)

Zhuang, Y.; Zou, B.; Ding, S.; Wang, X.; Liu, J. & Li, L. (2023), „Preparation of Pre-Impregnated Continuous Carbon Fiber Reinforced Nylon6 Filaments and the Mechanical Properties of 3d Printed Composites“, *Materials Today Communications*, 35, DOI: 10.1016/j.mtcomm.2023.106163.

List of Figures

Figure 1-1: Overview of the objectives and derived subtasks of the thesis	3
Figure 2-1: Qualitative illustration of normalized characteristics of composites for increasing fiber lengths with constant fiber content (based on (Chawla 2019, p. 155))	6
Figure 2-2: Flor structure of a vehicle made of continuous and discontinuous reinforced polyamide 6	7
Figure 2-3: Basic principle and sequence of FRP processing (based on (Neitzel & Mitschang et al. 2014, p. 207))	8
Figure 2-4: Cross section of fiber rovings and influence of matrix viscosity on the degree of impregnation (based on (Shi & Mizuno et al. 2022, p. 6))	9
Figure 2-5: Simplified representation of the cross-section of an UD-tape consisting of Co carbon fibers and thermoplastic matrix	10
Figure 2-6: Illustration of an idealized rough interface at time $t = 0$ without any pressure and $t > 0$ with applied pressure (based on (Lee & Springer 1987, p. 1030))	11
Figure 2-7: a) Process sequence from heating to consolidation to solidification; b) Development of intimate contact and autohesion in the interface area (based on (Narnhofer & Schledjewski et al. 2013, p. 707; Yang & Pitchumani 2002, p. 425))	11
Figure 2-8: Optimal qualitative curves of process parameters during consolidation and solidification for a semi-crystalline thermoplastic as matrix material (based on (Bourban & Bernet et al. 2001, p. 1047–1051))	12
Figure 2-9: Tendencies of selected thermoplastic manufacturing processes in terms of component size, shape complexity and output rates (based on (Neitzel & Mitschang et al. 2014, p. 203))	13
Figure 2-10: a) Thermoforming process chain for the production of components from UD-tapes with a press (based on (Link 2022, p. 9; Kupzik 2022, p. 9)); b) Basic principle of automated tape laying	14
Figure 2-11: Direct compression molding of LFT (based on (Chawla 2019, p. 155; Kupzik 2022, p. 8))	16

Figure 2-12: a) Hybridization combining thermoforming and compression molding; b) Hybridization combining compression molding and tape laying	17
Figure 2-13: (Left) Experimental setup of the Robotic Swing Folding process; (Right) Production of individual preforms from UD-tapes (based on (Kupzik 2022))	18
Figure 2-14: Process steps and main influencing factors of the Robotic Swing Folding (based on (Matkovic & Kupzik et al. 2022; Kupzik 2022))	19
Figure 2-15: Four types of material extrusion of fiber reinforced composites: a) Extrusion of pre-impregnated Co-fiber filaments; b) Extrusion and in-situ impregnation; c) Dual-nozzle extrusion; d) Extrusion of pre-impregnated DiCo-fiber filament (based on (Baumann & Scholz et al. 2017, p. 324))	21
Figure 2-16: Consolidation approaches in MEX: a) Post-processing consolidation; b) In-situ consolidation with controlled ambient conditions; c) Semi-in-situ consolidation with compaction roller; d) In-situ consolidation using a compaction roller	26
Figure 2-17: Qualitative evaluation of the four consolidation approaches based on Figure 2-16	29
Figure 2-18: Setup of a multi-axis MEX DES with a six-axis industrial robot	31
Figure 2-19: Coordinate transformation for robots using forward and inverse transformation based on (Gevatter & Grünhaupt 2006, p. 760)	33
Figure 2-20: Difference in printing strategies illustrated by the example of MEX: a) Planar MEX; b) three-axis non-planar MEX; c) Multi-axis non-planar MEX	35
Figure 3-1: Procedure and approach to achieve the objective	41
Figure 4-1: Required main functions and subsystems visualized with a diagram based on FAST	43
Figure 4-2: Overview and configuration of the conceptual target system consisting of the main subsystems	45
Figure 4-3: Ishikawa diagram of controllable and non-controllable influencing parameters	46
Figure 4-4: Hybridization strategies for integrating UD-tapes into the MEX process	49

Figure 4-5: First prototypical experimental setup consisting of a modified FDM printer for the investigation of the hybridization strategies	51
Figure 4-6: Experimental iterative identification of suitable process parameters for Consolidation I and II using PA6 for the MEX layers	52
Figure 4-7: Test specimen: a) Geometric dimensions and interface area crucial for the tensile shear test; b) ROI for the CT scans (based on (DIN EN 1465; A_Buschulte 2022; Baranowski & Schlotthauer et al. 2022, p. 9))	53
Figure 4-8: Volume of detected voids in the ROI and the trimmed ROI (based on (A_Kreusel 2022))	54
Figure 4-9: Voids detected with CT scans within a sectional plane in the ROI for PA6 GF for hybridization strategies S1 - S4 (Matkovic & Höger et al. 2023)	55
Figure 4-10: Mean shear stress and standard deviation of the individual hybridization strategies and material systems (Matkovic & Höger et al. 2023)	57
Figure 4-11: FRP specimen made of PA6 matrix with integrated UD-tape and a fiber volume fraction of $\varphi_F = 1.032\%$ (based on (DIN EN ISO 527-4))	59
Figure 4-12: Average tensile strengths and standard deviations achieved based on (DIN EN ISO 527-4) for hybridization strategies S2 and S4 for all material systems; Results for specimens without UD-tape (w.t.) reinforcement as reference	60
Figure 4-13: (Left) Distortion of the tensile specimens from the side view: PA6 without UD-tape (w.t.) as reference for S4 of PA6, PA6 GF and PA6 CF; (Right) Average deformation of five analyzed specimens	62
Figure 4-14: Principle setup of the parameterizable model in COMSOL for the stationary simulations with variable factors and constant boundary conditions	65
Figure 4-15: Thermal simulation results for the stationary case of Consolidation I for: a) $W = 30\text{ mm}$, $HS = 2\text{ mm}$, $HU = 2\text{ mm}$, $HA = 0\text{ mm}$, $ID = 100\%$ and $HT = 1$; b) $W = 100\text{ mm}$, $HS = 40\text{ mm}$, $HU = 10\text{ mm}$, $HA = 0\text{ mm}$, $ID = 20\%$ and $HT = 3$ (based on (A_Tritschler 2023))	67
Figure 4-16: Two-factor interaction plot for the temperature reached at the center of the lower interface for the stationary simulation of Consolidation I (based on (A_Tritschler 2023))	68

- Figure 4-17: Two-factor Interaction plot for the temperature reached at the center of the upper interface for the stationary simulation of Consolidation II (based on (A_Tritschler 2023)) 69
- Figure 4-18: Principle setup of the time-dependent model in COMSOL for the dynamic simulations with variable factors and constant boundary conditions 71
- Figure 4-19: Temperature curves at measuring positions 1 to 6 for Consolidation I with and without preheating for $HU = 1$ mm, $v = 10$ mm/s & $HT = 3$ (based on (A_Tritschler 2023)) 73
- Figure 4-20: Temperature curves at measuring points 1 to 6 for Consolidation II with and without preheating for $HU = 1$ mm, $v = 10$ mm/s & $HA = 3$ mm (based on (A_Tritschler 2023)) 73
- Figure 4-21: Influence of radiation preheating during Consolidation I: (Left) Numbering of the 8 simulated factor level combinations; (Right) Average temperature difference of measuring points 1 - 6 from the target temperature of 230 °C with and without radiation preheating (based on (A_Tritschler 2023)) 74
- Figure 4-22: Influence of radiation preheating during Consolidation II: (Left) Numbering of the 8 simulated factor level combinations; (Right) Average temperature difference of measuring points 1 - 6 from the target temperature of 230 °C with and without radiation preheating (based on (A_Tritschler 2023)) 75
- Figure 4-23: Momentary snapshot of the temperature distribution for factor combination No. 8 of Consolidation I, sectional view along half the component width: a) Temperature distribution without radiation preheating; b) Temperature distribution with radiation preheating (based on (A_Tritschler 2023)) 76
- Figure 4-24: Comparison of the temperature curves at measuring positions 1 to 6 for Consolidation I for $THP = 80$ °C, $TCR = 230$ °C, $TPH = 175$ °C, $HT = 1$ and $v = 5$ mm/s: Reference simulation with $HU = 3$ mm and a simulation with $HU = 100$ mm 78
- Figure 4-25: Visualization of Equation 4-5: Temperature TPH set as a function of HU and for selected HO in order to achieve the specified reference temperature in the interface area for Consolidation II 79

Figure 4-26: Overview and configuration of the target system consisting of the main subsystems with the Consolidation Unit, the Assembly Table and the Digital Process Chain and Control Architecture as subsystems still to be developed	81
Figure 5-1: a) Conceptually illustrated Consolidation Unit and its orientation in the direction of movement during consolidation; b) Possible implementation of a part of the Consolidation Unit with an additional seventh rotational axis	84
Figure 5-2: Achievable dextrous workspace for a Kuka KR180 R2500 extra for defined orientations of the end-effector: (Left) Use of the usual six axes; (Right) equipped with an additional seventh axis of rotation in the end-effector (based on (A_Larsch 2024))	85
Figure 5-3: Simplified illustration of the setup for the kinematic analysis to determine the resulting workspace as a function of the positioning of the Assembly Table including additional axes	86
Figure 5-4: Resulting workspace depending on the positioning of the Assembly Table and additional degrees of freedom (based on (A_Larsch 2024))	87
Figure 5-5: Usable workspace based on the world coordinate system as shown in Figure 5-3 with a rotatable and tiltable Assembly Table (based on (A_Larsch 2024))	88
Figure 5-6: Resulting workspace depending on the robot distance and the positioning of the Assembly Table with a rotational degree of freedom around the z-axis (A_Larsch 2024)	89
Figure 5-7: Overview of the entire experimental setup and the subsystems	90
Figure 5-8: Hybrid end-effector for MEX DES and consolidation; switch between MEX DES and consolidation mode by raising and lowering the Consolidation Unit	91
Figure 5-9: Main parts and subsystems of the Consolidation Unit	93
Figure 5-10: Main components for the pneumatic force control of the Consolidation Unit	94
Figure 5-11: Force equilibrium and resulting contact force FC as a function of the angle α of the Consolidation Unit and the applied pressures p_U and p_L	95
Figure 5-12: Calculated pressure distribution along the width of a consolidation and solidification roller in contact with PA6 CF for 6 N and 30 N contact force	97

Figure 5-13: Measured pressure distribution and analyzed area in contact in the lower interface after Consolidation I	99
Figure 5-14: Overview of the setup of the temperature control for the IR-preheating and consolidation roller	100
Figure 5-15: Overview Assembly Table: a) Subsystems five-zone temperature control, kinematic structure & control; b) Use of additional kinematic axis to ensure accessibility here, for example, with a rotation of 180° around its own z-axis	102
Figure 5-16: Measured output rate for PA6 with 30 % CF at 280 °C as a function of the angle of the single-screw extruder Massive Dimension MDPH2 for different RPM103	
Figure 5-17: a) Overview of the kinematic structure of the Assembly Table; b) Rotation around the y-axis from 0-60 ° by extending one linear axis (based on (A_Hinze 2022))	105
Figure 5-18: Overview of the control architecture and communication protocols	106
Figure 5-19: The four main process steps and an example process sequence	108
Figure 5-20: The two subprocess steps of the main process step Consolidation	109
Figure 5-21: Digital process steps and further building blocks for planning an entire manufacturing process	111
Figure 5-22: Four different segment types visualized using the example of a generic component to be manufactured from scratch	111
Figure 5-23: (Left) Digital twin for post-processing and collision control with RoboDK; (Center) GUI and integrated (Right) look-up table for parameterizing the temperature control of the Consolidation Unit subsystem	114
Figure 5-24: Segmentation and non-planar three- to five-axis transformation for the Overprinting, as explained in the example of overprinting curved surfaces	116
Figure 5-25: Prototypical experimental production system for subsequent individualization and individual production of CoDiCoFRP	118
Figure 6-1: Sample dimensions (based on (ASTM D5868-01)) for the tensile shear tests; Constant and variable factors and motion sequence during Consolidation I	122

Figure 6-2: Illustration of the optimum search: Factor variation according to the consolidation model and compliance with the limits of the process window and the damage model	123
Figure 6-3: 100 mm long consolidation tracks carried out with all 125-factor level combinations of the consolidation roller temperature TCR , contact force FC and velocity v based on the process sequence of Consolidation I	124
Figure 6-4: Close-up of selected consolidation tracks from Figure 6-3 and defect catalog with damage values for Consolidation I	125
Figure 6-5: (Left) 3D representation of the damage actually observed for all factor level combinations of the tracks in Consolidation I incl. process window; (Right) calculated damage values based on modeling with regression function	126
Figure 6-6: Histogram and probability plot for τ_{max} , $C1$ show that a normal distribution for Consolidation I can be assumed (based on (A_Beck 2024))	131
Figure 6-7: Main effect diagrams of Consolidation I PA6 CoDiCo CF	132
Figure 6-8: Interaction diagrams of Consolidation I PA6 CoDiCo CF (based on (A_Beck 2024))	133
Figure 6-9: Spline-interpolant plots of τ_{max} , $C1$ for $TCR = 230\text{ }^{\circ}\text{C}$ and $275\text{ }^{\circ}\text{C}$	133
Figure 6-10: Output of the consolidation model $\tau * max, C1TCR, FC, v$ for Consolidation I PA6 CoDiCo CF	135
Figure 6-11: Sample dimensions based on (ASTM D5868-01) for the tensile shear tests; Constant and variable factors and motion sequence during Consolidation II	139
Figure 6-12: 100 mm long consolidation tracks carried out with all 125 factor level combinations of the consolidation roller temperature TCR , contact force FC and velocity v based on the process sequence of Consolidation II	140
Figure 6-13: Close-up of selected consolidation tracks and defect catalog with damage degree for Consolidation II	141
Figure 6-14: (Left) Three-dimensional representation of the damage actually observed for all factor level combinations of the tracks in Consolidation II incl. process window; (Right) Calculated damage values based on modeling with regression function	142

Figure 6-15: Histogram and probability plot for τ_{max} , C2 show that a normal distribution for Consolidation II can be assumed (based on (A_Beck 2024))	144
Figure 6-16: Comparison of the resulting pressure when Overprinting measurement films at 68 RPM and 100 RPM	147
Figure 7-1: (Left) Degree of fulfillment for optimized and non-optimized process parameters using specimen type 2; (Right) Mechanical characteristics for specimen type 1 - 4 for optimized process parameters (based on (A_Beck 2024))	153
Figure 7-2: Based on (ASTM D5868-01) analyzed areas of an LFT sheet made of PA6 DiCo long CF	156
Figure 7-3: Three-dimensional subsequent reinforcement of LFT components with preformed UD-tapes using Robotic Swing Folding	159
Figure 7-4: Subsequently customized LFT sheet using MEX DES 3D printing and Consolidation I	160
Figure 0-1: Evaluation results based on the damage of the 125 tracks of Consolidation I to determine the process window and the damage model in Chapter 6.1.1	XII
Figure 0-2: Evaluation results based on the damage of the 125 tracks of Consolidation II to determine the process window and the damage model in Chapter 6.2.1	XIV

List of Tables

Table 4-1: Overview of material properties (based on ¹ (Matsuo & Hojo et al. 2019) and manufacturer's data sheets ² (Spectrum Group 2021), ³ (3DXTECH 2022a) and ⁴ (3DXTECH 2022b))	47
Table 4-2: Description and quantification of process parameter requirements for the hybridization of Co and DiCoFRP	48
Table 4-3: Experimentally determined process parameters for the hybridization of the UD-tapes with the different material systems of the MEX layers	51
Table 4-4: Voids detected with CT scans within a sectional plane in the ROI for PA6 GF	56
Table 4-5: Material properties required for the calculation of $RFRP$, $, th$ of the tensile specimens (based on ¹ (Matsuo & Hojo et al. 2019) and manufacturer's data sheets ² (Spectrum Group 2021), ³ (3DXTECH 2022a) and ⁴ (3DXTECH 2022b))	61
Table 4-6: Calculated theoretical tensile strengths $RFRP$, $, th$ and degree of fulfillment Df for all material systems, S2 and S4	61
Table 4-7: Material properties used for the thermal simulations (based on (Matsuo & Hojo et al. 2019; Behzad & Sein 2007; A_Tritschler 2023))	66
Table 4-8: Factor levels for the stationary thermal effect simulation of Consolidation I	66
Table 4-9: Factor levels for the stationary thermal effect simulation of Consolidation II	67
Table 4-10: Factor level combinations for the time-dependent dynamic simulations for Consolidation I and II	72
Table 5-1: Main process step to be executed based on the segment type	112
Table 6-1: Constant and variable process parameters/factors for the experimental analysis and optimization of Consolidation I and II	120
Table 6-2: Calculated technical equivalent stress $p * max, CR$ and $p * max, SR$. for the consolidation and solidification rollers for relevant contact forces FC	121
Table 6-3: Process window limits for Consolidation I of PA6 CoDiCo CF material system	127

Table 6-4: Factor levels for the analysis of Consolidation I for the material system PA6 CoDiCo CF	128
Table 6-5: Mean maximum shear stress τ_{max} , $C1$ based on ASTM D5868-01 from Consolidation I PA6 CoDiCo CF (based on (A_Beck 2024))	129
Table 6-6: Failure modes and corresponding factor level combination (based on (A_Beck 2024))	130
Table 6-7: Significance analysis of the factors and their combinations for Consolidation I PA6 CoDiCo CF (based on (A_Beck 2024))	131
Table 6-8: Comparison of optimized and non-optimized factor combinations	137
Table 6-9: Process window limits for Consolidation II of PA6 CoDiCo CF material system	142
Table 6-10: Mean maximum shear stress τ_{max} , $C2$ based on ASTM D5868-01 from Consolidation II PA6 CoDiCo CF (based on (A_Beck 2024))	144
Table 6-11: Mean maximum shear stress τ_{max} , OP from Overprinting PA6 Co CF with PA6 DiCo CF based on ASTM D5868-01	149
Table 7-1: Relevant optimized process parameters of the experiments carried out in this chapter for the process steps Consolidation I and Overprinting	151
Table 7-2: Different layer structures for the specimens based on (DIN EN ISO 20753) as well as relevant properties and mechanical characteristics	151
Table 7-3: Achieved tensile strengths $RFRP$, $, re$ and standard deviations σ based on (DIN EN ISO 527-4) and the resulting degree of fulfillment DF for specimen types 1- 4	152
Table 7-4: Classification of specimen types 1 - 4 produced with optimized process parameters according to the most frequent mode of failure (based on (A_Beck 2024))	154
Table 7-5: Process parameters used for the Consolidation I process with LFT specimens	157
Table 7-6: Results of the shear tests based on (DIN EN ISO 20753) for Consolidation I of LFT sheets	158

Table 0-1: Complete results of the ANOVA analysis for Consolidation I in Chapter 6.1.3

Appendix

Temp. [°C]	Force [N]	Velocity in mm/s				
		1	5	10	15	20
275	30	10	7	6	5	4
	24	10	6	6	4	4
	18	9	6	6	4	4
	12	9	6	5	4	4
	6	8	5	5	4	3
260	30	9	6	6	4	3
	24	9	6	5	3	3
	18	9	6	5	3	3
	12	8	6	5	3	3
	6	8	6	5	3	3
245	30	9	6	5	3	3
	24	9	6	5	3	3
	18	8	6	5	3	3
	12	8	6	5	3	3
	6	7	5	4	2	2
230	30	8	6	5	3	3
	24	8	5	5	3	3
	18	7	5	4	3	3
	12	7	4	4	3	3
	6	6	4	4	2	2
215	30	8	5	3	3	3
	24	7	4	2	2	2
	18	7	3	2	2	2
	12	7	2	2	2	2
	6	6	2	1	1	1

Figure 0-1: Evaluation results based on the damage of the 125 tracks of Consolidation I to determine the process window and the damage model in Chapter 6.1.1

$$\begin{aligned}
 S_{D,C1}(T_{CR}, F_C, v) &= -415.5441 + 4.7854 \frac{1}{\text{°C}} \cdot T_{CR} + 2.2703 \frac{1}{N} \cdot F_C + 0.5794 \frac{1}{\frac{mm}{s}} \cdot v - 0.0181 \frac{1}{\text{°C}^2} \\
 &\cdot T_{CR}^2 - 0.0159 \frac{1}{\text{°C} \cdot N} \cdot T_{CR} \cdot F_C - 0.0123 \frac{1}{N^2} \cdot F_C^2 - 0.0144 \frac{1}{\text{°C} \cdot \frac{mm}{s}} \cdot T_{CR} \cdot v \\
 &- 7.6011 \cdot 10^{-4} \frac{1}{N \cdot \frac{mm}{s}} \cdot F_C \cdot v + 0.0902 \frac{1}{\left(\frac{mm}{s}\right)^2} \cdot v^2 + 2.2716 \cdot 10^{-5} \frac{1}{\text{°C}^3} \cdot T_{CR}^3 \\
 &+ 3.1746 \cdot 10^{-5} \frac{1}{\text{°C}^2 \cdot N} \cdot T_{CR}^2 \cdot F_C - 5.2910 \cdot 10^{-6} \frac{1}{\text{°C} \cdot N^2} \cdot T_{CR} \cdot F_C^2 + 2.4691 \\
 &\cdot 10^{-4} \frac{1}{N^3} \cdot F_C^3 + 3.5157 \cdot 10^{-5} \frac{1}{\text{°C}^2 \cdot \frac{mm}{s}} \cdot T_{CR}^2 \cdot v - 4.7179 \cdot 10^{-6} \frac{1}{\text{°C} \cdot N \cdot \frac{mm}{s}} \\
 &\cdot T_{CR} \cdot F_C \cdot v - 4.6766 \cdot 10^{-5} \frac{1}{N^2 \cdot \frac{mm}{s}} \cdot F_C^2 \cdot v - 1.7340 \cdot 10^{-4} \frac{1}{\text{°C} \cdot \left(\frac{mm}{s}\right)^2} \cdot T_{CR} \\
 &\cdot v^2 + 6.94344 \cdot 10^{-5} \frac{1}{N \cdot \left(\frac{mm}{s}\right)^2} \cdot F_C \cdot v^2 - 0.0010 \frac{1}{\left(\frac{mm/s}\right)^3} \cdot v^3
 \end{aligned}$$

0-1

$T_{CR} \in [215 \text{ °C}; 300 \text{ °C}]; F_C \in [6 N; 30 N]; v \in [1 \text{ mm/s}; 20 \text{ mm/s}];$

Table 0-1: Complete results of the ANOVA analysis for Consolidation I in Chapter 6.1.3

	Df	Sum Sq	Mean Sq	F value	p value	Significance
T_{CR}	1	66.94	66.94	174.353	< 2e-16	***
F_C	1	24.15	24.15	62.890	1.13e-12	***
v	2	113.27	56.63	147.505	< 2e-16	***
$T_{CR} : F_C$	1	6.71	6.71	17.479	5.47e-05	***
$T_{CR} : v$	2	16.57	8.28	21.574	9.31e-09	***
$F_C : v$	2	5.64	2.82	7.345	0.000969	***
$T_{CR} : F_C : v$	2	7.96	3.98	10.362	6.93e-05	***
Residuals	123	47.23	0.38			

Temp. [°C]	Force [N]	Velocity in mm/s				
		1	5	10	15	20
275	30	10	7	6	4	4
	24	10	7	5	4	4
	18	10	7	5	4	4
	12	10	6	5	4	3
	6	10	5	5	3	3
260	30	10	7	6	4	4
	24	10	7	5	4	3
	18	10	6	5	3	3
	12	10	6	5	3	2
	6	10	6	5	3	2
245	30	10	7	5	4	3
	24	10	6	5	4	3
	18	10	6	5	3	2
	12	9	6	5	3	2
	6	9	5	4	3	2
230	30	9	4	3	4	2
	24	9	3	2	4	2
	18	8	3	2	3	2
	12	8	3	2	2	1
	6	8	3	2	2	1
215	30	7	3	2	2	2
	24	7	3	2	2	2
	18	7	3	2	2	2
	12	6	3	2	2	2
	6	6	2	2	1	1

Figure 0-2: Evaluation results based on the damage of the 125 tracks of Consolidation II to determine the process window and the damage model in Chapter 6.2.1

Forschungsberichte aus dem wbk
Institut für Produktionstechnik
Karlsruher Institut für Technologie (KIT)

Bisher erschienene Bände:

Band 0

Dr.-Ing. Wu Hong-qi

Adaptive Volumenstromregelung mit Hilfe von drehzahlgeregelten Elektroantrieben

Band 1

Dr.-Ing. Heinrich Weiß

**Fräsen mit Schneidkeramik - Verhalten des System
Werkzeugmaschine-Werkzeug-Werkstück und Prozessanalyse**

Band 2

Dr.-Ing. Hans-Jürgen Stierle

**Entwicklung und Untersuchung hydrostatischer Lager für die
Axialkolbenmaschine**

Band 3

Dr.-Ing. Herbert Hörner

Untersuchung des Geräuschverhaltens druckgeregelter Axialkolbenpumpen

Band 4

Dr.-Ing. Rolf-Dieter Brückbauer

**Digitale Drehzahlregelung unter der besonderen Berücksichtigung
von Quantisierungseffekten**

Band 5

Dr.-Ing. Gerhard Staiger

Graphisch interaktive NC-Programmierung von Drehteilen im Werkstattbereich

Band 6

Dr.-Ing. Karl Peters

**Ein Beitrag zur Berechnung und Kompensation von Positionierfehlern an
Industrierobotern**

Band 7

Dr.-Ing. Paul Stauss

Automatisierte Inbetriebnahme und Sicherung der Zuverlässigkeit und Verfügbarkeit numerisch gesteuerter Fertigungseinrichtungen

Band 8

Dr.-Ing. Günter Möckesch

Konzeption und Realisierung eines strategischen, integrierten Gesamtplanungs- und -bearbeitungssystems zur Optimierung der Drehteilorganisation für auftragsbezogene Drehereien

Band 9

Dr.-Ing. Thomas Oestreicher

Rechnergestützte Projektierung von Steuerungen

Band 10

Dr.-Ing. Thomas Selinger

Teilautomatisierte werkstattnahe NC-Programmerstellung im Umfeld einer integrierten Informationsverarbeitung

Band 11

Dr.-Ing. Thomas Buchholz

Prozessmodell Fräsen, Rechnerunterstützte Analyse, Optimierung und Überwachung

Band 12

Dr.-Ing. Bernhard Reichling

Lasergestützte Positions- und Bahnvermessung von Industrierobotern

Band 13

Dr.-Ing. Hans-Jürgen Lesser

Rechnergestützte Methoden zur Auswahl anforderungsgerechter Verbindungselemente

Band 14

Dr.-Ing. Hans-Jürgen Lauffer

Einsatz von Prozessmodellen zur rechnerunterstützten Auslegung von Räumwerkzeugen

Band 15

Dr.-Ing. Michael C. Wilhelm

Rechnergestützte Prüfplanung im Informationsverbund moderner Produktionssysteme

Band 16

Dr.-Ing. Martin Ochs

Entwurf eines Programmsystems zur wissensbasierten Planung und Konfigurierung

Band 17

Dr.-Ing. Heinz-Joachim Schneider

Erhöhung der Verfügbarkeit von hochautomatisierten Produktionseinrichtungen mit Hilfe der Fertigungsleittechnik

Band 18

Dr.-Ing. Hans-Reiner Ludwig

Beanspruchungsanalyse der Werkzeugschneiden beim Stirnplanfräsen

Band 19

Dr.-Ing. Rudolf Wieser

Methoden zur rechnergestützten Konfigurierung von Fertigungsanlagen

Band 20

Dr.-Ing. Edgar Schmitt

Werkstattsteuerung bei wechselnder Auftragsstruktur

Band 21

Dr.-Ing. Wilhelm Enderle

Verfügbarkeitssteigerung automatisierter Montagesysteme durch selbsttätige Behebung prozessbedingter Störungen

Band 22

Dr.-Ing. Dieter Buchberger

Rechnergestützte Strukturplanung von Produktionssystemen

Band 23

Prof. Dr.-Ing. Jürgen Fleischer

Rechnerunterstützte Technologieplanung für die flexibel automatisierte Fertigung von Abkantteilen

Band 24

Dr.-Ing. Lukas Loeffler

Adaptierbare und adaptive Benutzerschnittstellen

Band 25

Dr.-Ing. Thomas Friedmann

Integration von Produktentwicklung und Montageplanung durch neue rechnergestützte Verfahren

Band 26

Dr.-Ing. Robert Zurrin

Variables Formhonen durch rechnergestützte Hornprozesssteuerung

Band 27

Dr.-Ing. Karl-Heinz Bergen

Langhub-Innenrundhonen von Grauguss und Stahl mit einem elektromechanischem Vorschubsystem

Band 28

Dr.-Ing. Andreas Liebisch

Einflüsse des Festwalzens auf die Eigenspannungsverteilung und die Dauerfestigkeit einsatzgehärteter Zahnräder

Band 29

Dr.-Ing. Rolf Ziegler

Auslegung und Optimierung schneller Servopumpen

Band 30

Dr.-Ing. Rainer Bartl

Datenmodellgestützte Wissensverarbeitung zur Diagnose und Informationsunterstützung in technischen Systemen

Band 31

Dr.-Ing. Ulrich Golz

Analyse, Modellbildung und Optimierung des Betriebsverhaltens von Kugelgewindetrieben

Band 32

Dr.-Ing. Stephan Timmermann

Automatisierung der Feinbearbeitung in der Fertigung von Hohlformwerkzeugen

Band 33

Dr.-Ing. Thomas Noe

Rechnergestützter Wissenserwerb zur Erstellung von Überwachungs- und Diagnoseexpertensystemen für hydraulische Anlagen

Band 34

Dr.-Ing. Ralf Lenschow

Rechnerintegrierte Erstellung und Verifikation von Steuerungsprogrammen als Komponente einer durchgängigen Planungsmethodik

Band 35

Dr.-Ing. Matthias Kallabis

Räumen gehärteter Werkstoffe mit kristallinen Hartstoffen

Band 36

Dr.-Ing. Heiner-Michael Honeck

Rückführung von Fertigungsdaten zur Unterstützung einer fertigungsgerechten Konstruktion

Band 37

Dr.-Ing. Manfred Rohr

Automatisierte Technologieplanung am Beispiel der Komplettbearbeitung auf Dreh-/Fräszellen

Band 38

Dr.-Ing. Martin Steuer

Entwicklung von Softwarewerkzeugen zur wissensbasierten Inbetriebnahme von komplexen Serienmaschinen

Band 39

Dr.-Ing. Siegfried Beichter

Rechnergestützte technische Problemlösung bei der Angebotserstellung von flexiblen Drehzellen

Band 40

Dr.-Ing. Thomas Steitz

Methodik zur marktorientierten Entwicklung von Werkzeugmaschinen mit Integration von funktionsbasierter Strukturierung und Kostenschätzung

Band 41

Dr.-Ing. Michael Richter

Wissensbasierte Projektierung elektrohydraulischer Regelungen

Band 42

Dr.-Ing. Roman Kuhn

Technologieplanungssystem Fräsen. Wissensbasierte Auswahl von Werkzeugen, Schneidkörpern und Schnittbedingungen für das Fertigungsverfahren Fräsen

Band 43

Dr.-Ing. Hubert Klein

Rechnerunterstützte Qualitätssicherung bei der Produktion von Bauteilen mit frei geformten Oberflächen

Band 44

Dr.-Ing. Christian Hoffmann

Konzeption und Realisierung eines fertigungsintegrierten Koordinatenmessgerätes

Band 45

Dr.-Ing. Volker Frey

Planung der Leittechnik für flexible Fertigungsanlagen

Band 46

Dr.-Ing. Achim Feller

Kalkulation in der Angebotsphase mit dem selbsttätig abgeleiteten Erfahrungswissen der Arbeitsplanung

Band 47

Dr.-Ing. Markus Klaiber

Produktivitätssteigerung durch rechnerunterstütztes Einfahren von NC-Programmen

Band 48

Dr.-Ing. Roland Minges

Verbesserung der Genauigkeit beim fünfachsigen Fräsen von Freiformflächen

Band 49

Dr.-Ing. Wolfgang Bernhart

Beitrag zur Bewertung von Montagevarianten: Rechnergestützte Hilfsmittel zur kostenorientierten, parallelen Entwicklung von Produkt und Montagesystem

Band 50

Dr.-Ing. Peter Ganghoff

**Wissensbasierte Unterstützung der Planung technischer Systeme:
Konzeption eines Planungswerkzeuges und exemplarische Anwendung
im Bereich der Montagesystemplanung**

Band 51

Dr.-Ing. Frank Maier

**Rechnergestützte Prozessregelung beim flexiblen Gesenkbiegen durch
Rückführung von Qualitätsinformationen**

Band 52

Dr.-Ing. Frank Debus

**Ansatz eines rechnerunterstützten Planungsmanagements für die Planung
in verteilten Strukturen**

Band 53

Dr.-Ing. Joachim Weinbrecht

**Ein Verfahren zur zielorientierten Reaktion auf Planabweichungen in der
Werkstattregelung**

Band 54

Dr.-Ing. Gerd Herrmann

**Reduzierung des Entwicklungsaufwandes für anwendungsspezifische
Zellenrechnersoftware durch Rechnerunterstützung**

Band 55

Dr.-Ing. Robert Wassmer

**Verschleissentwicklung im tribologischen System Fräsen: Beiträge
zur Methodik der Prozessmodellierung auf der Basis tribologischer
Untersuchungen beim Fräsen**

Band 56

Dr.-Ing. Peter Uebelhoer

Inprocess-Geometriemessung beim Honen

Band 57

Dr.-Ing. Hans-Joachim Schelberg

Objektorientierte Projektierung von SPS-Software

Band 58

Dr.-Ing. Klaus Boes

Integration der Qualitätsentwicklung in featurebasierte CAD/CAM-Prozessketten

Band 59

Dr.-Ing. Martin Schreiber

Wirtschaftliche Investitionsbewertung komplexer Produktionssysteme unter Berücksichtigung von Unsicherheit

Band 60

Dr.-Ing. Ralf Steuernagel

Offenes adaptives Engineering-Werkzeug zur automatisierten Erstellung von entscheidungsunterstützenden Informationssystemen

Band 62

Dr.-Ing. Uwe Schauer

Qualitätsorientierte Feinbearbeitung mit Industrierobotern: Regelungsansatz für die Freiformflächenfertigung des Werkzeug- und Formenbaus

Band 63

Dr.-Ing. Simone Loeper

Kennzahlengestütztes Beratungssystem zur Verbesserung der Logistikleistung in der Werkstattfertigung

Band 64

Dr.-Ing. Achim Raab

Räumen mit hartstoffbeschichteten HSS-Werkzeugen

Band 65,

Dr.-Ing. Jan Erik Burghardt

Unterstützung der NC-Verfahrenskette durch ein bearbeitungselementorientiertes, lernfähiges Technologieplanungssystem

Band 66

Dr.-Ing. Christian Tritsch

Flexible Demontage technischer Gebrauchsgüter: Ansatz zur Planung und (teil-)automatisierten Durchführung industrieller Demontageprozesse

Band 67

Dr.-Ing. Oliver Eitrich

Prozessorientiertes Kostenmodell für die entwicklungsbegleitende Vorkalkulation

Band 68

Dr.-Ing. Oliver Wilke

Optimierte Antriebskonzepte für Räummaschinen - Potentiale zur Leistungssteigerung

Band 69

Dr.-Ing. Thilo Sieth

Rechnergestützte Modellierungsmethodik zerspantechnologischer Prozesse

Band 70

Dr.-Ing. Jan Linnenbuerger

Entwicklung neuer Verfahren zur automatisierten Erfassung der geometrischen Abweichungen an Linearachsen und Drehschwenkköpfen

Band 71

Dr.-Ing. Mathias Klimmek

Fraktionierung technischer Produkte mittels eines frei beweglichen Wasserstrahlwerkzeuges

Band 72

Dr.-Ing. Marko Hartel

Kennzahlenbasiertes Bewertungssystem zur Beurteilung der Demontage- und Recyclingeignung von Produkten

Band 73

Dr.-Ing. Jörg Schaupp

Wechselwirkung zwischen der Maschinen- und Hauptspindelantriebsdynamik und dem Zerspanprozess beim Fräsen

Band 74

Dr.-Ing. Bernhard Neisius

Konzeption und Realisierung eines experimentellen Telemanipulators für die Laparoskopie

Band 75

Dr.-Ing. Wolfgang Walter

Erfolgsversprechende Muster für betriebliche Ideenfindungsprozesse. Ein Beitrag zur Steigerung der Innovationsfähigkeit

Band 76

Dr.-Ing. Julian Weber

Ein Ansatz zur Bewertung von Entwicklungsergebnissen in virtuellen Szenarien

Band 77

Dr.-Ing. Dipl. Wirtsch.-Ing. Markus Posur

Unterstützung der Auftragsdurchsetzung in der Fertigung durch Kommunikation über mobile Rechner

Band 78

Dr.-Ing. Frank Fleissner

Prozessorientierte Prüfplanung auf Basis von Bearbeitungsobjekten für die Kleinserienfertigung am Beispiel der Bohr- und Fräsbearbeitung

Band 79

Dr.-Ing. Anton Haberkern

Leistungsfähigere Kugelgewindetriebe durch Beschichtung

Band 80

Dr.-Ing. Dominik Matt

Objektorientierte Prozess- und Strukturinnovation (OPUS)

Band 81

Dr.-Ing. Jürgen Andres

Robotersysteme für den Wohnungsbau: Beitrag zur Automatisierung des Mauerwerkbaus und der Elektroinstallation auf Baustellen

Band 82

Dr.-Ing. Dipl. Wirtschaftsing. Simone Riedmiller

Der Prozesskalender - Eine Methodik zur marktorientierten Entwicklung von Prozessen

Band 83

Dr.-Ing. Dietmar Tilch

Analyse der Geometrieparameter von Präzisionsgewinden auf der Basis einer Least-Squares-Estimation

Band 84

Dr.-Ing. Dipl.-Kfm. Oliver Stiefbold

Konzeption eines reaktionsschnellen Planungssystems für Logistikketten auf Basis von Software-Agenten

Band 85

Dr.-Ing. Ulrich Walter

Einfluss von Kühlschmierstoff auf den Zerspanprozess beim Fräsen: Beitrag zum Prozessverständnis auf Basis von zerspanntechnischen Untersuchungen

Band 86

Dr.-Ing. Bernd Werner

Konzeption von teilautonomer Gruppenarbeit unter Berücksichtigung kultureller Einflüsse

Band 87

Dr.-Ing. Ulf Osmers

Projektieren Speicherprogrammierbarer Steuerungen mit Virtual Reality

Band 88

Dr.-Ing. Oliver Doerfel

Optimierung der Zerspantechnik beim Fertigungsverfahren Wälzstossen: Analyse des Potentials zur Trockenbearbeitung

Band 89

Dr.-Ing. Peter Baumgartner

Stufenmethode zur Schnittstellengestaltung in der internationalen Produktion

Band 90

Dr.-Ing. Dirk Vossmann

Wissensmanagement in der Produktentwicklung durch Qualitätsmethodenverbund und Qualitätsmethodenintegration

Band 91

Dr.-Ing. Martin Plass

Beitrag zur Optimierung des Honprozesses durch den Aufbau einer Honprozessregelung

Band 92

Dr.-Ing. Titus Konold

Optimierung der Fünffachsfräsbearbeitung durch eine kennzahlenunterstützte CAM-Umgebung

Band 93

Dr.-Ing. Jürgen Brath

Unterstützung der Produktionsplanung in der Halbleiterfertigung durch risikoberücksichtigende Betriebskennlinien

Band 94

Dr.-Ing. Dirk Geisinger

Ein Konzept zur marktorientierten Produktentwicklung

Band 95

Dr.-Ing. Marco Lanza

Entwurf der Systemunterstützung des verteilten Engineering mit Axiomatic Design

Band 96

Dr.-Ing. Volker Hüntrup

Untersuchungen zur Mikrostrukturierbarkeit von Stählen durch das Fertigungsverfahren Fräsen

Band 97

Dr.-Ing. Frank Reinboth

Interne Stützung zur Genauigkeitsverbesserung in der Inertialmesstechnik: Beitrag zur Senkung der Anforderungen an Inertialsensoren

Band 98

Dr.-Ing. Lutz Trender

Entwicklungsintegrierte Kalkulation von Produktlebenszykluskosten auf Basis der ressourcenorientierten Prozesskostenrechnung

Band 99

Dr.-Ing. Cornelia Kafka

Konzeption und Umsetzung eines Leitfadens zum industriellen Einsatz von Data-Mining

Band 100

Dr.-Ing. Gebhard Selinger

Rechnerunterstützung der informellen Kommunikation in verteilten Unternehmensstrukturen

Band 101

Dr.-Ing. Thomas Windmüller

Verbesserung bestehender Geschäftsprozesse durch eine mitarbeiterorientierte Informationsversorgung

Band 102

Dr.-Ing. Knud Lembke

Theoretische und experimentelle Untersuchung eines bistabilen elektrohydraulischen Linearantriebs

Band 103

Dr.-Ing. Ulrich Thies

Methode zur Unterstützung der variantengerechten Konstruktion von industriell eingesetzten Kleingeräten

Band 104

Dr.-Ing. Andreas Schmäzle

Bewertungssystem für die Generalüberholung von Montageanlagen –Ein Beitrag zur wirtschaftlichen Gestaltung geschlossener Facility- Management-Systeme im Anlagenbau

Band 105

Dr.-Ing. Thorsten Frank

Vergleichende Untersuchungen schneller elektromechanischer Vorschubachsen mit Kugelgewindetrieb

Band 106

Dr.-Ing. Achim Agostini

Reihenfolgeplanung unter Berücksichtigung von Interaktionen: Beitrag zur ganzheitlichen Strukturierung und Verarbeitung von Interaktionen von Bearbeitungsobjekten

Band 107

Dr.-Ing. Thomas Barrho

Flexible, zeitfenstergesteuerte Auftragseinplanung in segmentierten Fertigungsstrukturen

Band 108

Dr.-Ing. Michael Scharer

Quality Gate-Ansatz mit integriertem Risikomanagement

Band 109

Dr.-Ing. Ulrich Suchy

**Entwicklung und Untersuchung eines neuartigen Mischkopfes für das Wasser
Abrasive Strahl schneiden**

Band 110

Dr.-Ing. Sellal Mussa

Aktive Korrektur von Verlagerungsfehlern in Werkzeugmaschinen

Band 111

Dr.-Ing. Andreas Hühsam

Modellbildung und experimentelle Untersuchung des Wälzschälprozesses

Band 112

Dr.-Ing. Axel Plutowsky

**Charakterisierung eines optischen Messsystems und den Bedingungen des
Arbeitsraums einer Werkzeugmaschine**

Band 113

Dr.-Ing. Robert Landwehr

**Konsequent dezentralisierte Steuerung mit Industrial Ethernet und offenen
Applikationsprotokollen**

Band 114

Dr.-Ing. Christoph Dill

Turbulenzreaktionsprozesse

Band 115

Dr.-Ing. Michael Baumeister

Fabrikplanung im turbulenten Umfeld

Band 116

Dr.-Ing. Christoph Gönninger

**Konzept zur Verbesserung der Elektromagnetischen Verträglichkeit (EMV) in
Produktionssystemen durch intelligente Sensor/Aktor-Anbindung**

Band 117

Dr.-Ing. Lutz Demuß

**Ein Reifemodell für die Bewertung und Entwicklung von Dienstleistungs-
organisationen: Das Service Management Maturity Modell (SMMM)**

Band 118

Dr.-Ing. Jörg Söhner

Beitrag zur Simulation zerspanungstechnologischer Vorgänge mit Hilfe der Finite-Element-Methode

Band 119

Dr.-Ing. Judith Elsner

Informationsmanagement für mehrstufige Mikro-Fertigungsprozesse

Band 120

Dr.-Ing. Lijing Xie

Estimation Of Two-dimension Tool Wear Based On Finite Element Method

Band 121

Dr.-Ing. Ansgar Blessing

Geometrischer Entwurf mikromechatronischer Systeme

Band 122

Dr.-Ing. Rainer Ebner

Steigerung der Effizienz mehrachsiger Fräsprozesse durch neue Planungsmethoden mit hoher Benutzerunterstützung

Band 123

Dr.-Ing. Silja Klinkel

Multikriterielle Feinplanung in teilautonomen Produktionsbereichen – Ein Beitrag zur produkt- und prozessorientierten Planung und Steuerung

Band 124

Dr.-Ing. Wolfgang Neithardt

Methodik zur Simulation und Optimierung von Werkzeugmaschinen in der Konzept- und Entwurfsphase auf Basis der Mehrkörpersimulation

Band 125

Dr.-Ing. Andreas Mehr

Hartfeinbearbeitung von Verzahnungen mit kristallinen diamantbeschichteten Werkzeugen beim Fertigungsverfahren Wälzstoßen

Band 126

Dr.-Ing. Martin Gutmann

Entwicklung einer methodischen Vorgehensweise zur Diagnose von hydraulischen Produktionsmaschinen

Band 127

Dr.-Ing. Gisela Lanza

Simulative Anlaufunterstützung auf Basis der Qualitätsfähigkeiten von Produktionsprozessen

Band 128

Dr.-Ing. Ulf Dambacher

Kugelgewindetrieb mit hohem Druckwinkel

Band 129

Dr.-Ing. Carsten Buchholz

Systematische Konzeption und Aufbau einer automatisierten Produktionszelle für pulverspritzgegossene Mikroteile

Band 130

Dr.-Ing. Heiner Lang

Trocken-Räumen mit hohen Schnittgeschwindigkeiten

Band 131

Dr.-Ing. Daniel Nesges

Prognose operationeller Verfügbarkeiten von Werkzeugmaschinen unter Berücksichtigung von Serviceleistungen

Im Shaker Verlag erschienene Bände:

Band 132

Dr.-Ing. Andreas Bechle

Beitrag zur prozesssicheren Bearbeitung beim Hochleistungsfertigungsverfahren Wälzschälern

Band 133

Dr.-Ing. Markus Herm

Konfiguration globaler Wertschöpfungsnetzwerke auf Basis von Business Capabilities

Band 134

Dr.-Ing. Hanno Tritschler

Werkzeug- und Zerspanprozessoptimierung beim Hartfräsen von Mikrostrukturen in Stahl

Band 135

Dr.-Ing. Christian Munzinger

**Adaptronische Strebe zur Steifigkeitssteigerung
von Werkzeugmaschinen**

Band 136

Dr.-Ing. Andreas Stepping

**Fabrikplanung im Umfeld von Wertschöpfungsnetzwerken und
ganzheitlichen Produktionssystemen**

Band 137

Dr.-Ing. Martin Dyck

**Beitrag zur Analyse thermische bedingter Werkstückdeformationen
in Trockenbearbeitungsprozessen**

Band 138

Dr.-Ing. Siegfried Schmalzried

**Dreidimensionales optisches Messsystem für eine effizientere
geometrische Maschinenbeurteilung**

Band 139

Dr.-Ing. Marc Wawerla

Risikomanagement von Garantieleistungen

Band 140

Dr.-Ing. Ivesa Buchholz

**Strategien zur Qualitätssicherung mikromechanischer Bauteile
mittels multisensorieller Koordinatenmesstechnik**

Band 141

Dr.-Ing. Jan Kotschenreuther

**Empirische Erweiterung von Modellen der Makrozerspannung
auf den Bereich der Mikrobearbeitung**

Band 142

Dr.-Ing. Andreas Knödel

Adaptronische hydrostatische Drucktascheneinheit

Band 143

Dr.-Ing. Gregor Stengel

**Fliegendes Abtrennen räumlich gekrümmter Strangpressprofile mittels
Industrierobotern**

Band 144

Dr.-Ing. Udo Weismann

Lebenszyklusorientiertes interorganisationelles Anlagencontrolling

Band 145

Dr.-Ing. Rüdiger Pabst

Mathematische Modellierung der Wärmestromdichte zur Simulation des thermischen Bauteilverhaltens bei der Trockenbearbeitung

Band 146

Dr.-Ing. Jan Wieser

Intelligente Instandhaltung zur Verfügbarkeitssteigerung von Werkzeugmaschinen

Band 147

Dr.-Ing. Sebastian Haupt

Effiziente und kostenoptimale Herstellung von Mikrostrukturen durch eine Verfahrenskombination von Bahnerosion und Laserablation

Band 148

Dr.-Ing. Matthias Schlipf

Statistische Prozessregelung von Fertigungs- und Messprozess zur Erreichung einer variabilitätsarmen Produktion mikromechanischer Bauteile

Band 149

Dr.-Ing. Jan Philipp Schmidt-Ewig

Methodische Erarbeitung und Umsetzung eines neuartigen Maschinenkonzeptes zur produktflexiblen Bearbeitung räumlich gekrümmter Strangpressprofile

Band 150

Dr.-Ing. Thomas Ender

Prognose von Personalbedarfen im Produktionsanlauf unter Berücksichtigung dynamischer Planungsgrößen

Band 151

Dr.-Ing. Kathrin Peter

Bewertung und Optimierung der Effektivität von Lean Methoden in der Kleinserienproduktion

Band 152

Dr.-Ing. Matthias Schopp

Sensorbasierte Zustandsdiagnose und -prognose von Kugelgewindetrieben

Band 153

Dr.-Ing. Martin Kipfmüller

Aufwandsoptimierte Simulation von Werkzeugmaschinen

Band 154

Dr.-Ing. Carsten Schmidt

Development of a database to consider multi wear mechanisms within chip forming simulation

Band 155

Dr.-Ing. Stephan Niggeschmidt

Ausfallgerechte Ersatzteilbereitstellung im Maschinen- und Anlagenbau mittels lastabhängiger Lebensdauerprognose

Band 156

Dr.-Ing. Jochen Conrad Peters

Bewertung des Einflusses von Formabweichungen in der Mikro-Koordinatenmesstechnik

Band 157

Dr.-Ing. Jörg Ude

Entscheidungsunterstützung für die Konfiguration globaler Wertschöpfungsnetzwerke

Band 158

Dr.-Ing. Stefan Weiler

Strategien zur wirtschaftlichen Gestaltung der globalen Beschaffung

Band 159

Dr.-Ing. Jan Rühl

Monetäre Flexibilitäts- und Risikobewertung

Band 160

Dr.-Ing. Daniel Ruch

Positions- und Konturerfassung räumlich gekrümmter Profile auf Basis bauteilimmanenter Markierungen

Band 161

Dr.-Ing. Manuel Tröndle

Flexible Zuführung von Mikrobauteilen mit piezoelektrischen Schwingförderern

Band 162

Dr.-Ing. Benjamin Viering

Mikroverzahnungsnormal

Band 163

Dr.-Ing. Chris Becke

Prozesskraftrichtungsangepasste Frässtrategien zur schädigungsarmen Bohrungsbearbeitung an faserverstärkten Kunststoffen

Band 164

Dr.-Ing. Patrick Werner

Dynamische Optimierung und Unsicherheitsbewertung der lastabhängigen präventiven Instandhaltung von Maschinenkomponenten

Band 165

Dr.-Ing. Martin Weis

Kompensation systematischer Fehler bei Werkzeugmaschinen durch self-sensing Aktoren

Band 166

Dr.-Ing. Markus Schneider

Kompensation von Konturabweichungen bei gerundeten Strangpressprofilen durch robotergestützte Führungswerkzeuge

Band 167

Dr.-Ing. Ester M. R. Ruprecht

Prozesskette zur Herstellung schichtbasierter Systeme mit integrierten Kavitäten

Band 168

Dr.-Ing. Alexander Broos

Simulationsgestützte Ermittlung der Komponentenbelastung für die Lebensdauerprognose an Werkzeugmaschinen

Band 169

Dr.-Ing. Frederik Zanger

Segmentspannbildung, Werkzeugverschleiß, Randschichtzustand und Bauteileigenschaften: Numerische Analysen zur Optimierung des Zerspanungsprozesses am Beispiel von Ti-6Al-4V

Band 170

Dr.-Ing. Benjamin Behmann

Servicefähigkeit

Band 171

Dr.-Ing. Annabel Gabriele Jondral

Simulationsgestützte Optimierung und Wirtschaftlichkeitsbewertung des Lean-Methodeneinsatzes

Band 172

Dr.-Ing. Christoph Ruhs

Automatisierte Prozessabfolge zur qualitätssicheren Herstellung von Kavitäten mittels Mikrobahnerosion

Band 173

Dr.-Ing. Steven Peters

Markoffsche Entscheidungsprozesse zur Kapazitäts- und Investitionsplanung von Produktionssystemen

Band 174

Dr.-Ing. Christoph Kühlewein

Untersuchung und Optimierung des Wälzschälverfahrens mit Hilfe von 3D-FEM-Simulation – 3D-FEM Kinematik- und Spannbildungssimulation

Band 175

Dr.-Ing. Adam-Mwanga Dieckmann

Auslegung und Fertigungsprozessgestaltung sintergefügter Verbindungen für μ MIM-Bauteile

Band 176

Dr.-Ing. Heiko Hennrich

Aufbau eines kombinierten belastungs- und zustandsorientierten Diagnose- und Prognosesystems für Kugelgewindetriebe

Band 177

Dr.-Ing. Stefan Herder

Piezoelektrischer Self-Sensing-Aktor zur Vorspannungsregelung in adaptiven Kugelgewindetriebe

Band 178

Dr.-Ing. Alexander Ochs

Ultraschall-Strömungsgreifer für die Handhabung textiler Halbzeuge bei der automatisierten Fertigung von RTM-Bauteilen

Band 179

Dr.-Ing. Jürgen Michna

Numerische und experimentelle Untersuchung zerspanungsbedingter Gefügeumwandlungen und Modellierung des thermo-mechanischen Lastkollektivs beim Bohren von 42CrMo4

Band 180

Dr.-Ing. Jörg Elser

Vorrichtungsfreie räumliche Anordnung von Fügepartnern auf Basis von Bauteilmarkierungen

Band 181

Dr.-Ing. Katharina Klimscha

Einfluss des Fügespalts auf die erreichbare Verbindungsqualität beim Sinterfügen

Band 182

Dr.-Ing. Patricia Weber

Steigerung der Prozesswiederholbarkeit mittels Analyse akustischer Emissionen bei der Mikrolaserablation mit UV-Pikosekundenlasern

Band 183

Dr.-Ing. Jochen Schädel

Automatisiertes Fügen von Tragprofilen mittels Faserwickeln

Band 184

Dr.-Ing. Martin Krauß

Aufwandsoptimierte Simulation von Produktionsanlagen durch Vergrößerung der Geltungsbereiche von Teilmodellen

Band 185

Dr.-Ing. Raphael Moser

Strategische Planung globaler Produktionsnetzwerke

Bestimmung von Wandlungsbedarf und Wandlungszeitpunkt mittels multikriterieller Optimierung

Band 186

Dr.-Ing. Martin Otter

Methode zur Kompensation fertigungsbedingter Gestaltabweichungen für die Montage von Aluminium Space-Frame-Strukturen

Band 187

Dr.-Ing. Urs Leberle

Produktive und flexible Gleitförderung kleiner Bauteile auf phasenflexiblen Schwingförderern mit piezoelektrischen 2D-Antriebs-elementen

Band 188

Dr.-Ing. Johannes Book

Modellierung und Bewertung von Qualitätsmanagementstrategien in globalen Wertschöpfungsnetzwerken

Band 189

Dr.-Ing. Florian Ambrosy

Optimierung von Zerspanungsprozessen zur prozesssicheren Fertigung nanokristalliner Randschichten am Beispiel von 42CrMo4

Band 190

Dr.-Ing. Adrian Kölmel

Integrierte Messtechnik für Prozessketten unreifer Technologien am Beispiel der Batterieproduktion für Elektrofahrzeuge

Band 191

Dr.-Ing. Henning Wagner

Featurebasierte Technologieplanung zum Preforming von textilen Halbzeugen

Band 192

Dr.-Ing. Johannes Gebhardt

Strukturoptimierung von in FVK eingebetteten metallischen Lasteinleitungselementen

Band 193

Dr.-Ing. Jörg Bauer

Hochintegriertes hydraulisches Vorschubsystem für die Bearbeitung kleiner Werkstücke mit hohen Fertigungsanforderungen

Band 194

Dr.-Ing. Nicole Stricker

Robustheit verketteter Produktionssysteme

Robustheitsevaluation und Selektion des Kennzahlensystems der Robustheit

Band 195

Dr.-Ing. Anna Sauer

Konfiguration von Montagelinien unreifer Produkttechnologien am Beispiel der Batteriemontage für Elektrofahrzeuge

Band 196

Dr.-Ing. Florian Sell-Le Blanc

Prozessmodell für das Linearwickeln unrunder Zahnspulen

Ein Beitrag zur orthozyklischen Spulenwickeltechnik

Band 197

Dr.-Ing. Frederic Förster

Geregeltes Handhabungssystem zum zuverlässigen und energieeffizienten Handling textiler Kohlenstofffaserzuschnitte

Band 198

Dr.-Ing. Nikolay Boev

Numerische Beschreibung von Wechselwirkungen zwischen Zerspanprozess und Maschine am Beispiel Räumen

Band 199

Dr.-Ing. Sebastian Greinacher

Simulationsgestützte Mehrzieloptimierung schlanker und ressourceneffizienter Produktionssysteme

Band 200

Dr.-Ing. Benjamin Häfner

Lebensdauerprognose in Abhängigkeit der Fertigungsabweichungen bei Mikroverzahnungen

Band 201

Dr.-Ing. Stefan Klotz

Dynamische Parameteranpassung bei der Bohrungsherstellung in faserverstärkten Kunststoffen unter zusätzlicher Berücksichtigung der Einspannsituation

Band 202

Dr.-Ing. Johannes Stoll

Bewertung konkurrierender Fertigungsfolgen mittels Kostensimulation und stochastischer Mehrzieloptimierung

Anwendung am Beispiel der Blechpaketfertigung für automobiler Elektromotoren

Band 203

Dr.-Ing. Simon-Frederik Koch

Fügen von Metall-Faserverbund-Hybridwellen im Schleuderverfahren

ein Beitrag zur fertigungsgerechten intrinsischen Hybridisierung

Band 204

Dr.-Ing. Julius Ficht

Numerische Untersuchung der Eigenspannungsentwicklung für sequenzielle Zerspanungsprozesse

Band 205

Dr.-Ing. Manuel Baumeister

Automatisierte Fertigung von Einzelblattstapeln in der Lithium-Ionen-Zellproduktion

Band 206

Dr.-Ing. Daniel Bertsch

Optimierung der Werkzeug- und Prozessauslegung für das Wälzschälen von Innenverzahnungen

Band 207

Dr.-Ing. Kyle James Kippenbrock

Deconvolution of Industrial Measurement and Manufacturing Processes for Improved Process Capability Assessments

Band 208

Dr.-Ing. Farboud Bejnoud

Experimentelle Prozesskettenbetrachtung für Räumbauteile am Beispiel einer einsatzgehärteten PKW-Schiebemuffe

Band 209

Dr.-Ing. Steffen Dosch

Herstellungsübergreifende Informationsübertragung zur effizienten Produktion von Werkzeugmaschinen am Beispiel von Kugelgewindetrieben

Band 210

Dr.-Ing. Emanuel Moser

Migrationsplanung globaler Produktionsnetzwerke

Bestimmung robuster Migrationspfade und risiko-effizienter Wandlungsbefähiger

Band 211

Dr.-Ing. Jan Hochdörffer

Integrierte Produktallokationsstrategie und Konfigurationssequenz in globalen Produktionsnetzwerken

Band 212

Dr.-Ing. Tobias Arndt

Bewertung und Steigerung der Prozessqualität in globalen Produktionsnetzwerken

Band 213

Dr.-Ing. Manuel Peter

Unwuchtminimale Montage von Permanentmagnetrotoren durch modellbasierte Online-Optimierung

Band 214

Dr.-Ing. Robin Kopf

Kostenorientierte Planung von Fertigungsfolgen additiver Technologien

Band 215

Dr.-Ing. Harald Meier

**Einfluss des Räumens auf den Bauteilzustand in der Prozesskette
Weichbearbeitung – Wärmebehandlung – Hartbearbeitung**

Band 216

Dr.-Ing. Daniel Brabandt

**Qualitätssicherung von textilen Kohlenstofffaser-Preforms mittels
optischer Messtechnik**

Band 217

Dr.-Ing. Alexandra Schabunow

**Einstellung von Aufnahmeparametern mittels projektionsbasierter Qualitäts-
kenngrößen in der industriellen Röntgen-Computertomographie**

Band 218

Dr.-Ing. Jens Bürgin

Robuste Auftragsplanung in Produktionsnetzwerken

Mittelfristige Planung der variantenreichen Serienproduktion unter Unsicherheit der Kundenauftragskonfigurationen

Band 219

Dr.-Ing. Michael Gerstenmeyer

**Entwicklung und Analyse eines mechanischen Oberflächenbehandlungs-
verfahrens unter Verwendung des Zerspanungswerkzeuges**

Band 220

Dr.-Ing. Jacques Burtscher

**Erhöhung der Bearbeitungsstabilität von Werkzeugmaschinen durch
semi-passive masseneinstellbare Dämpfungssysteme**

Band 221

Dr.-Ing. Dietrich Berger

**Qualitätssicherung von textilen Kohlenstofffaser-Preforms mittels prozess-
integrierter Wirbelstromsensor-Arrays**

Band 222

Dr.-Ing. Fabian Johannes Ballier

Systematic gripper arrangement for a handling device in lightweight production processes

Band 223

Dr.-Ing. Marielouise Schäferling, geb. Zaiß

Development of a Data Fusion-Based Multi-Sensor System for Hybrid Sheet Molding Compound

Band 224

Dr.-Ing. Quirin Spiller

Additive Herstellung von Metallbauteilen mit dem ARBURG Kunststoff-Freiformen

Band 225

Dr.-Ing. Andreas Spohrer

Steigerung der Ressourceneffizienz und Verfügbarkeit von Kugelgewindetrieben durch adaptive Schmierung

Band 226

Dr.-Ing. Johannes Fisel

Veränderungsfähigkeit getakteter Fließmontagesysteme

Planung der Fließbandabstimmung am Beispiel der Automobilmontage

Band 227

Dr.-Ing. Patrick Bollig

Numerische Entwicklung von Strategien zur Kompensation thermisch bedingter Verzüge beim Bohren von 42CrMo4

Band 228

Dr.-Ing. Ramona Pfeiffer, geb. Singer

Untersuchung der prozessbestimmenden Größen für die anforderungsgerechte Gestaltung von Pouchzellen-Verpackungen

Band 229

Dr.-Ing. Florian Baumann

Additive Fertigung von endlosfaserverstärkten Kunststoffen mit dem ARBURG Kunststoff-Freiform Verfahren

Band 230

Dr.-Ing. Tom Stähr

Methodik zur Planung und Konfigurationsauswahl skalierbarer Montagesysteme – Ein Beitrag zur skalierbaren Automatisierung

Band 231

Dr.-Ing. Jan Schwennen

Einbringung und Gestaltung von Lasteinleitungsstrukturen für im RTM-Verfahren hergestellte FVK-Sandwichbauteile

Band 232

Dr.-Ing. Sven Coutandin

Prozessstrategien für das automatisierte Preforming von bebinderten textilen Halbzeugen mit einem segmentierten Werkzeugsystem

Band 233

Dr.-Ing. Christoph Liebrecht

Entscheidungsunterstützung für den Industrie 4.0-Methodeneinsatz
Strukturierung, Bewertung und Ableitung von Implementierungsreihenfolgen

Band 234

Dr.-Ing. Stefan Treber

Transparenzsteigerung in Produktionsnetzwerken
Verbesserung des Störungsmanagements durch verstärkten Informationsaustausch

Band 235

Dr.-Ing. Marius Dackweiler

Modellierung des Fügewickelprozesses zur Herstellung von leichten Fachwerkstrukturen

Band 236

Dr.-Ing. Fabio Echsler Minguillon

Prädiktiv-reaktives Scheduling zur Steigerung der Robustheit in der Matrix-Produktion

Band 237

Dr.-Ing. Sebastian Haag

Entwicklung eines Verfahrensablaufes zur Herstellung von Batteriezellstapeln mit großformatigem, rechteckigem Stapelformat und kontinuierlichen Materialbahnen

Band 238

Dr.-Ing. Raphael Wagner

Strategien zur funktionsorientierten Qualitätsregelung in der Serienproduktion

Band 239

Dr.-Ing. Christopher Ehrmann

Ausfallfrüherkennung von Ritzel-Zahnstangen- Trieben mittels Acoustic Emission

Band 240

Dr.-Ing. Janna Hofmann

Prozessmodellierung des Fünf-Achs-Nadelwickelns zur Implementierung einer trajektoriebasierten Drahtzugkraftregelung

Band 241

Dr.-Ing. Andreas Kuhnle

Adaptive Order Dispatching based on Reinforcement Learning Application in a Complex Job Shop in the Semiconductor Industry

Band 242

Dr.-Ing. Andreas Greiber

Fertigung optimierter technischer Oberflächen durch eine Verfahrenskombination aus Fliehkraft-Tauchgleitschleifen und Laserablation Prozesseinflüsse und Prozessauslegung

Band 243

Dr.-Ing. Jan Niclas Eschner

Entwicklung einer akustischen Prozessüberwachung zur Porenbestimmung im Laserstrahlschmelzen

Band 244

Dr.-Ing. Sven Roth

Schädigungsfreie Anbindung von hybriden FVK/Metall-Bauteilen an metallische Tragstrukturen durch Widerstandspunktschweißen

Band 245

Dr.-Ing. Sina Kathrin Peukert

Robustheitssteigerung in Produktionsnetzwerken mithilfe eines integrierten Störungsmanagements

Band 246

Dr.-Ing. Alexander Jacob

Hochiterative Technologieplanung

Rekursive Optimierung produkt- und fertigungsbezogener Freiheitsgrade am Beispiel der hybrid-additiven Fertigung

Band 247

Dr.-Ing. Patrick Moll

Ressourceneffiziente Herstellung von Langfaser-Preforms im Faserblasverfahren

Band 248

Dr.-Ing. Eric Thore Segebade

Erhöhung der Verschleißbeständigkeit von Bauteilen aus Ti-6Al-4V mittels simulationsgestützter Zerspanung und mechanischer Mikrotexturierung

Band 249

Dr.-Ing. Shun Yang

Regionalized implementation strategy of smart automation within assembly systems in China

Band 250

Dr.-Ing. Constantin Carl Hofmann

Vorausschauende und reaktive Mehrzieloptimierung für die Produktionssteuerung einer Matrixproduktion

Band 251

Dr.-Ing. Paul Ruhland

Prozesskette zur Herstellung von hybriden Faser-Metall-Preforms

Modellbildung und Optimierung des Binderauftrags und der Drapierung für stabförmige Bauteile

Band 252

Dr.-Ing. Leonard Schild

Erzeugung und Verwendung von Anwendungswissen in der industriellen Computertomographie

Band 253

Dr.-Ing. Benedikt Klee

Analyse von Phaseninformationen in Videodaten zur Identifikation von Schwingungen in Werkzeugmaschinen

Band 254

Dr.-Ing. Bruno Vargas

Wälzschälern mit kleinen Achskreuzwinkeln

Prozessgrenzen und Umsetzbarkeit

Band 255

Dr.-Ing. Lucas Bretz

Function-oriented in-line quality assurance of hybrid sheet molding compound

Band 256

Dr.-Ing. Bastian Rothaupt

Dämpfung von Bauteilschwingungen durch einstellbare Werkstückdirektspannung mit Hydrodehnspanntechnik

Band 257

Dr.-Ing. Daniel Kupzik

Robotic Swing Folding of three-dimensional UD-tape-based Reinforcement Structures

Band 258

Dr.-Ing. Bastian Verhaelen

(De-)Zentralisierung von Entscheidungen in globalen Produktionsnetzwerken

Strategie- und komplexitätsorientierte Gestaltung der Entscheidungsautonomie

Band 259

Dr.-Ing. Hannes Wilhelm Weinmann

Integration des Vereinzelungs- und Stapelbildungsprozesses in ein flexibel und kontinuierlich arbeitendes Anlagenmodul für die Li-Ionen Batteriezellfertigung

Band 260

Dr.-Ing. Florian Stamer

Dynamische Lieferzeit-Preisgestaltung in variantenreicher Produktion

Ein adaptiver Ansatz mithilfe von Reinforcement Learning

Band 261

Dr.-Ing. Patrick Neuenfeldt

Modellbildung des Tauchgleitschleifens zur Abtrag- und

Topografievorhersage an komplexen Geometrien

Band 262

Dr.-Ing. Boris Matuschka

Energieeffizienz in Prozessketten: Analyse und Optimierung von

Energieflüssen bei der Herstellung eines PKW-Getriebebauteils aus 16MnCr5

Band 263

Dr.-Ing. Tobias Schlagenhauf

Bildbasierte Quantifizierung und Prognose des Verschleißes an

Kugelgewindetriebspindeln

Ein Beitrag zur Zustandsüberwachung von Kugelgewindetrieben mittels

Methoden des maschinellen Lernens

Band 264

Dr.-Ing. Benedict Stampfer

Entwicklung eines multimodalen Prozessmodells zur

Oberflächenkonditionierung beim Außenlängsdrehen von 42CrMo4

Band 265

Dr.-Ing. Carmen Maria Krahe

KI-gestützte produktionsgerechte Produktentwicklung

Automatisierte Wissensextraktion aus vorhandenen Produktgenerationen

Band 266

Dr.-Ing. Markus Netzer

Intelligente Anomalieerkennung für hochflexible Produktionsmaschinen

Prozessüberwachung in der Brownfield Produktion

Band 267

Dr.-Ing. Simon Raphael Merz

Analyse der Kinematik und Kinetik von Planetenwalgwindetrieben

Band 268

Dr.-Ing. Rainer Maria Silbernagel

Funktionsorientierte Qualitatsregelung in Produktionsnetzwerken

Qualitatsmanagement in der Produktion hochpraziser Produkte durch netzwerkweite Datenintegration

Band 269

Dr.-Ing. Jonas Nieschlag

Gestaltung und Prozessanalyse fur im Schleuderverfahren hergestellte FKV-Metall-Hohlstrukturen

Band 270

Dr.-Ing. Lukas Matthias Weiser

In-Process Porositatserkennung fur den PBF-LB/M-Prozess

Band 271

Dr.-Ing. Leonard Vincent Overbeck

Digital Twins of production systems

Automated validation and update of material flow simulation models with real data

Band 272

Dr.-Ing. Felix Klenk

Transparenzsteigerung in der Ruckfuhrungslogistik zur Verbesserung der Materialbedarfsplanung fur das Remanufacturing

Band 273

Dr.-Ing. Benjamin Bold

Kompensation der Wrinkle-Bildung beim Kalandrieren von Lithium-Ionen-Kathoden

Vom Prozessverstandnis des Kalandrierens bis zur Prozessoptimierung mittels Anti-Wrinkle-Modul

Band 274

Dr.-Ing. Daniel Gauder

Adaptive in-line Qualitatsregelung in der Mikro-Verzahnungsfertigung

Band 275

Dr.-Ing. Fabian Sasse

Ontologie-basierte Entscheidungsunterstützung für die Auswahl von Messsystemen in unreifen Produktionsprozessen

Band 276

Dr.-Ing. Jonas Hillenbrand

Unsupervised Condition-Monitoring für Kugelgewindetriebe mittels Acoustic Emission

Band 277

Dr.-Ing. Manuela Neuenfeldt

Untersuchung des Einflusses der PBF-LB-Stellgrößen auf die zerspanende Bearbeitung additiv gefertigter Stahlbauteile

Band 278

Dr.-Ing. Marvin Carl May

Intelligent production control for time-constrained complex job shops

Band 279

Dr.-Ing. Philipp Gönzheimer

Automatisierte Bereitstellung von Maschinensteuerungsdaten in Brownfield-Produktionssystemen

Ein Beitrag zur Digitalisierung von Bestandsanlagen am Beispiel von Werkzeugmaschinen

Band 280

Dr.-Ing. Markus Schäfer

Kollisionsvermeidung für Endeffektoren mit integriertem LiDAR-System in der MRK

Ein Beitrag zur Mensch-Roboter-Kollaboration

Band 281

Dr.-Ing. Oliver Brützel

Decision Support System for the Optimisation of Global Production Networks

Development of a Digital Twin for Product Allocation and Robust Line Configuration

Band 282

Dr.-Ing. Gregor Graf

Qualifizierung der Legierung FeNiCoMoVTiAl im LPBF-Prozess unter Verwendung einer Doppellaser-Belichtungsstrategie

Band 283

Dr.-Ing. Maximilian Torsten Halwas

Kompaktwickelprozess zur Erhöhung der Performance von Statoren elektrischer Traktionsantriebe

Band 284

Dr.-Ing. Magnus Kandler

Menschzentriertes Implementierungsvorgehen für das Digitale Shopfloor Management - Förderung der Selbstorganisation unter Berücksichtigung der Mitarbeiterakzeptanz

Band 285

Dr.-Ing. Michael Baranowski

Additive Herstellung endlosfaserverstärkter Kunststoffbauteile mit dem Laser-Sinterprozess

Maschinenteknik, Prozessentwicklung und -modellierung

Band 286

Dr.-Ing. Tobias Storz

Flexibel automatisierte Assemblierung von Li-Ionen-Pouchzellen

Agile Anlagentechnik für die Prozesskette Stapelbildung, Kontaktierung und Heißsiegeln

Band 287

Dr.-Ing. Nikolas Sven Matkovic

Additive Individualization of Continuous-Discontinuous Reinforced Thermoplastics

